UNIVERSIDAD TÉCNICA FEDERICO SANTA MARÍA
DEPARTAMENTO DE FÍSICA
VALPARAÍSO - CHILE

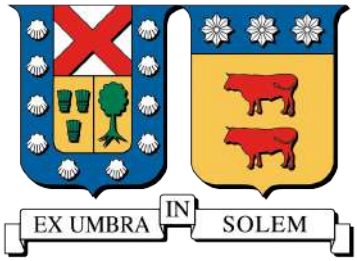

GENERATION OF A LOOK-UP TABLE FOR WATER CHERENKOV DETECTORS AT SWGO FOR THE HIGHEST ENERGY GAMMA RAYS

TAMARA PETROSILLO LAGO

THESIS FOR THE DEGREE OF
MAGÍSTER EN CIENCIAS, MENCIÓN FÍSICA

Advisor	:	Claudio Dib Venturelli
Co-Advisor	:	Sebastián Tapia Araya
Academic Committee:	:	Hayk Hakobyan
		Andrea Chiavassa

July 4, 2025

CONSTANCIA DE VALIDACIÓN Y CONFIDENCIALIDAD DE MONOGRAFÍA A REPOSITORIO ACADÉMICO

1.- IDENTIFICACIÓN DEL TRABAJO ACADÉMICO

Tipo de monografía (marcar una opción): ☐ Memoria o trabajo de título; ☒ Tesis de Postgrado;

Título del trabajo: Generation of a look-up table for water Cherenkov detectors at SWGO for the highest energy gamma rays

Nombre del candidato(a): Tamara Petrosillo Lago

Carrera / Grado: Magíster en ciencias mención Física

Campus: Casa Central Valparaiso **;** **Departamento**: Física

2.- VALIDACIÓN DEL PROFESOR GUÍA/DIRECTOR DE TESIS

Yo, Claudio Dib Venturelli, en mi calidad de profesor(a) guía/director(a) del trabajo académico mencionado anteriormente **DEJO CONSTANCIA** que:

- He revisado esta versión del documento y corresponde a la versión final aprobada del trabajo.
- El trabajo cumple con los requisitos académicos y de formato establecidos por la institución

3.- EVALUACIÓN DE CONFIDENCIALIDAD POR PROPIEDAD INDUSTRIAL

☒ El trabajo **NO contiene información que amerite confidencialidad** y puede ser publicado de inmediato en repositorio con acceso abierto.

☐ El trabajo **CONTIENE** información con potenciales implicancias de propiedad industrial o intelectual y requiere un periodo de confidencialidad (embargo) por:

☐ 6 meses; ☐ 12 meses; ☐ 2 años; ☐ 3 años; ☐ 5 años; ☐ 10 años

Fundamentación de la necesidad de confidencialidad (obligatorio si se solicita embargo):

4.- FIRMAS

Profesor(a) guía o director(a) de memoria o tesis:

Fecha: 11/07/2025 ; **Firma:** 

Estudiante o Candidato(a):

Fecha: 11/07/2025 ; **Firma:** 

Este formulario debe ser insertado como página 2 de la memoria o tesis, completado y firmado por estudiante y profesor(a) antes de la entrega en portal PRISMA de Biblioteca USM.

Acknowledgements

I would like to thank everyone that was there with me throughout this process. To my advisors, thank you very much for your wisdom and patience. Claudio, you have been an essential guide and mentor to me since my undergraduate studies. I have always admired you, not only for your deep understanding of physics, but also for your talent with people and leadership. You have a powerful voice that always gets your ideas across. I hope to use my own voice for good, too. Sebastián, although we met only recently, your help and kindness were crucial to completing this work. You are incredibly smart and hardworking, and in just a few months, you helped me learn more about programming than I ever thought possible. Thank you for your patience and dedication, and for taking on the challenge of being my co-advisor.

To the people that helped me prepare and revise this work, thank you. To Professor Andrea Chiavassa and his team, thank you for guiding me, for believing in my work and taking the time to introduce me to it. Special thanks to Andrea Negro, who was invested in explaining every little detail and solving every doubt I had along the way. To Professor Mário Pimenta and his team, thank you for welcoming me into your research with open arms, and for helping me with the rocks along the way. A special mention to Ruben Conceição, who was very kind, helpful and patient with me. Thank you, Professor Hayk Hakobyan, for taking the time to revise this document.

To my family, I am infinitely grateful for everything you have given me. Mom, you are always the first person I think of when I think of love and commitment. You have always been the most understanding, sincere, and loving woman in my life. You taught me to believe in myself, to listen to my heart, to stay true to my values, and to pursue my goals. You are the reason I am here, and without your unconditional support, I would not be the same. I hope to have you by my side, cheering for me and holding me in your arms when I have doubts, for many years to come. To my dad, thank you for always being the voice of reason and for having the best jokes. You remind me that nothing is too serious, and laughing with you is the best therapy. I admire you most for keeping your peace when everything seems to be going wrong. You have a very special character, and I feel happiest when I make you proud. Pau, thank you for being you. Watching you become such a beautiful and empathetic person fills my heart. Your creativity, attention to detail, and dedication are admirable. Your sense of humor and quick-thinking always amaze me. You are the bridge in our family, and we all have so much to learn from you. I love you very deeply, and I am so proud to be your sister. I look forward to spending my life beside you and seeing you achieve all your goals.

Thank you, Benja, my love and friend. Sharing your company has been a gift. I have learned so much from you, you are truly a free soul. Your intuition is amazing, you always seem to know what has to be done. Your optimistic way of facing life, and your calmness over the things you can't control, are my favorite parts of your charming personality. I love your simple way of seeing the world. Thank you for teaching me how to dance, and for understanding my very sensitive personality. I love you very much, and I love the way you love me. Thank you to my friends, especially Domi, Sergio, and Jorge. You've supported me when I didn't know what I was doing, and you've taught me valuable lessons in both science and life. Thank you, Domi, for your incredible emotional intelligence, for reminding me it's okay to feel my feelings, and for our yoga practices. Thank you, Jorge, for showing me what

unconditional friendship looks like, and for always joining me in my hobby adventures. Thank you, Sergio, for teaching me generosity, and for giving me a place in your pure heart.

Lastly, I would like to thank Fondecyt Regular Grant 1210131, Universidad Técnica Federico Santa María M.Sc. Scholarship, and the SWGO Collaboration, for making this thesis possible.

Abstract

The reconstruction of atmospheric showers induced by high-energy gamma rays is crucial for optimizing the design and performance of the Southern Wide-field Gamma-ray Observatory (SWGO). Although the primary scientific goal of SWGO is the detection of astrophysical gamma rays, the presence of cosmic rays represents a major source of background. Accurate modeling of detector responses is thus essential for enabling future improvements in distinguishing between particle types.

Currently, several design options for the outer array layout of SWGO are under consideration, each with different configurations of Cherenkov detector tanks and photomultiplier tube (PMT) arrangements. In this work, we focus on one specific tank design known as the M1mT1m model—a plastic rotomolded tank equipped with two multi-photomultiplier tube (multiPMT) arrangements. By simulating the interactions of various particle types with this design, we aim to model the resulting Cherenkov light signals.

Given the computational cost of full shower simulations at very high energies, this study contributes to the development of an efficient approach—FastSim—that simulates individual particle arrivals at the detector and constructs a detailed lookup table (LUT) of detector responses. The LUT parametrizes the detector's response across multiple variables, enabling fast and reliable predictions of Cherenkov signals under diverse conditions. The analysis reveals that the multiPMT module provides rich directional information through distinct photoelectron counts and timing patterns across PMTs, which enhances event reconstruction capabilities. Future work will refine the fitting procedures and validate the LUT approach by comparing full simulations with and without the fast simulation method, aiming to confirm its accuracy and computational advantages for large-scale SWGO data processing.

Contents

Chapter 1

Introduction

Astronomical observations have played a key role in the development of scientific knowledge throughout history, and the act of looking to the skies has been a constant presence across cultures. Exploring the universe has always been one of the most fascinating areas of science, and over time, we have developed better and more advanced tools to help us understand the physics behind what we observe. From optical telescopes to X-ray observatories, our ability to study space has grown as technology advances.

In the past, studying phenomena in the sky has proven very beneficial to our society, leading to major scientific breakthroughs with real-world applications. One example is the discovery of antimatter, which was first predicted by Paul Dirac in 1928 through theoretical work in quantum mechanics [1], and later confirmed with the discovery of the positron in 1932 by Carl Anderson while studying cosmic rays [2]. This finding not only changed our understanding of particle physics, but also paved the way for practical technologies and advances in other fields of study, such as medicine. Today, positrons are used in Positron Emission Tomography (PET) scanners, a powerful imaging technique that helps diagnose conditions such as cancer and neurological disorders [3].

Although we have made significant advances in physics and astronomy, many fundamental questions remain unanswered. We continue to explore some of the most fascinating and extreme phenomena in the universe, such as the origins of cosmic rays, the behavior of black holes, and the nature of dark matter. In the last few decades, gamma-ray astronomy has emerged as a fast-developing field, offering one of the most powerful tools available to study the most energetic and extreme processes in the cosmos. It also plays a key role in the broader field of multi-messenger astronomy, where gamma rays are combined with other cosmic messengers such as neutrinos and gravitational waves to provide a more complete understanding of astrophysical events.

Gamma rays are essentially high-energy photons that travel across vast distances, and by studying them we can gain a deeper understanding of our universe. When gamma rays reach Earth, they can interact with the atmosphere and produce a cascade of secondary particles. These interactions, along with other methods of detection, such as observing Cherenkov light or measuring gamma rays directly through space-based observatories, allow us to infer the

properties of the original gamma-ray source.

There are currently many observatories dedicated to searching for gamma-ray sources and developing methods to detect and characterize them. One of the next major projects in this field is the Southern Wide-field Gamma-ray Observatory (SWGO), which will be located in South America and is expected to begin construction during 2026. Until then, ongoing efforts are focused on optimizing its design, evaluating different detector components, and ensuring that its performance and efficiency will meet the scientific goals of the collaboration.

In this context of optimizing the design of SWGO, the collaboration is running simulations to test different detector designs and array layouts. However, this process faces a major challenge: since SWGO is aimed at detecting very high-energy particles, the simulations involved are extremely time-consuming and computationally demanding. However, efficient simulation strategies are essential, not only to make the best use of available resources, but also to ensure that the final design makes a strong and meaningful contribution to the field.

One of the solutions currently being developed to tackle the challenge of simulating high-energy particle showers is a software tool called FastSim (short for Fast Simulation). Its main goal is to predict the detector response to a given particle shower without having to simulate every individual interaction, since these are the most computationally expensive steps.

As part of this effort, this thesis aims to provide one of the components required by FastSim: the Lookup Table (LUT). This LUT contains precomputed detector responses to individual particles, and is essential for FastSim to accurately approximate the full simulation of extensive air showers. In particular, this work focuses on building the LUT corresponding to one of the water Cherenkov detector (WCD) designs currently under consideration by the collaboration. This involves simulating individual particles under controlled conditions to characterize how the detector responds to each type, energy, and geometry of incidence. The resulting LUT will then be integrated into the fastsim framework to evaluate the performance of this specific detector configuration as part of the overall optimization process.

1.1 Astrophysical Phenomena in Gamma-ray Astronomy

Gamma-ray astronomy is the branch of astrophysics focused on the detection and study of gamma rays emitted by different sources throughout the universe. Gamma rays are the most energetic form of electromagnetic radiation, typically produced in environments involving extreme conditions, with photon energies ranging from about 100 keV (10^5 eV) to beyond 100 TeV (10^{14} eV). Because of their high energy, they provide unique insight into physical processes that cannot be studied through other wavelengths, making them a powerful tool for understanding the most violent and energetic events in the cosmos.

The path toward gamma-ray astronomy began in 1900 when Paul Villard first identified gamma rays while studying the products of radioactive decay [5]. At the time, this new form of penetrating radiation was understood only in the context of terrestrial phenomena, and

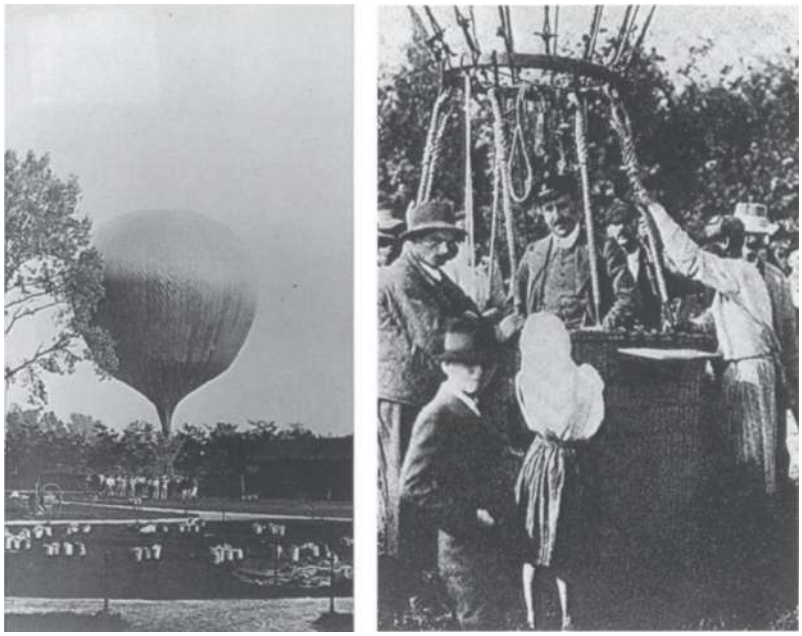

Figure 1.1: Victor Hess discovers Cosmic Rays [4]

its astrophysical relevance remained unexplored. A major breakthrough came in 1912, when Victor Hess conducted a series of balloon flights using electroscopes to measure ionizing radiation as a function of altitude [6]. His observations revealed that ionization increased with height, which he attributed to a penetrating radiation incident on the atmosphere from above. This led to the discovery of cosmic rays: a stream of high-energy particles, mostly protons and atomic nuclei, originating from space [7].

Although gamma rays themselves were not detected in these early experiments, Hess's discovery marked the beginning of high-energy astrophysics. As our understanding of cosmic rays advanced, it became increasingly evident that similarly energetic photons (gamma rays) could also originate from extreme astrophysical environments. Theoretical predictions of such emissions eventually led to their detection in space, beginning with satellite-based observations in the 1960s [8]. This motivated further research focused on understanding gamma rays themselves, setting the stage for investigating their nature and what they can reveal about cosmic events.

Several distinctive properties of gamma rays make them well-suited for probing the environments in which they originate. As electrically neutral particles, gamma rays do not interact with the electromagnetic field and therefore travel in straight lines through space. This lack of deflection allows astronomers to trace their paths back to their astrophysical sources with high directional accuracy, providing critical information about the location and nature of the emitting objects [4]. Additionally, because they can originate from nuclear reactions or particle interactions, gamma rays can provide information about the physical and chemical conditions of their sources, offering valuable clues about the environments in which they are produced.

Although gamma rays are very useful for studying extreme astrophysical events, they are

not easy to detect. When they reach Earth's atmosphere, they interact almost immediately with atomic nuclei and other particles, producing a cascade of secondary particles known as an extensive air shower. As a result, ground-based detection is only possible through indirect methods that observe the byproducts of these interactions. Alternatively, gamma rays can be detected directly by space-based instruments aboard satellites, which operate above the atmosphere.

Despite these challenges, gamma rays are produced in a wide range of astrophysical contexts, making them a rich subject of study. The following sections will look into some of the main examples.

1.1.1 Transient Sources

Transients are astrophysical phenomena or objects that evolve or appear on short timescales, ranging from milliseconds to years, which is brief when compared to the typical lifespans of astrophysical processes, often on the order of millions or even billions of years. They can be detected across the electromagnetic spectrum, from radio to gamma rays, as well as through gravitational waves and neutrinos in the context of multi-messenger astronomy [9]. Many transient events are associated with high-energy gamma-ray emission, such as gamma-ray bursts (GRBs) and flaring episodes from active galactic nuclei (AGNs).

Gamma-Ray Bursts

Gamma-Ray Bursts (GRBs) are among the most luminous phenomena in the universe, releasing in seconds more energy than the Sun will emit over its entire lifetime. While they are on, they outshine every other source of gamma-rays in the sky. First discovered in the late 1960s by the Vela satellites [8], GRBs quickly became one of the most intriguing puzzles in astrophysics. They appear as brief flashes of gamma radiation, lasting from milliseconds to several minutes, without any immediate precursor or repetition. Their sudden and unpredictable nature introduced a new observational paradigm: the study of phenomena that appear only once and vanish rapidly [10].

Initially, the origin of GRBs was the subject of intense debate. Without distance measurements, early hypotheses ranged from nearby neutron stars to sources at cosmological distances. However, the isotropic distribution of bursts across the sky and the absence of parallax or solar system signatures ultimately supported an extragalactic origin [11]. Today, GRBs are broadly classified into two categories: long-duration bursts, associated with the collapse of massive stars, and short-duration bursts, likely resulting from the merger of compact objects such as neutron stars [12].

Major observational advances, particularly from the Swift satellite, have confirmed the existence of these two distinct progenitor classes and enabled the detection of afterglows across the electromagnetic spectrum. Swift has also extended the reach of GRB studies to redshifts beyond 6, demonstrating their utility as probes of the early universe. Despite

this progress, many questions remain open, especially regarding the mechanisms behind their extreme energy output and the structure of the jets involved. As gravitational-wave and high-energy neutrino observatories join the effort, GRBs continue to stand as key targets in the era of multi-messenger astrophysics.

Active Galactic Nuclei

Active Galactic Nuclei (AGNs), as the name suggests, are extremely energetic regions located at the centers of certain galaxies. The emissions from AGNs span the entire electromagnetic spectrum (from radio waves to gamma rays) and exhibit features such as rapid variability, high luminosity, and strong non-thermal components, all of which indicate that their origin is not stellar [13]. The most widely accepted model attributes this energy output to the accretion of matter onto a supermassive black hole, typically ranging from millions to billions of solar masses, situated at the galaxy's core [14].

During this active phase, the black hole grows by consuming surrounding material, releasing gravitational energy in the form of radiation and sometimes collimated, relativistic jets. These jets can carry a substantial fraction of the accretion energy and are capable of accelerating particles to extremely high energies. When the jet is aligned closely with our line of sight, the object is classified as a blazar: a subclass of AGN that dominates the extragalactic gamma-ray sky. In addition to powering jets and radiation, this energy output is believed to regulate star formation in the host galaxy through a process known as AGN feedback, although the details of how and when this occurs remain uncertain [15]. Despite significant progress, key questions persist regarding how jets are launched and how energy is transported and dissipated to produce the observed radiation. High-energy gamma-ray observations, particularly those from instruments like Fermi-LAT and AGILE, have been instrumental in addressing these questions and will continue to guide the development of theoretical models [16].

1.1.2 PeVatrons

PeVatrons are astrophysical accelerators capable of energizing particles such as protons, nuclei, or electrons to at least 10^{15} eV (1 PeV). This energy scale marks the so-called "knee" of the cosmic-ray spectrum (a steepening observed around 3 PeV that is widely interpreted as marking the upper limit of Galactic accelerators) and represents a fundamental threshold in high-energy astrophysics. The study of PeVatrons is tightly connected to the question of the origin of Galactic cosmic rays (CRs).

PeVatrons are typically classified as hadronic or leptonic, depending on the nature of the primary accelerated particles. In hadronic PeVatrons, gamma-ray emission results mainly from inelastic collisions between protons and ambient matter or radiation fields (pp and $p\gamma$ interactions), producing neutral pions that decay into high-energy photons. Approximately 10% of the energy from the parent protons is transferred to these secondary particles, so for protons with energies around 1 PeV, a gamma ray in the 100 TeV range is produced. These processes are also expected to produce neutrinos, providing a complementary observational

signature [17]. In leptonic PeVatrons, by contrast, gamma rays are produced via inverse Compton (IC) scattering, where relativistic electrons boost low-energy photons, such as those from the cosmic microwave background (CMB), to very high energies. For instance, 1 PeV electrons interacting with CMB photons can generate gamma rays up to about 370 TeV [18].

From these perspectives, ultra-high-energy (UHE, $\mathrm{E} > 100$ TeV) gamma-ray emission emerges as a key observational probe for exploring PeVatron sources. Since cosmic rays are deflected by Galactic magnetic fields, the direct detection of hadronic PeVatrons is not feasible. This limitation makes indirect signatures, like UHE gamma rays and neutrinos, essential for their study, emphasizing the importance of multi-wavelength (MWL) and multi-messenger approaches. Ground-based gamma-ray observatories like HAWC, LHAASO, and the upcoming SWGO are key instruments in the hunt for Galactic PeVatrons.

Several classes of astrophysical objects have been proposed as potential Galactic PeVatrons. These include pulsar wind nebulae (PWNe), young massive star clusters, and binary systems with strong stellar winds, each offering different environments for particle acceleration. However, one the most prominent candidates are supernova remnants (SNRs), long considered the main sources of Galactic cosmic rays below the "knee" of the energy spectrum.

SNRs are formed by the explosive deaths of massive stars and generate expanding shock waves capable of accelerating particles via diffusive shock acceleration. Their energetics, prevalence in the Galaxy, and observed non-thermal emission make them natural candidates for cosmic-ray acceleration. Despite decades of study and numerous detections of TeV gamma-ray emission, conclusive evidence for proton acceleration up to PeV energies remains elusive [19]. SNRs also play a key role in shaping the interstellar medium: they heat surrounding gas, distribute heavy elements formed in stellar interiors, and fill the universe with the material necessary to form other stars, planets, and life itself. While around 300 SNRs are currently cataloged in the Milky Way, population studies suggest many more remain undetected [20].

1.1.3 Dark Matter

Although the evidence for astrophysical dark matter (DM) is extensive, ranging from galactic rotation curves and galaxy cluster dynamics to observations of the cosmic microwave background, its elusive nature and the lack of direct detection continue to puzzle scientists [21]. One of the primary directions for DM research is the indirect search for Weakly Interacting Massive Particles (WIMPs): hypothetical particles in the GeV–TeV mass range with weak-scale interactions. In this mass range, WIMP annihilation or decay into secondary particles, such as gamma rays, could produce observable signatures in astrophysical environments [22]. These signals are expected to be strongest in regions of high dark matter density, such as the Galactic Center and nearby satellite galaxies.

Dark matter detection is therefore one of the key scientific goals of the Southern Wide-field Gamma-ray Observatory (SWGO). Its location in the Southern Hemisphere grants it privileged access to the Galactic Center and the Galactic halo—regions believed to host dense concentrations of DM. At the highest energies, where SWGO's sensitivity peaks, astrophysical backgrounds are expected to be minimal, enabling the potential detection of extremely faint

DM signals. The Galactic Center, in particular, is predicted to be the brightest source of DM annihilation in the gamma-ray sky by several orders of magnitude. Even in the presence of background contamination from conventional astrophysical sources, it remains one of the most promising regions to uncover signs of new, massive particles [23].

While WIMPs remain one of the most studied dark matter candidates, the lack of conclusive signals has led to growing interest in alternative scenarios, such as axion-like particles or primordial black holes. These possibilities reflect the wide range of viable dark matter models still under consideration, highlighting the need for diverse and complementary approaches across theory and observation.

1.1.4 Multi-Messenger Context

Multi-messenger astronomy refers to the coordinated study of astrophysical phenomena through different types of signals, or "messengers": electromagnetic radiation (ranging from radio to gamma rays), gravitational waves, high-energy neutrinos, and cosmic rays. This integrated approach allows us to probe the universe in ways that are not possible using a single messenger alone. By combining information from multiple channels, we can better constrain the properties of astrophysical sources, test models of high-energy processes, and uncover connections between different classes of events.

An example of this approach was the detection of the gravitational-wave event GW170817, associated with a binary neutron star merger and accompanied by a short gamma-ray burst and a kilonova. It was the first time that gravitational waves and electromagnetic radiation were observed from the same source. This event not only confirmed that such mergers are a source of short GRBs, but also demonstrated that they are sites of r-process nucleosynthesis, responsible for the formation of many of the universe's heaviest elements, such as gold and platinum [24]. The optical and infrared emission from the kilonova provided strong evidence of this synthesis, showcasing the power of multi-messenger efforts to understand fundamental astrophysical processes.

As part of this growing field, gamma-ray observatories like SWGO will play a key role in identifying potential counterparts to neutrino or gravitational-wave events, offering critical temporal and directional information. While SWGO is primarily designed for gamma-ray detection, its sensitivity to cosmic rays and the potential for real-time alerts make it a valuable contributor to future multi-messenger efforts.

1.2 Extensive Air Showers

When a high-energy cosmic particle coming from outer space reaches the top of Earth's atmosphere, it is very likely to undergo a nuclear interaction within a few tens of kilometers (typically less than 50 km) due to the relatively high density of atmospheric nuclei at those altitudes [25]. The atmosphere, composed mainly of nitrogen and oxygen, acts as a dense target for these incoming primaries, which may include protons, heavier nuclei, electrons, and

gamma rays. Upon interacting with an atmospheric nucleus, the primary particle produces a number of secondary particles, each carrying a fraction of the original energy. These secondary particles can then interact again, triggering further particle production. The result is a cascading process that develops over several generations, forming what is known as an Extensive Air Shower, or EAS (see Figure 1.2).

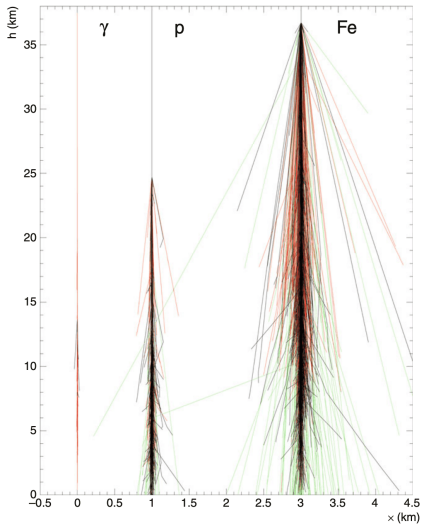

Figure 1.2: Side view of trajectories of particles of energy ≥ 10 GeV of a photon, a proton and an iron nucleus initiated shower having a total primary energy of 105 GeV each. The electromagnetic component is shown in red, hadrons are black and muons green. The widely spread particles in the lower region of the atmosphere in the hadron showers are mostly muons. Taken from [25].

The development and structure of the air shower depend strongly on the type of primary particle. Gamma rays initiate electromagnetic (EM) showers, the interactions dominated by pair production and bremsstrahlung, with resulting particles being electrons, positrons, and photons. In contrast, hadronic primaries (such as protons or iron nuclei) produce hadronic showers, which involve the production of mesons and baryons through strong interactions. These hadronic showers also give rise to electromagnetic sub-showers via the decay of neutral pions into gamma rays. Thus, while both types of showers can have electromagnetic components, the underlying processes and shower profiles are distinct.

1.2.1 Hadronic EAS

Hadronic Extensive Air Showers (EAS) is a general term used to describe showers that are initiated by primary particles other than gamma rays. These primaries include protons and heavier nuclei, collectively referred to as cosmic rays. Unlike gamma-induced showers, hadronic showers proceed through strong nuclear interactions, which involve multiple reaction channels such as nucleon-nucleon scattering and meson production. These processes can generate a wide variety of secondary particles, including hadrons, photons, electrons, muons, and neutrinos [26].

Hadronic showers typically exhibit a broader and more irregular lateral distribution compared to electromagnetic (EM) showers. This is primarily due to the nature of hadronic interactions, where secondary particles, particularly pions and kaons, are produced with significant transverse momentum (p_T) relative to the primary particle's direction. On average, secondary hadrons are produced with a p_T of approximately $350 - 400$ MeV, nearly independent of the primary particle's energy. This large transverse momentum causes the shower to spread more widely and appear less collimated than EM showers.

One of the key signatures of hadronic showers is the presence of muons. These are mainly produced from the decay of charged pions ($\pi^{\pm} \rightarrow \mu^{\pm} + \nu_{\mu}$) and kaons, which are abundant in hadronic cascades (see Figure 1.3. In contrast, muons are nearly absent in gamma-ray-induced showers, making muon content an important observable for gamma/hadron separation in ground-based detectors. Additionally, since many pions are produced at later stages of the shower and are relatively low in energy, the muons they decay into often have a broad lateral spread, extending far from the shower core.

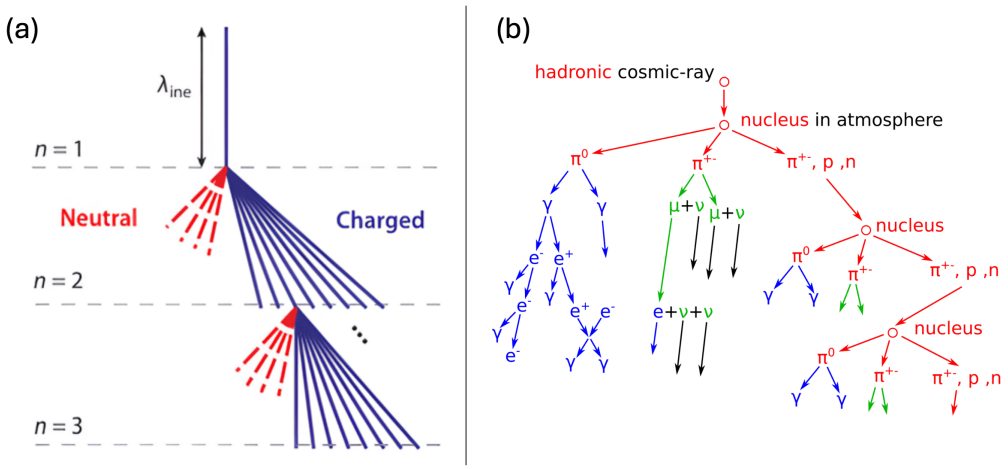

Figure 1.3: Hadronic Shower Development. (a) The hadronic component of a hadron-induced shower; dashed lines represent neutral particles (π^0), and solid lines represent charged particles ($\pi^{\pm}$). Only one charged hadron interaction is shown for each generation. From [26]. (b) A primary cosmic ray interacts in the atmosphere, producing a cascade of secondary particles. The development of the shower through the atmosphere includes the production of hadrons, muons and electromagnetic sub-showers. From [27].

1.2.2 Electromagnetic EAS

Electromagnetic (EM) showers are particle cascades initiated by a high-energy gamma ray (or sometimes an electron or positron) interacting with the Earth's atmosphere. The first interaction of a gamma ray with an atomic nucleus typically results in pair production, creating an electron and a positron. These charged particles, in turn, lose energy mainly through bremsstrahlung as they travel through the electric fields of atmospheric nuclei, emitting more photons. These photons can again undergo pair production, continuing the cycle. This repeating chain of pair production and bremsstrahlung results in an electromagnetic

cascade [28] (see Figure 1.4).

Compared to hadronic showers, EM showers are more compact and symmetric, with most secondary particles being strongly collimated in the forward direction and staying close to the shower axis. This gives them a narrow lateral profile and makes them appear more "tidy" and organized in particle detector arrays. In contrast, hadronic showers tend to be wider and more irregular due to the higher transverse momentum of secondary hadrons [29].

The main constituents of EM showers are photons, electrons, and positrons, with only a negligible fraction of other particle types. Muons can appear, but their production is highly suppressed due to the much larger mass of the muon compared to the electron (by a factor of about 200), which raises the energy threshold for muon pair production significantly.

Importantly, EM showers lack the hadronic core present in cosmic-ray-induced showers. As a result, their muon content is minimal, typically around 1% of that observed in hadronic showers of similar energy [26]. This low muon yield is one of the key distinguishing features that gamma-ray observatories like SWGO exploit to separate gamma-ray events from the overwhelming background of cosmic rays.

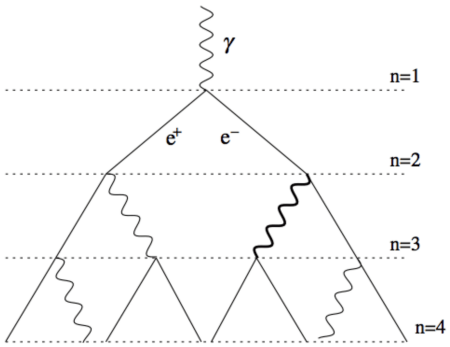

Figure 1.4: Electromagnetic Shower Development: A high-energy gamma-ray initiates a particle shower, producing e^-e^+ pairs and secondary photons through successive interactions developing in new generations n of the shower. From [30]

1.3 Gamma-ray Detection

Gamma rays cannot be directly detected from the ground, as they are absorbed by the Earth's atmosphere. However, the secondary particles and radiation produced during the development of the extensive air showers (EAS) they initiate can be observed using various techniques. One of the earliest and most successful detection methods involves observing the ultraviolet fluorescence light emitted by atmospheric nitrogen when excited by shower particles. This technique, employed by observatories like the Pierre Auger Observatory, allows for precise reconstruction of the longitudinal development of the shower, but it is limited to operation during dark, moonless nights, leading to a duty cycle of roughly 10–15% [31].

Radio detection has emerged as a promising complementary technique. The radio emission stems from coherent mechanisms like geomagnetic deflection of charged particles and the Askaryan effect [32]. Radio detectors can operate continuously under virtually all weather conditions, making them a useful complement to optical systems [33]. Another method employs scintillator arrays, which detect secondary charged particles that reach the ground by converting deposited energy into light. While useful for sampling particle densities at the surface, these detectors lack the ability to discriminate well between electromagnetic and hadronic components [34].

In addition to ground-based methods, gamma rays can be directly detected from space. Satellites like Fermi-LAT and AGILE are equipped with pair-conversion detectors that allow for the reconstruction of both energy and arrival direction of the incoming photon [35]. These instruments are ideal for observing gamma rays below about 100 GeV, but their small collection areas limit their sensitivity at higher energies.

The following sections focus on ground-based Cherenkov techniques, which are designed to capture the Cherenkov light emitted by relativistic charged particles passing through water, the atmosphere, or other material medium. We will put special attention into Water Cherenkov Detectors (WCDs), the technology that SWGO will be built around. These detectors are particularly well-suited for high-energy gamma ray detection due to their large field of view, high duty cycle, and sensitivity to shower particle content.

1.3.1 Cherenkov Radiation

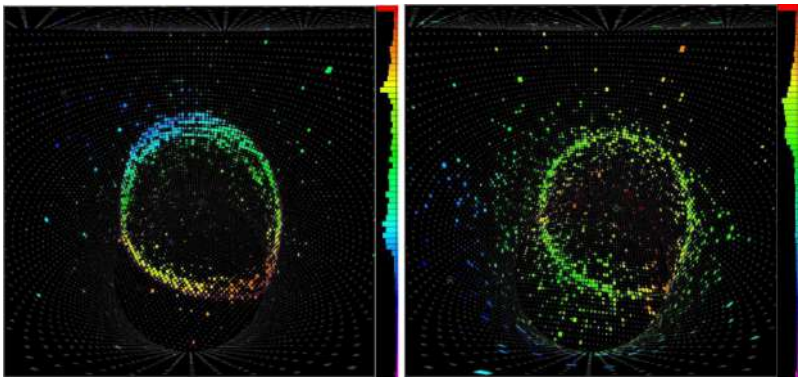

Figure 1.5: Two events displayed for the Super-Kamiokande detector. Left: a muon event. Notice the cleaner outer ring of the Cherenkov cone. Right: an electron event. Notice that the ring is much more ragged due to the many particles of the electromagnetic shower and multiple scattering of the shower particles. From [36].

Cherenkov radiation occurs when a charged particle travels inside a dielectric medium at a velocity higher than the phase velocity of light in that medium. This effect was discovered by Pavel Cherenkov in 1934, for which he was awarded the 1958 physics Nobel Prize. This phenomenon is analogous to a sonic boom, where an object moves faster than the speed of sound, resulting in a shockwave. In the case of Cherenkov radiation, the charged particle

induces a shockwave of electromagnetic radiation, manifesting as a characteristic blue glow, commonly observed in nuclear reactors submerged in water.

From a classical perspective, as the charged particle moves through the medium, it polarizes the surrounding molecules. When these molecules return to their ground state, they emit photons. If the particle's speed is less than the speed of light in the medium, these emissions are out of phase and cancel out. However, if the particle's speed exceeds the light speed in the medium, the emissions constructively interfere, resulting in the observed Cherenkov radiation.

The radiation is emitted in a conical shape, as shown in Figure 1.6, with the angle θ determined by the relation:

$$\cos\theta = (n\beta)^{-1}$$

where n is the refractive index of the medium and $\beta = v/c$ is the ratio of the particle's velocity to the speed of light in a vacuum. This relationship indicates that the emission angle depends on both the particle's speed and the optical properties of the medium.

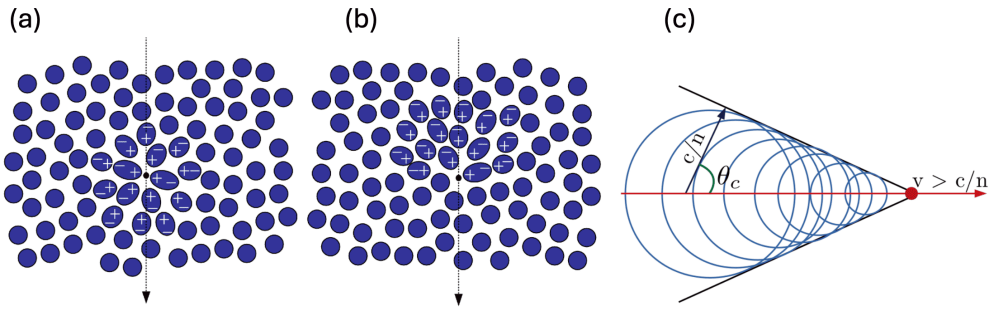

Figure 1.6: Diagram depicting polarization of molecules while non-relativistic and relativistic charged particle travelling through a dielectric medium are shown in (a) and (b), respectively. (c) Diagram showing the production of Cherenkov light and the geometric expansion of the wave-front. From [37]

The number of Cherenkov photons emitted per unit interaction depth X by a medium with refractive index $n(\lambda)$, over a wavelength interval $\lambda_1 \leq \lambda \leq \lambda_2$, is given by [38]:

$$\frac{\mathrm{d}N}{\mathrm{d}X} = 2\pi\alpha\left(1 - \frac{1}{\beta^2 n^2(\lambda)}\right)\left(\frac{1}{\lambda_2} - \frac{1}{\lambda_1}\right), \tag{1.1}$$

where $\alpha = (e^2/\hbar c)$ is the fine structure constant. This expression holds under the assumption that $n(\lambda)$ remains approximately constant over the wavelength interval.

For more general cases where the refractive index varies significantly with frequency, the Frank–Tamm formula can be used [39]:

$$\frac{\partial^2 E}{\partial x \partial \omega} = \frac{q^2}{4\pi}\mu(\omega)\omega\left(1 - \frac{c^2}{v^2 n^2(\omega)}\right) \tag{1.2}$$

which gives the energy emitted per unit frequency per unit path length of a charged particle. Here, $\mu(\omega)$ and $n(\omega)$ denote the frequency-dependent permeability and refractive index of the medium, respectively.

The Geant4 framework (see 2.3.1) includes internal routines for simulating Cherenkov photon emission based on these theoretical expressions. For each charged particle propagating through a medium, Geant4 checks whether the Cherenkov condition is satisfied and, if so, generates photons according to the appropriate spectral distribution.

Cherenkov radiation falls within the visible light spectrum, and can be detected using photomultipliers. These measurements reveal information about the characteristics of the original particle, such as its type, energy and direction (see Figure 1.5).

1.3.2 Ground-based Detectors

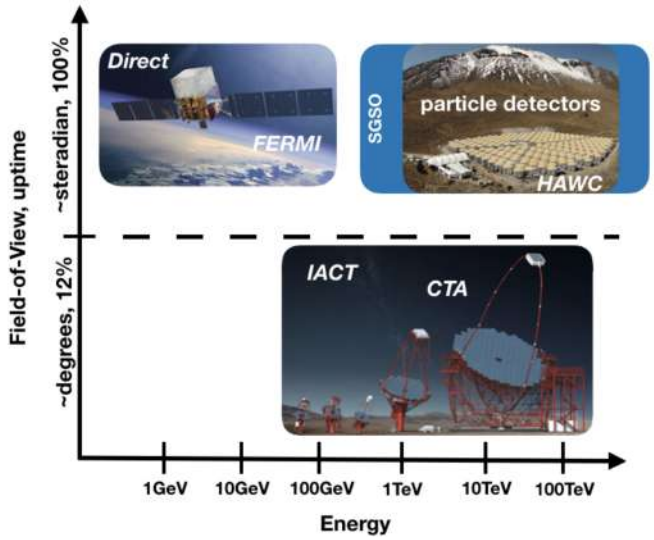

Figure 1.7: Illustration of the various complementary detection techniques of high-energy gamma rays. From [23].

Ground-based detection has become the dominant technique for observing high-energy gamma rays today. While satellites were responsible for the initial discovery of cosmic gamma-ray sources in the 1960s, their role is now primarily limited to lower-energy gamma rays (up to a few hundred GeV). This is due to the extremely low flux of the highest energy gamma rays, which is on the order of 1 particle per square kilometer per year for TeV–PeV energies, which makes it impractical to rely on the relatively small effective area of satellite-based instruments [40]. While satellites like Fermi-LAT offer excellent angular and energy resolution, they are limited by size and exposure. To study these rare high-energy events, large-scale observatories on the ground are required. These installations monitor vast areas—often several square kilometers, and rely on the detection of the extensive air showers (EAS) produced when gamma rays interact with the Earth's atmosphere.

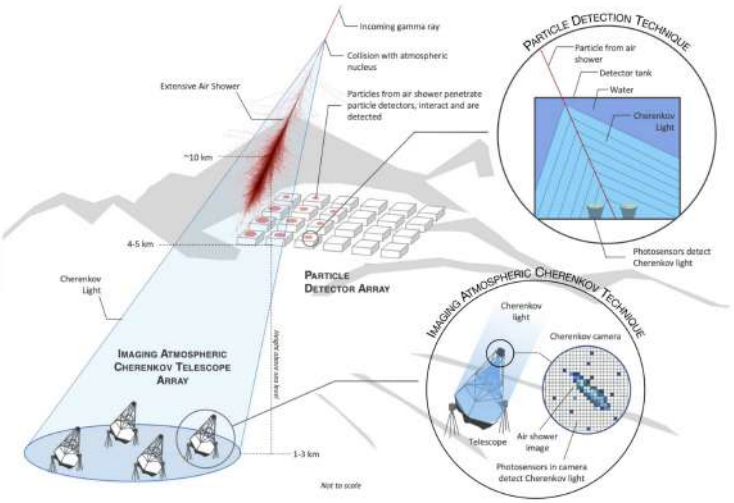

Figure 1.8: Schematic representation of air-shower detection at ground level with a water Cherenkov detector and the imaging atmospheric Cherenkov telescopes. From [41]

Imaging Air Cherenkov Telescopes (IACTs)

Imaging Air Cherenkov Telescopes (IACTs) detect Cherenkov light produced by the charged particles in extensive air showers initiated by high-energy gamma rays and cosmic rays. This Cherenkov light is emitted as the air shower propagates through the atmosphere and is focused by large segmented mirrors onto a camera composed of sensitive photon detectors such as photomultiplier tubes (PMTs) or silicon photomultipliers (SiPMs). The resulting images of gamma-ray showers typically appear elliptical, with orientation and shape encoding information about the shower direction and geometry. When multiple telescopes observe the same shower (stereoscopic mode), its arrival direction can be reconstructed from the intersection of the major axes of the shower images. The energy of the primary gamma ray is estimated from the total light intensity, corrected for atmospheric effects and impact parameter.

IACTs rely on image shape and distribution to distinguish gamma-ray showers from the dominant hadronic background. Modern analysis techniques go beyond classical geometric reconstruction and use likelihood-based methods, comparing recorded images with libraries of simulated templates. Despite their high sensitivity and low energy thresholds (tens of GeV to several TeV), IACTs are background-limited at low energies and strongly affected by observational constraints. They operate only during clear, moonless nights, limiting their duty cycle to about 10%. Furthermore, their narrow field of view and pointing nature make them best suited for deep observations of known sources or follow-up of transient alerts. Major current facilities include H.E.S.S. in Namibia [42], MAGIC and FACT on La Palma, and VERITAS in the US [43]. The next-generation Cherenkov Telescope Array (CTA) [44] will extend this capability with dual sites in both hemispheres.

Water Cherenkov Detectors (WCDs)

Water Cherenkov Detectors (WCDs) offer an alternative ground-based method for gamma-ray detection. Instead of capturing light in the atmosphere, they measure Cherenkov radiation produced by the secondary particles in air showers as they pass through water. WCDs are typically composed of large pools or modular tanks filled with several meters of purified water and instrumented with PMTs. Event reconstruction in WCDs uses both the timing and the magnitude of the Cherenkov light signals. The arrival direction of the primary gamma-ray photon is determined by the timing gradient of the shower front detection across the PMT array. The energy is determined by the total signal (i.e. the amount of light) observed across the array. The spatial distribution of signal magnitudes across the array can be used to distinguish gamma-ray induced air showers from those induced by cosmic rays (the primary source of backgrounds for gamma-ray searches).

Unlike IACTs, WCDs are not limited by daylight or weather. Their enclosed, light-tight design allows for continuous operation, with duty cycles close to 100%. While they have higher energy thresholds (typically hundreds of GeV, depending on altitude), they are capable of detecting very high energy gamma rays into the PeV regime. Their wide field of view and high uptime make them particularly suited for surveying the sky and detecting transient or rare events. This technique was first demonstrated by the Cygnus and Milagro experiments, and is currently used by HAWC in Mexico [45] and LHAASO in China [46]. SWGO, currently in development, will expand these capabilities in the Southern Hemisphere. The differences between IACTs and WCDs enable complementary capabilities for observing the gamma-ray sky, as detailed in Table 1.1.

	IACT Arrays	Ground-Particle Arrays
Field-of-view diameter	$3° - 10°$	$90°$
Duty cycle	$10\% - 30\%$	$> 95\%$
Energy range	$30\mathrm{GeV} - > 100\mathrm{TeV}$	$\sim 500\mathrm{GeV} - > 100\mathrm{TeV}$
Angular resolution	$0.05° - 0.02°$	$0.4° - 0.1°$
Energy resolution	$\sim 7\%$	$60\% - 20\%$
Background rejection	$> 95\%$	$90\% - 99.8\%$

Table 1.1: Comparison of typical performance of current and planned IACT arrays and ground particle arrays for gamma-ray astrophysics. From [23].

1.4 The Southern Wide-field Gamma-ray Observatory (SWGO)

The Southern Wide-field Gamma-ray Observatory (SWGO) collaboration was established in 2019, emerging from the convergence of several earlier initiatives, including the SGSO Alliance [23]. The central concept behind SWGO is the development of a gamma-ray observatory based on ground-level particle detection, featuring a near-continuous duty cycle of around 90% and a wide field of view on the order of a steradian. The proven success of similar detectors, such as HAWC, strongly motivated the construction of the first water Cherenkov detector (WCD) dedicated to gamma-ray astronomy in the Southern Hemisphere.

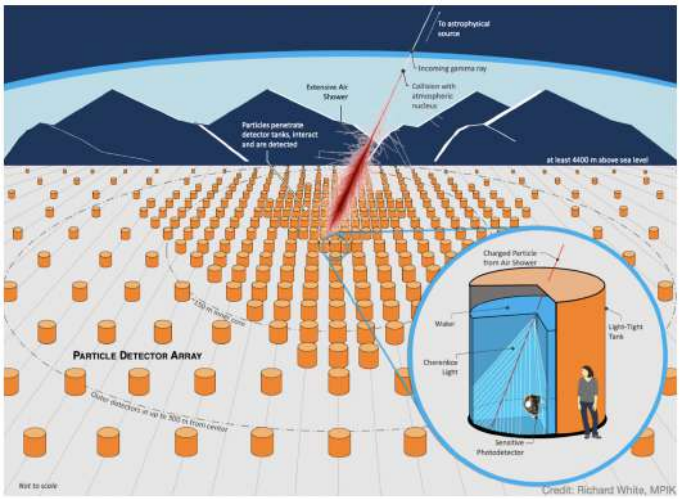

Figure 1.9: Layout of the SWGO detector array. Each orange cylinder represents a Cherenkov detector, while the red burst illustrates a particle shower arriving at the array. From [47].

From the begining, South America was the target region for SWGO, ideally at a latitude between -30 and -10. This range optimizes sky coverage for southern-sky targets and provides unique access to the Galactic Center, which is not visible to observatories in the Northern Hemisphere. In order to detect air showers close to their maximum development, the observatory must be built at high altitude of at least 4.4 km above sea level, where the density of secondary particles is greatest. Based on previous observations from experiments like HAWC and LHAASO, SWGO aims to cover an energy range spanning from hundreds of GeV up to PeV energies.

To improve upon the sensitivity of its predecessors, SWGO will feature a dense, high fill-factor core array with a total area significantly larger than HAWC. This will be complemented by a sparser outer array, designed to enhance sensitivity to the highest-energy gamma rays by extending the effective area and improving reconstruction of very large showers.

1.4.1 The selected site

In July 2024, the preferred site for SWGO was officially selected. The observatory will be located near San Pedro de Atacama, in the Calama commune, northern Chile. The site lies within the Atacama Astronomical Park, specifically in an area known as Pampa La Bola (coordinates: $22°$ S, $67°$ W). Pampa La Bola is placed on a broad plateau at the summit of the Andes, at an altitude of 4,770 meters above sea level (See Figure 1.11).

The surrounding region is already home to several prominent astronomical facilities, most notably the Atacama Large Millimeter/submillimeter Array (ALMA) [48], which underscores the site's proven suitability for long-term scientific operations. The environmental and logistical conditions at Pampa La Bola make it an excellent location for the SWGO array. A backup

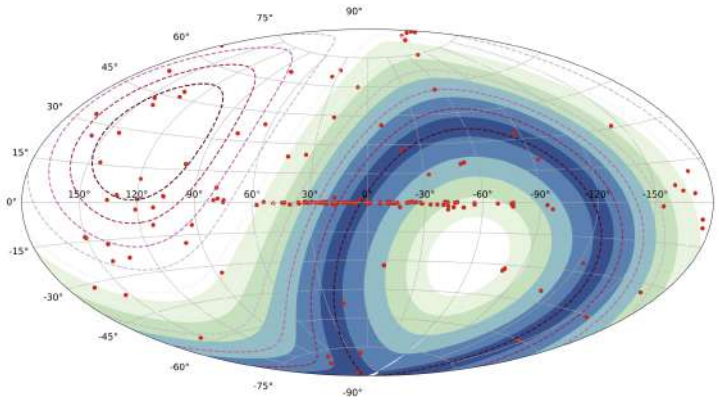

Figure 1.10: Sky-map in galactic coordinates showing the complementarity of the visibility ranges between HAWC and SWGO. The color bands correspond to $10°$ in zenith angle (up to $45°$) for SWGO at latitude $25°$ South. The dashed contours show the same for HAWC, with the darkest line marking the edge of the field-of-view at $45°$ from zenith. The red markers correspond to TeV gamma-ray sources discovered by H.E.S.S., MAGIC and VERITAS. From [23].

site has also been identified: Imata, located in the Arequipa district of southern Peru. The Imata site is located at 4450 meters above sea level at a latitude of $15.9°S$.

1.4.2 Array Layout and Detector stations

As its southern hemisphere counterpart, the structure and operation of SWGO are strongly inspired by HAWC. Like HAWC, SWGO will consist of numerous Water Cherenkov Detectors (WCDs) distributed over a large area to maximize the instrumented surface and enhance detection capabilities.The SWGO array is composed of independent WCD units arranged in a three-zone configuration:

- Zone 1, the central core, is a disk with a radius of 156 m, featuring a 70% fill factor and housing $2,587$ detectors. This region is densely packed, with minimal spacing between tanks—just enough to allow for construction and maintenance. Its high density is crucial for achieving sensitivity to low- and medium-energy gamma rays, as well as for the detection of transient events and distant gamma-ray sources.
- Zone 2 surrounds Zone 1 as a concentric ring, with an inner radius of 156 m and an outer radius of 400 m. It has a reduced fill factor of 4%, containing 792 detectors.
- Zone 3 is the outermost region, extending from 400 m to 560 m in radius. This area has a fill factor of 1.7%, with 384 detectors. The inclusion of these outer zones expands the instrumented area to approximately $1\mathrm{km}^2$, enhancing the sensitivity to high-energy gamma rays.

For the inner zones (Zones 1 and 2), the SWGO Collaboration has adopted a double-layer tank design. Each tank consists of two optically separated detection volumes: the upper layer,

Figure 1.11: Location of the preferred SWGO site Pampa La Bola, Atacama Astronomical Park, Chile. The photo in the bottom right shows the view of the site and the elevation contour of the site. From SWGO Collaboration.

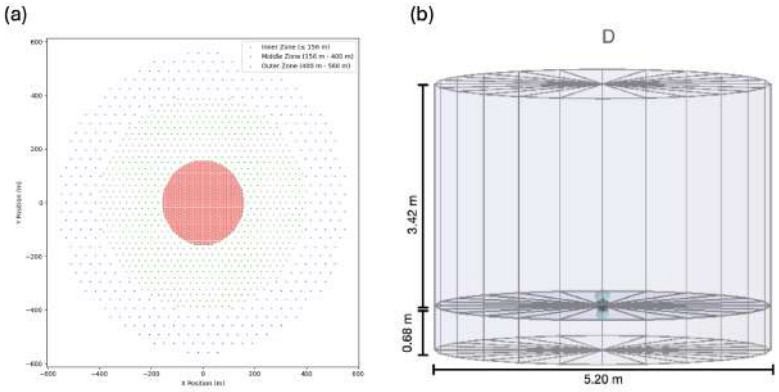

Figure 1.12: (a) Distribution of the WCDs used in the simulations. The red dots represent the inner dense zone (Zone 1), while the green (Zone 2) and blue regions (Zone 3) correspond to the outer rings with lower detector density. (b) Illustration of the detector design 'D' generated with Geant4. From SWGO Collaboration.

optimized for detecting electromagnetic particles, and the lower layer, dedicated to muon detection. Both layers are instrumented with photomultiplier tubes (PMTs) to collect the Cherenkov light produced by charged particles traversing the water.

In this configuration, the PMT in the upper layer is mounted at the center of the base and oriented upward, while the PMT in the lower layer is installed on the ceiling, pointing downward. Each tank has a height of $4.1\mathrm{m}$ and a radius of $5.2\mathrm{m}$.

While the detector units for Zones 1 and 2 have already been established, the collaboration is still conducting simulations to test and decide the best cherenkov tank for Zone 3. This thesis focuses on the assessment of a specific tank candidate, referred to as Mercedes, which will be described in detail in the following section.

Chapter 2

Framework

Although the main design specifications of SWGO have already been established, studies are still being conducted to evaluate possible configurations for the outer array. In this work, a specific detector unit known as M1mT1m was investigated. It consists of a Cherenkov tank—commonly referred to as the "Mercedes" tank—equipped with one MultiPMT module at the bottom (M1m) and another at the top (T1m). In this section, the specifications and simulation setup associated with the M1mT1m configuration are presented.

2.1 Detector model

The Mercedes tank is an innovative design developed by the collaboration to minimize the production, installation, and maintenance costs of detector stations for SWGO. Its volume is significantly smaller than that of other tank options, reducing the amount of water required for its functioning. The original Mercedes design included three PMTs arranged at 120° angles, with a potential slot for a fourth PMT at the center, hence the name “Mercedes,” due to its resemblance to the car logo.

Since then, the Mercedes design has evolved and different PMT configurations are being tested, but the name has remained. The collaboration is currently researching into PMT arrays that strike a balance between cost-efficiency and effective muon detection, which is essential for improving background rejection in air-shower events.

The Mercedes tank is a rotomolded polyethylene vessel designed and manufactured by Rotoplastyc, a company based in Rio Grande do Sul, Brazil. This company is also known for producing the high-quality tanks used in the Pierre Auger Observatory [49], which has operated in the Argentinean Pampa for over fifteen years and serves as a tested and cost-effective model for water Cherenkov detectors.

The Mercedes tank features a robust double-wall (jacketed) structure filled with polyurethane foam (PU), which provides thermal insulation crucial for high-altitude deployment

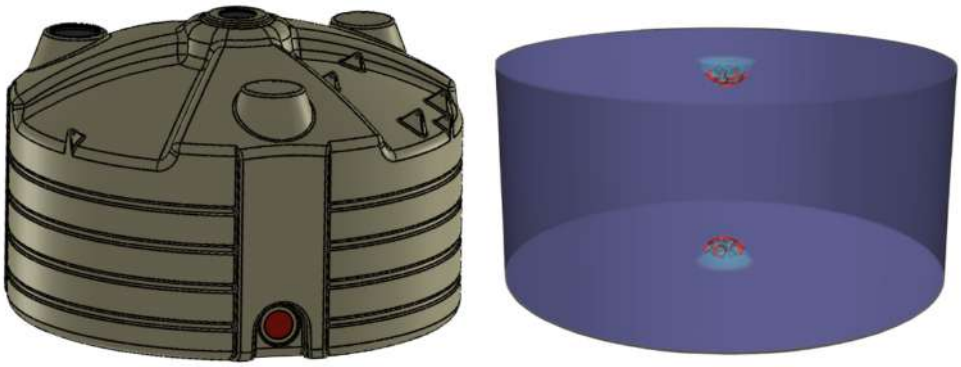

Figure 2.1: Left: 3D Model of the Mercedes tank. Right: Mercedes station simplified model in Geant4. Both from SWGO Collaboration.

(see Figure 2.2). Both the inner and outer walls are made of high-density polyethylene (HDPE) using a resin equivalent to Exxon-Mobil 8661, as used in the Auger experiment, but with improved ultraviolet protection and enhanced mechanical properties. Each wall has a thickness of 10 mm, designed to withstand the specific mechanical stresses expected in the field. Additional lateral reinforcements along the tank's circumference further improve its structural integrity.

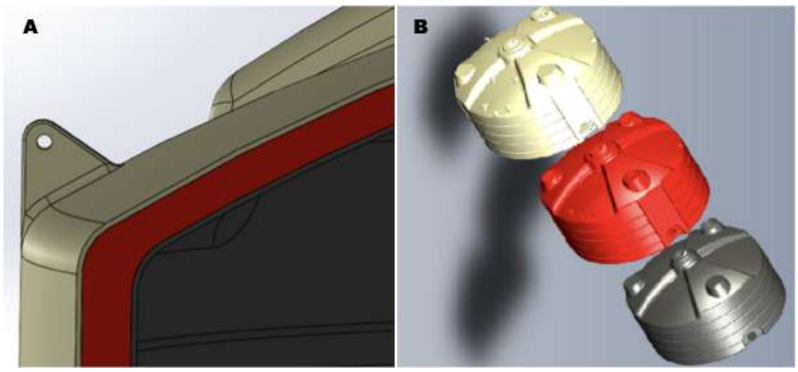

Figure 2.2: Jacketed-tank structure. (A) Detail of the jacketed-tank structure showing the 10 cm polyurethane thermal insulating layer (in red), and the outer (beige) and inner (carbon black) HDPE walls. (B) Blown-up image of the jacketed tank showing the three layer tank structure. From [50].

To achieve the necessary light-tightness and UV resistance, pigments are incorporated into the composite resin during the molding process. The inner wall contains 2% carbon black to ensure opacity to photons, while the outer beige wall includes hindered-amine light stabilizers with a UV-30 protection rating, providing long-term durability at altitudes of up to 5,000 meters above sea level. These materials ensure the tank can operate safely for at least 20 years in harsh environmental conditions.

The 10 cm PU-insulated spacing between the jacketed walls serves not only to prevent freezing of the water—thereby protecting the Tyvek® liner from damage—but also acts as a housing for all cabling and electronics. This allows for complete pre-installation and testing

of the detector's internal systems at low altitude, enabling a rapid and reliable "plug-and-play" deployment in the field with minimal ground preparation. The tanks can be placed directly on flattened terrain, streamlining the installation process across the array.

Inside, the water volume is enclosed in a flexible bladder lined with DuPont™ Tyvek® 1025-BL, a high-diffusivity material made from non-woven high-density polyethylene fibers. The Tyvek layer maximizes the reflection and collection of Cherenkov light by the photodetectors. Once filled with purified water, the liner remains tightly secured within the tank, maintaining both water- and light-tightness throughout operation. The hatch cover, composed of dual-color polyethylene sheets with the same thickness as the tank walls, includes a polyurethane gasket that acts as a reliable light seal. The structural strength of the tank lid allows it to support the weight of up to three adults (well over $200\mathrm{kg}$) without significant deformation, ensuring safety during maintenance.

A mechanical drawing of the tank design is shown in Figure 2.1 (Left), while the simplified model used for simulations is illustrated in Figure 2.1 (Right). The simplified tank has an outer diameter of $360\mathrm{cm}$, consisting of a water volume with a radius of $178.5\mathrm{cm}$ and tank walls $1.5\mathrm{cm}$ thick. The height of the cylindrical water volume is $175\mathrm{cm}$, and the total height of the tank, including the top and bottom layers of wall, is $178\mathrm{cm}$. The detector unit under study corresponds to a shallow plastic tank equipped with two multi-PMT modules: one installed at the bottom and one at the top. Each multi-PMT contains seven photomultiplier tubes (PMTs), with one at the center and six evenly spaced along a circular ring. The PMTs are not in direct contact with the water but are optically coupled to transparent domes.

2.2 Multi-PMT

The multi-PMT (mPMT) module was first proposed for the KM3NeT experiment [51], where it combines several 3-inch photomultiplier tubes (PMTs), power supplies, and readout electronics inside a pressure-resistant vessel. Since then, this innovative design has been adopted (with various modifications) by other large-scale neutrino observatories such as Hyper-Kamiokande (Hyper-K) [52] and IceCube-Gen2 [53].

For SWGO, a simplified and adapted version of the multi-PMT module is proposed. Unlike deep-sea or underground detectors, the SWGO environment does not require high-pressure resistance, allowing for a lighter and more cost-effective design. To match the total photocathode area of the 8-inch PMTs used in the reference design, the SWGO multi-PMT module adopts a baseline configuration with seven Hamamatsu R14374 3-inch PMTs arranged in a hemisphere (see Figure 2.3).

In the module, the PMTs are mounted on a lightweight support structure enclosed in a transparent acrylic vessel (see Figure 2.4), which also accommodates the front-end electronics and may include a calibration light source. As illustrated in Figure 2.3, the mechanical design incorporates a supporting steel plate that adds structural stiffness, provides thermal dissipation, and balances buoyancy. The dome itself is constructed from UV-transparent G4 Plexiglas (acrylic), with additional components including optical coupling silicone gel and reflective

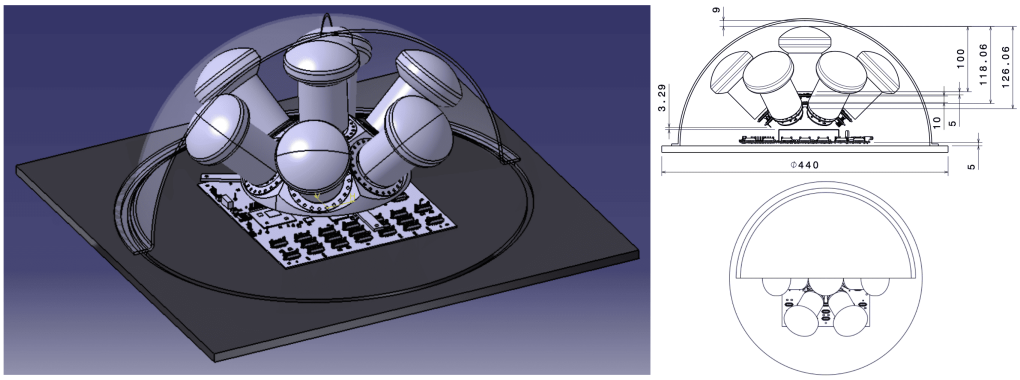

Figure 2.3: Drawings of the multiPMT model we studied. From SWGO Collaboration.

elements to enhance light collection.

The multi-PMT design is being considered for SWGO's outer array due to its potential to improve detection and reconstruction in regions where traditional dual-layer configurations may be less effective. Studies from Hyper-Kamiokande show that using several small PMTs instead of a single large one can enhance time resolution (thanks to the smaller size and faster response of the 3-inch PMTs), reduce dark noise, and offer intrinsic directional sensitivity (from the segmented PMT geometry); features that can help distinguish between gamma rays and hadronic backgrounds. Additional advantages include greater dynamic range and improved reliability, as multi-PMT modules distribute the light signal across multiple channels and have proven robust in large-scale, hard-to-access detectors.

Figure 2.4: Left: 3D printed PMT support structure. Right: The seven PMTs in the support structure. Both from SWGO Collaboration.

2.2.1 Hamamatsu R14374 3-inch PMTs

A photomultiplier tube (PMT) is a highly sensitive light detector capable of converting faint optical signals into measurable electrical pulses. Its operation is based on the photoelectric effect: when a photon strikes the photocathode, it may eject a photoelectron, provided its energy exceeds the material's work function. This photoelectron is then accelerated and directed toward a series of dynodes (electrodes held at progressively higher voltages) where each impact releases multiple secondary electrons, resulting in a cascade multiplication process,

as shown in Figure 2.5.

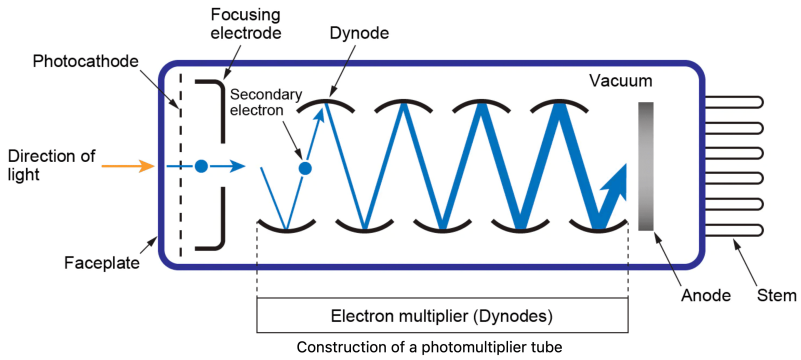

Figure 2.5: Schematic of a photomultiplier tube and its working principle. From [54].

The total amplification of this process, known as the gain, is defined as the number of electrons collected at the anode per single photoelectron emitted at the photocathode. Depending on the applied high voltage and the number of dynode stages, the gain can exceed 10^6 [55, 56]. The resulting current is proportional to the intensity of the incident light, enabling precise time and charge measurements of the detected pulse. This allows reconstruction of key properties of the original event, such as the number and arrival time of photons, which in turn provides indirect information about the energy, direction, and nature of the primary particle. Combined with nanosecond-scale timing resolution, these features make PMTs exceptionally well suited for detecting low-intensity light signals such as Cherenkov radiation, as well as for time-of-flight and air shower reconstruction applications.

In the context of this work, the specific model used in the multi-PMT module for this study is the Hamamatsu R14374. This photomultiplier tube has a 80mm hemisphere and is designed for high-energy physics applications requiring fast timing, low noise, and high sensitivity. It features a 10-stage linear-focused dynode structure and a bialkali photocathode enclosed in a borosilicate glass window. The tube provides a typical gain of 1×10^7 at 1250V, with a transit time spread (TTS) of approximately 1.3 ns full width at half maximum (FWHM), supporting precise time measurements essential for Cherenkov-based particle reconstruction. The anode pulse rise time is around 2.9 ns, and the electron transit time is about 35 ns. These timing characteristics, combined with its compact geometry, make it especially well suited for use in multi-PMT modules.

In terms of sensitivity, the R14374 exhibits a spectral response range from 300 to 650 nm, with peak quantum efficiency around 420 nm—well aligned with the spectrum of Cherenkov light in water. The quantum efficiency at 380 nm is approximately 27.5%, ensuring high detection efficiency in the UV-blue region. The anode dark current, measured after 30 minutes in darkness, is typically 50 nA, indicating low background noise. The photocathode has a minimum effective area of 72 mm and the housing follows the JEDEC B14-38 base standard. Together, these features ensure both high detection efficiency and mechanical compatibility within densely packed multi-PMT configurations.

The technical details provided here are taken from the official datasheet of the R14374 model, as published by Hamamatsu Photonics [57].

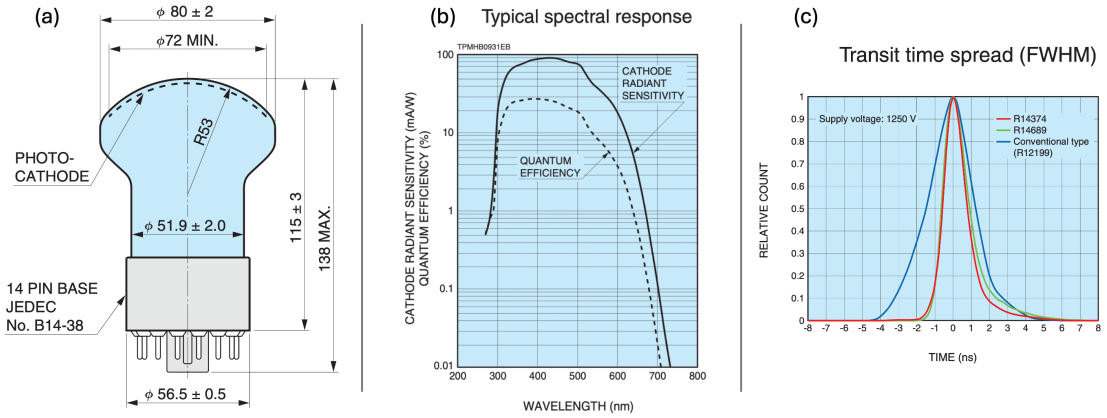

Figure 2.6: Key specifications of the Hamamatsu R14374 photomultiplier tube. (a) Dimensional outline of the tube (in mm). (b) Quantum efficiency and cathode sensitivity as a function of wavelength. (c) Transit time spread (TTS). From [57].

2.3 Simulation Framework and FastSim Development

The simulation framework currently used by the SWGO collaboration follows a structured chain of software tools, each responsible for a specific stage of the analysis process, often called 'simulation and reconstruction chain' (see Figure 2.7). It begins with the generation of atmospheric particle showers (using CORSIKA), followed by the simulation of the detector's response to secondary particles (using HAWCSim), and concludes with the reconstruction and classification of the primary particles. Each step is handled by a dedicated executable or library developed and maintained within the collaboration. This work is situated within the detector simulation stage, where efforts are ongoing to develop a faster alternative to the full HAWCSim simulation currently in use.

Program/Library	Description	Language
`corsika`	simulates particles showers	fortran
`hawc-sim`	simulate detector response to particles	C++
`swgo-reco`	• Simulates PMT response. • Reconstructs air shower properties. • Outputs: event level parameters, charges and times, muon-tagging info, mc-true values.	C++
`pyswgo-make-event-level`	• Reduces output of swgo-reco to only event level parameters. • Adds variables (including "analysis bin")	python
`pyswgo-classify-events`	• Add single variable for GH • Generates cut values for IRFs	python
`pyswgo-make-irfs`	Generates from event lists and selection criteria instrument response functions.	python
`gammapy`	Simulate and study science benchmarks.	python

Figure 2.7: Overview of the simulation and reconstruction chain. From SWGO Collaboration.

2.3.1 HAWCSim

The first step in the simulation chain involves the use of CORSIKA (COsmic Ray SImulations for KAscade), a well-established Monte Carlo code for simulating the production and development of extensive air showers [58]. It models the interactions of primary cosmic or gamma rays with the atmosphere and tracks the resulting secondary particles down to the ground.

After the EAS simulation, detector response is modeled using HAWCSim, a Geant4-based simulation tool originally developed for the HAWC observatory and adapted for SWGO. HAWCSim is one of the core components of the AERIE framework (Analysis and Event Reconstruction Integrated Environment), which provides an integrated infrastructure for event processing and data analysis. AERIE is structured as a set of modular C++ projects that offer batch execution control, data storage classes, and utilities for managing detector geometry and timing information, along with the flexibility to integrate custom algorithms.

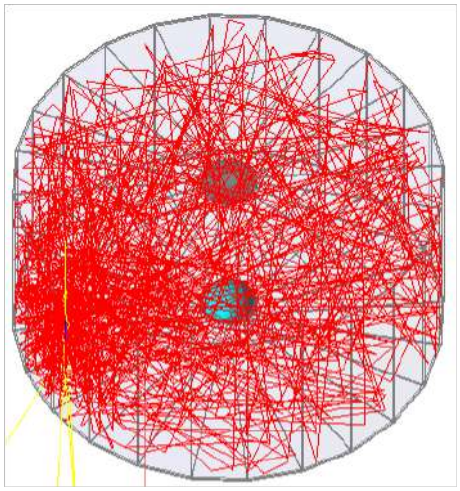

Figure 2.8: Simulation of a 10GeV photon entering a M1mT1m detector, made in Geant4. The greyish blue circles are the multiPMT modules, and the red lines represent cherenkov photons. The tank is seen from a tilted overhead view.

Within this framework, HAWCSim takes as input the secondary particles produced by CORSIKA air showers and uses the external Geant4 toolkit [59] to simulate their interactions with the water Cherenkov detectors in a given SWGO configuration. HAWCSim tracks each particle's path through the detector volume, models the production of Cherenkov photons, and follows those photons through the water until they are either absorbed or detected by a photomultiplier tube (see Figure 2.8).

In order to run Geant4, a physics list must be chosen. A physics list is a collection of physics models that define how different types of particles interact with matter during the simulation [60]. These lists group together processes such as electromagnetic interactions, hadronic scattering, decay mechanisms, and optical photon behavior, among others. Because

no single model performs optimally across all energy ranges or particle types, Geant4 provides a variety of predefined physics lists and also allows for custom configurations. These options are designed to balance accuracy and computational efficiency depending on the application, such as high-energy collisions, medical physics, or space radiation.

To achieve this, Geant4 offers a broad selection of physics models to simulate the interaction of particles with matter. For applications involving the production and propagation of Cherenkov radiation, such as this work, two main types of processes are relevant: those responsible for the electromagnetic interactions of charged particles that produce Cherenkov light, and those that handle the behavior of the resulting optical photons.

The Cherenkov process is included in Geant4's electromagnetic physics package. When enabled, this process calculates the number, direction, and energy of Cherenkov photons emitted as the particle traverses a medium. The emission spectrum is derived from the Frank–Tamm formula Equation 1.2 (among other relevant theoretical expressions, see [61]), and the model respects the local refractive index of the medium, allowing for material-dependent behavior.

Once Cherenkov photons are produced, their transport is managed by Geant4's optical photon processes. These include bulk absorption, Rayleigh scattering, boundary interactions (reflection, refraction, and total internal reflection), and wavelength shifting [61]. Boundary processes are particularly important in detectors where surfaces are defined with specific optical properties, such as reflective coatings or rough interfaces. These physics models allow for realistic tracking of each photon until it is absorbed, escapes the geometry, or reaches a sensitive detector element.

In this work, a physics list that includes the Cherenkov process and optical photon transport was used to simulate the emission and propagation of Cherenkov light in the detector medium, with additional configurations reflecting the detector's material properties and geometry.

This detailed photon tracking means that for a single incoming particle, the emission, propagation, and interaction of each Cherenkov photon with the detector surfaces are individually simulated. Each photon undergoes processes such as refraction, reflection, scattering, and potential absorption, depending on the optical properties assigned to the materials and interfaces in the detector geometry. While this level of precision is essential for accurately modeling the detector response, it also contributes significantly to the computational load, as the simulation must follow the individual trajectory of each photon until it is either absorbed or reaches a photomultiplier tube (PMT). The output of HAWCSim (based on the Geant4 calculations) consists of individual photon arrival times at the PMT photocathodes.

Table 2.1 summarizes some of the most relevant HAWCSim output variables used in this work. The abbreviation WH stands for Water Hit, referring to particles that reach the water volume, and each event contains HAWCSim.Evt.nWHit water hits. The properties of each hit are stored in vectors (of size HAWCSim.Evt.nWHit) and correspond to those prefixed with HAWCSim.WH. Similarly, PE stands for Photo-Electron, representing Cherenkov photons that successfully reach a PMT and produce a photo-electron. Each event includes Evt.nPE photo-electrons, whose attributes are likewise stored in vectors prefixed with HAWCSim.PE. For clarity, the common HAWCSim. prefix has been omitted from the field names. Additional

Field	Description	Unit
Evt.Num	Event number, monotonically increasing.	–
Evt.Energy	Primary particle energy	GeV
Evt.pType	Primary particle type	–
Evt.Theta / Phi	Zenith / Azimuthal angle of the primary particle impacting the atmosphere	deg
Evt.nPE	Total number of photoelectrons (PE) detected by the PMTs	–
Evt.nWHit	Total number of particles that hit the water	–
Evt.firstTime	Arrival time of the first particle detected in each event	ns
Evt.X / Y	Event core position for each event	cm
WH.XNE / YNE / ZNE	X, Y, Z position of WH entering water	cm
WH.Theta / Phi	WH zenith / azimuthal angle	deg
WH.TankID	ID of the tank impacted by the water hit	–
WH.Energy	Energy of the water hit	GeV
PE.PMTID	ID of the PMT on which the PE is incident	–
PE.Time	Time at which PE arrives at photo-cathode	ns
PE.Radius	Radius from the center of the PMT where the photoelectron hit	cm
PE.Energy	Energy of each photoelectron	eV
PE.origPartType	Particle type of the particle responsible for the PE	–

Table 2.1: Overview of the main simulation outputs from HAWCSim.

details can be found in the output file structure within the HAWCSim source code.

The output of HAWCSim can then be passed on to subsequent stages, such as digitization and reconstruction. These steps, while crucial for transforming raw simulation output into usable physical observables, are handled by other components within the AERIE framework and are beyond the scope of this work.

2.3.2 FastSim

While full detector simulations using HAWCSim offer detailed and accurate modeling of particle interactions and Cherenkov photon propagation, they are extremely computationally expensive, particularly when simulating large arrays. A single extensive air shower (EAS) at TeV–PeV energies can produce tens of millions of secondary particles. Each of these must be individually tracked through water volumes, their Cherenkov photon production simulated, and the resulting photons traced to the photomultiplier tubes. For full array simulations involving thousands of detector units, this leads to runtimes that are impractical for large-scale studies. As of now, simulating ultra-high-energy events for full SWGO-like arrays is beyond our computational reach, making it impossible to generate sufficient statistics in reasonable timeframes for detector design and layout optimization.

To address this limitation, the SWGO collaboration is developing a fast simulation tool called FastSim, designed to bypass full Geant4-based tracking. Instead of tracing every particle

and Cherenkov photon, FastSim uses a parameterized model of the detector response derived from detailed single-detector simulations. This parameterization is stored in a Lookup Table (LUT), which describes the expected signal in a tank as a function of key particle variables such as type, energy, position, and incidence angle. Once a LUT is available, FastSim can rapidly estimate the response of a full array to a given shower by querying the LUT for each particle in the event, thus avoiding the computationally expensive full-length tracking.

FastSim takes as input a CORSIKA file describing the particle shower at ground level, an array layout specifying the position of each detector unit, a configuration file with runtime parameters, and one or more LUTs — one per detector design in the array. For each secondary particle in the CORSIKA event, FastSim determines whether the particle intersects any detector. If so, it identifies the closest matching LUT entry using fast interpolation over the particle's parameters and retrieves the corresponding detector response (see Figure 2.9). This includes information such as the number of photoelectrons detected by each PMT and the time of the first hit.

These responses are used to generate a simplified event record, which mimics the output of a full simulation but with drastically reduced computational cost. Once all particles are processed, the results are saved in a format compatible with downstream analysis tools. This approach enables high-statistics array simulations that would otherwise be computationally unfeasible, making FastSim a promising alternative for performance studies and design decisions at the scale required by SWGO.

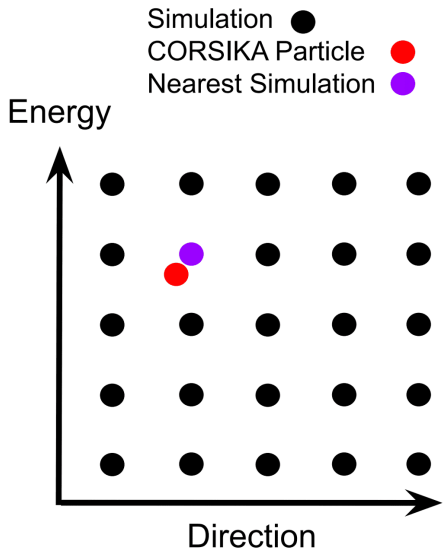

Figure 2.9: Conceptual illustration of the FastSim simulation approach. In the diagram, black dots represent simulated points in the parameterized phase space. When a CORSIKA particle (red dot) reaches a detector unit, the closest set of pre-simulated parameters (purple dot) is identified and used to determine the corresponding detector response.

At the time of writing, FastSim is still under active development and has not yet been

integrated into the official SWGO software stack. This work contributes to the development of FastSim by generating a dedicated LUT for the M1mT1m detector configuration introduced in section 2.1. A standalone simulation setup is used to inject individual particles into a single tank, systematically scanning over parameters of interest.

Because FastSim relies on parameterized responses, certain considerations are applied during LUT generation. For instance, electrons and positrons are treated identically, as their electromagnetic interactions in water are effectively indistinguishable at the energies relevant to this work. The same assumption is applied to muons and antimuons, reducing the number of simulated particle types from five (photons, electrons, positrons, muons, and antimuons) to just three. Another important feature is that gamma rays are electrically neutral and do not emit Cherenkov light directly. They must first interact, typically by pair production or Compton scattering, to produce charged particles that can then radiate. As a result, they are expected to produce fewer photoelectrons on average, their light yield is generally lower and more variable than that of charged particles, especially at lower energies. These differences in signal generation are encoded directly in the LUTs, allowing FastSim to preserve key physics features of particle detection while maintaining computational efficiency.

Despite its advantages, FastSim introduces several approximations that can impact the accuracy of the simulation. First, the detector response is modeled using parameterizations fitted to the output of detailed single-tank simulations. These fits, while effective in many regions of parameter space, are not perfect and may fail to capture more complex behaviors, especially near the boundaries of validity. Moreover, the lookup tables themselves are discretized representations of a continuous detector response. To extract predictions from them, FastSim relies on nearest-neighbor interpolation, which can introduce additional inaccuracies, particularly in sparsely sampled regions.

Another inherent limitation arises from the simplified treatment of electromagnetic particles such as electrons and photons. In reality, these particles can traverse multiple tanks and generate Cherenkov light in each. While FastSim includes an approximate treatment of this multi-detector crossing behavior, it remains a simplified model that cannot fully replicate the detailed tracking performed by Geant4. These limitations are the trade-off for the significant gains in speed, and highlight the importance of validating FastSim outputs against full simulations in critical regions of phase space.

Chapter 3

Methodology

3.1 Detector parametrization

In order to simulate the detector's response to different types of particles, the first step is to develop a suitable parametrization of the detector model. This process begins by identifying the key parameters that describe the detector's geometry and structure. Once these parameters are defined, appropriate ranges and step sizes are chosen for each of them. Based on these, the detector is then divided into a finite set of points, which serve as reference positions for the simulations. This discretization is essential to make the simulation manageable while still capturing the relevant features of the detector's behavior. Once this is done, the intrinsic symmetries of the tank can be analyzed and exploited to reduce the number of simulations required to accurately describe its behavior.

3.1.1 Definition of parameter space

To accurately describe a particle interacting with a cylindrical detector, two sets of parameters are required (see Figure 3.1). The first corresponds to the particle's position in the tank and is naturally expressed in cylindrical coordinates (r, α, z) . The second set describes the direction of the particle's momentum upon entering the tank, and consists of two angular variables: θ and ϕ . These angles define the orientation of the momentum vector in three-dimensional space. Since the particle energy is fixed for each simulation run, the momentum vector has only two degrees of freedom, which are fully captured by the angular coordinates.

The spatial coordinates (r, α, z) are defined following the standard cylindrical coordinate system. The radial coordinate r ranges from 0 at the central axis of the tank to the full radius of the detector, which is $180\mathrm{cm}$ for the M1mT1m configuration. The azimuthal angle α spans from $0°$ to $360°$, covering the entire circular cross-section and measured from the center of the PMT 1 (see Figure 3.3). The vertical coordinate z ranges from the base of the tank ($z = 0$) to its full height, which is $175\mathrm{cm}$ in the M1mT1m design.

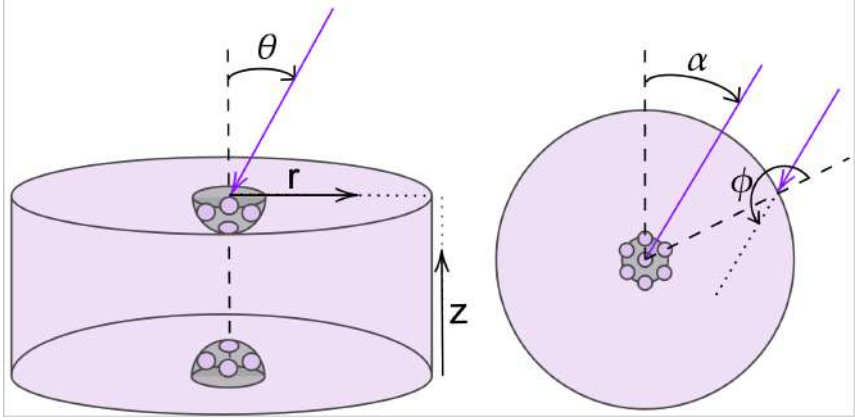

Figure 3.1: Graphic representation of the detector parameters. The left panel shows a side view, and the right panel shows a top view of the cylindrical tank. The dark grey domes represent the multi-PMTs. The coordinates (r, α, z) correspond to the standard cylindrical coordinate system, while θ and ϕ define the direction of the incident particle's momentum.

On the other hand, the incident momentum is defined by two angles: the zenith angle θ, measured downwards from the vertical axis and ranging from $0°$ to $90°$; and an azimuthal angle ϕ, which describes the deviation of the particle's direction from a radial trajectory in the horizontal plane. The second angle, phi, is defined with respect to the radial direction at the point of incidence, and captures the orientation of the particle's momentum in the transverse plane. It ranges from $0°$ to $360°$.

The choice of step sizes was informed by prior experience with similar detector simulations within the collaboration, and reflects a balance between resolution and computational cost. In particular, previous studies with different detector geometries indicated that using finer steps did not yield significant improvements in the accuracy of the detector response, suggesting that the chosen discretization is adequate for the purposes of this study. Diagrams showing this discretization are shown in Figure 3.2.

For the vertical coordinate z, it was recommended within the collaboration to avoid step sizes smaller than $25 - 30\mathrm{cm}$, regardless of the tank's total height. Given that the M1mT1m prototype has a height of $178\mathrm{cm}$, six intervals of $25\mathrm{cm}$ were used, with the final bin covering the remaining $28\mathrm{cm}$. This approach results in seven discrete levels, preserving the full height of the tank while keeping the spacing within the advised range.

As for the radial coordinate r, it was recommended to use a total of ten or eleven bins, regardless of the exact step size. Given that the tank has a total radius of $180\mathrm{cm}$, a step size of $18\mathrm{cm}$ was selected. However, this binning applies only at the top of the tank, where $z = \mathrm{tank\ height} = 178\mathrm{cm}$. This is due to the fact that the parametrization targets the possible impact points of particles arriving from outside the detector, which necessarily lie on the tank surface. For all other values of z , r is fixed at $180\mathrm{cm}$.

The azimuthal coordinate α required a different approach, since this is the first detector

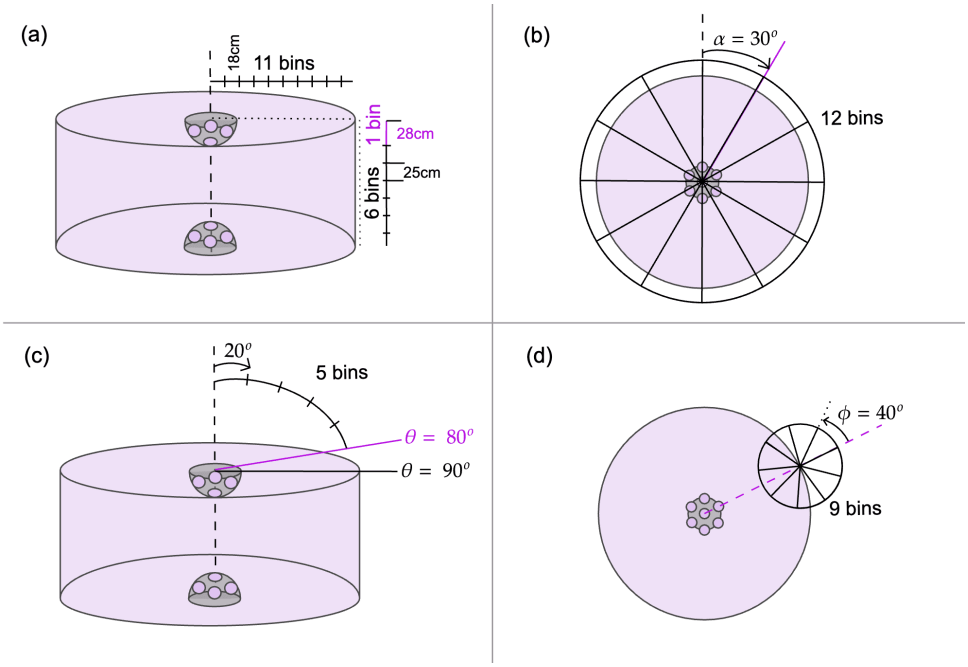

Figure 3.2: Diagrams showing the binning and step sizes for each variable. (a) Ten bins with 18cm steps for r ; six bins with 25cm steps for z, plus an additional bin (in pink) with a width of 28cm. (b) Twelve bins with $30°$ steps for α. (c) Five bins with $20°$ steps for θ. (d) Nine bins with $40°$ steps for ϕ.

design in the collaboration that breaks cylindrical symmetry. As a result, this was also the first time α had to be explicitly included in the parametrization, and there were no prior results to guide the choice of step size. Given that the six side-facing PMTs in the multi-PMT module are evenly spaced at $60°$ intervals, it was natural to adopt $30°$ steps for α (resulting in twelve bins). This allows us to consider two representative cases: particles arriving directly toward a PMT, and particles arriving midway between two PMTs. This simplified sampling was advised as a reasonable starting point, with the option to refine the LUT by adding more α values if needed.

The range for θ was set between $0°$ and $80°$, excluding the $90°$ value, as particles with a zenith angle of $90°$ do not enter the detector, since the CORSIKA particles are initialized 10m above it. Although particles at larger zenith angles ($60°$ to $90°$) must traverse a larger atmospheric depth, which tends to attenuate the signal and increase variability, previous studies have also considered this range for θ. In particular, some SWGO simulation studies have modeled air showers with zenith angles up to approximately $65°$ [62]. Since secondary particles often spread over a wider angular range than the primary gamma ray, extending coverage near $90°$ is considered reasonable.

Regarding the binning for θ, previous LUTs used $10°$ steps in θ. In this work, $20°$ steps (five bins) are used to reduce computational time and to evaluate whether coarser binning is sufficient for accurately predicting detector response. If successful, this approach could significantly reduce the resources required for future LUT generation and simulations. To evaluate the adequacy of this binning, all other parameters, such as NPE distributions and time histograms, can be held fixed while comparing detector responses across θ. Significant

changes between bins (e.g., shifts in the mean by an order of magnitude) would justify a finer resolution.

The initial range for the ϕ angle spans from $0°$ to $360°$, although this will be significantly reduced after analyzing the symmetries of the model (see subsection 3.1.2). As a first approach, this work considered $40°$ steps in ϕ, resulting in nine bins (noting that $0°$ and $360°$ represent the same direction).

The ranges and steps for each coordinate are summarized in Table 3.1. The combination of all parameters results in a total of 9720 PID (Points in Detector). For convenience, the term PID is used to refer to all parameter combinations, including those describing momentum direction. These 9720 PIDs represent the full parametrization of the detector unit and define the entries of the LUT. However, not all of them will be simulated with HAWCSim. A significant portion will be excluded from simulations by exploiting the symmetries of the detector.

Variable	Unit	Range	Step	# bins
r	cm	$[0, 180]$	18	11
α	° (deg)	$[0, 360]$	30	12
z	cm	$[25, 150], 178$	$25, 28$	$6, 1$
θ	° (deg)	$[0, 80]$	20	5
ϕ	° (deg)	$[0, 360]$	40	9

Table 3.1: Summary of the relevant detector parameters, including their units, ranges, and step sizes. Note that the additional value at $z = 178\text{cm}$ corresponds to the last bin, which has a different width (28cm).

There are five types of particles considered in this work: gamma rays, electrons, positrons, muons, and antimuons. However, as mentioned in subsection 2.3.2, this number can be reduced to three, since the detector response to a particle and its antiparticle is effectively the same for the purposes of this simulation. Therefore, the focus will be on gamma rays, electrons, and muons. The energy ranges for these particles are based on previous LUTs, which were tuned using the energy distributions obtained from CORSIKA simulations; the specific values are presented in Table 3.2. It is worth noting that, although the muon energy range extends higher than that of the other particles, it is divided into fewer bins. This is because the detector response to muons varies less significantly with energy compared to electrons and gammas, as shown in previous simulation studies (e.g., [38]). Once above the Cherenkov threshold, muons produce a relatively consistent number of photons, allowing for coarser energy binning without a loss in accuracy.

When combining all PIDs, particle types, and energy bins, the total number of points in the LUT reaches an overwhelming 311040. The next step is therefore to analyze the symmetries of the detector unit in order to simulate as few of those points as possible.

Particle	Energy [GeV]	# bins
Gamma	0.001, 0.003, 0.007, 0.01, 0.03, 0.07, 0.1, 0.3, 0.7, 1, 3, 7, 10	13
Electron	0.001, 0.003, 0.007, 0.01, 0.03, 0.07, 0.1, 0.3, 0.7, 1, 3, 7, 10	13
Muon	0.3, 1, 3, 10, 30, 100	6

Table 3.2: Energy values and number of bins used for each particle type.

3.1.2 Symmetry Considerations

The M1mT1m detector exhibits several symmetries, the most apparent being its cylindrical symmetry. Although the inclusion of multi-PMT modules breaks this symmetry to some extent, some of it is preserved. Since all PMTs are identical and the multi-PMT modules are located on the axis of the tank, the system is symmetric under rotations of $60°$. In practical terms, it makes no difference, regarding the detector response, whether a particle hits PMT 1 or PMT 3; the signal is the same. Although PMT ID is essential for shower reconstruction, where directional information about the particle is extracted, it is not a relevant parameter for the detector response itself.

As a result, the azimuthal coordinate α only needs to take two values: $0°$ and $30°$. The remaining ten possible positions around the tank can be reproduced by rotating the setup and relabeling the PMT accordingly. This reduces the simulations by a factor of 83%, leaving fewer than $1/6$ of the original PIDs to simulate. The diagrams in Figure 3.3 show the PMT numbering convention used in the simulation framework. Although symmetry reduces the parameter space for LUT generation, maintaining distinct PMT IDs remains essential for reconstruction.

In order to take full advantage of the remaining symmetries, it is useful to divide the detector into three regions: Top, Corner, and Side. The Top region corresponds to the tank cover and includes all PIDs with $z = 178\text{cm}$ and $r \neq 180\text{cm}$. The Corner region corresponds to the tank rim, where $z = 178\text{cm}$ and $r = 180\text{cm}$. The Side region comprises all remaining PIDs, characterized by $z \neq 178\text{cm}$ and $r = 180\text{cm}$, which form the detector liner. A summary of these conditions is shown in Table 3.3.

Region	Condition on r	Condition on z	Cylindrical Analogue
Top	$r \neq 180\text{cm}$	$z = 178\text{cm}$	Detector cover (top layer)
Corner	$r = 180\text{cm}$	$z = 178\text{cm}$	Rim of the tank (outer edge)
Side	$r = 180\text{cm}$	$z \neq 178\text{cm}$	Liner of the detector (side walls)

Table 3.3: Description of each region of the detector: Top, Corner and Side.

Once the tank is divided, the special considerations for the case $\theta = 0°$ become straightforward. In the Top region, and as is typical in spherical coordinates, the azimuthal angle ϕ becomes arbitrary when $\theta = 0°$; that is, ϕ is not a meaningful degree of freedom in this

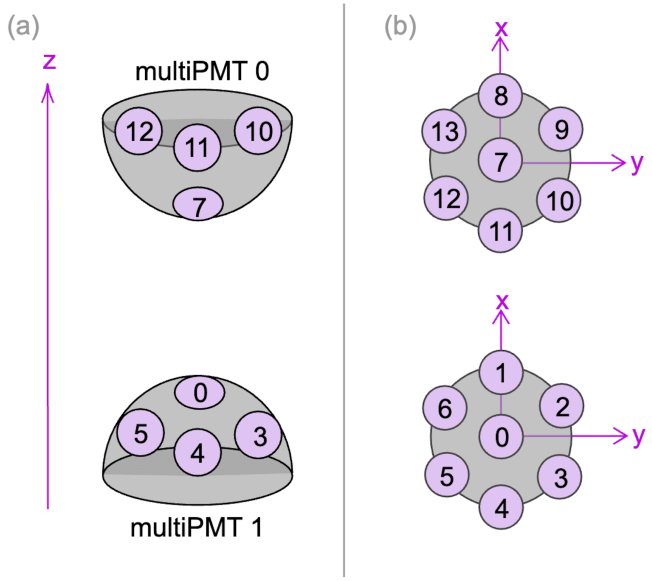

Figure 3.3: Representation of the multiPMT modules and PMT numbering used in the simulation framework. Each purple circle represents a PMT. (a) Front view of the multiPMT units (not to scale). The upper module is labeled zero, and the lower one is labeled one. For simplicity, PMTs on the back side are not shown. (b) Top view of the same modules (not to scale). The central PMT is numbered first, followed by the surrounding PMTs in a clockwise direction starting from the $x-$axis.

case. This leads to two distinct situations: either $\theta = 0°$, in which case ϕ is undefined and should not be binned; or $\theta \neq 0°$, in which case ϕ takes on defined values. Accounting for this reduces the number of PIDs to simulate in the Top region by a factor of

$$\frac{(N_{\text{bins}}(\phi) - 1)}{N_{\text{bins}}(\phi) \cdot N_{\text{bins}}(\theta)},$$

where $\mathrm{N_{bins}(x)}$ is the number of bins for the variable x. This ammount corresponds to nearly 18% of the Top region, in this case.

In the Corner and Side regions, by contrast, a particle with $\theta = 0°$ will not enter the detector. At this angle, the particle's momentum is entirely along the $z-$direction, that is, $p = p_z$. Therefore, $\theta = 0°$ can be directly excluded from the parameter space on Corner and Side, reducing the number of required simulations in those regions by 20%.

Symmetry considerations for the azimuthal angle ϕ also significantly reduce the amount of required simulations. An initial observation is that, for Corner and Side regions, not all values of ϕ correspond to particles entering the detector. Only those particles for which $90° < \phi < 270°$ will enter the tank. This restriction, however, does not apply to particles entering from the Top, where all ϕ values remain valid.

The final symmetry considered is the reflectional symmetry in the azimuthal angle ϕ. For

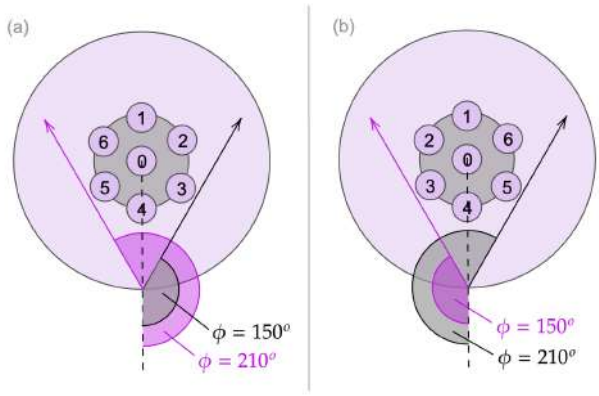

Figure 3.4: Illustration of the reflectional symmetry in ϕ. The pink vector can be unambiguously described in both frames, (a) and (b), demonstrating that it is unnecessary to simulate both the pink and black particle trajectories. In each frame, the angles are equidistant from the plane $\phi = 180°$.

a clearer illustration, see Figure 3.4. In the M1mT1m configuration, this symmetry is more challenging to exploit, as it requires carefully relabeling the PMT IDs that are not located along the axis of reflection. However, once this is done, the range of ϕ, and thus the number of simulations, can be reduced by half. For the Top region, this results in five bins of $40°$ steps, ranging from $0°$ to $160°$. The value $\phi = 180°$ is then manually added to complete the parametrization. It is important to emphasize that $0° \neq 180°$ in this region, as shown in Figure 3.5.

For the Side and Corner regions, applying both considerations related to the azimuthal angle phi — namely the restriction to particles entering the detector and the reflectional symmetry — results in a limited set of valid values. To achieve a more refined parametrization, the binning step for ϕ in these regions is reduced from $40°$ to $30°$, yielding a final range from $120°$ to $180°$. This range is obtained by first excluding the boundary values $\phi = 90°$ and $\phi = 270°$, which correspond to particles that do not enter the detector, and then applying the reflectional symmetry about $\phi = 180°$. In this work, an additional bin of $210°$ was added to the simualtions, for testing and validation pur

Loc	**r**	**step**	**z**	**step**	α	θ	**step**	ϕ	**step**	**PID**
T	[0, 162]	18	178	-	0, 30	0	-	-	-	20
T	[0, 162]	18	178	-	0, 30	[20,80]	20	[0,160]	40	400
T	[0, 162]	18	178	-	0, 30	[20,80]	20	180	-	80
S	180	-	[25,150]	25	0, 30	[20,80]	20	[120,210]	30	192
C	180	-	178	-	0, 30	[20, 80]	20	[120,180]	30	24
Total										716

Table 3.4: Definitive summary of the PID (Points in Detector) that will be simulated. The first column, Loc, indicates the corresponding region in the detector: Top, Side, or Corner..

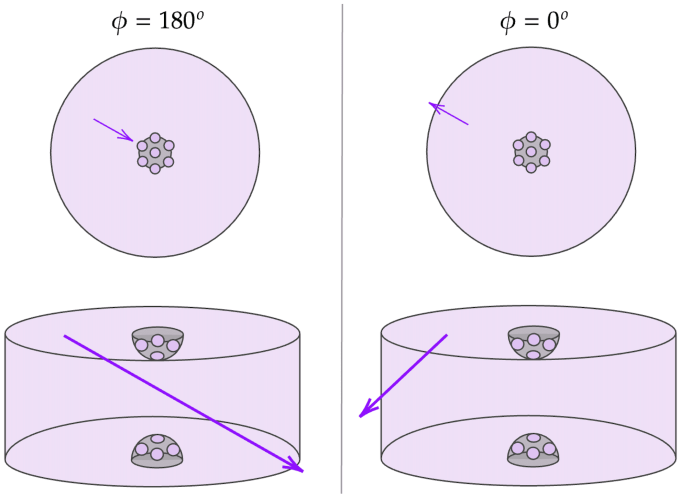

Figure 3.5: Diagram evidencing that $\phi = 0°$ is not equivalent to $\phi = 180°$ in the Top region. The particle trajectories differ in the distances they cover within the detector, which demonstrates that one cannot be obtained from the other through any symmetry transformation.

Table 3.4 summarizes the parameter space after applying all symmetry considerations. The number of detector points to be simulated has been reduced to 716, a significant reduction from the original 9720. When the 716 PIDs are combined with the 32 energy and particle-type bins (shown in Table 3.2), the result is a total of 22912 different parameter combinations, each corresponding to an individual simulation.

3.2 Conversion of Parameters to Cartesian Coordinates

Although it is natural to describe the detector in curvilinear coordinates for symmetry analysis, the simulation software HAWCSim requires input files written in Cartesian coordinates. Consequently, both the particle's position and momentum must be converted to (x, y, z) components before running the simulation, as reflected in the format of the generated `.in` files.

The angular parameters θ , ϕ , and α were initially expressed in degrees and were therefore converted to radians prior to performing any trigonometric operations. Once this conversion is done, the transformation of the position vector is straightforward, as it was already expressed in cylindrical coordinates (see Figure 3.1):

$$\vec{r}_{\text{cyl}} = \begin{pmatrix} r \\ \alpha \\ z \end{pmatrix} \rightarrow \vec{r}_{\text{cart}} = \begin{pmatrix} x \\ y \\ z \end{pmatrix} = \begin{pmatrix} r\cos\alpha \\ r\sin\alpha \\ z \end{pmatrix}$$

Unlike the position vector, the momentum vector has not yet been defined explicitly. In

order to express it in Cartesian coordinates, it is necessary to analyze the angular components that define its orientation in space—namely, the zenith and azimuthal angles. This is illustrated in Figure 3.6.

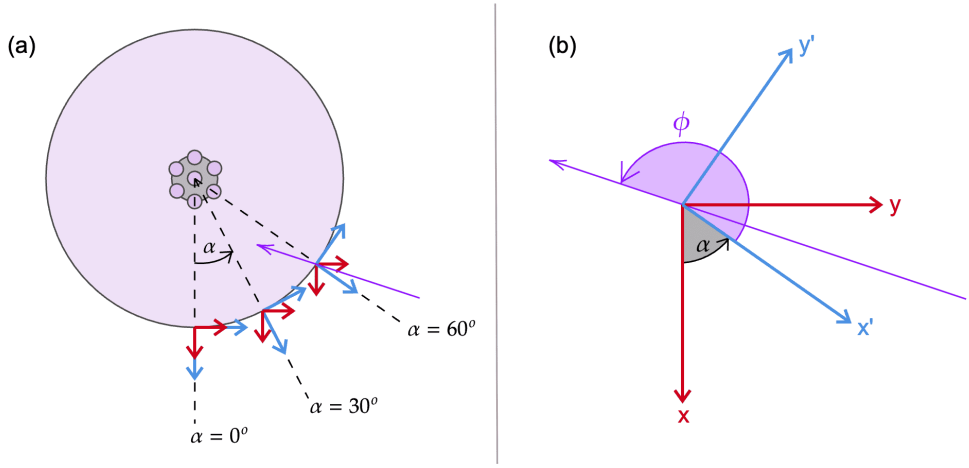

Figure 3.6: Illustration of the coordinate systems. (a) The fixed Cartesian system is shown in red, while the position-dependent curvilinear system (radial and azimuthal coordinates) is shown in blue. An incoming particle is represented in purple. (b) Zoomed-in view of the same configuration. In grey, azimuthal angle α. In lighter purple, azimuthal angle ϕ.

It can be seen from Figure 3.6 that, if $\vec{v}$ is a vector representing the direction of an incoming particle in the plane, it can be expressed in the curvilinear system as

$$\vec{v} = \cos\phi\ \hat{x}' + \sin\phi\ \hat{y}'$$

where the two coordinate systems are related through

$$\hat{x}' = \cos\alpha\ \hat{x} + \sin\alpha\ \hat{y} \quad ; \quad \hat{y}' = -\sin\alpha\ \hat{x} + \cos\alpha\ \hat{y}$$

And therefore

$$\vec{v} = \cos(\phi+\alpha)\ \hat{x} + \sin(\phi+\alpha)\ \hat{y}$$

Which evidences that the azimuthal angle of the momentum vector is effectively the sum of the two azimuthal angles defined in the original coordinate system; that is, $\phi_{\text{eff}} = \phi + \alpha$. With this established, and recalling that θ has already been defined as the zenith angle, the momentum vector can be expressed in spherical coordinates and subsequently transformed into the Cartesian system as follows

$$\overrightarrow{p}_{\text{spher}} = \begin{pmatrix} |\vec{p}| \\ \theta \\ \phi+\alpha \end{pmatrix} \rightarrow \overrightarrow{p}_{\text{cart}} = \begin{pmatrix} p_x \\ p_y \\ p_z \end{pmatrix} = \begin{pmatrix} |\vec{p}|\sin\theta\cos(\phi+\alpha) \\ |\vec{p}|\sin\theta\sin(\phi+\alpha) \\ -|\vec{p}|\cos\theta \end{pmatrix}$$

The magnitude of the particle's momentum is computed based on its energy and rest mass. For photons, the momentum is equal to the energy, while for electrons and muons, it is determined using the relativistic energy-momentum relation:

$$p = \sqrt{E^2 - m^2}$$

Particle Type	Mass name	Numeric value	Units
Photon	m_γ	0	-
Electron	m_e	0.00051099895000	GeV/c^2
Muon	m_μ	0.1056583755	GeV/c^2

Table 3.5: Rest mass values (in natural units) for the particle types considered in the simulation.

assuming natural units, where $c = 1$. The values used for the masses of each particle are summarized in Table 3.5.

Conditional checks in the code ensured that momenta were set to zero in directions where they would be trivially null due to angular symmetry (for example, $\theta = 0°$ yields $p_x = p_y = 0$). The resulting values were used to generate input files with the particle's type, initial position, and momentum vector in Cartesian coordinates.

3.3 Simulation Pipeline

3.3.1 Input file generation

The simulation process begins with the creation of input files for HAWCSim. In this work, the input files were written in ASCII format, a plain-text structure commonly used for specifying particle event data. Each line in an input file corresponds to a single primary particle event and follows the format:

$$\text{ptype} \quad r_x \quad r_y \quad r_z \quad p_x \quad p_y \quad p_z$$

Here, ptype denotes the particle reaching the detector: photon, muon, or electron. The variables r_i $(i = x, y, z)$ represent the components of the particle's position in Cartesian coordinates, and p_i correspond to the components of the particle's momentum vector, also in Cartesian coordinates. HAWCSim supports multiple particle input events within a single file, as long as each line follows the required format and represents a separate particle event. All quantities are given in Geant4 units, that is, centimeters (cm) for position and Giga-electron Volts (GeV/c) for momentum.

These input files were generated using a dedicated C++ script, which scans across the parameter space (see Table 3.4) using nested `for` loops. The binning for each parameter is hardcoded directly into the script, allowing full control over the simulation grid and ensuring reproducibility. The script accounts for the different binning schemes defined for each detector region (Top, Side, and Corner), as detailed in subsection 3.1.2. This ensures that the full parameter space is systematically and consistently covered across all configurations.

Each input file corresponds to a unique combination of parameter values and contains 1000 identical primary particles, providing sufficient statistics to compute meaningful average

detector responses. The filenames follow a structured convention that encodes all relevant simulation parameters, allowing for automated processing and straightforward identification of the simulation settings during post-processing. Each filename is constructed as follows:

`type_n_e{`*energy*`}GeV_theta{`θ`}deg_phi{`ϕ`}deg_alpha{`α`}deg_r{r}cm_h{z}cm.in`

where:

- `type` indicates the particle type (`"gamma"`, `"mu-"`, or `"e-"`).
- `n` is the number of particles in the file. In this work, `n`= 1000 for every file.
- `energy` is the particle energy, in GeV.
- θ, ϕ, and α are the angular parameters already introduced, expressed in degrees.
- `r` is the radial distance from the detector center, in cm.
- `z` is the particle's vertical starting height, in cm.
- `.in` is the file extension (ASCII type).

For example, a file named:

`mu_1000_e3GeV_theta80deg_phi120deg_alpha30deg_r180cm_h25cm.in`

contains 1000 muons of $3\,\mathrm{GeV}$ each, incident at a zenith angle of $80°$. The particle direction is offset by $120°$ from the radial axis and by $30°$ from the orientation of a PMT. The muons originate from a radial distance of $180\,\mathrm{cm}$ and a height of $25\,\mathrm{cm}$ above the detector.

3.3.2 HAWCSim simulations

Due to technical limitations encountered across multiple high-performance computing clusters, where installation of the simulation framework was not successful despite consultation with system administrators, all simulations were executed locally on a small set of desktop machines running Linux Mint 20.3. The simulation software, including HAWCSim and its dependencies, was installed and managed within a dedicated Conda environment. A Bash automation script was developed to sequentially execute HAWCSim for each input configuration, manage input/output files, and monitor the simulation status. Although the computational resources were modest—consisting of four standalone computers—this setup proved sufficient for running the full set of simulations through careful scheduling and parallelization.

At the time of this work, the simulation was carried out using a private version of HAWCSim, which is part of the AERIE software suite developed by the HAWC Collaboration. While the collaboration intends to make AERIE fully public in the future, it is currently shared privately within the SWGO Collaboration. Access to the simulation framework, including HAWCSim, supporting data, and documentation, is restricted to members of this group. Consequently, version control and public release notes are not yet available. For reproducibility, users

interested in running the same simulations should request access to the SWGO Collaboration by contacting the group maintainers.

HAWCSim relies on Geant4 for modeling particle interactions and optical processes within the detector. It employs a variety of physical models to accurately simulate the behavior and interactions of particles and photons with detector materials. These models are registered within the `PhysicsList` class of HAWCSim and defined in corresponding header (.hh) files. A summary of the main physics models employed in this work is presented in Table 3.6. For more information on the physics models, see [61].

Model	Description
`EMPhysics`	Custom electromagnetic physics constructor that handles standard EM interactions and optical processes such as Cerenkov radiation, absorption, Rayleigh scattering, Mie scattering, and boundary effects.
`G4EmExtraPhysics`	Adds additional electromagnetic processes not included in the standard EM package, such as synchrotron radiation and gamma-nuclear interactions.
`G4DecayPhysics`	Handles the decay of unstable particles, such as muons, pions, and kaons.
`G4HadronElasticPhysics`	Simulates elastic scattering of hadrons, important for low-energy hadronic interactions.
`G4HadronHElasticPhysics`	An alternative or complementary model for elastic hadronic interactions based on a high-energy formalism.
`G4HadronPhysicsQGSP_BIC`	Main hadronic interaction model. QGSP (Quark-Gluon String Precompound) models high-energy inelastic collisions, while BIC (Binary Cascade) handles lower-energy interactions through intranuclear cascade simulations.
`G4StoppingPhysics`	Models the behavior of particles that come to rest, especially those that stop and decay, such as muons and anti-protons.
`G4IonBinaryCascadePhysics`	Simulates ion-ion interactions using the Binary Cascade model, relevant for modeling the heavy ion component of cosmic rays.

Table 3.6: Physics models used in the HAWCSim simulation framework.

All simulations were run in *injection mode*, meaning that the particles defined in the ASCII input files are placed at specific positions above the tank with defined momenta. This bypasses shower development and focuses solely on the local detector response, which is central to the construction of the Look-Up Table (LUT). Each simulation configuration corresponds to a single input file containing 1000 identical particles.

Even in injection mode, running HAWCSim across the full parameter space was computationally expensive. The runtime is strongly dependent on the energy of the primary particle,

as higher energies produce more Cherenkov photons, which in turn require more detailed photon tracking and physics processing. The runtime of individual input files ranged from a few seconds for lower energy particles (e.g., $0.01\,\mathrm{GeV}$ photons) to around 30 minutes for the highest energy particles (such as $10\,\mathrm{GeV}$ electrons). In total, completing the entire grid of simulations took approximately three months of computing time.

3.3.3 Output Processing and Fitting

Output Filtering

The output of HAWCSim is an eXplicitly Compacted Data Format (XCDF) file - a binary data format designed to store structured data fields. These files contain the detector response for each simulation.

Immediately after generation, these XCDF files are converted into ROOT files to facilitate further analysis. ROOT is a data analysis framework developed at CERN, widely used in high-energy physics and astrophysics. It provides an efficient structure for storing and accessing large-scale datasets. Each converted file contains a `TTree` with event-level information, including PMT hits (time, ID), metadata about the event geometry, and simulated truth information.

To construct the Look-Up Table (LUT), two key observables are needed from the simulation outputs:

- Number of PhotoElectrons (nPE) recorded per event, for each PMT.
- Time of arrival of the PhotoElectrons at each PMT.

Accurately modeling the full arrival time distribution of all photoelectrons (PEs) at each PMT is a complex task, and previous efforts have not succeeded in identifying a robust functional form to describe this observable. Instead, a more practical approach—adopted in previous LUT constructions—has been to use the arrival time of the first PE per PMT, commonly referred to as the First Time (fTime). his quantity preserves essential timing information while avoiding the complications of fitting the complete time distribution, and is therefore used in this work.

In HAWCSim, the particle's internal clock starts at the point of generation and is not reset upon reaching the detector. As a result, the simulated arrival times of the photoelectrons at the PMTs include the propagation time from the generation point to the detector. To isolate the detector response and obtain physically meaningful timing information, a correction must be applied. Specifically, the vertex z-position (in meters) is used to compute the time it would take for the primary particle to reach the detector, assuming it travels at the speed of light c. This correction is then subtracted from all arrival times:

```
double time_correction = (vertex_z / c) * 1e9;  (in nanoseconds)
```

This ensures that the timing information used for analysis reflects only the processes occurring within the detector volume, independent of the particle's initial trajectory.

After conversion from XCDF to ROOT format, the files are filtered to isolate these observables and reduce the dataset to its essential components. This step significantly decreases storage and processing demands. The filtering is performed using a C++ script that loops over all events in the `TTree` and builds histograms for each observable. Specifically, for each input configuration, the script generates 14 fTime histograms and 14 nPE histograms, corresponding to the 14 PMTs in the detector. The filtered output is stored in a new, lightweight ROOT file that contains only the relevant histograms, streamlining subsequent analysis and fitting.

For each configuration, histograms were filled using the binning schemes shown in Table 3.7. The binning parameters were selected to balance resolution and statistical robustness. For the number of photoelectrons (nPE), two different schemes were adopted: the Short nPE configuration for simulations where the signal per PMT was relatively low, and the Long nPE configuration for cases with higher PE counts, typically associated with higher-energy particles. This separation ensures that the histogram resolution is appropriate for the signal range of each dataset.

Histogram	Number of bins	Range	Units
Short nPE	50	$0 - 50$	PE
Long nPE	100	$0 - 250$	PE
fTime	100	$0 - 100$	ns

Table 3.7: Binning schemes used for the fTime and nPE histograms generated from filtered simulation output.

The fTime histograms consistently used a fixed binning from 0 to 100 ns, which intended to capture the typical spread of first-arrival times observed across simulations, balancing resolution with statistical significance. While this approach works well in most cases, it may not be optimal for every configuration.

The statistical uncertainties associated with each bin in the histograms were calculated as the square root of the number of entries N in that bin, i.e., $\sqrt{N}$. No additional statistical uncertainties, such as event weights, were applied during the histogram filling process. These errors are internally used by `RooFit` during the fitting procedure (see section 3.3.3), although they are not explicitly shown in the plots.

Fitting Procedure

To model the distribution of First Time (fTime) and number of PhotoElectrons (nPE) values for each PMT, a composite fit function was employed using the `RooFit` toolkit [63]. The chosen model combines a Gaussian and a Crystal Ball (CB) function, which together provide both flexibility and physical interpretability. The Gaussian component is meant to capture the core of the distribution—typically dominated by direct Cherenkov photons—while the CB

function accounts for the asymmetric tail produced by delayed or scattered photoelectrons.

The Crystal Ball function is a widely used probability density function (PDF) in high-energy physics, originally introduced by the Crystal Ball collaboration at SLAC (see [64]). This function combines a Gaussian core with a power-law tail, allowing for a smooth modeling of asymmetric features such as energy loss or detector inefficiencies.

The Crystal Ball function depends on four parameters: the mean μ, the standard deviation σ, the shape parameter α, and the exponent n. The parameters μ and σ define the location and width of the Gaussian core, while α controls the point where the distribution transitions into a power-law tail, and n determines the steepness of that tail. This can be visualized in Figure 3.7.

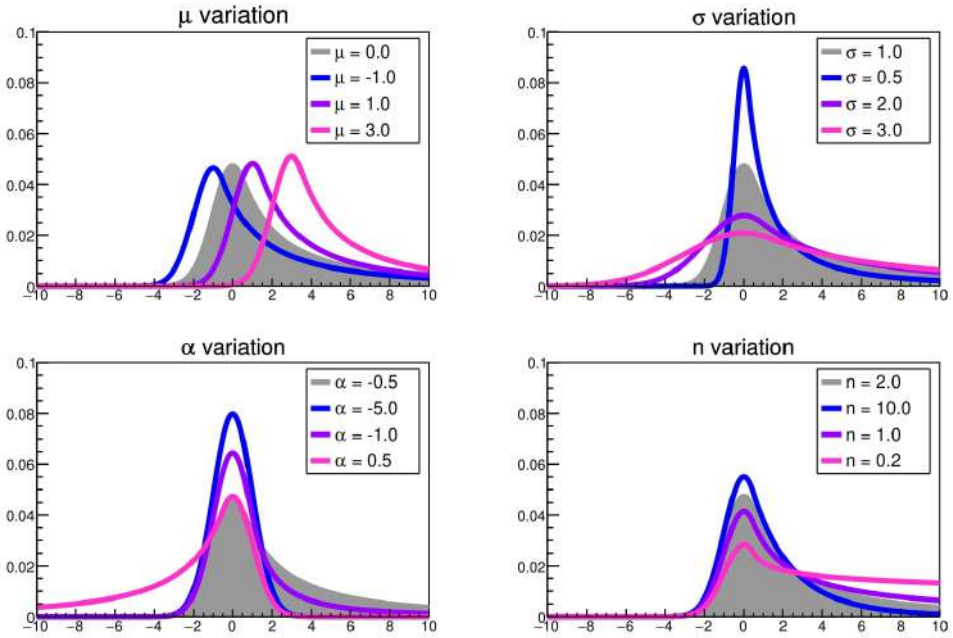

Figure 3.7: Crystal Ball probability density functions illustrating the effect of varying each of the four parameters individually: the mean μ (top left), the width σ (top right), the tail parameter α(bottom left), and the exponent n (bottom right). In each subplot, the other parameters are held fixed.

The parameters of the Crystal Ball in the simulation are denoted by (`CB-mean`, `CB-sigma`, `CB-`α, `CB-n`). The Gaussian is described by a mean and sigma (`G-mean`, `G-sigma`). A fractional coefficient (`Frac`) determines the relative weight of the two components in the final model. The combined model is constructed as:

$$\texttt{model} = \texttt{frac} \cdot \texttt{Gauss} + (1 - \texttt{frac}) \cdot \texttt{CrystalBall}$$

where

$$\texttt{Gauss} = \texttt{Gauss}(\texttt{G-mean},\ \texttt{G-sigma})$$
$$\texttt{CrystalBall} = \texttt{CrystalBall}(\texttt{CB-mean}, \texttt{CB-sigma}, \texttt{CB-}\alpha, \texttt{CB-n})$$

Initial values for the parameters are inferred from the histogram's mean and RMS or based on educated guesses, and the fit is performed using the `fitTo` method, which adjusts the model parameters to best match the data. The method uses the bin errors of the histogram as statistical weights (via `SumW2Error(true)`), and each parameter is fitted within user-defined bounds to ensure numerical stability and physically meaningful results. The `Strategy(1)` option was used to select a more robust minimization procedure compared to the default `Strategy(0)`. Although slightly slower, it increases the chances of successful convergence for more complex models like the one used in this work.

This hybrid approach provides stable fits across most PMTs and configurations, even when the fTime distribution exhibits significant skewness or non-Gaussian behavior. The parameters extracted from the fits are later used as entries in the Look-Up Table (LUT), serving as the representative observables for each PMT.

Chapter 4

Results

This chapter presents a selection of results from the simulation and fitting procedures. Specifically, it includes outputs from six distinct simulation configurations, with additional results provided in the chapter 5. To ensure clarity and consistency, a fixed structure is followed throughout: each configuration is allocated four pages. The first two pages display the 14 histograms corresponding to the number of photoelectrons (nPE), shown in pink. The following two pages present the 14 histograms of first photoelectron arrival times (fTime), shown in purple. The color scheme of the fitting models remains consistent across all 28 histograms to facilitate visual interpretation.

Each histogram is labeled with the identifier of the corresponding PMT being analyzed. At the end of each group of 14 histograms, a brief comment summarizes and contextualizes the most relevant observations. Once all configurations have been presented, a general discussion of the results follows.

The selected configurations aim to provide a rough sampling of the parameter space. They are listed below, in order of appearance:

- `e-_1000_e0.07GeV_theta60deg_phi180deg_alpha30deg_r180cm_h50cm.root`
- `e-_1000_e7GeV_theta20deg_phi0deg_alpha30deg_r90cm_h178cm.root`
- `mu-_1000_e100GeV_theta80deg_phi180deg_alpha30deg_r180cm_h125cm.root`
- `mu-_1000_e1GeV_theta20deg_phi80deg_alpha0deg_r36cm_h178cm.root`
- `gamma_1000_e0.3GeV_theta40deg_phi40deg_alpha0deg_r54cm_h178cm.root`
- `gamma_1000_e10GeV_theta60deg_phi120deg_alpha0deg_r180cm_h178cm.root`

These results are based on a limited number of simulated events (1000 per configuration), which constrains the statistical precision of the fits. In some cases, particularly at lower energies, the histograms may exhibit low statistics. Therefore, the results presented here should

be interpreted as a preliminary step toward a more comprehensive study. The computational cost of simulations remains a practical constraint.

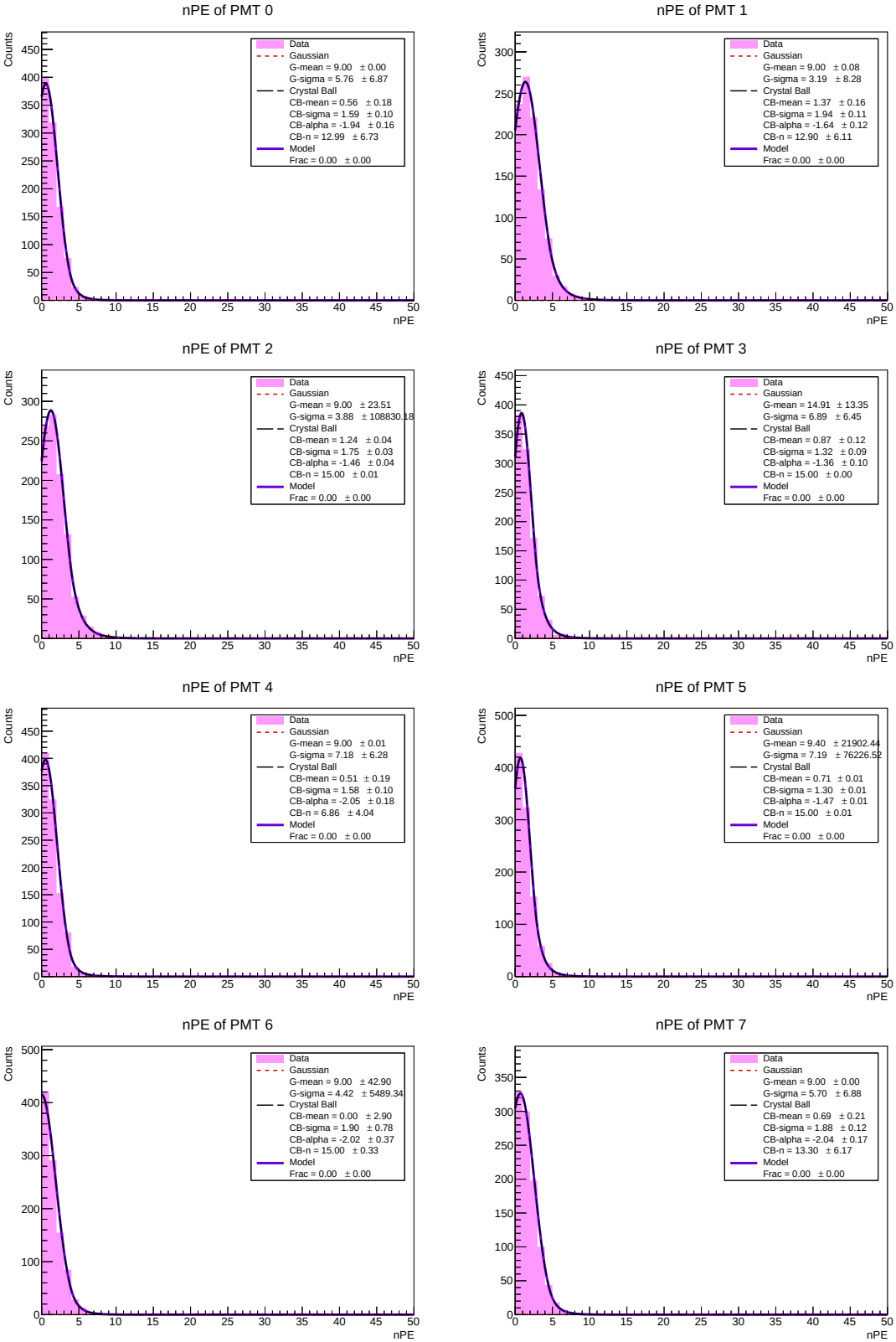

Figure 4.1: Number of photoelectrons recorded by PMTs 0 to 7, for configuration e-_1000_e0.07GeV_theta60deg_phi180deg_alpha30deg_r180cm_h50cm.root.

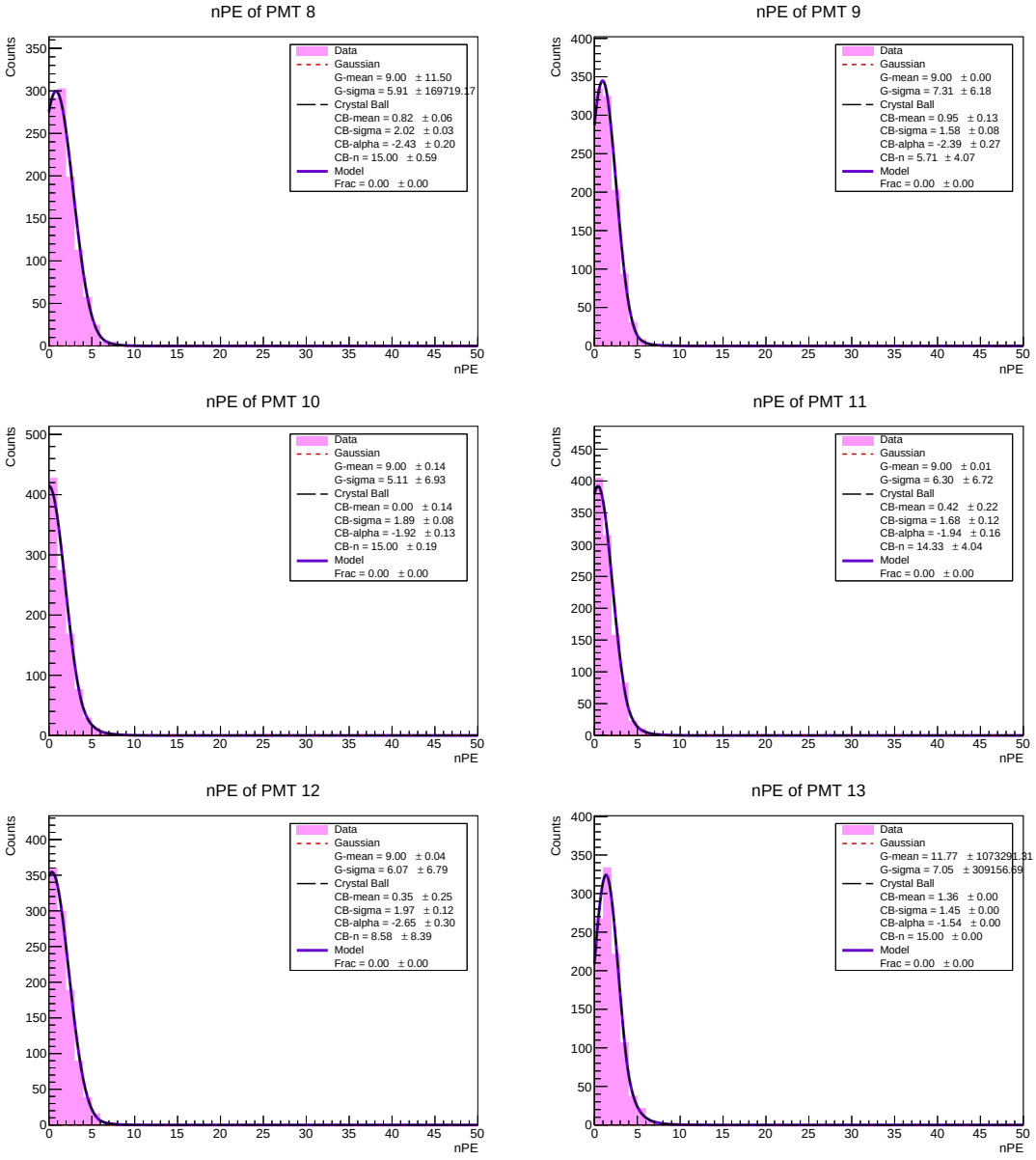

Figure 4.2: Number of photoelectrons recorded by PMTs 8 to 13, for configuration e-_1000_e0.07GeV_theta60deg_phi180deg_alpha30deg_r180cm_h50cm.root.

In Figure 4.1 and Figure 4.2, it is evident that the `CrystalBall` function alone provides a satisfactory fit to the data for this configuration. As expected for a low-energy particle (0.07 GeV), there is a strong tendency for the PMTs to register zero photoelectrons. The large uncertainties observed for `G-mean` and `G-sigma` in some histograms may indicate that the Gaussian component of the model is not converging properly, potentially due to suboptimal initial parameter guesses or fit ranges. However, this does not significantly affect the fit quality in this case: all 14 histograms have `Frac` $= 0.0$, meaning the Gaussian component contributes nothing to the model. The fit remains representative of the data, and the Gaussian function could likely be removed without altering the results.

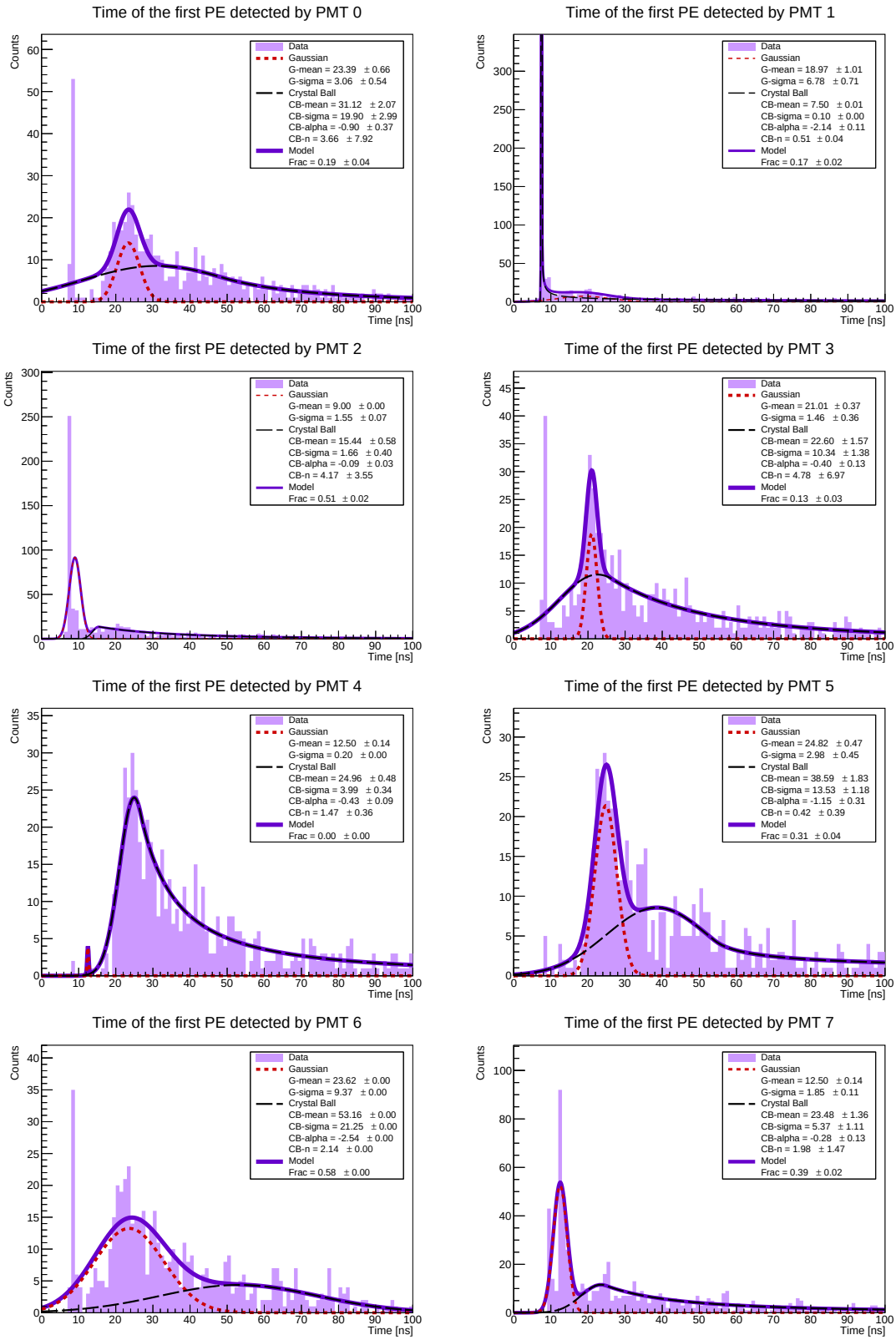

Figure 4.3: First PE arrival time (fTime) at PMTs 0 to 7, for configuration e-_1000_e0.07GeV_theta60deg_phi180deg_alpha30deg_r180cm_h50cm.root.

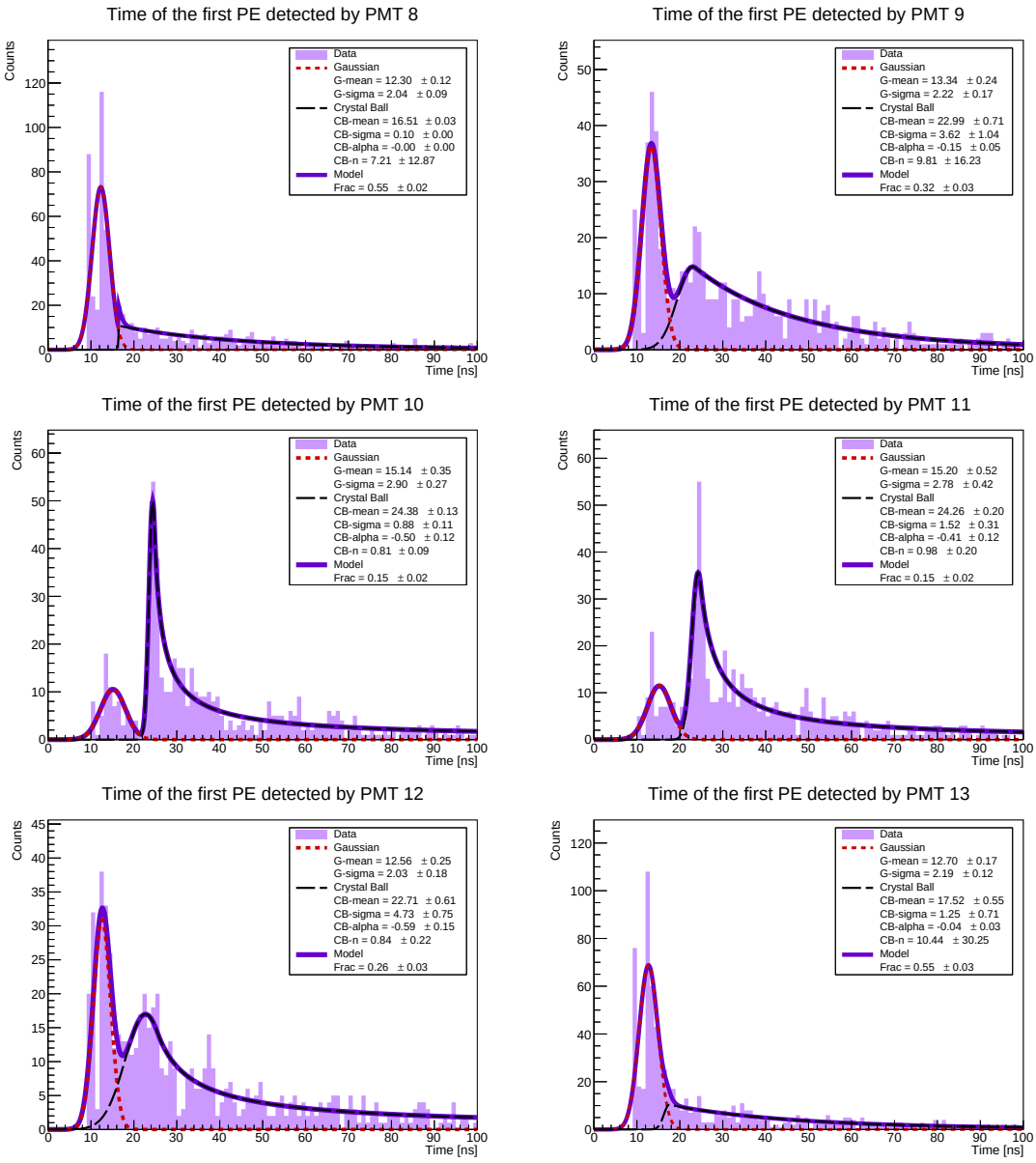

Figure 4.4: First PE arrival time (fTime) at PMTs 8 to 13, for configuration e-_1000_e0.07GeV_theta60deg_phi180deg_alpha30deg_r180cm_h50cm.root.

In Figure 4.3 and Figure 4.4, the fits appear promising. While the nPE histograms for this configuration showed very similar behavior across PMTs, the fTime histograms reveal clear differences among the 14 PMTs. The fitting procedure performed well on this dataset, with uncertainty values falling within reasonable ranges for nearly all PMTs.
It is worth noting that the range of the y-axis is not uniform across the plots; it is automatically adjusted to fit the range of each dataset. This highlights that PMTs 1 and 2 received a particularly strong signal, with most photoelectrons detected at early times. This observation is supported by the corresponding nPE plots for the same configuration, where PMTs 1 and 2 exhibit a `G-mean` greater than 1, whereas most other PMTs show `G-mean` values below zero. These findings underscore the value of jointly analyzing both the number of photoelectrons and the timing information.

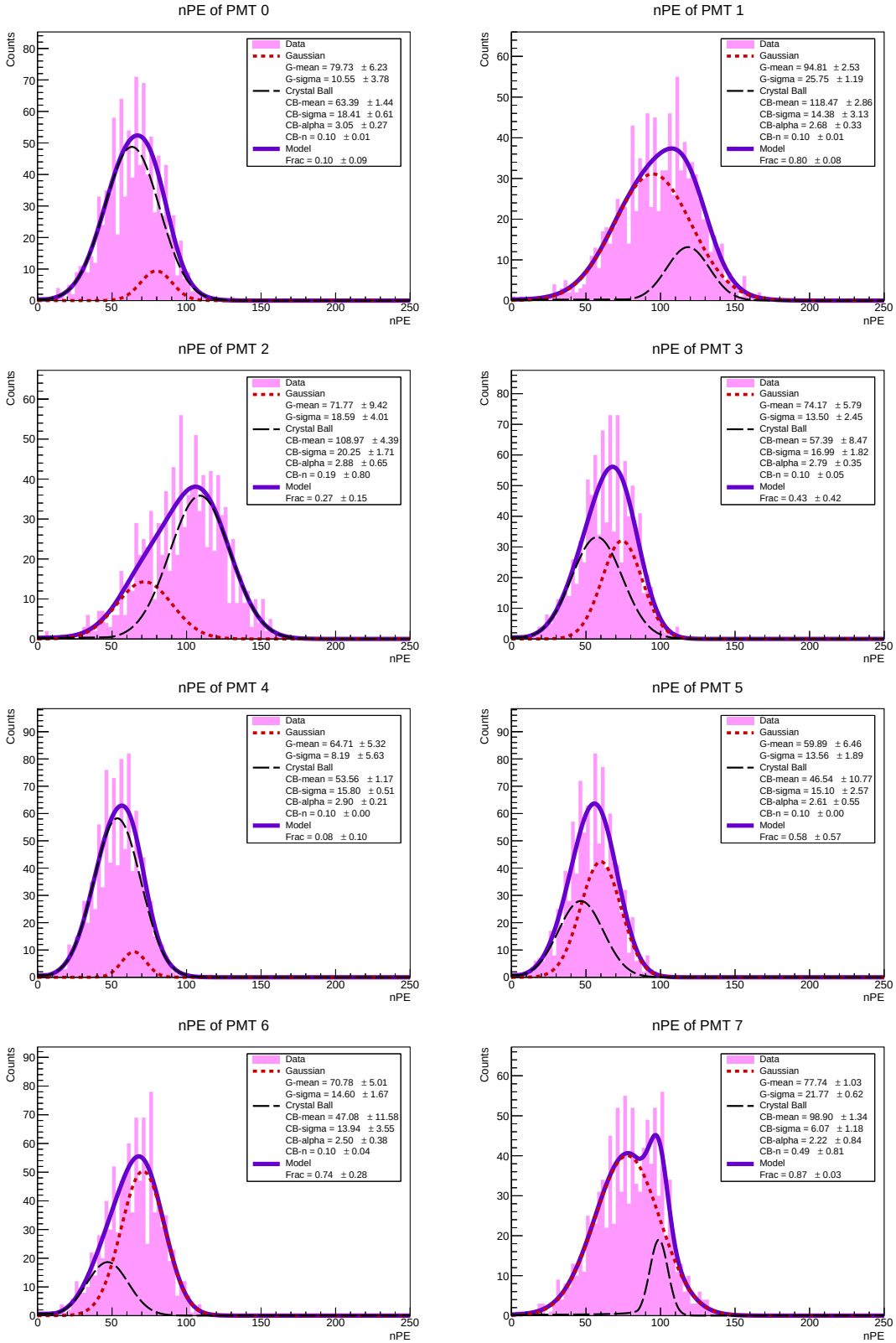

Figure 4.5: Number of photoelectrons recorded by PMTs 0 to 7, for configuration e-_1000_e7GeV_theta20deg_phi0deg_alpha30deg_r90cm_h178cm.root.

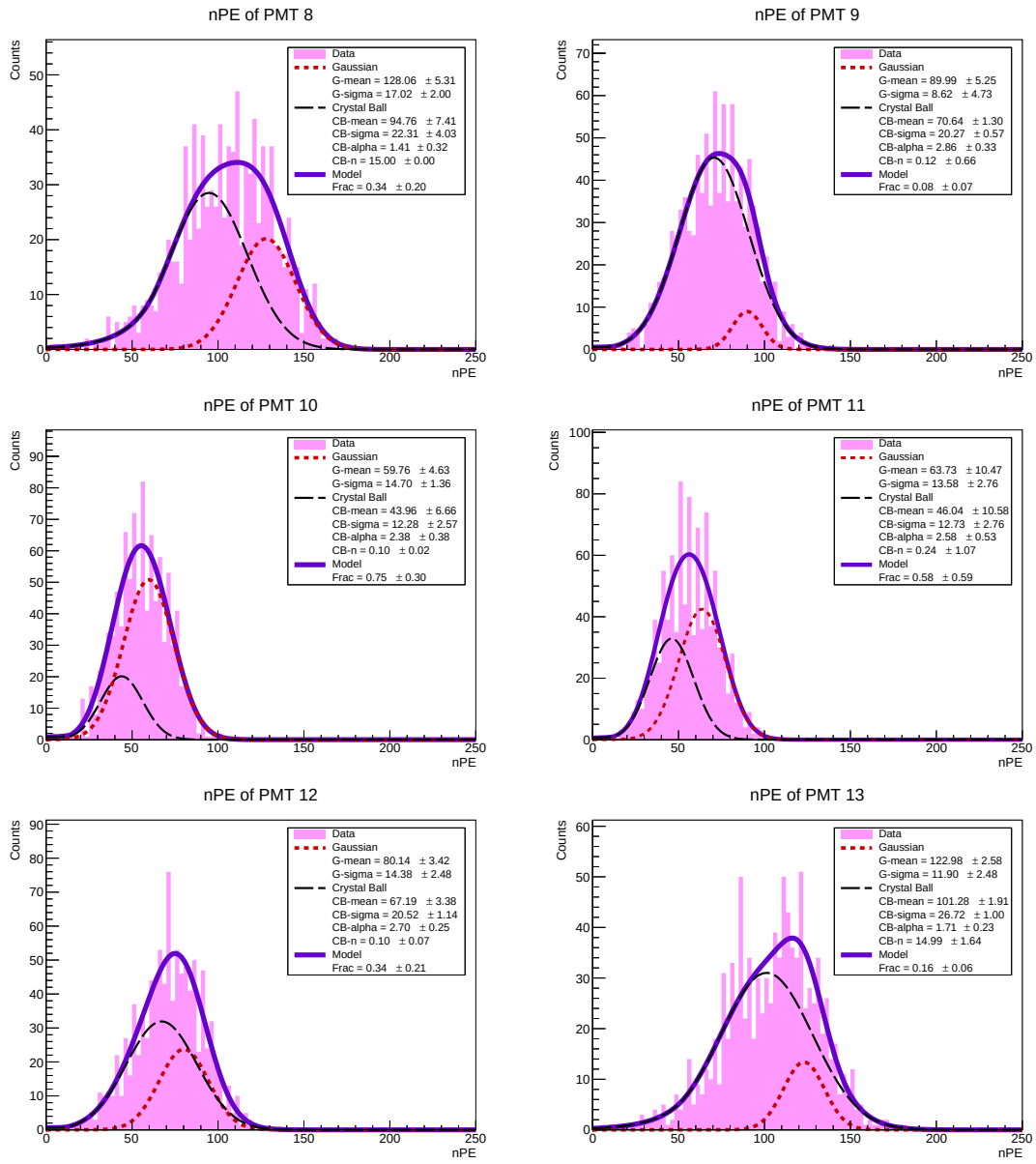

Figure 4.6: Number of photoelectrons recorded by PMTs 8 to 13, for configuration e-_1000_e7GeV_theta20deg_phi0deg_alpha30deg_r90cm_h178cm.root.

In Figure 4.5 and Figure 4.6, we first observe that the range of the nPE axis is broader (0 to 250), which is expected given that this configuration involves a higher-energy electron (7 GeV). Unlike the previous case, the distributions are no longer centered around 0 photoelectrons, which is consistent with the predicted behaviour, as high-energy particles are expected to generate a larger number of Cherenkov photons.
The fitting procedure appears to have performed very well, with error estimates falling within normal ranges across all PMTs. Additionally, the mean values of the distributions vary significantly among the PMTs, suggesting that the multi-PMT module provides meaningful directional information. It is also worth noting that the binning may be slightly too high for this dataset, as indicated by noticeable fluctuations in height between adjacent bins.

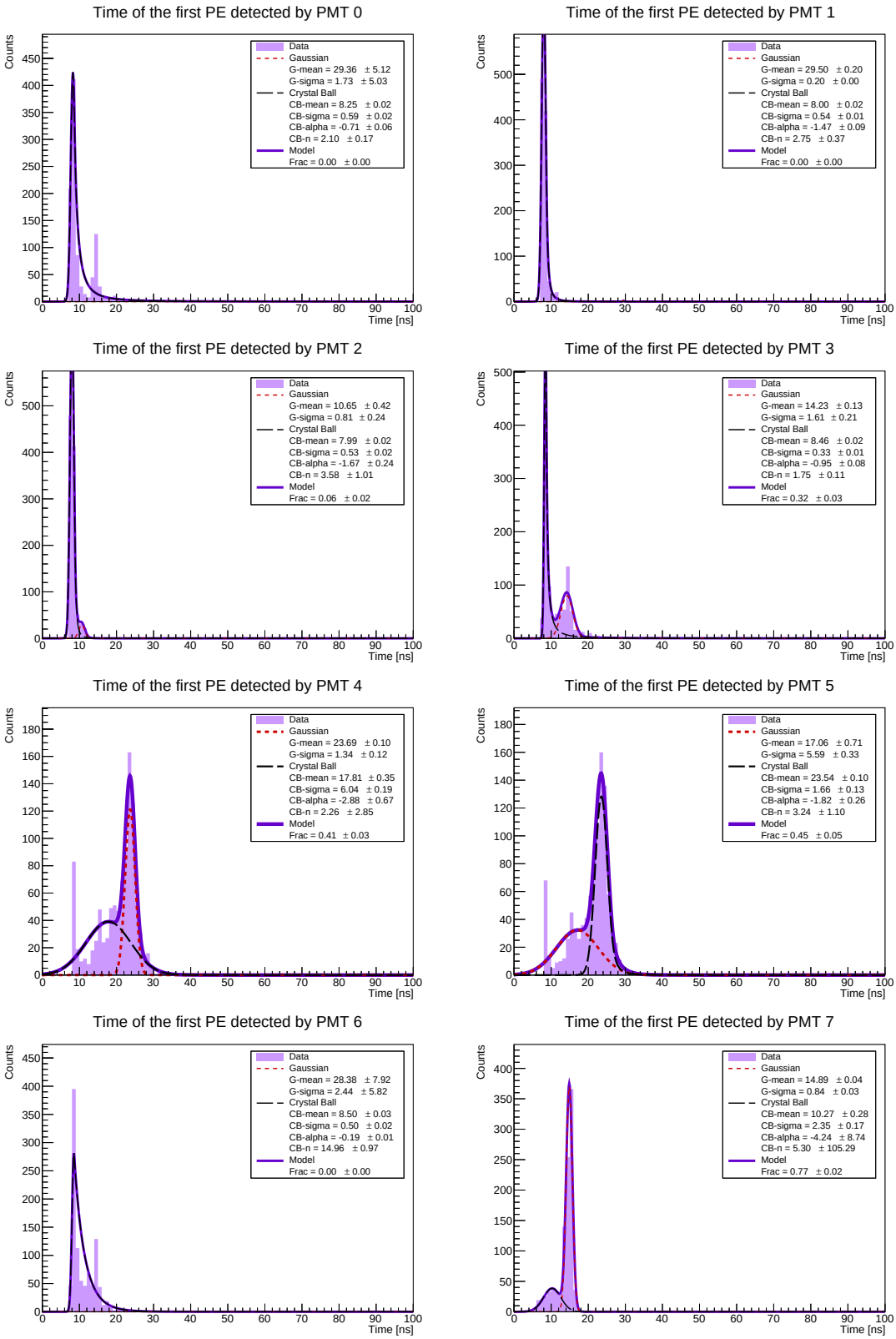

Figure 4.7: First PE arrival time (fTime) at PMTs 0 to 7, for configuration e-_1000_e7GeV_theta20deg_phi0deg_alpha30deg_r90cm_h178cm.root.

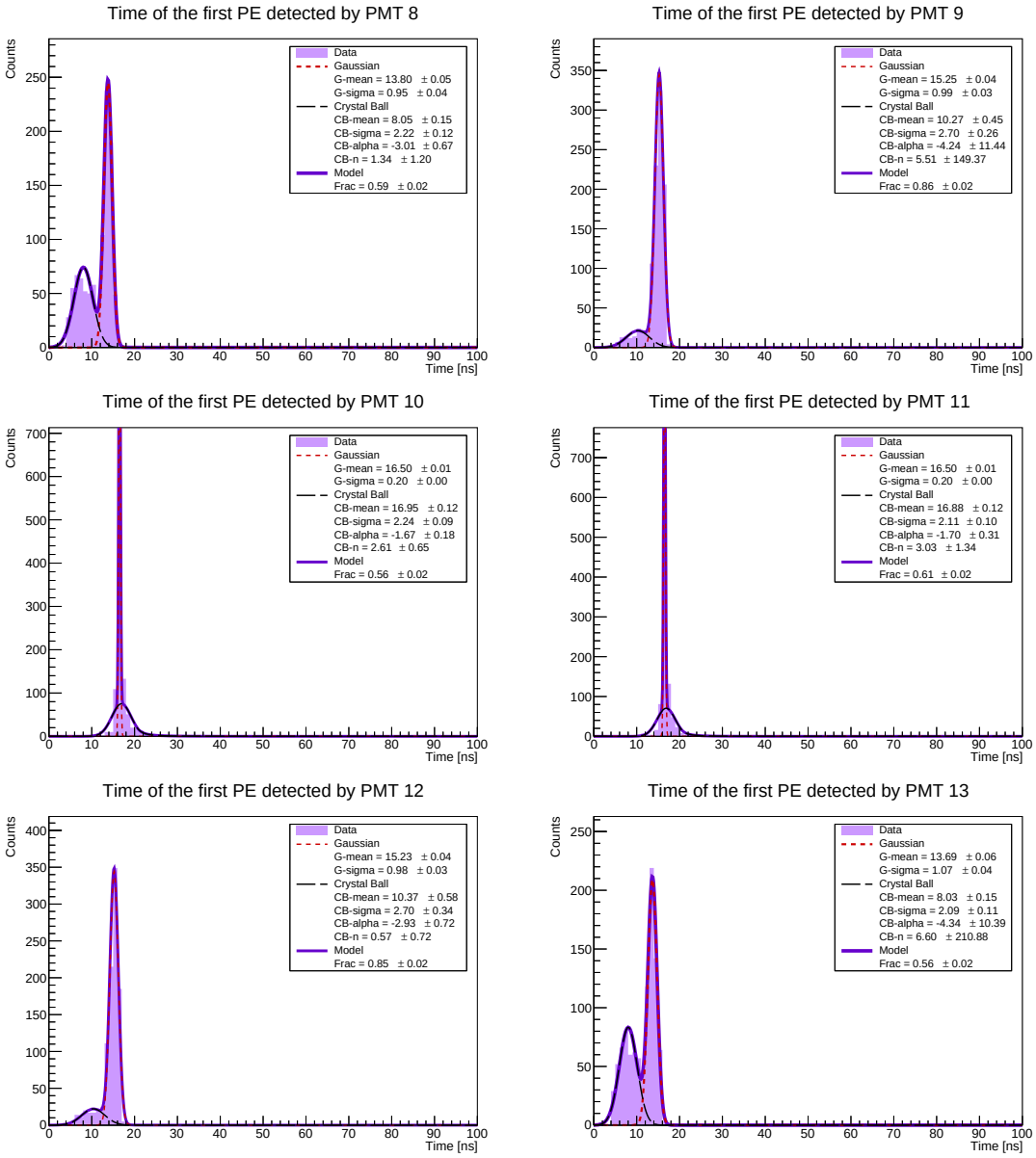

Figure 4.8: First PE arrival time (fTime) at PMTs 8 to 13, for configuration e-_1000_e7GeV_theta20deg_phi0deg_alpha30deg_r90cm_h178cm.root.

In Figure 4.7 and Figure 4.8, we observe that the range chosen for the fTime axis appears too broad. Most PMTs detect the first photoelectrons at approximately $10\,\mathrm{ns}$, except for PMTs 4 and 5, which show a peak around $25\,\mathrm{ns}$. This is consistent with expectations: the particle enters the detector from the top ($h = 178\,\mathrm{cm}$), while PMTs 4 and 5 are located near the bottom ($h \sim 0\,\mathrm{cm}$). These PMTs are also spatially distant from PMTs 1 and 2, which are positioned at $\alpha = 0°$ and $\alpha = 60°$, respectively (see Figure 3.3). Since the particle injection is configured at either $\alpha = 0°$ or $\alpha = 30°$, it is a promising result that PMTs aligned along the opposite direction register the first photoelectrons at later times.

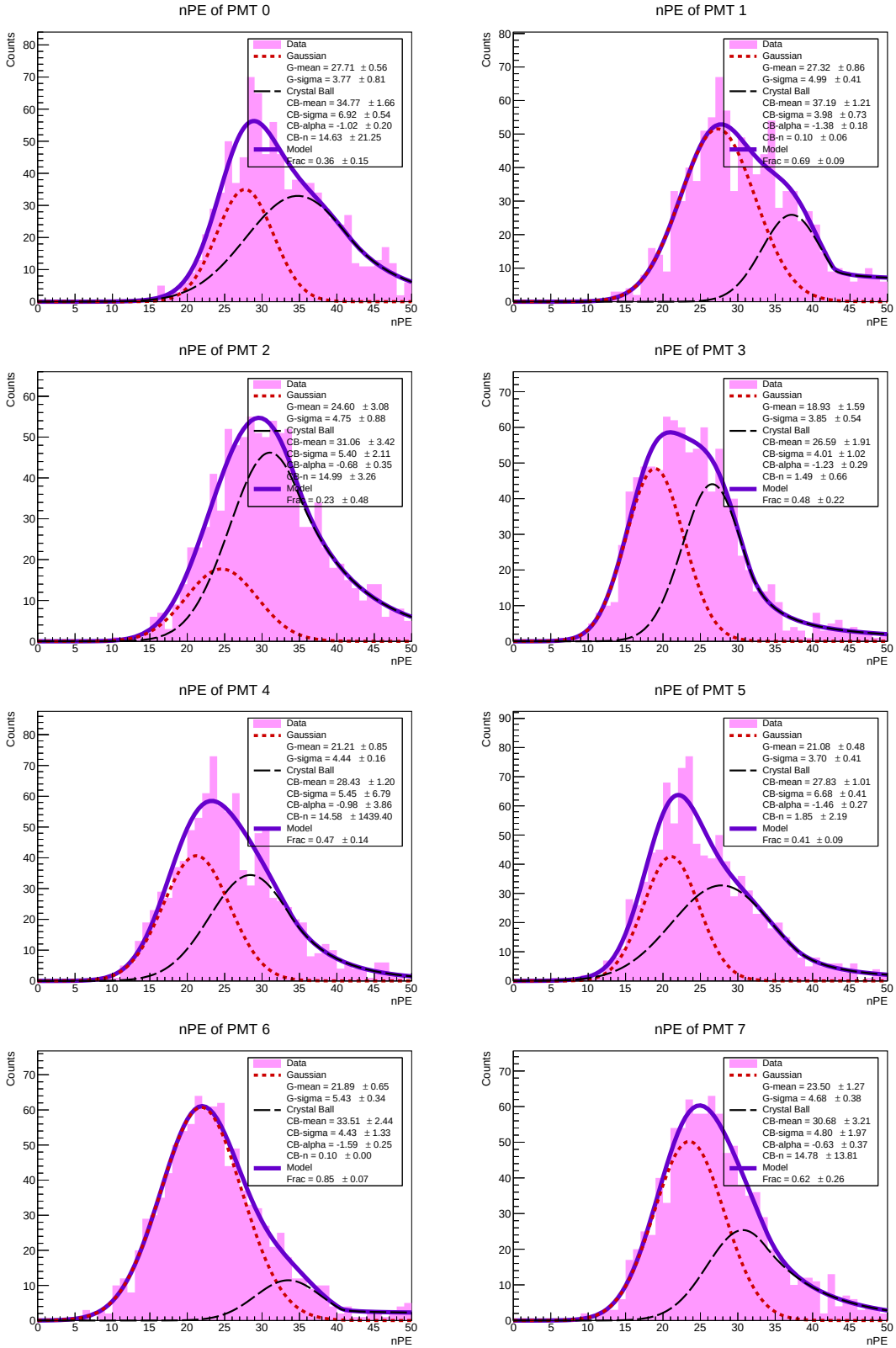

Figure 4.9: Number of photoelectrons recorded by PMTs 0 to 7, for configuration mu-_1000_e100GeV_theta80deg_phi180deg_alpha30deg_r180cm_h125cm.root.

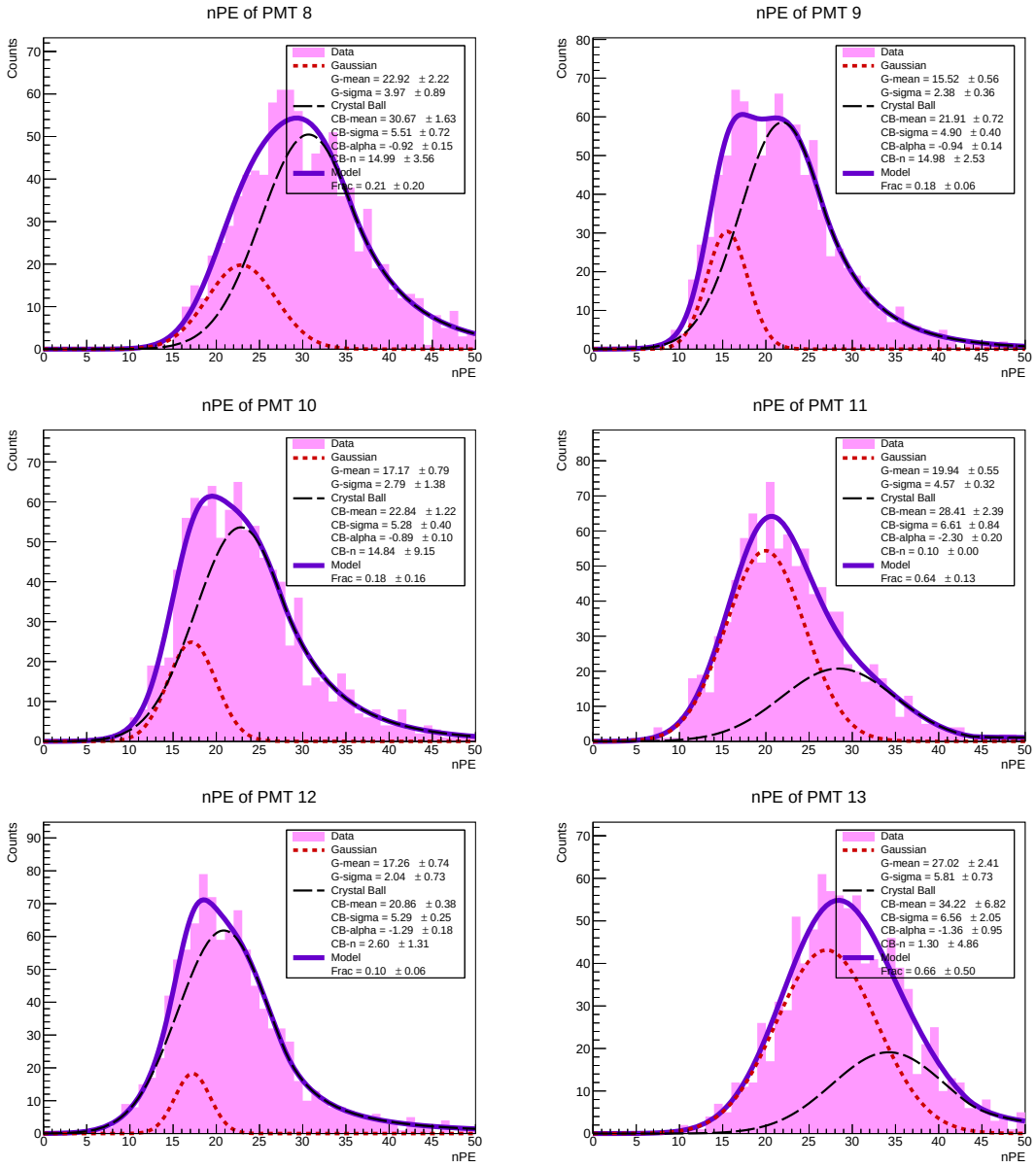

Figure 4.10: Number of photoelectrons recorded by PMTs 8 to 13, for configuration mu-_1000_e100GeV_theta80deg_phi180deg_alpha30deg_r180cm_h125cm.root.

In Figure 4.9 and Figure 4.10, the fits appear satisfactory, with error values within normal ranges. It is somewhat unexpected that a very high-energy muon ($100\,\mathrm{GeV}$) does not produce a broader distribution in the nPE histograms. However, this may be explained by its incident angle: with $\theta = 80°$, the muon's trajectory is nearly horizontal, limiting the amount of water it traverses and therefore reducing the production of Cherenkov photons. This angular configuration may also account for the uniformity observed across the PMTs, as the nPE distributions are centered around similar values for all channels.

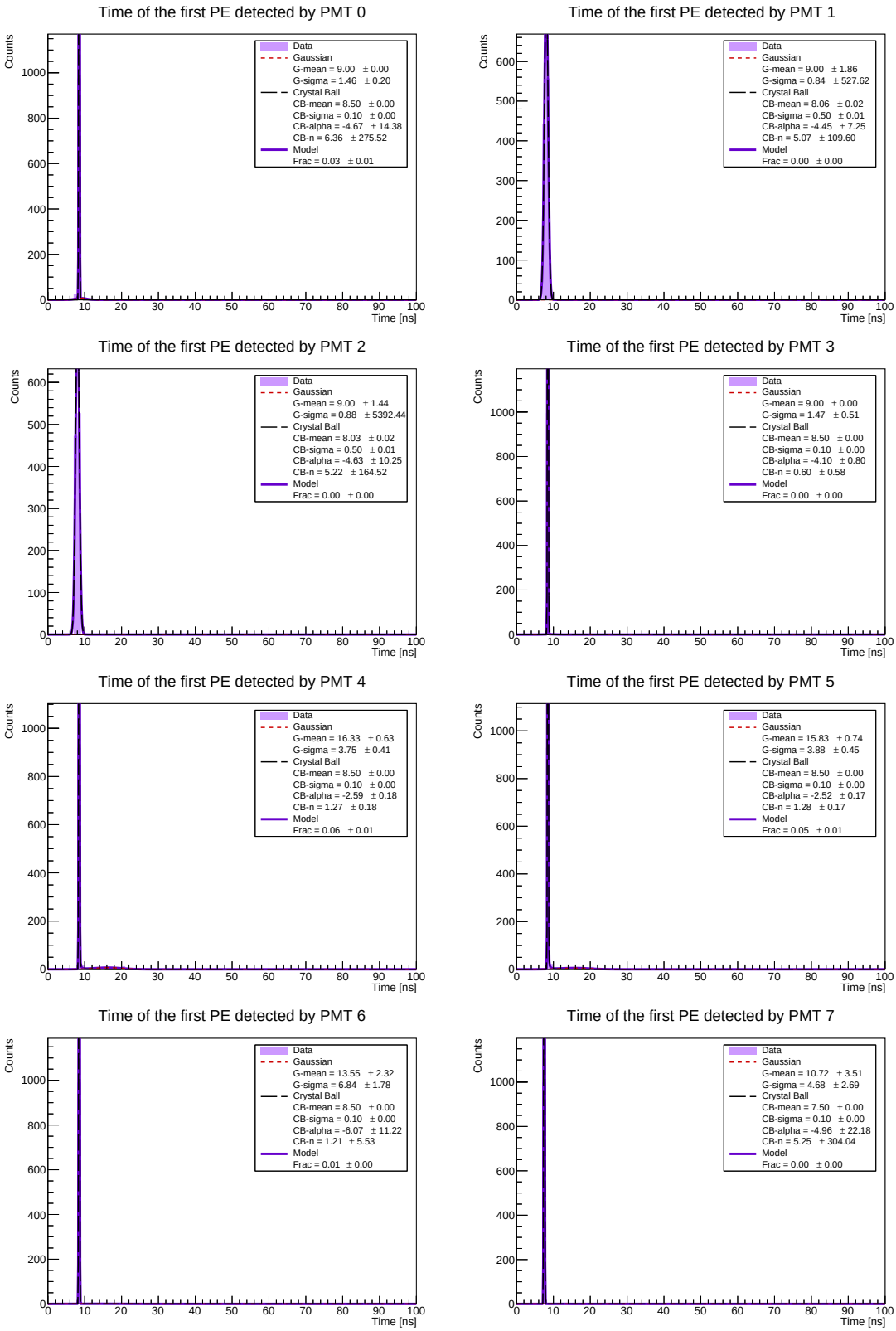

Figure 4.11: First PE arrival time (fTime) at PMTs 0 to 7, for configuration mu-_1000_e100GeV_theta80deg_phi180deg_alpha30deg_r180cm_h125cm.root.

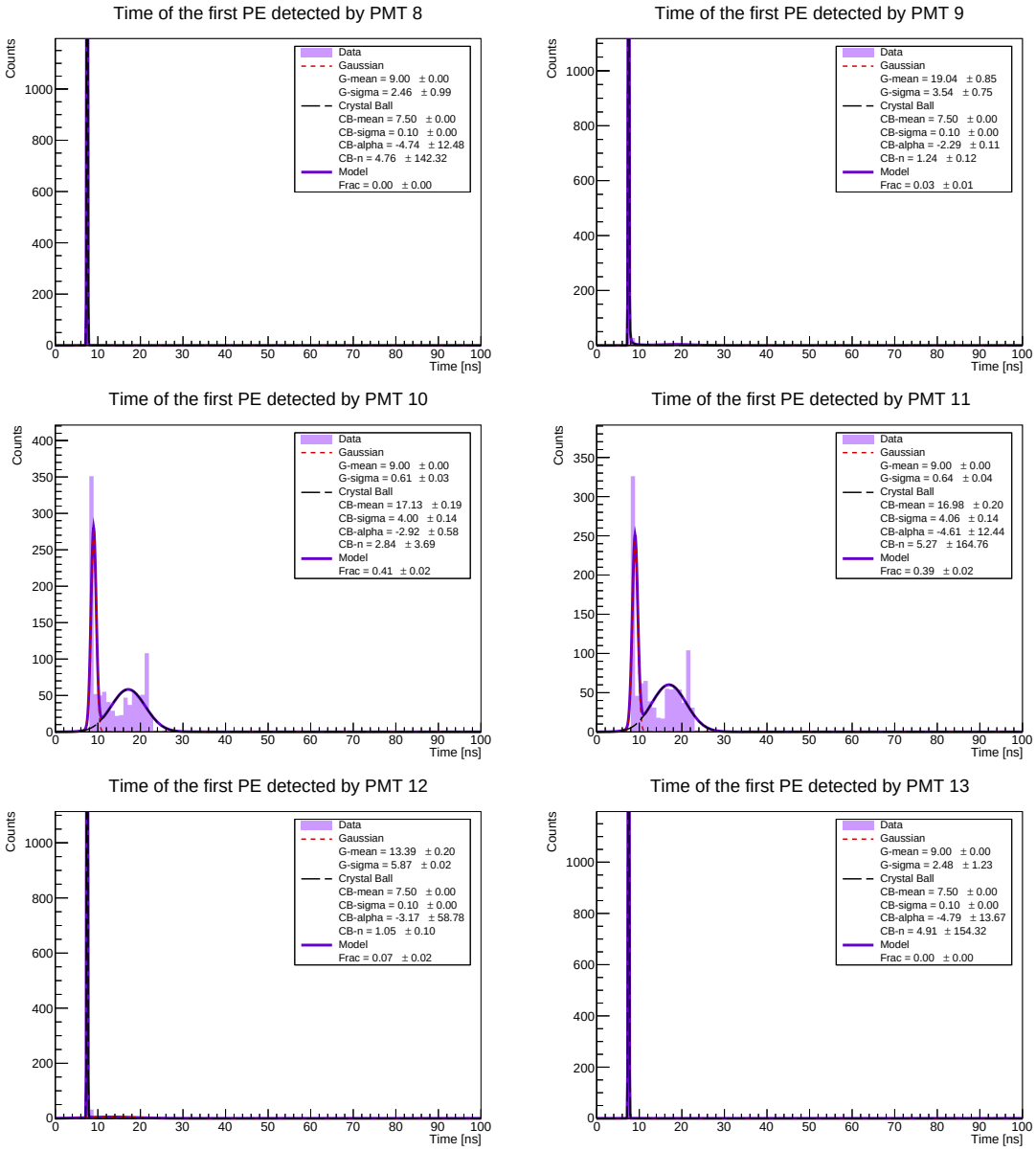

Figure 4.12: First PE arrival time (fTime) at PMTs 8 to 13, for configuration mu-_1000_e100GeV_theta80deg_phi180deg_alpha30deg_r180cm_h125cm.root.

In Figure 4.11 and Figure 4.12, it is evident that the fixed range for fTime should be adjusted to better suit the data. In this case, the fTime distributions are tightly clustered around $10\,\mathrm{ns}$, with no events observed beyond $25\,\mathrm{ns}$, making the current range of 0–$100\,\mathrm{ns}$ unnecessarily broad. Additionally, several plots report errors of 0.00 for both `G-mean` and `CB-mean`, indicating issues in the fitting process. This may result from overly restrictive parameter bounds for these means. If the range is too wide, the optimizer may converge to a local rather than a global minimum; conversely, overly narrow ranges may force the fit to stop at a value that does not represent the data well.

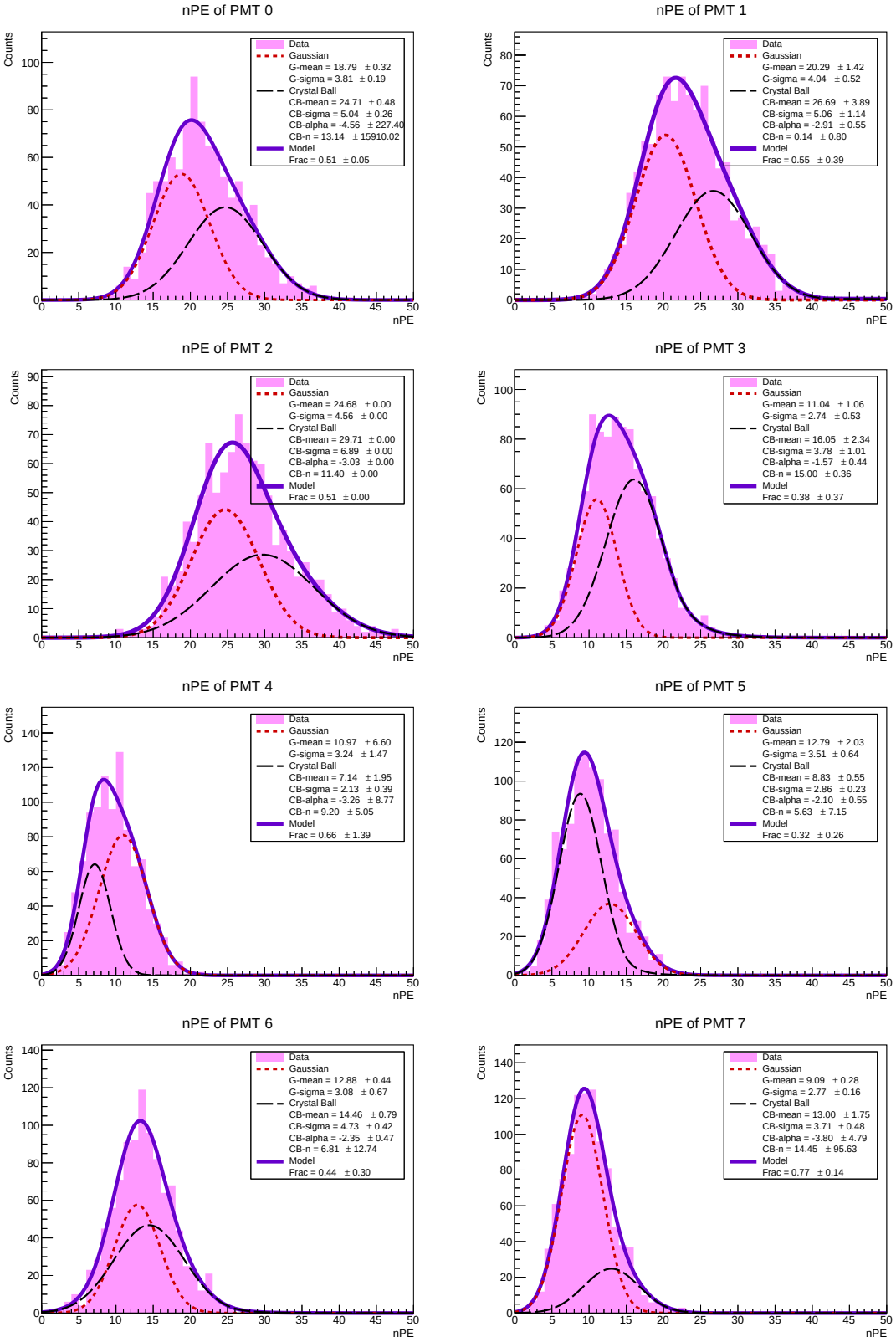

Figure 4.13: Number of photoelectrons recorded by PMTs 0 to 7, for configuration mu-_1000_e1GeV_theta20deg_phi80deg_alpha0deg_r36cm_h178cm.root.

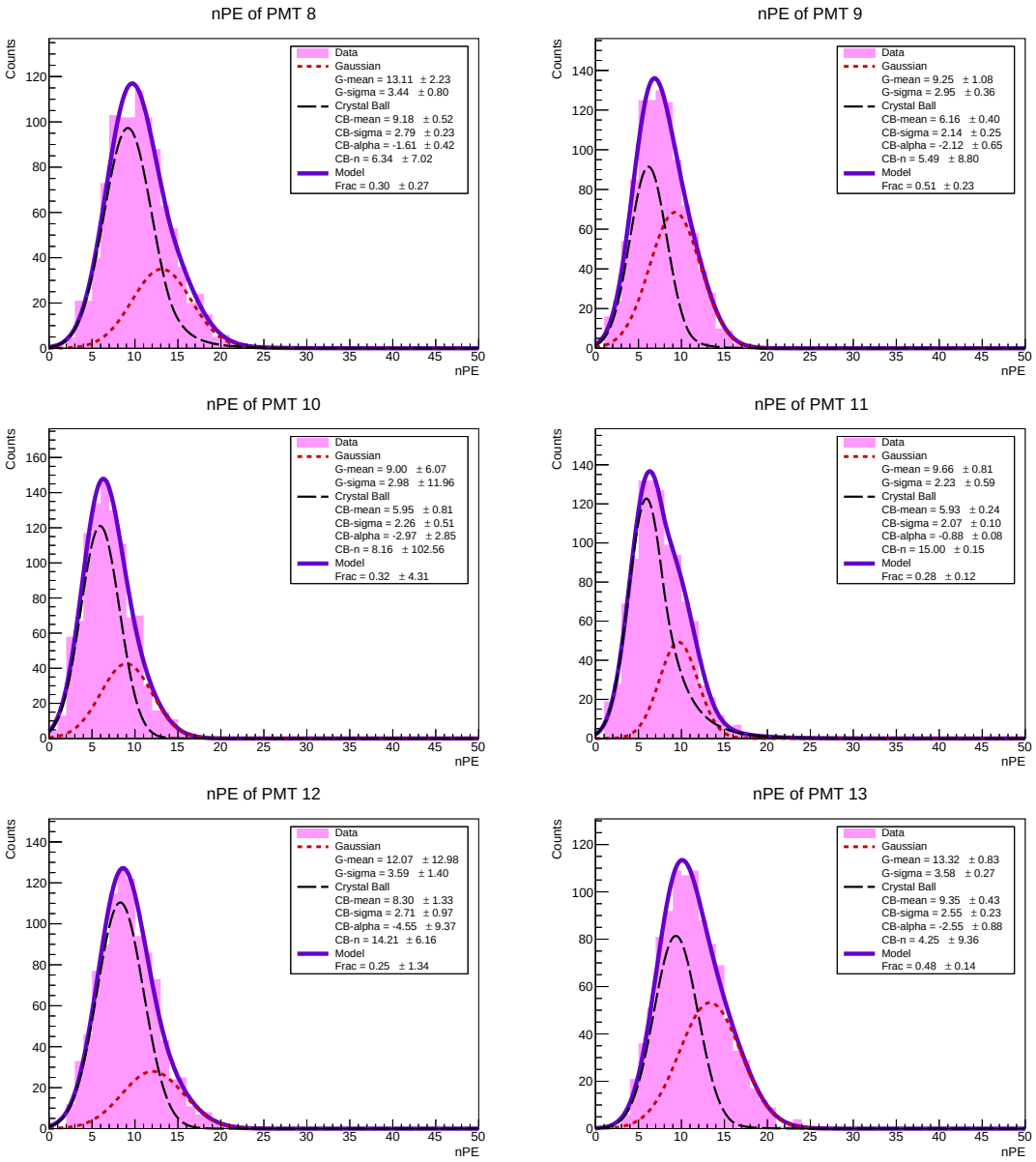

Figure 4.14: Number of photoelectrons recorded by PMTs 8 to 13, for configuration mu-_1000_e1GeV_theta20deg_phi80deg_alpha0deg_r36cm_h178cm.root.

In Figure 4.13 and Figure 4.14, the results appear very satisfactory. The fit parameters fall within normal ranges, and the histogram binning and axis limits are appropriately set. While a high-energy muon is expected to generate a significant number of Cherenkov photons, the particle's trajectory—defined by $\theta = 20°$ and $\phi = 80°$—suggests it traverses only a limited portion of the water volume. This shorter path length reduces the overall photon production. Furthermore, PMTs located at the bottom of the detector (0 to 6) received more photoelectrons than those at the top (7 to 13), which is consistent with the muon's downward direction. Cherenkov photons emitted along this path tend to travel downward and may require multiple reflections off the tank walls before reaching the multi-PMT module at the top.

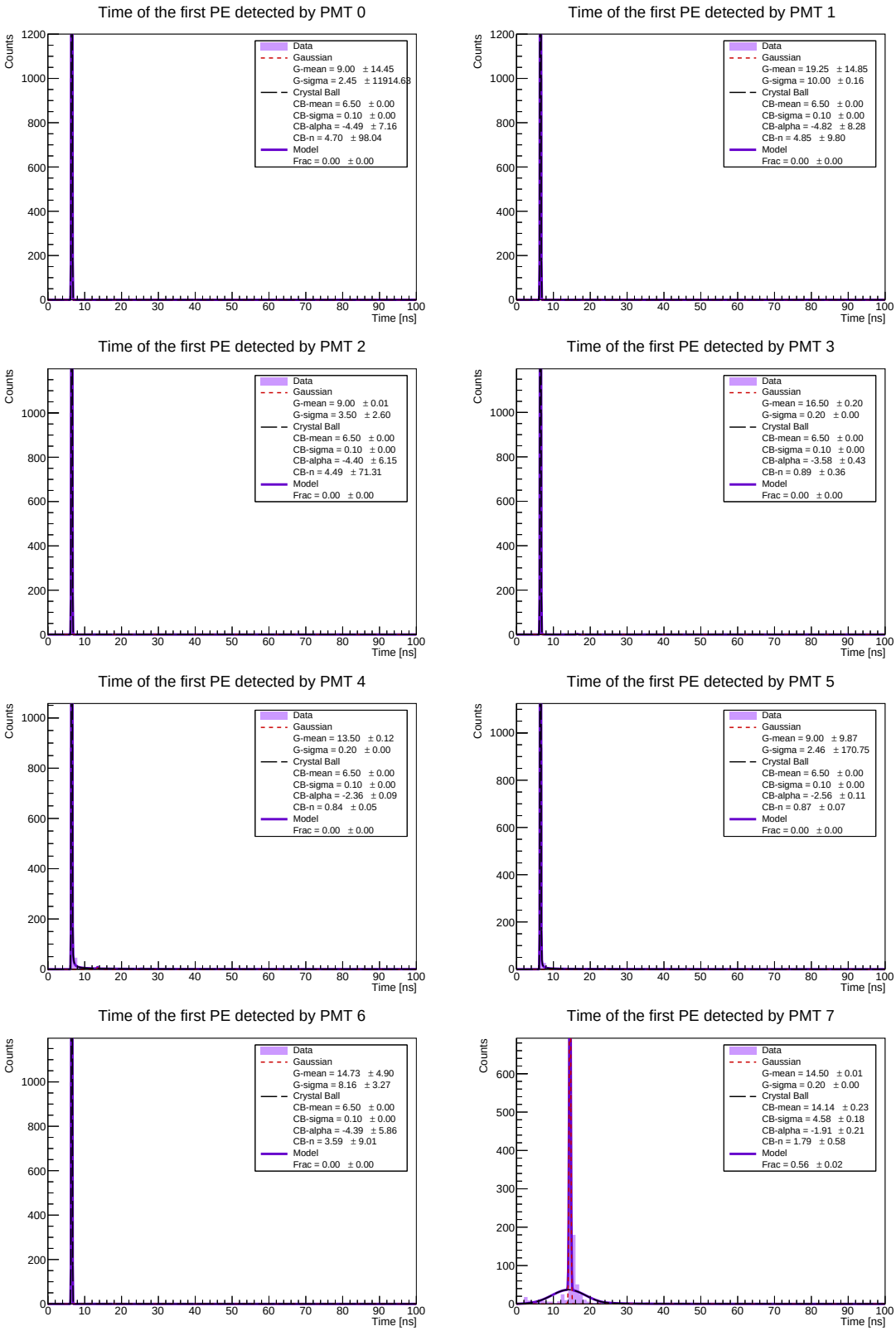

Figure 4.15: First PE arrival time (fTime) at PMTs 0 to 7, for configuration mu-_1000_e1GeV_theta20deg_phi80deg_alpha0deg_r36cm_h178cm.root.

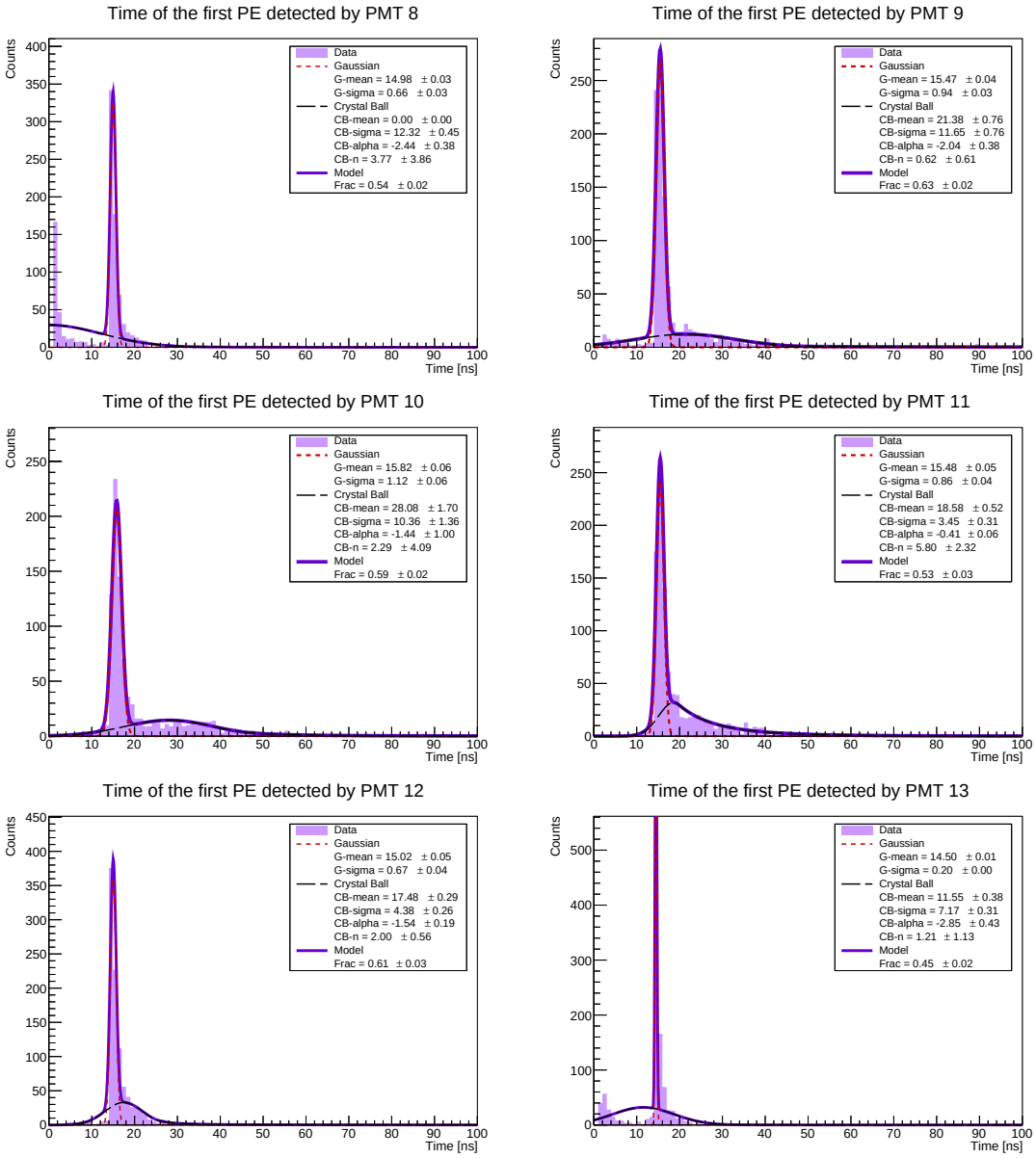

Figure 4.16: First PE arrival time (fTime) at PMTs 8 to 13, for configuration mu-_1000_e1GeV_theta20deg_phi80deg_alpha0deg_r36cm_h178cm.root.

In Figure 4.15 and Figure 4.16, the contrast between the signals detected by the PMTs at the bottom and those at the top of the multi-PMT module becomes evident. For the bottom PMTs (0 to 6), the signal is sharply peaked, resembling a Dirac delta, with first photoelectron arrival times (`fTime`) around 8 ns. In contrast, the top PMTs (7 to 13) show a broader distribution with later arrival times. Notably, PMTs 8 and 13 exhibit an additional early peak near 1 ns, likely corresponding to Cherenkov photons arriving directly without reflections. These early peaks are not captured by the current fitting model but could provide valuable information for the lookup table (LUT). Once again, the `fTime` histogram ranges should be shortened, and the fitting parameter bounds require careful revision.

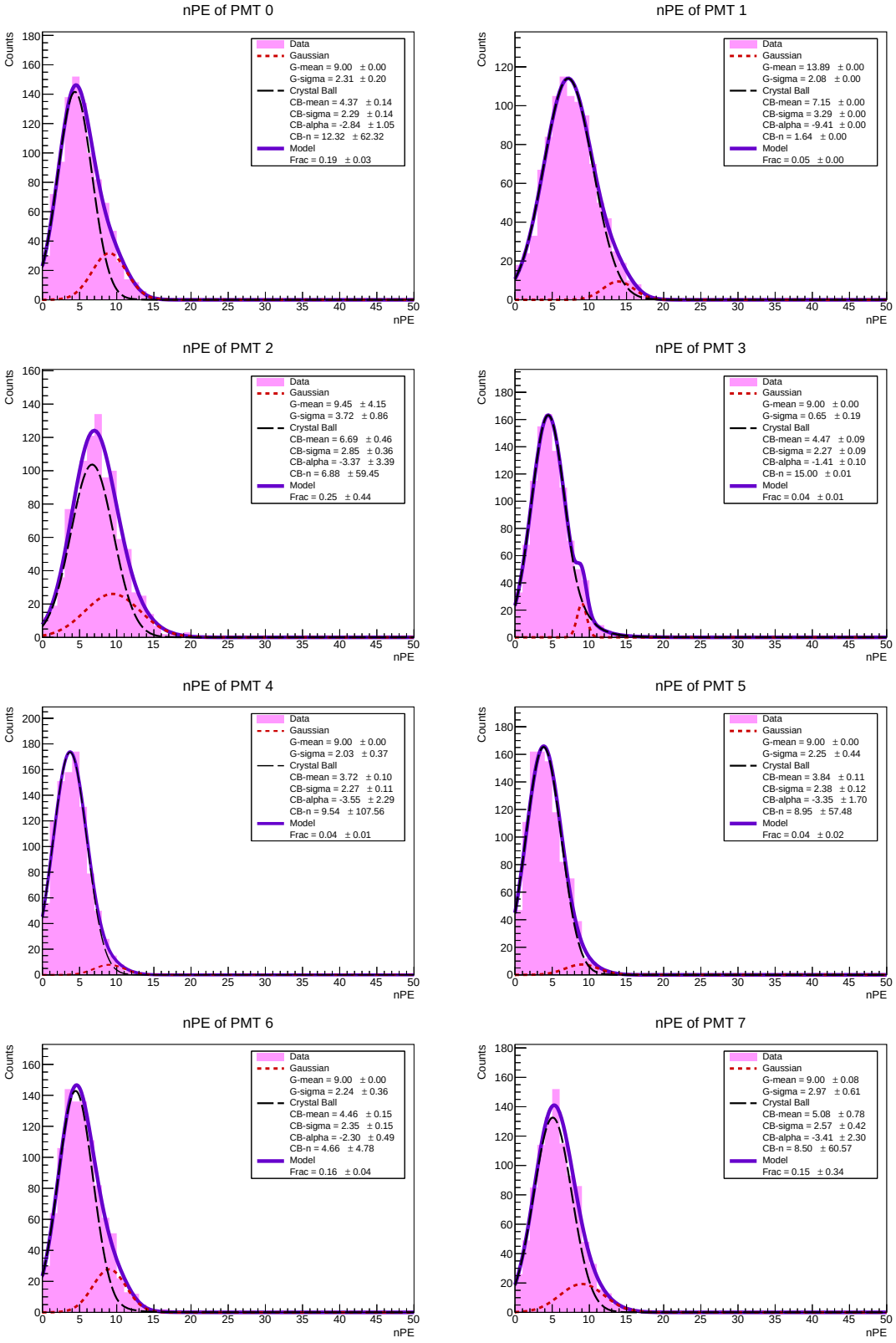

Figure 4.17: Number of photoelectrons recorded by PMTs 0 to 7, for configuration gamma_1000_e0.3GeV_theta40deg_phi40deg_alpha0deg_r54cm_h178cm.root.

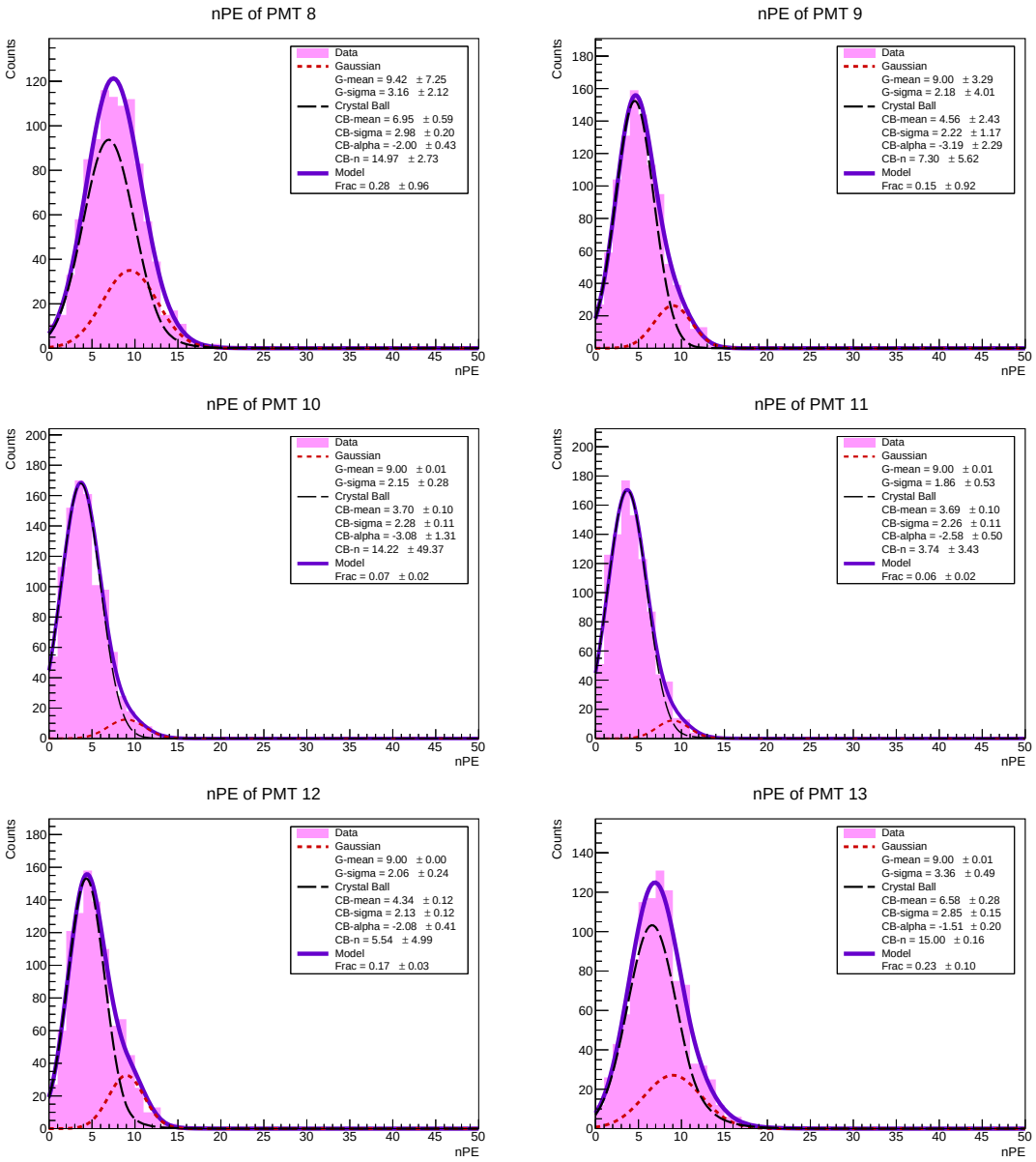

Figure 4.18: Number of photoelectrons recorded by PMTs 8 to 13, for configuration gamma_1000_e0.3GeV_theta40deg_phi40deg_alpha0deg_r54cm_h178cm.root.

In Figure 4.17 and Figure 4.18, the fitting parameters appear normal and the histogram ranges are well set. In some of the plots, `Frac` is very close to zero, suggesting that the CrystalBall function alone could sufficiently describe the data. Although the particle is a gamma ray, which must undergo pair production to generate Cherenkov photons, the nPE counts are rarely zero. This is likely due to the gamma's relatively high energy ($0.3\,\mathrm{GeV}$). PMTs 1, 2, 8, and 13 register higher photoelectron counts, consistent with the particle's direction. Specifically, $\mathrm{phi} = 40°$ indicates that the particle is exiting the detector, implying it entered the detector across the point where it was placed (see Figure 3.5). This, together with the other directional parameters, explains why PMT 13 detected a notably higher number of photoelectrons.

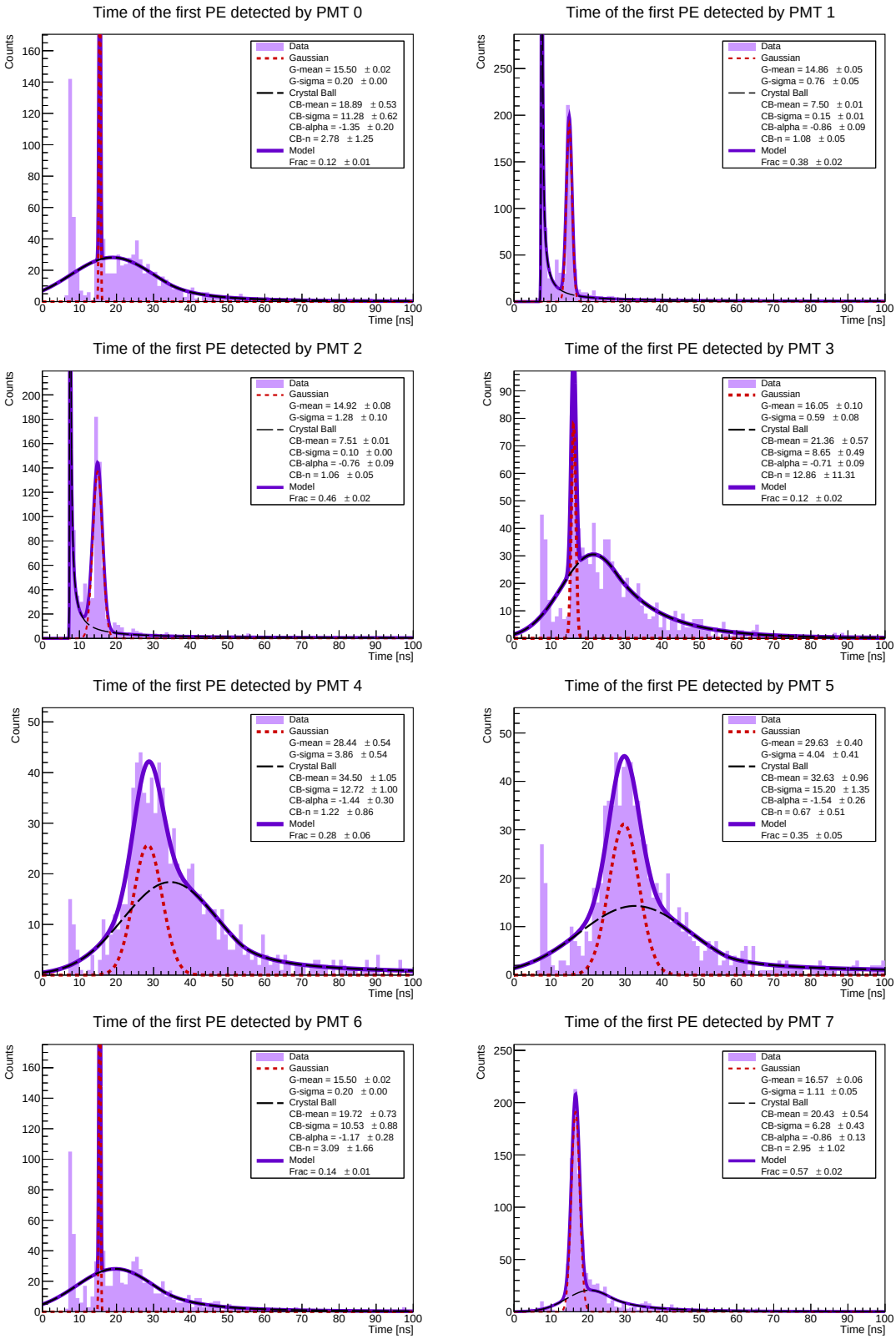

Figure 4.19: First PE arrival time (fTime) at PMTs 0 to 7, for configuration gamma_1000_e0.3GeV_theta40deg_phi40deg_alpha0deg_r54cm_h178cm.root.

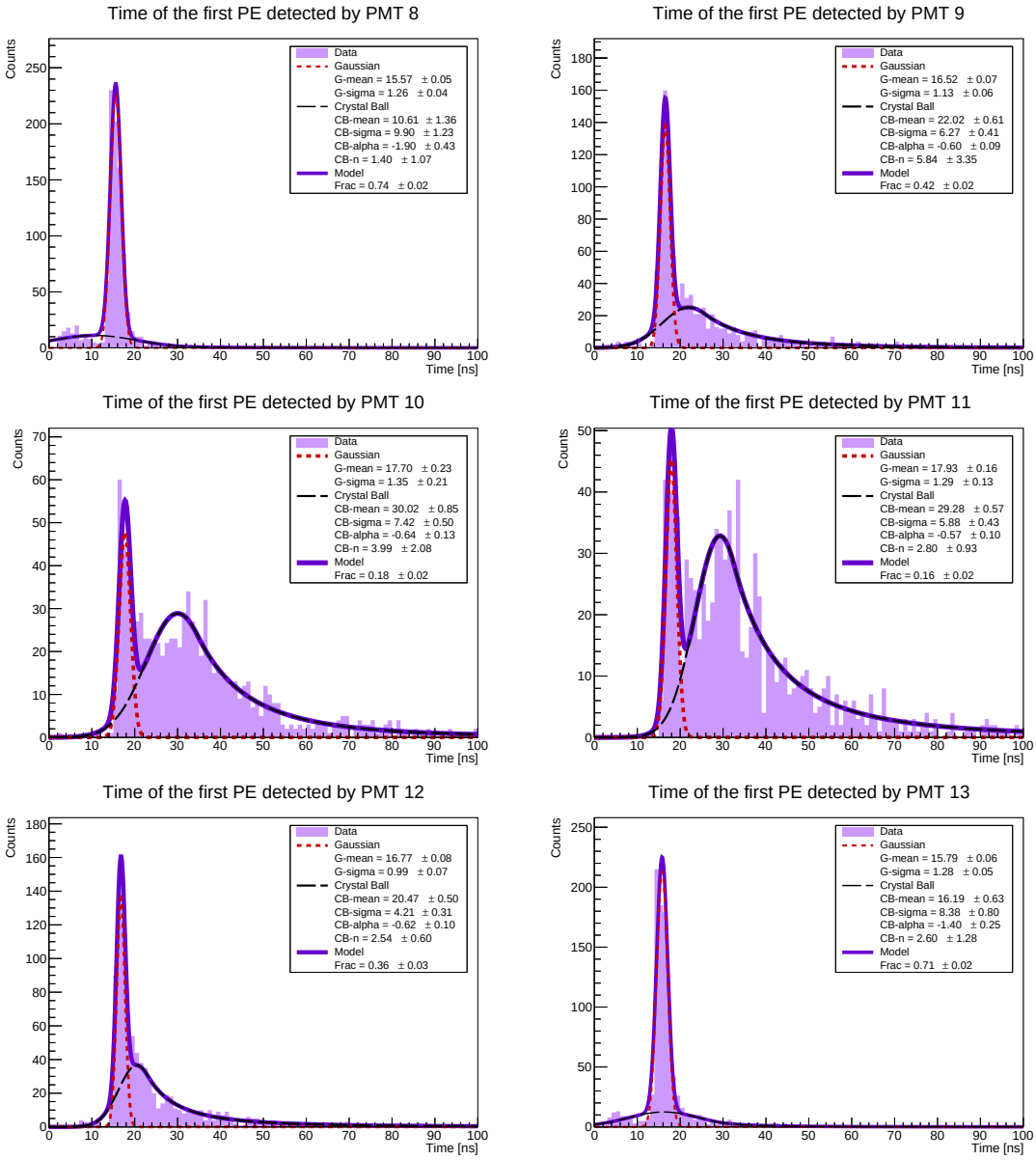

Figure 4.20: First PE arrival time (fTime) at PMTs 8 to 13, for configuration gamma_1000_e0.3GeV_theta40deg_phi40deg_alpha0deg_r54cm_h178cm.root.

In Figure 4.19 and Figure 4.20, the differences in the signals between PMTs are very clear. For instance, PMT 10 and PMT 13, which are positioned across from each other in the multiPMT at the top, show markedly different fTime signals. This is a promising indication that the multiPMT module can provide significant advantages compared to a single PMT unit. Some histograms exhibit peaks that were not captured by the fits, reinforcing the need to revise the ranges for the fit parameters. At the top, PMTs 3, 4, and 5 display later signals with lower counts relative to others; similarly, at the bottom, PMTs 10 and 11 show the same behavior. These observations are consistent with the nPE signals seen in the previous plots for this configuration.

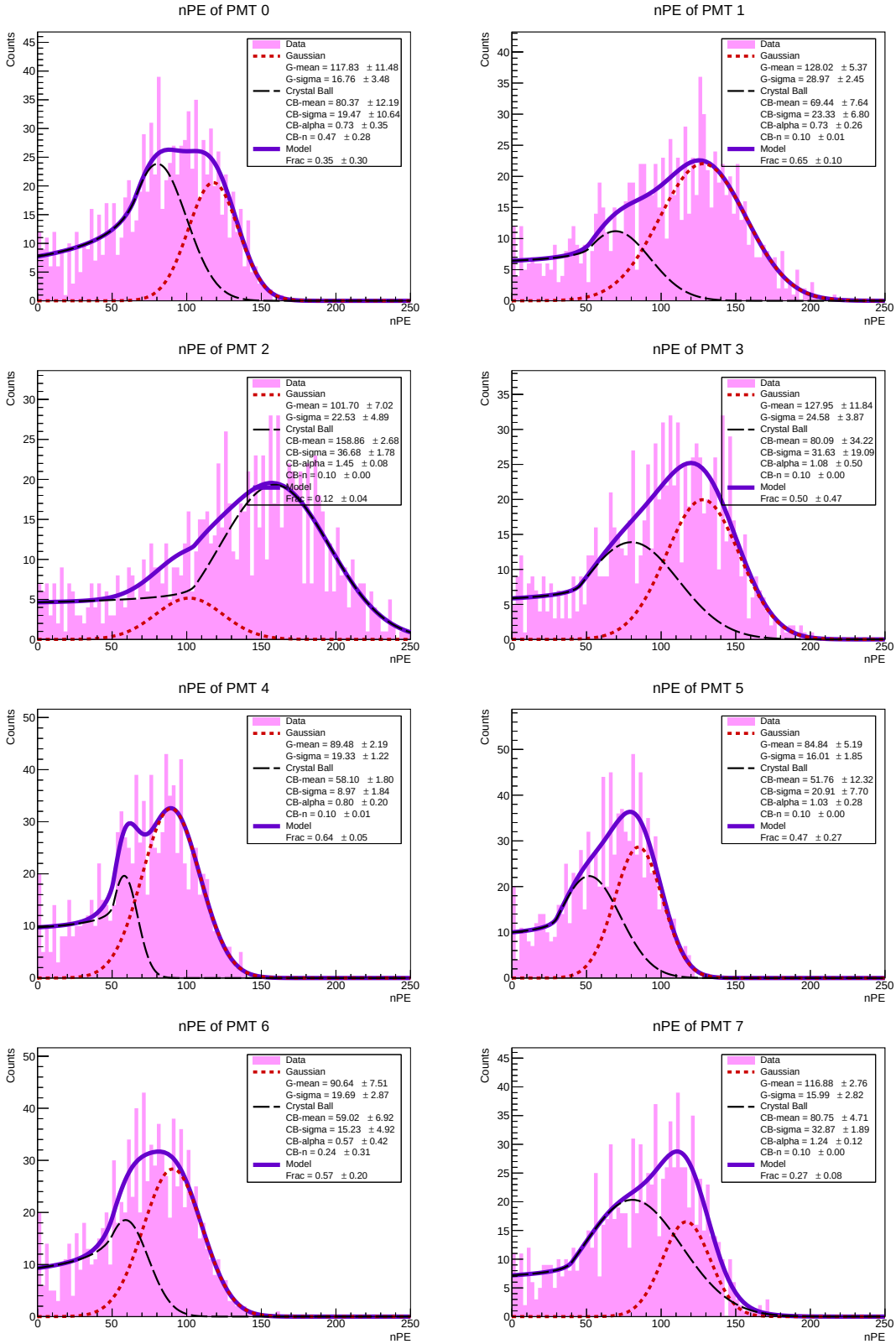

Figure 4.21: Number of photoelectrons recorded by PMTs 0 to 7, for configuration gamma_1000_e10GeV_theta60deg_phi120deg_alpha0deg_r180cm_h178cm.root.

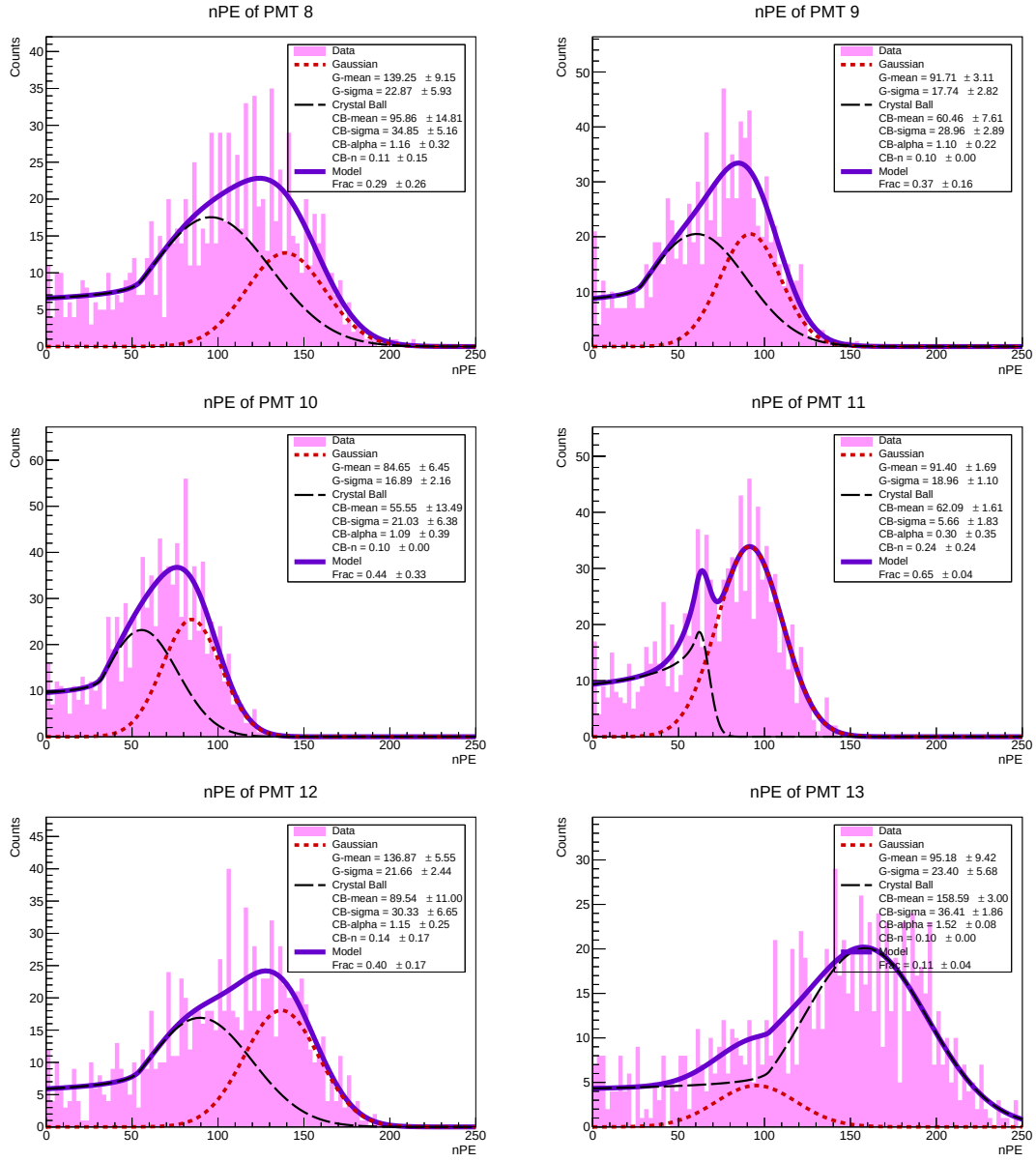

Figure 4.22: Number of photoelectrons recorded by PMTs 8 to 13, for configuration gamma_1000_e10GeV_theta60deg_phi120deg_alpha0deg_r180cm_h178cm.root.

In Figure 4.21 and Figure 4.22, it is evident that the binning is finer than necessary. The fits appear good, with the CrystalBall function effectively capturing the pronounced left tail in all histograms. For this dataset, the model performs very well, as both the Gaussian and CrystalBall components are necessary to accurately represent the data. Although the particle is a gamma, which might typically yield a low signal due to the requirement of pair production, the statistics are sufficient to produce a reliable fit. This is encouraging for LUT production and demonstrates that gammas at high energies ($10\mathrm{GeV}$ in this case) can be detected effectively. Additionally, the plots show markedly different distributions across the various PMTs, once again highlighting the advantages of using a multiPMT module.

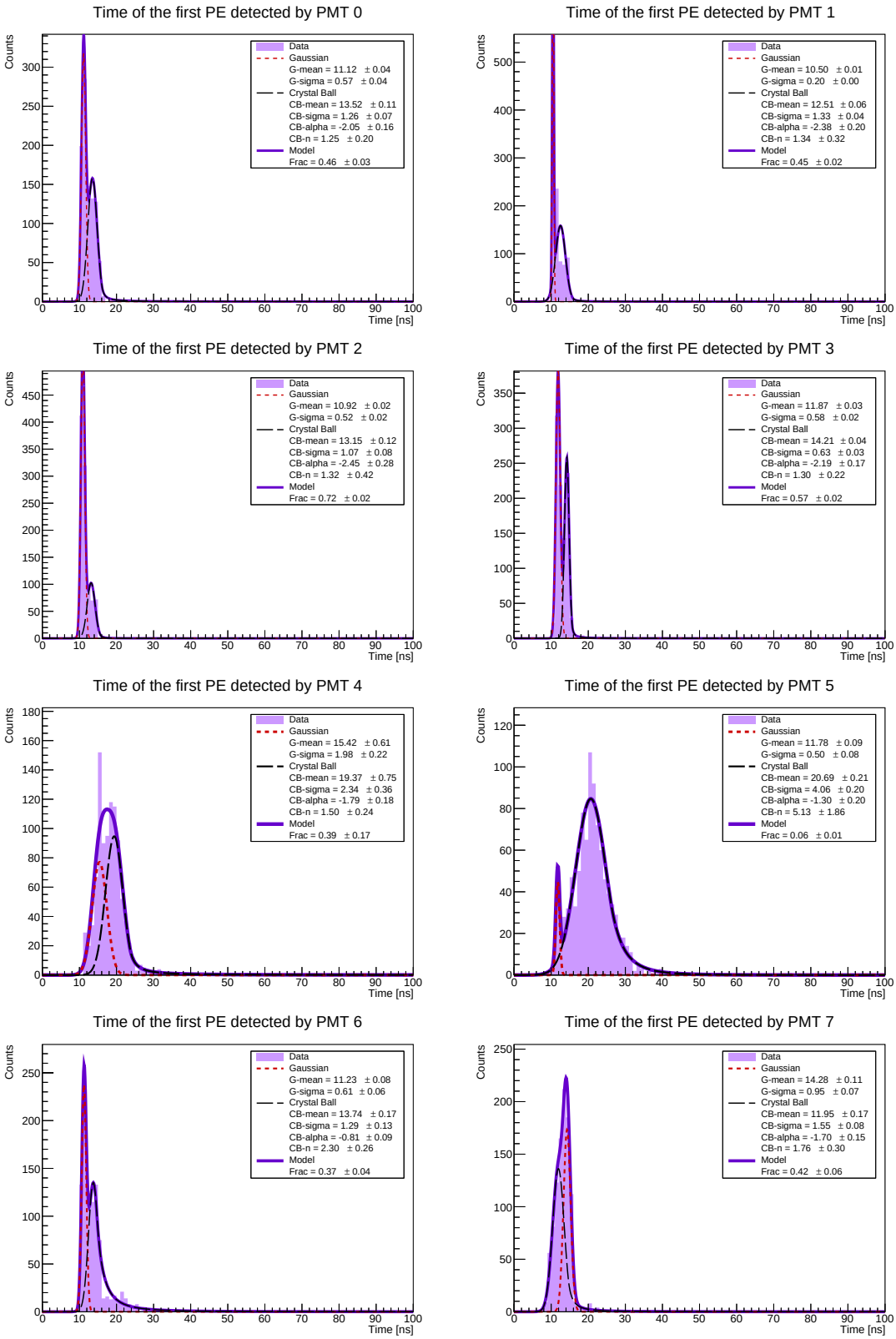

Figure 4.23: First PE arrival time (fTime) at PMTs 0 to 7, for configuration gamma_1000_e10GeV_theta60deg_phi120deg_alpha0deg_r180cm_h178cm.root.

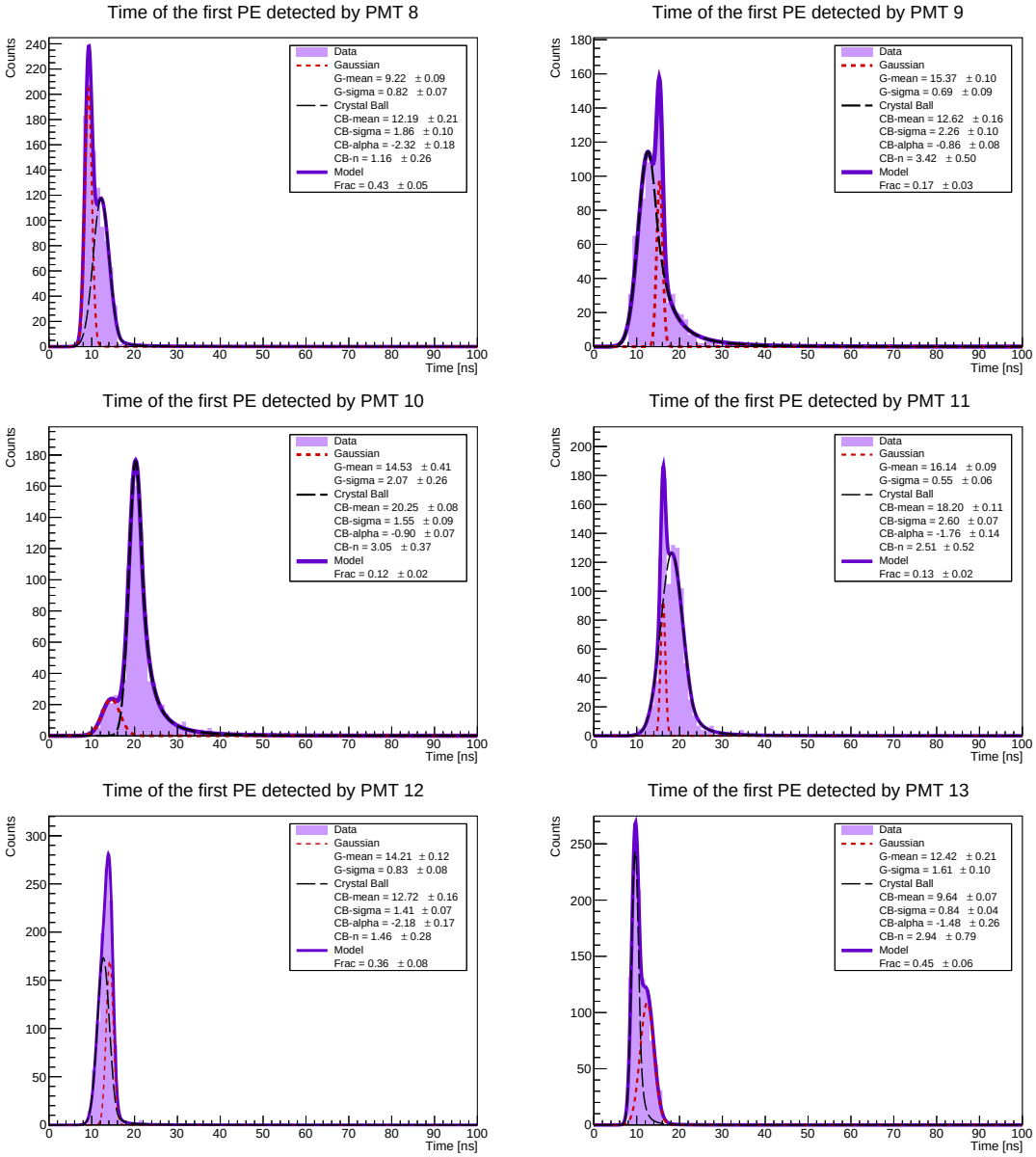

Figure 4.24: First PE arrival time (fTime) at PMTs 8 to 13, for configuration gamma_1000_e10GeV_theta60deg_phi120deg_alpha0deg_r180cm_h178cm.root.

In Figure 4.23 and Figure 4.24, the fitting process appears very successful, with all peaks properly accounted for. Some plots, such as that for PMT 12, display only a single peak but were still fitted using both functions in the model. While this does not pose a problem, reducing the number of fit parameters when possible is preferable. This suggests that the fitting process could be optimized by segmenting it according to whether the data requires one or two distributions.

4.1 Discussion of Results

The analysis of the nPE and fTime distributions across different simulation configurations reveals several key insights into the performance of the multiPMT detector module and the behavior of Cherenkov photons under varying particle conditions.

First, it is evident that the range selection for fTime histograms and fit parameters is crucial. For some configurations, the selected range (0–$100\,\mathrm{ns}$) was too wide, resulting in uninformative histograms and misleading fits. Conversely, excessively narrow parameter ranges led to fit values fixed at boundaries, as evidenced by some of the `G-mean` and `CB-mean` errors being exactly 0.00. This highlights the need for adaptive range setting, possibly based on a more thorough preliminary scan of the data.

The comparison between PMTs at the top and bottom of the detector consistently showed significant asymmetries in both nPE and fTime. The bottom PMTs (0–6) often detect earlier and stronger signals than the top PMTs (7–13), reflecting the downward motion of particles (and the Cherenkov photons they produce) and evidencing the importance of the optical properties of the tank. In some cases, top PMTs exhibited delayed and weaker signals, likely due to reflections or longer optical paths. In some cases, specific PMTs- such as PMTs 8 and 13 in Figure 4.16- showed early secondary peaks in fTime, suggesting some photons reached them directly, bypassing multiple scattering or reflections. These features were not captured by the fits, suggesting that the current fitting model might need to be revised or extended.

Encouragingly, several configurations exhibited very successful fits. The chosen fit model, combination of Gaussian and CrystalBall functions, accurately captures the behavior observed in the simulations. In particular, the simulation of a $10\,\mathrm{GeV}$ gamma shown in Figure 4.21 and Figure 4.22 demonstrates that, at higher energies, gamma-induced events produce enough Cherenkov photons to be effectively described by this model. The resulting nPE and fTime distributions show good agreement with the fits and reveal distinctive patterns across the PMTs.

For the lowest-energy particles, the number of detected photoelectrons was often too small to produce statistically meaningful results. This led to poor, or in some cases empty, histograms and correspondingly vague or unreliable fits. A few examples are included in the chapter 5. This highlights a limitation of the current analysis: the absence of a systematic method to assess data quality. For instance, introducing a threshold on the minimum number of photoelectrons could help determine whether a dataset is suitable for further analysis.

For some of the highest-energy particles, even the extended range used in the nPE plots proved insufficient. The number of photoelectrons was higher than expected, with the data mean approaching the upper limit of the x-axis. Examples of this behavior can be found in the chapter 5. This indicates that the nPE range definitions should be re-evaluated, potentially introducing a third, extra-long range option to accommodate such cases.

Another important observation is that not all PMTs require both fitting components. In an important fraction of the cases, a single peak was present, but both Gaussian and CrystalBall functions were used for fitting. This implies that the fitting process could be made more

efficient by tailoring the model to the data, fitting only one component when appropriate.

Finally, it is important to remember that directionality is one of the main features we aim to study through the detector response. The geometry of the multiPMT module—with its many individual detectors, each collecting its own set of measurements—leads to distinctive patterns in both spatial and timing distributions. These patterns contain valuable information that can enhance reconstruction methods, particularly those based on LUTs.

Overall, these results underline the potential of the multiPMT detector configuration. The angular and spatial sensitivity observed in the response maps can significantly enhance event characterization. However, refinements in the fitting procedure and histogram settings are still needed to ensure robustness and maximize the physics reach of the LUT approach.

Chapter 5

Conclusions and Future Work

This work contributes to the ongoing development of the Southern Wide-field Gamma-ray Observatory (SWGO) by enhancing the understanding of detector responses in multiPMT modules. Accurate modeling and reconstruction of particle-induced signals are crucial for improving gamma-ray detection and background rejection in SWGO. The insights gained here help pave the way toward more efficient and reliable simulations of the M1mT1m tank, which are essential for the design and optimization of the future observatory.

The analysis revealed significant variation in responses among individual PMTs within a single multiPMT module, highlighting the rich directional information these configurations can provide. Both the number of photoelectrons (nPE) and the arrival time of the first photoelectron (fTime) distributions exhibit distinctive patterns that can be leveraged to improve event reconstruction. The fitting model combining Gaussian and CrystalBall functions successfully captured the behavior of higher-energy events, although fits for the lowest-energy simulations suffered from limited statistics and vague parameter estimation, ultimately resulting in unreliable fits.

Additionally, the current histogram ranges for both number of PhotoElectrons (nPE) and arrival time of the first PE (fTime) should be carefully reassessed—especially since some of the highest-energy events produce nPE values that exceed the preset limits—potentially adding a third, extended range option for such cases. As for the fTime plots, in the majority of the configurations a shorter range was needed.

The multiPMT module demonstrated remarkable capability in capturing directional information. The significant differences observed between individual PMTs within the same module—visible in both the nPE and fTime distributions—were beyond initial expectations, revealing intrinsic spatial and timing diversity. This richness of information provides valuable complementary data for enhancing particle direction reconstruction, highlighting the multiPMT setup as a strong candidate for the SWGO outer array configuration.

Looking forward, the fitting process could be improved by adopting a staged approach: first fitting a single distribution and introducing additional components only if necessary. To do this effectively, it will be important to define quantitative criteria to assess fit quality and

establish a minimum photoelectron threshold to exclude low-statistics simulations from further analysis. Prior to filling the LUT, it is crucial to finalize the histogram range adjustments and implement these quality controls to ensure reliable and efficient parametrization of the detector response.

Finally, future work should focus on testing full detector simulations both with and without the FastSim LUT approach. Such comparisons will evaluate the potential computational speed gains and verify the accuracy of this parameterized method, ultimately determining whether the LUT-based fast simulation offers a reliable and efficient solution suitable for large-scale data production and analysis within the SWGO framework.

Appendix

More results are shown in this chapter. Below is the list of configurations included in this file, in order of appearance.

- e-_1000_e0.001GeV_theta20deg_phi180deg_alpha0deg_r72cm_h178cm.root
- e-_1000_e0.003GeV_theta20deg_phi150deg_alpha0deg_r180cm_h75cm.root
- e-_1000_e0.007GeV_theta60deg_phi150deg_alpha30deg_r180cm_h178cm.root
- e-_1000_e0.3GeV_theta0deg_phi0deg_alpha0deg_r36cm_h178cm.root
- e-_1000_e1GeV_theta60deg_phi180deg_alpha30deg_r180cm_h100cm.root
- e-_1000_e1GeV_theta80deg_phi40deg_alpha30deg_r18cm_h178cm.root
- e-_1000_e7GeV_theta60deg_phi150deg_alpha30deg_r180cm_h178cm.root
- e-_1000_e7GeV_theta80deg_phi180deg_alpha30deg_r180cm_h100cm.root
- gamma_1000_e0.001GeV_theta60deg_phi150deg_alpha30deg_r180cm_h178cm.root
- gamma_1000_e0.003GeV_theta20deg_phi180deg_alpha30deg_r72cm_h178cm.root
- gamma_1000_e0.007GeV_theta20deg_phi150deg_alpha30deg_r180cm_h150cm.root
- gamma_1000_e10GeV_theta60deg_phi40deg_alpha0deg_r126cm_h178cm.root
- gamma_1000_e10GeV_theta80deg_phi180deg_alpha0deg_r180cm_h50cm.root
- gamma_1000_e3GeV_theta40deg_phi40deg_alpha0deg_r54cm_h178cm.root
- gamma_1000_e7GeV_theta40deg_phi0deg_alpha30deg_r144cm_h178cm.root
- mu-_1000_e0.3GeV_theta60deg_phi150deg_alpha30deg_r180cm_h178cm.root
- mu-_1000_e100GeV_theta0deg_phi0deg_alpha0deg_r72cm_h178cm.root
- mu-_1000_e10GeV_theta20deg_phi180deg_alpha30deg_r54cm_h178cm.root
- mu-_1000_e1GeV_theta20deg_phi120deg_alpha0deg_r180cm_h178cm.root
- mu-_1000_e1GeV_theta60deg_phi120deg_alpha30deg_r54cm_h178cm.root

- mu-_1000_e30GeV_theta40deg_phi120deg_alpha0deg_r180cm_h50cm.root
- mu-_1000_e3GeV_theta20deg_phi120deg_alpha30deg_r144cm_h178cm.root
- mu-_1000_e3GeV_theta80deg_phi180deg_alpha0deg_r180cm_h75cm.root

e-_1000_e0.001GeV_theta20deg_phi180deg_alpha0deg_r72cm_h178cm.root

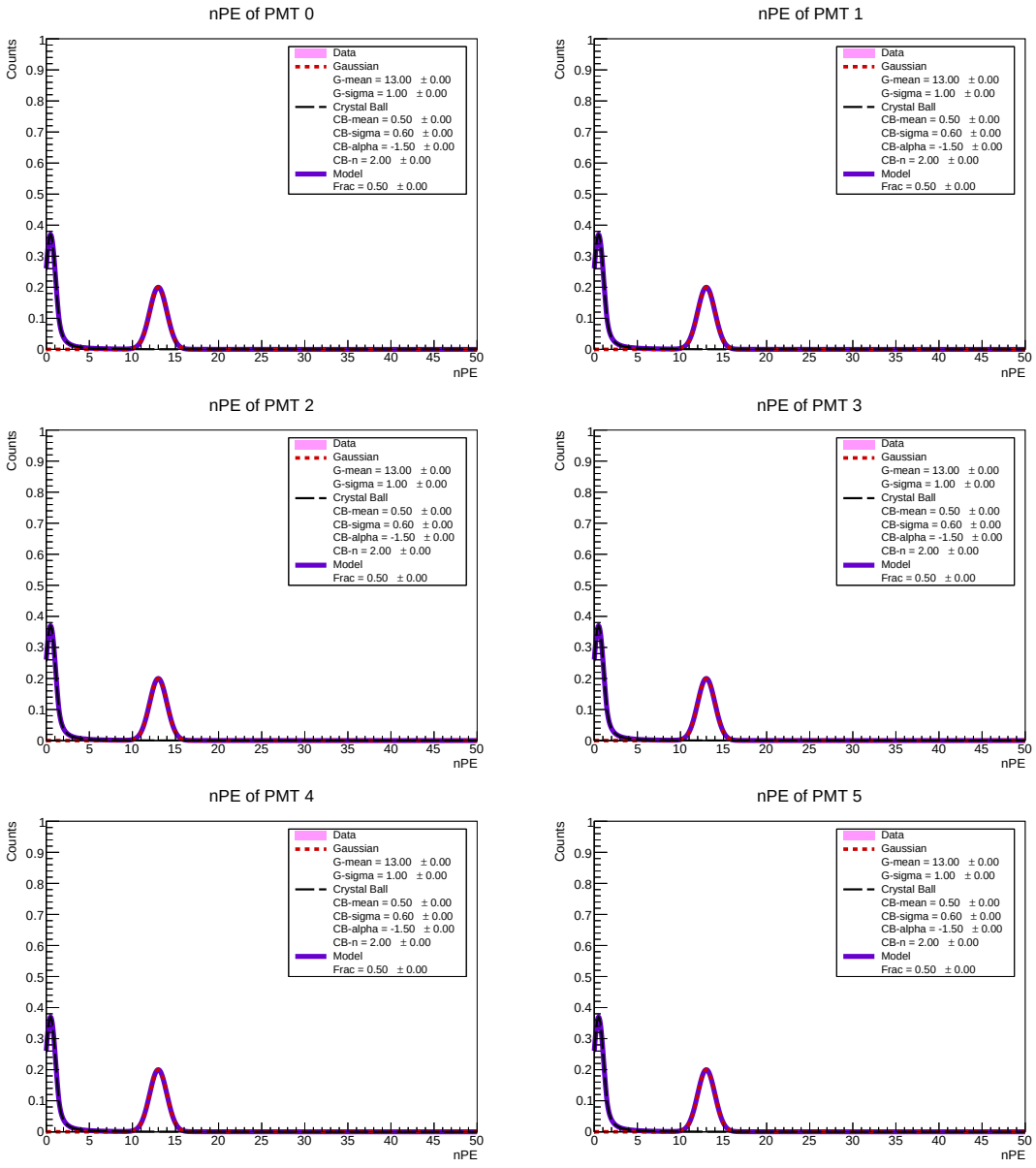

Figure 5.1: Number of photoelectrons recorded by PMTs 0 to 5, for configuration e-_1000_e0.001GeV_theta20deg_phi180deg_alpha0deg_r72cm_h178cm.root.

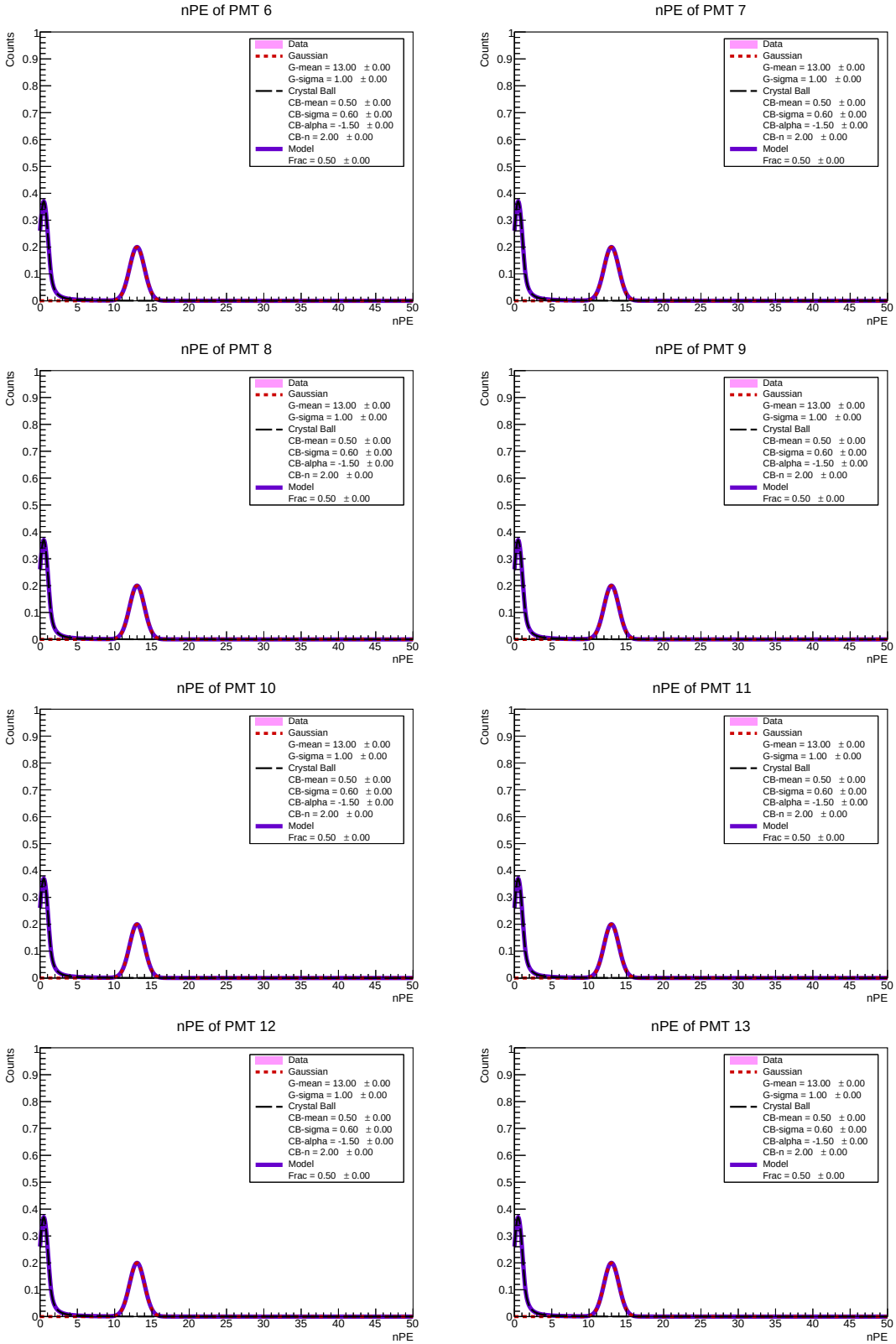

Figure 5.2: Number of photoelectrons recorded by PMTs 6 to 13, for configuration e-_1000_e0.001GeV_theta20deg_phi180deg_alpha0deg_r72cm_h178cm.root.

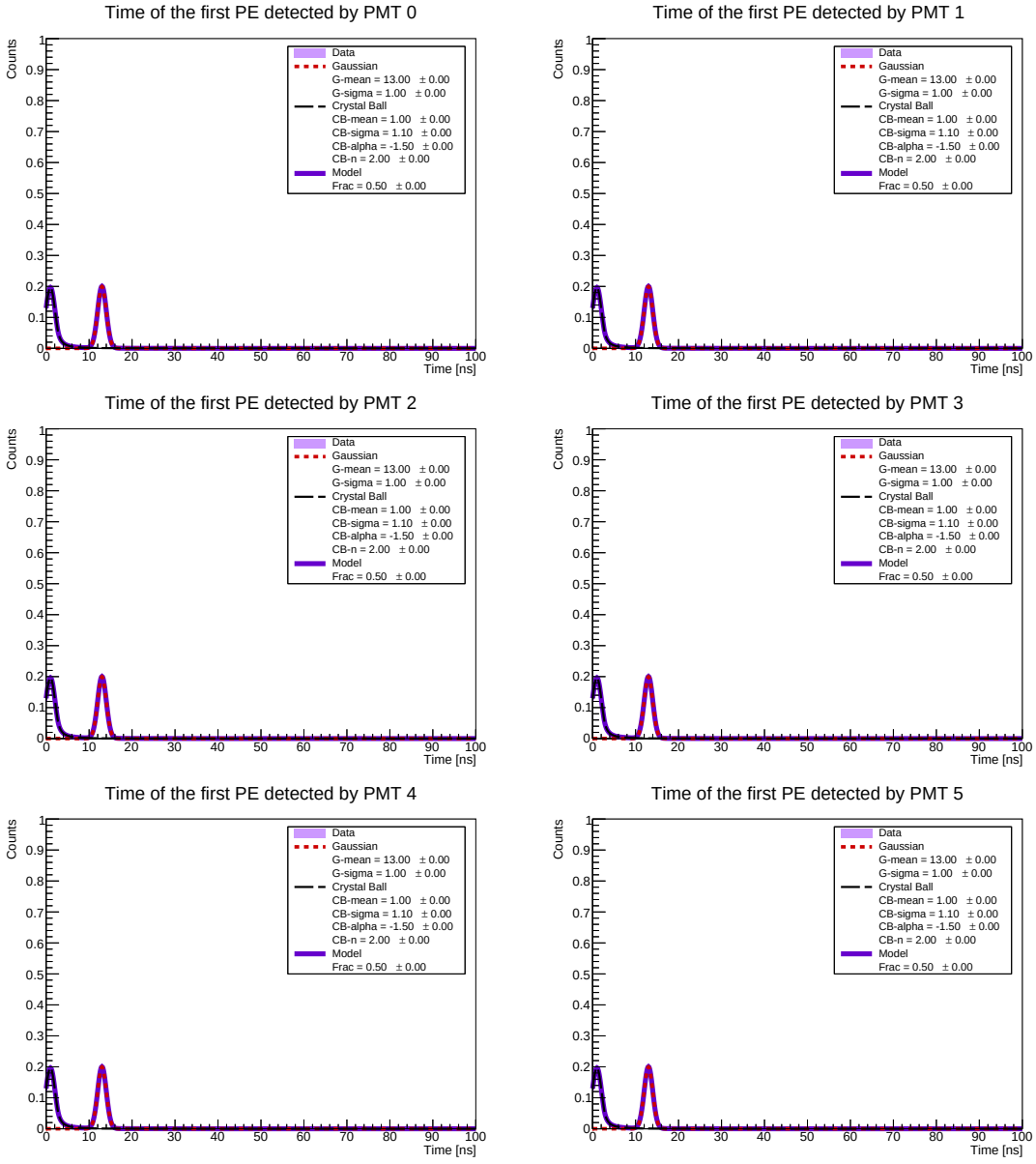

Figure 5.3: First PE arrival time (fTime) at PMTs 0 to 5, for configuration e-_1000_e0.001GeV_theta20deg_phi180deg_alpha0deg_r72cm_h178cm.root.

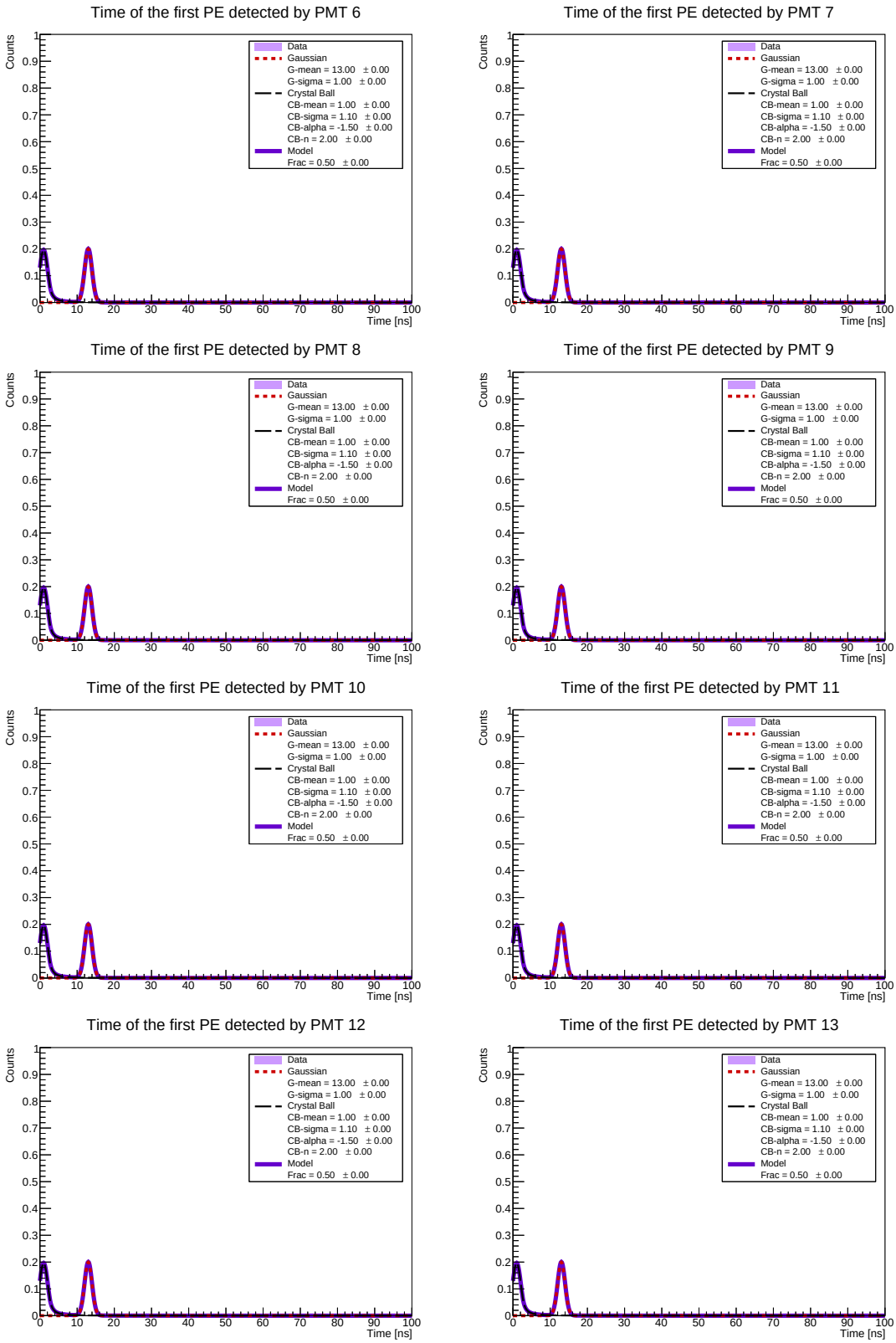

Figure 5.4: First PE arrival time (fTime) at PMTs 6 to 13, for configuration e-_1000_e0.001GeV_theta20deg_phi180deg_alpha0deg_r72cm_h178cm.root.

e-_1000_e0.003GeV_theta20deg_phi150deg_alpha0deg_r180cm_h75cm.root

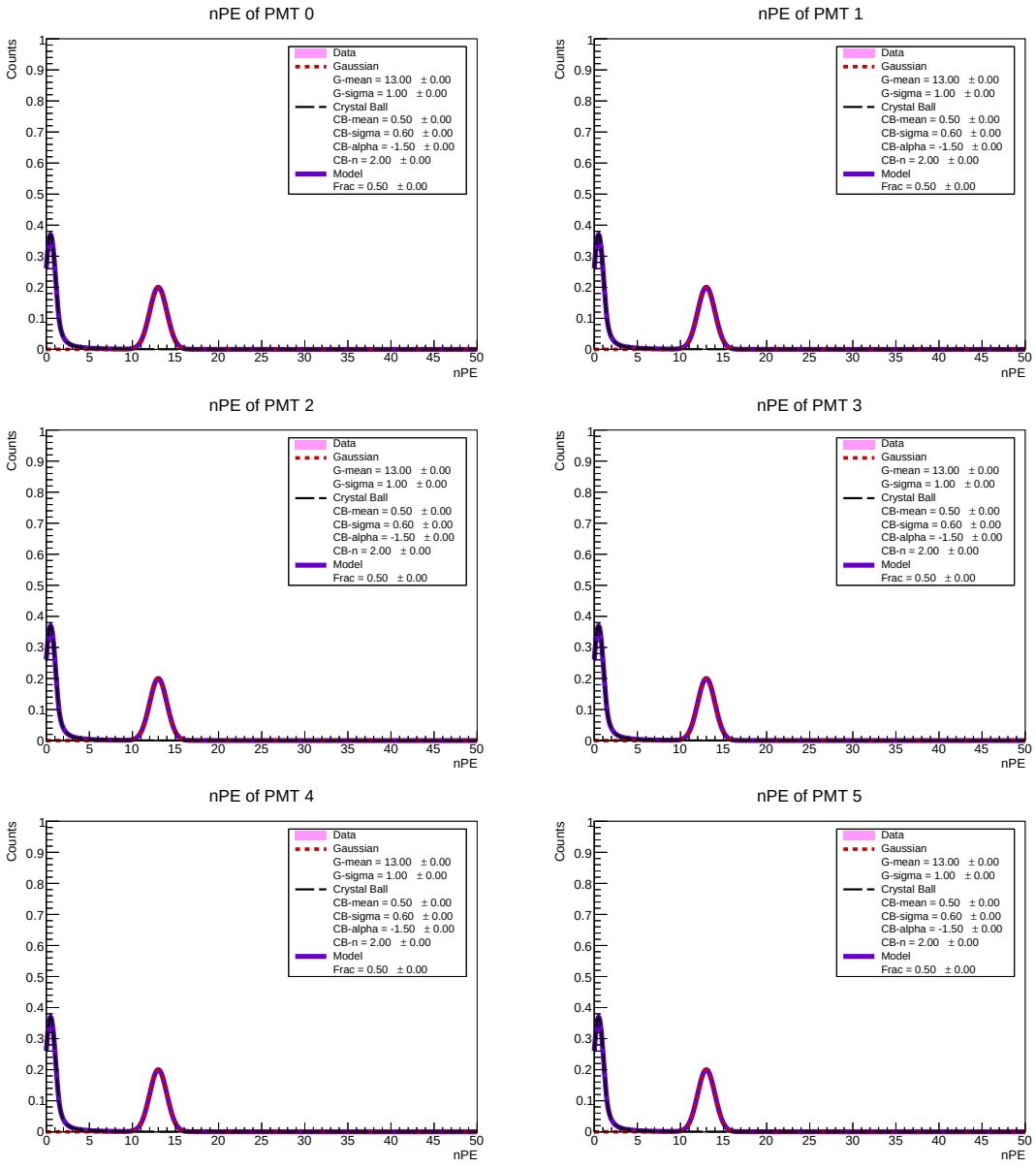

Figure 5.5: Number of photoelectrons recorded by PMTs 0 to 5, for configuration e-_1000_e0.003GeV_theta20deg_phi150deg_alpha0deg_r180cm_h75cm.root.

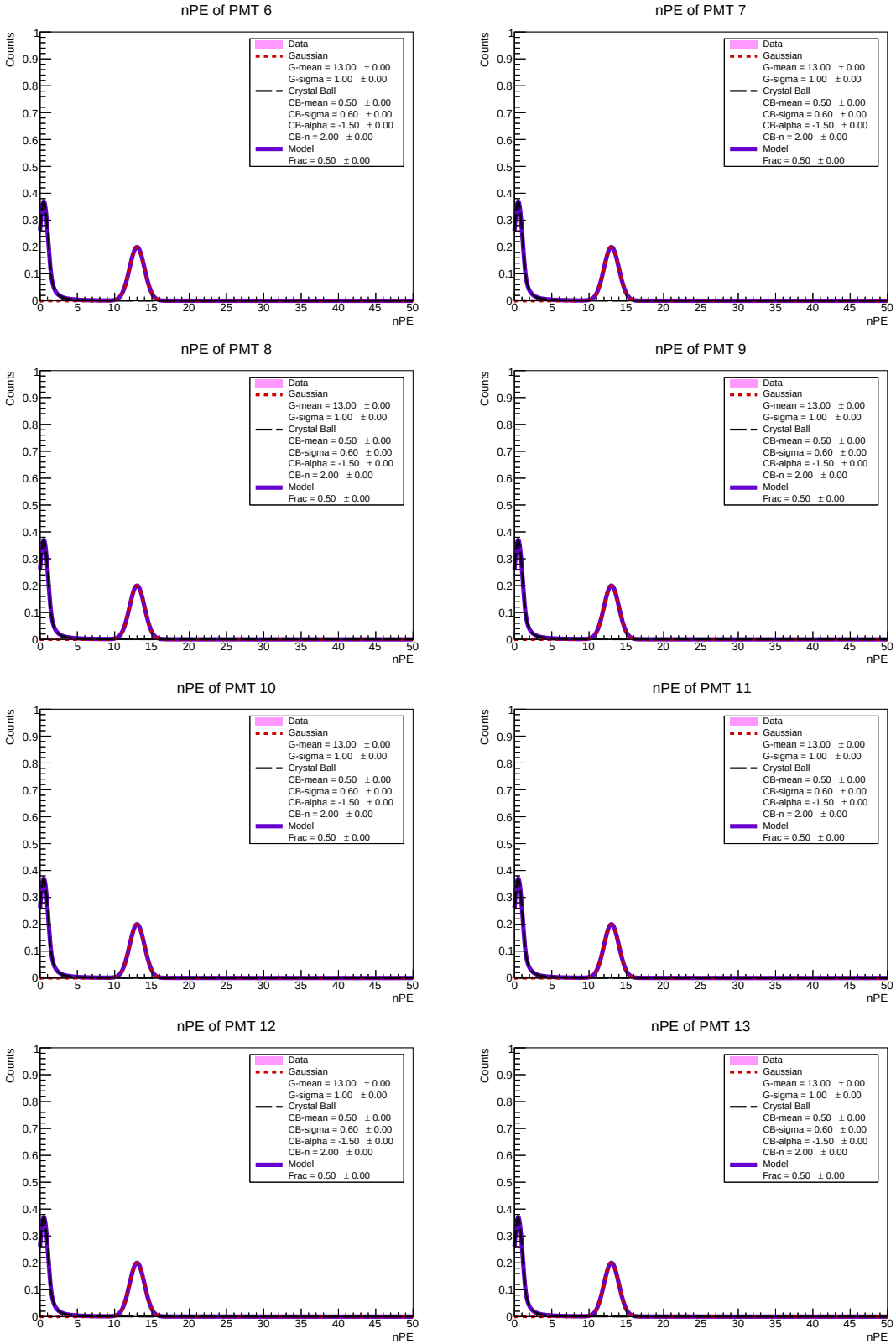

Figure 5.6: Number of photoelectrons recorded by PMTs 6 to 13, for configuration e-_1000_e0.003GeV_theta20deg_phi150deg_alpha0deg_r180cm_h75cm.root.

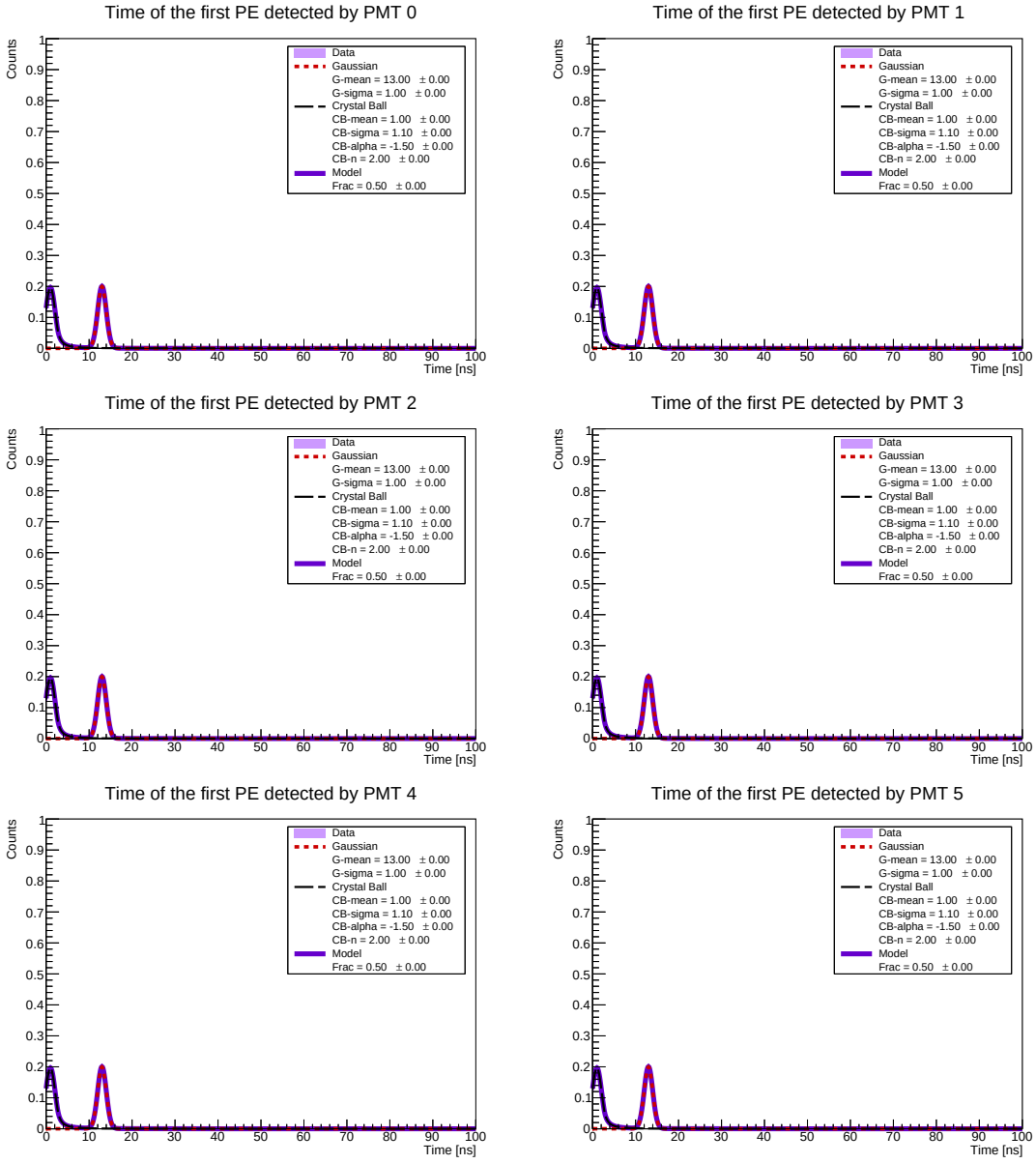

Figure 5.7: First PE arrival time (fTime) at PMTs 0 to 5, for configuration e-_1000_e0.003GeV_theta20deg_phi150deg_alpha0deg_r180cm_h75cm.root.

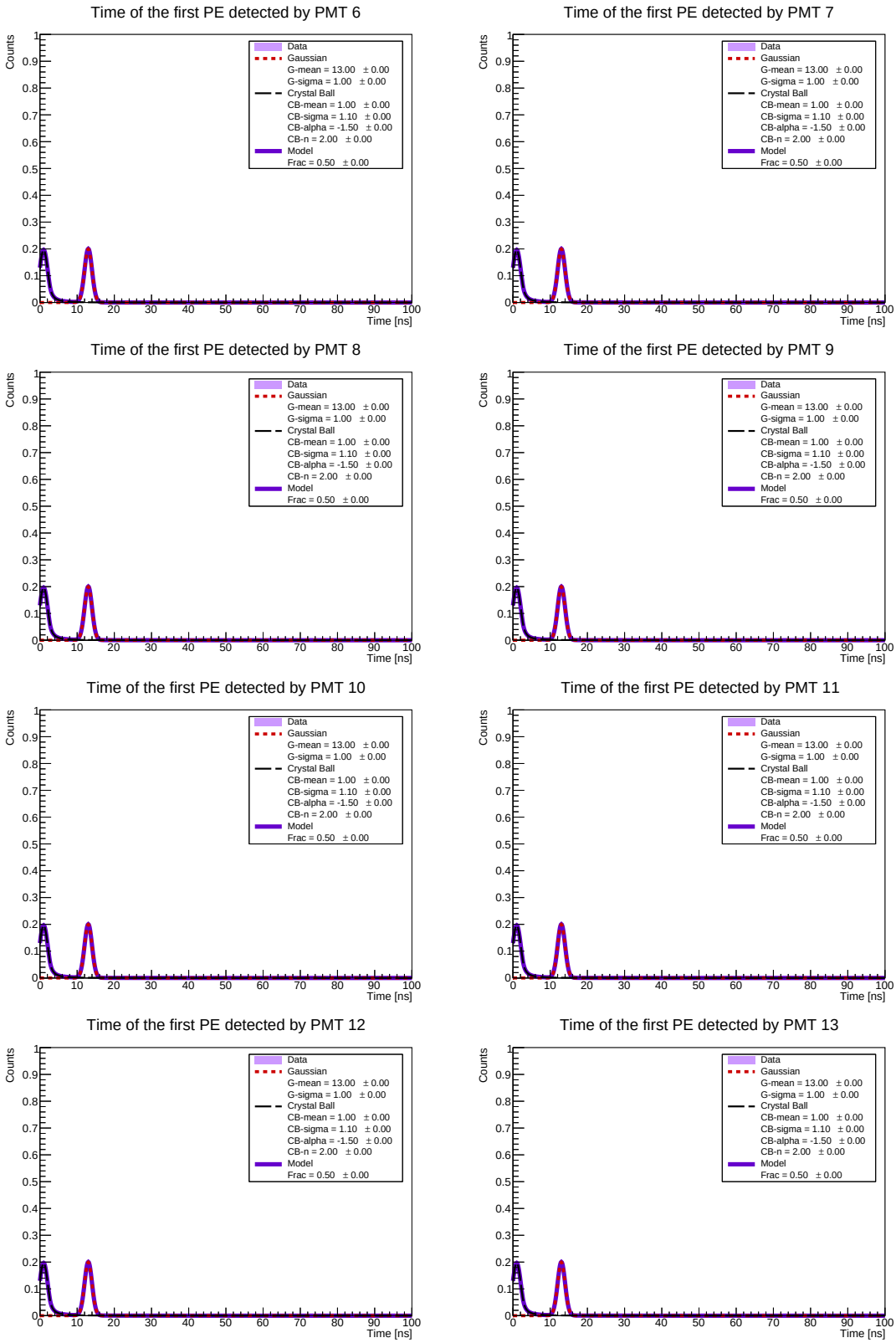

Figure 5.8: First PE arrival time (fTime) at PMTs 6 to 13, for configuration e-_1000_e0.003GeV_theta20deg_phi150deg_alpha0deg_r180cm_h75cm.root.

e-_1000_e0.007GeV_theta60deg_phi150deg_alpha30deg_r180cm_h178cm.root

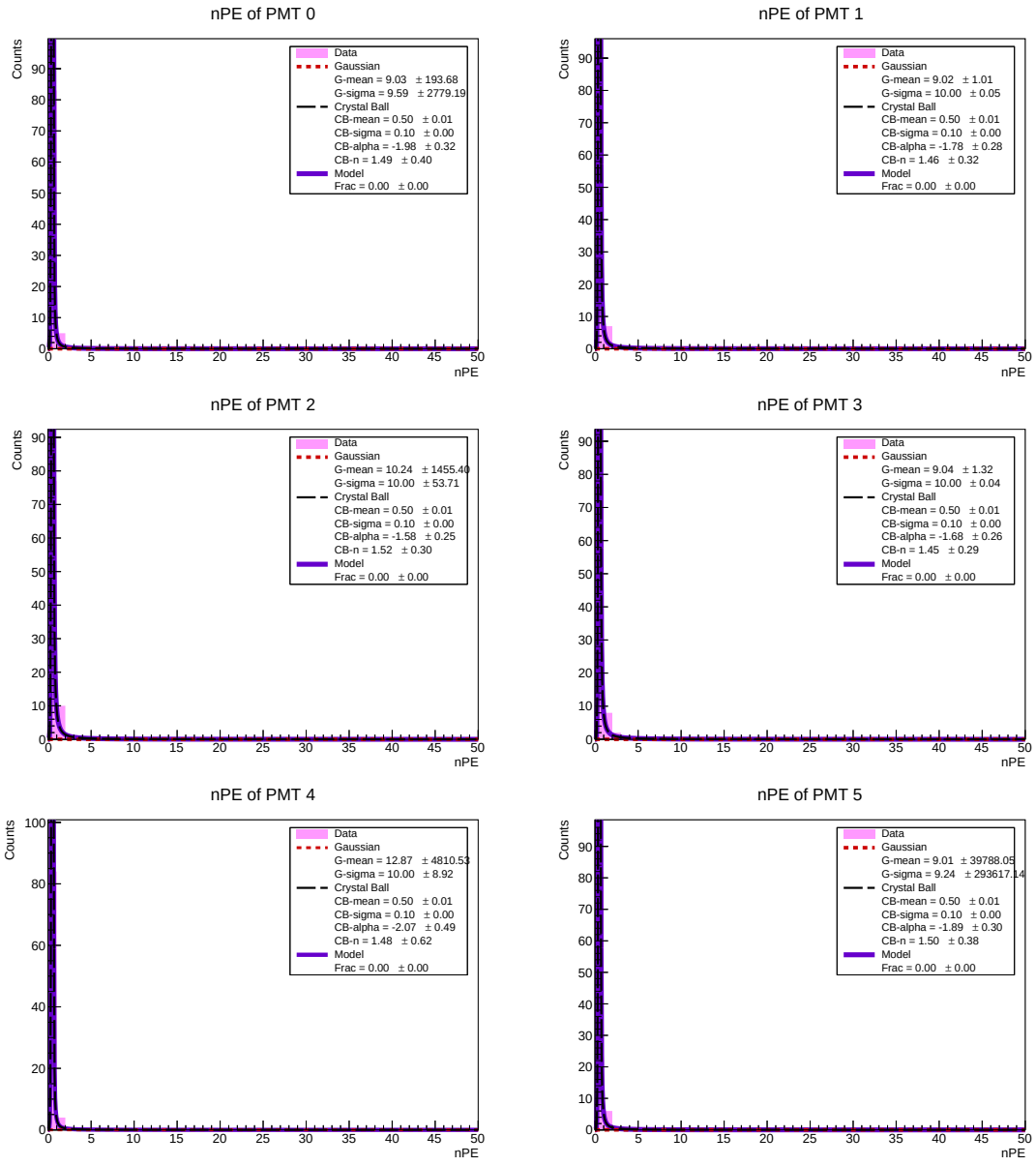

Figure 5.9: Number of photoelectrons recorded by PMTs 0 to 5, for configuration e-_1000_e0.007GeV_theta60deg_phi150deg_alpha30deg_r180cm_h178cm.root.

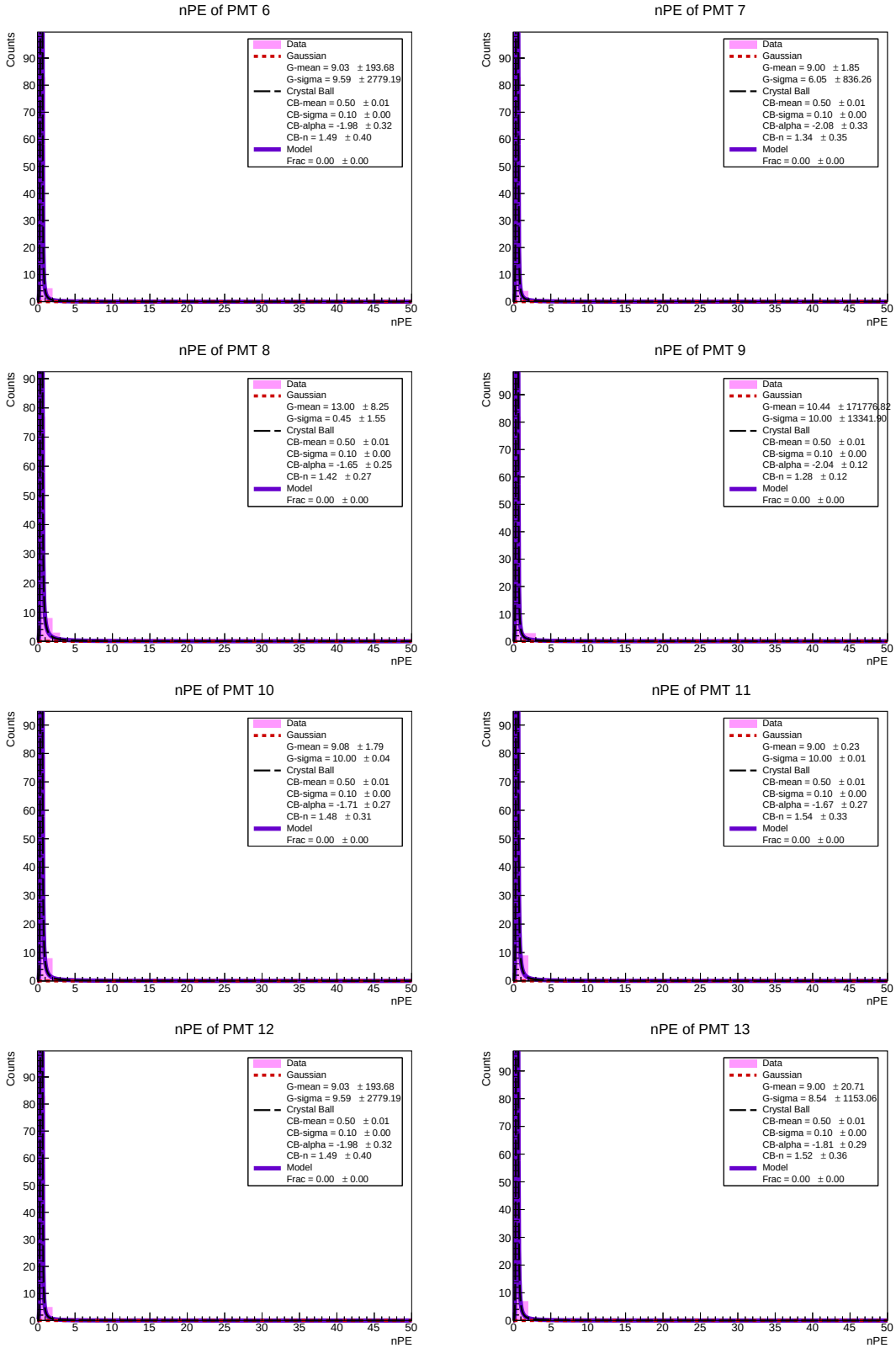

Figure 5.10: Number of photoelectrons recorded by PMTs 6 to 13, for configuration e-_1000_e0.007GeV_theta60deg_phi150deg_alpha30deg_r180cm_h178cm.root.

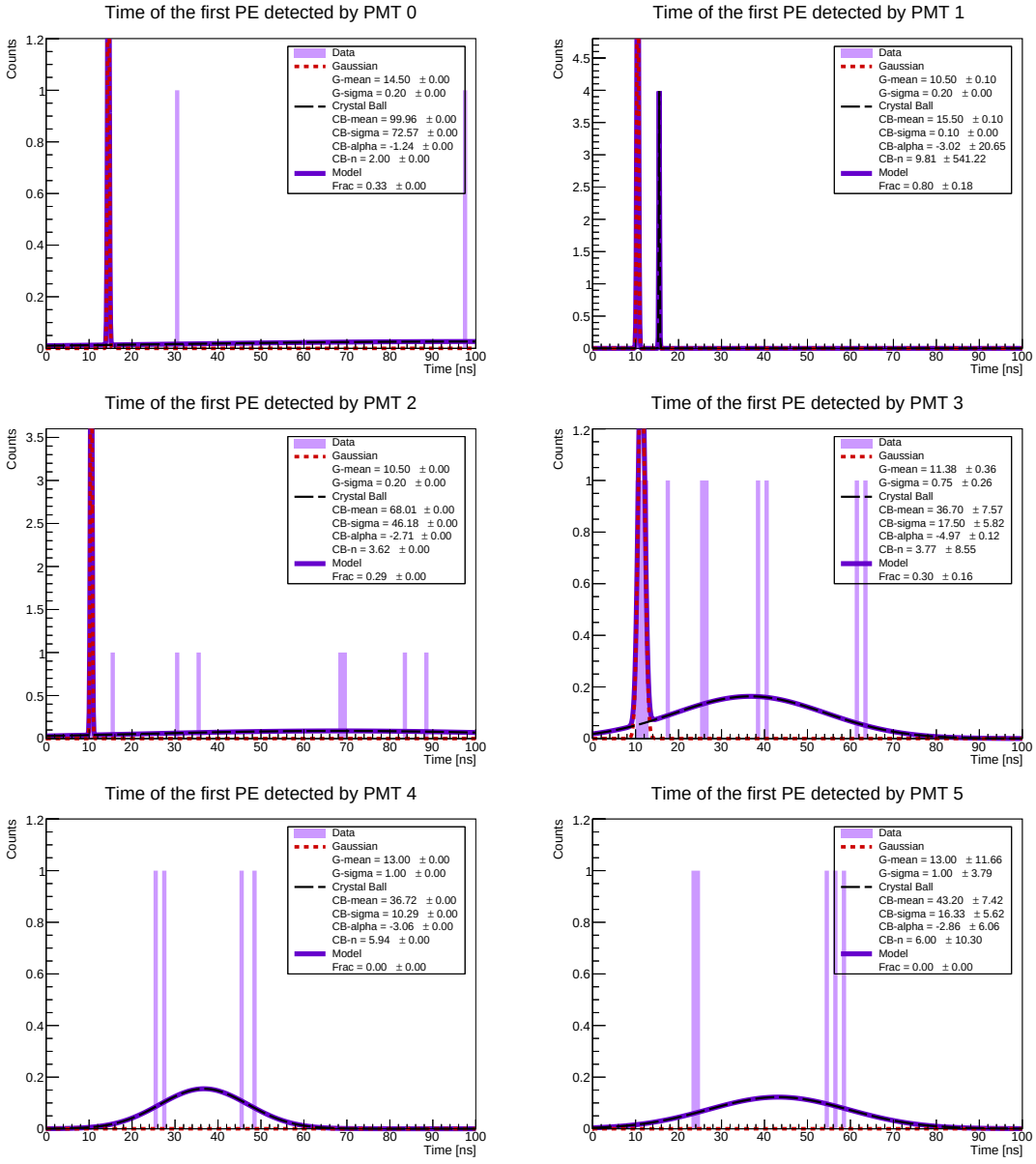

Figure 5.11: First PE arrival time (fTime) at PMTs 0 to 5, for configuration e-_1000_e0.007GeV_theta60deg_phi150deg_alpha30deg_r180cm_h178cm.root.

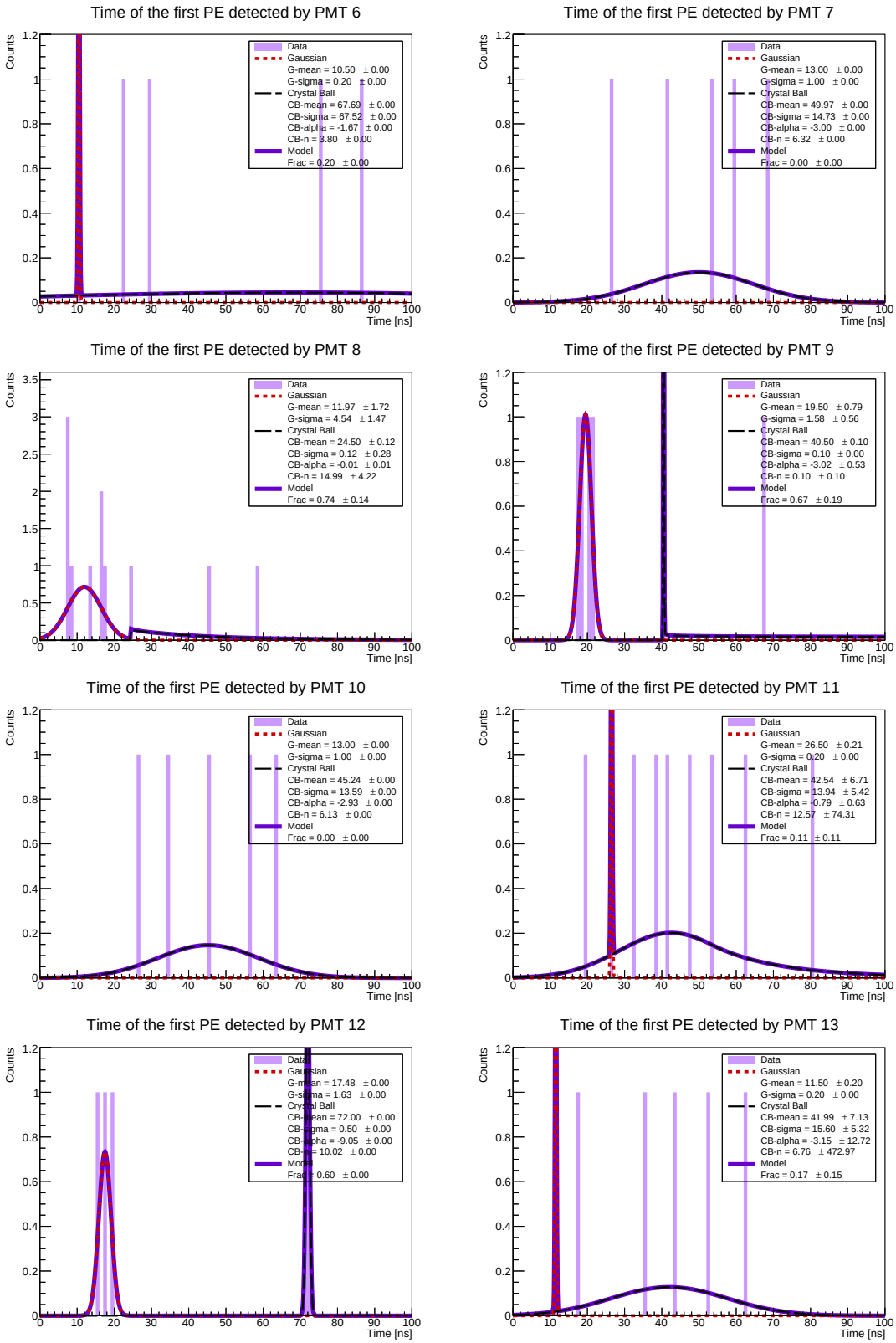

Figure 5.12: First PE arrival time (fTime) at PMTs 6 to 13, for configuration e-_1000_e0.007GeV_theta60deg_phi150deg_alpha30deg_r180cm_h178cm.root.

e-_1000_e0.3GeV_theta0deg_phi0deg_alpha0deg_r36cm_h178cm.root

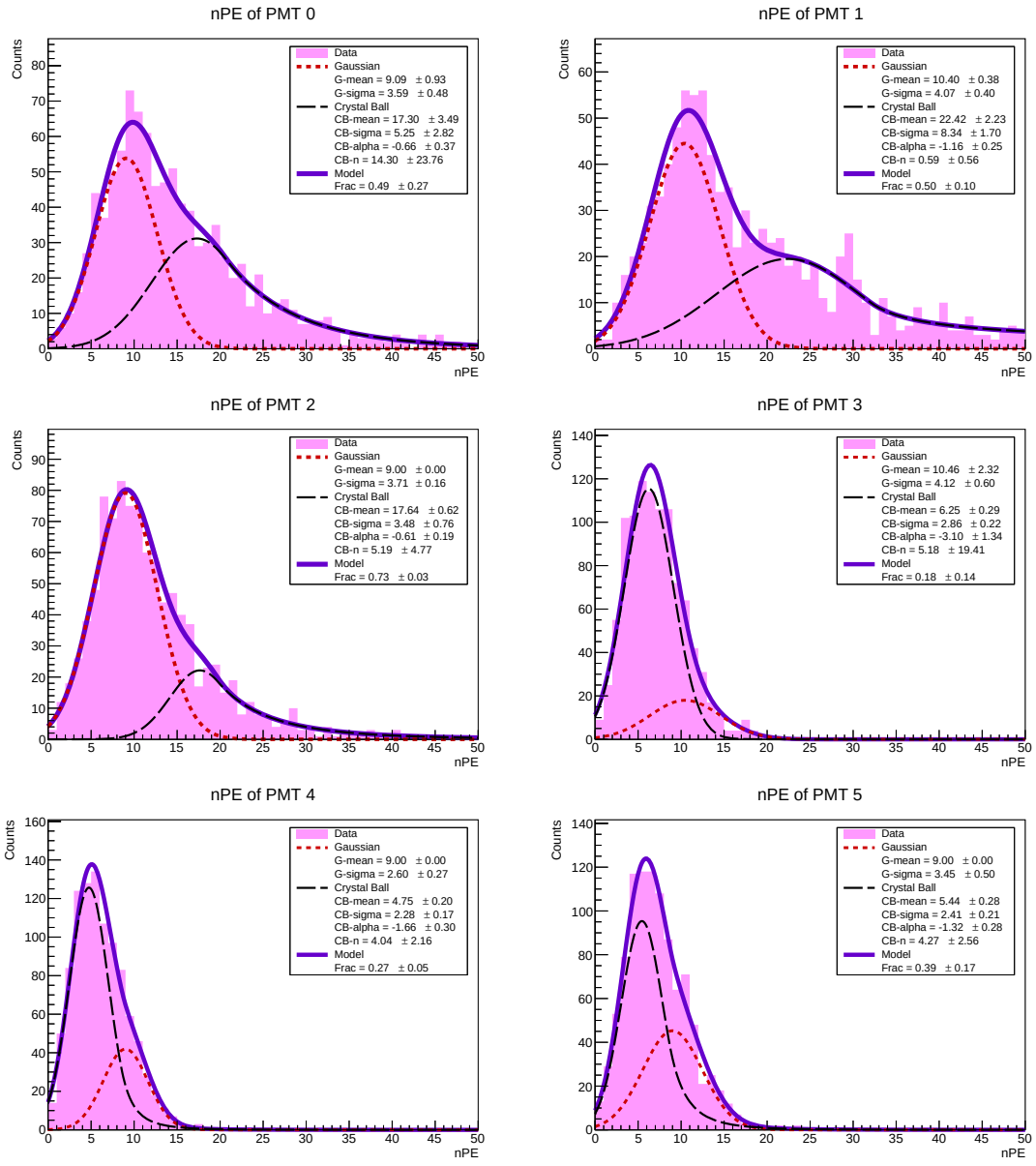

Figure 5.13: Number of photoelectrons recorded by PMTs 0 to 5, for configuration e-_1000_e0.3GeV_theta0deg_phi0deg_alpha0deg_r36cm_h178cm.root.

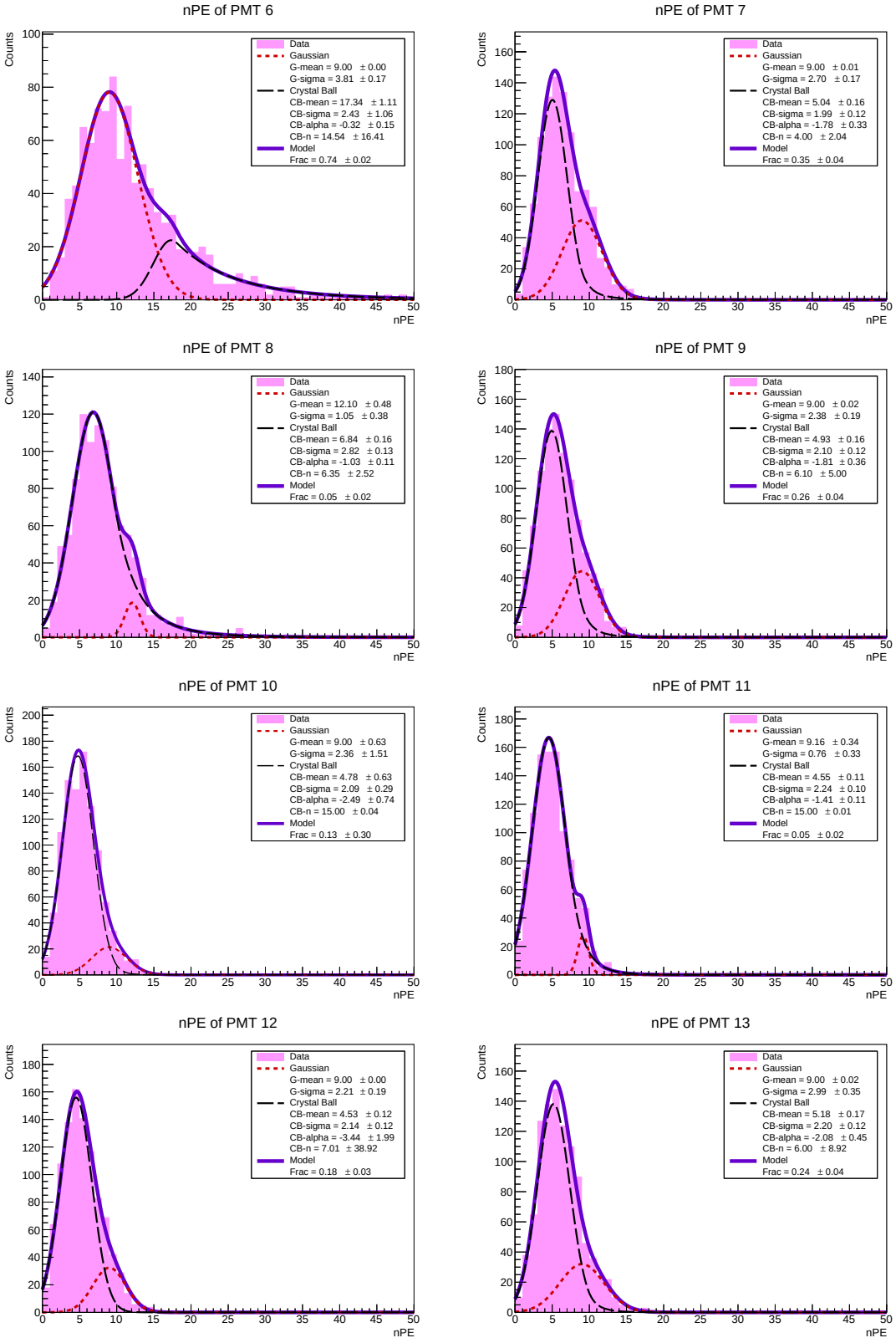

Figure 5.14: Number of photoelectrons recorded by PMTs 6 to 13, for configuration e-_1000_e0.3GeV_theta0deg_phi0deg_alpha0deg_r36cm_h178cm.root.

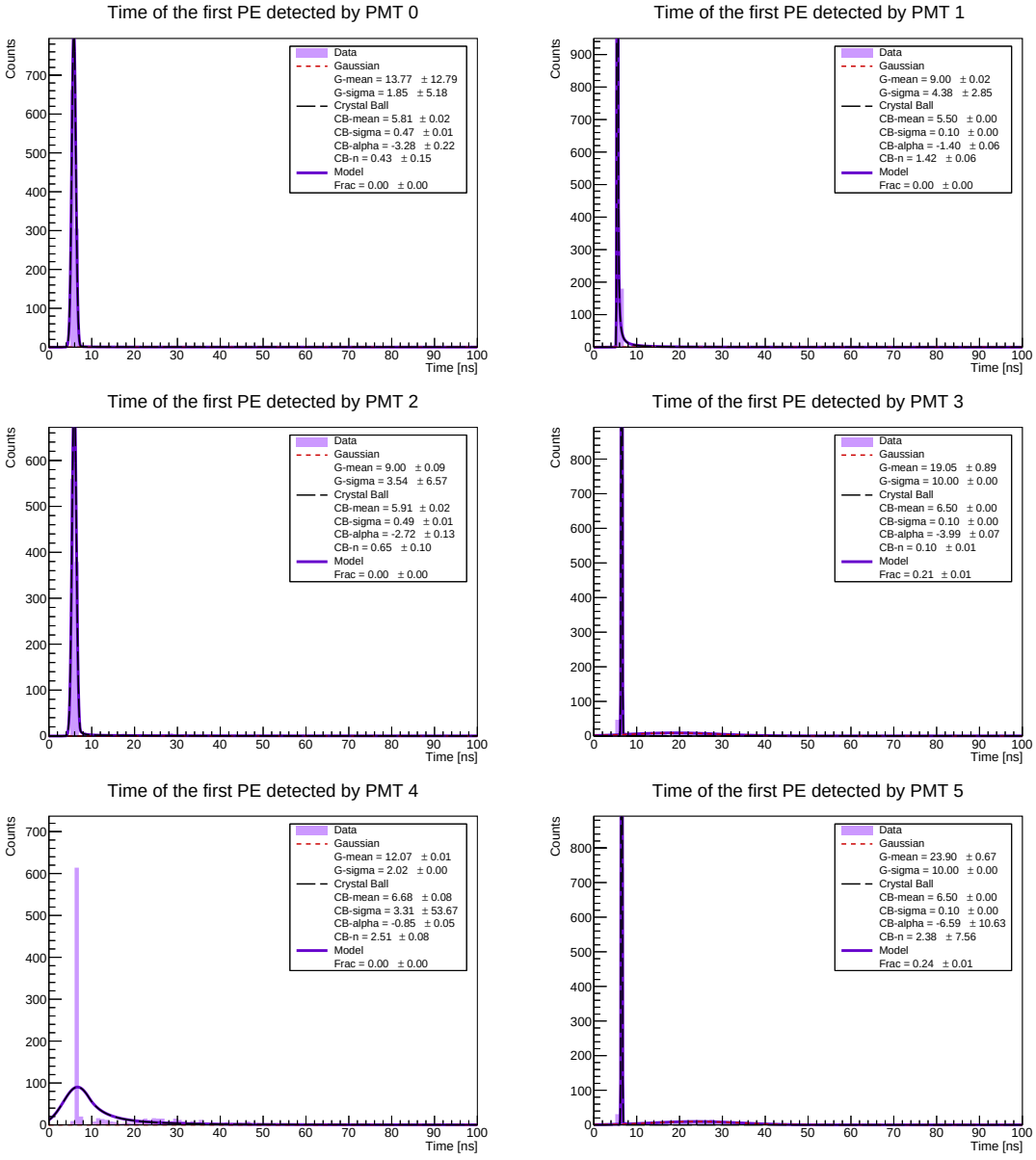

Figure 5.15: First PE arrival time (fTime) at PMTs 0 to 5, for configuration e-_1000_e0.3GeV_theta0deg_phi0deg_alpha0deg_r36cm_h178cm.root.

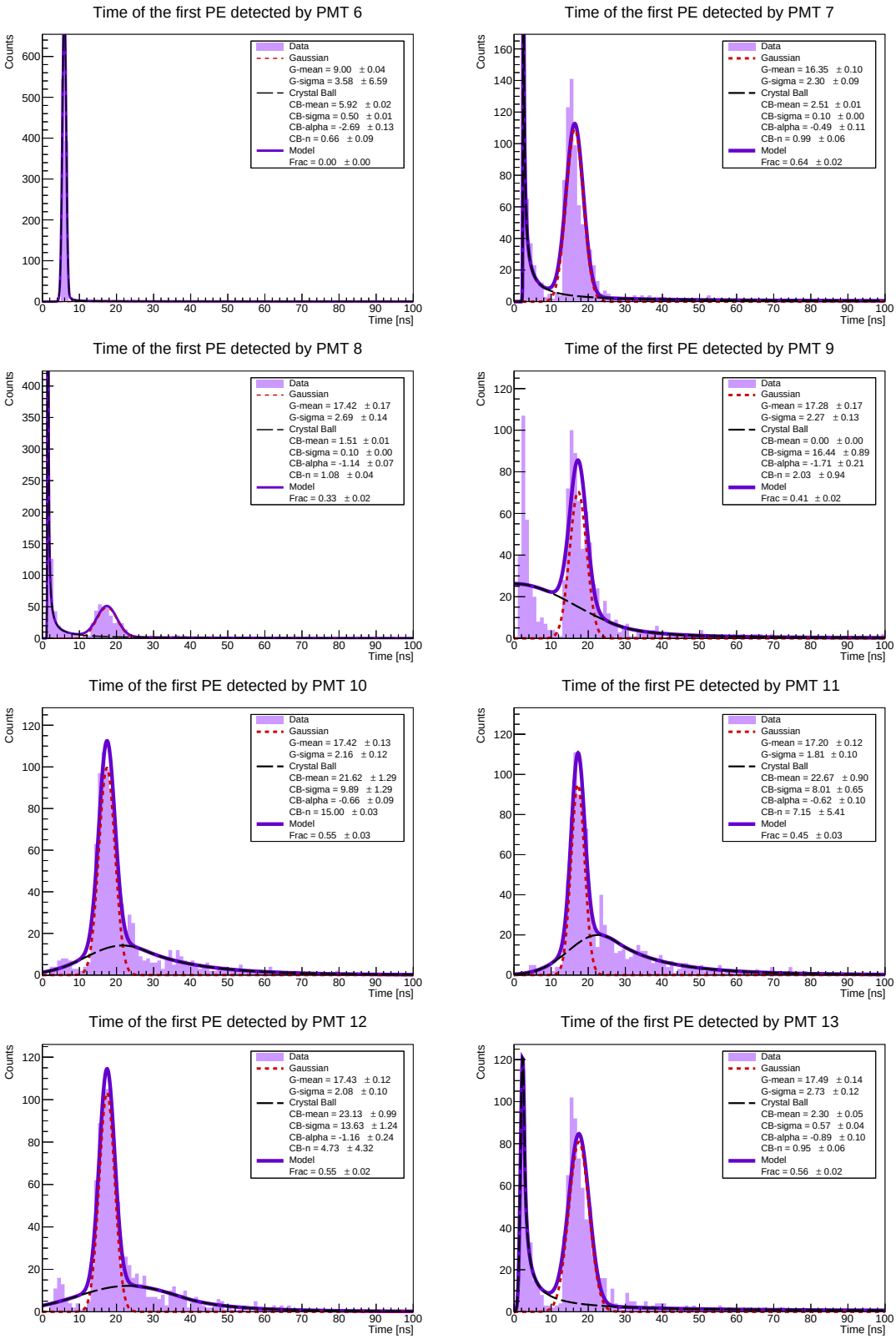

Figure 5.16: First PE arrival time (fTime) at PMTs 6 to 13, for configuration e-_1000_e0.3GeV_theta0deg_phi0deg_alpha0deg_r36cm_h178cm.root.

e-_1000_e1GeV_theta60deg_phi180deg_alpha30deg_r180cm_h100cm.root

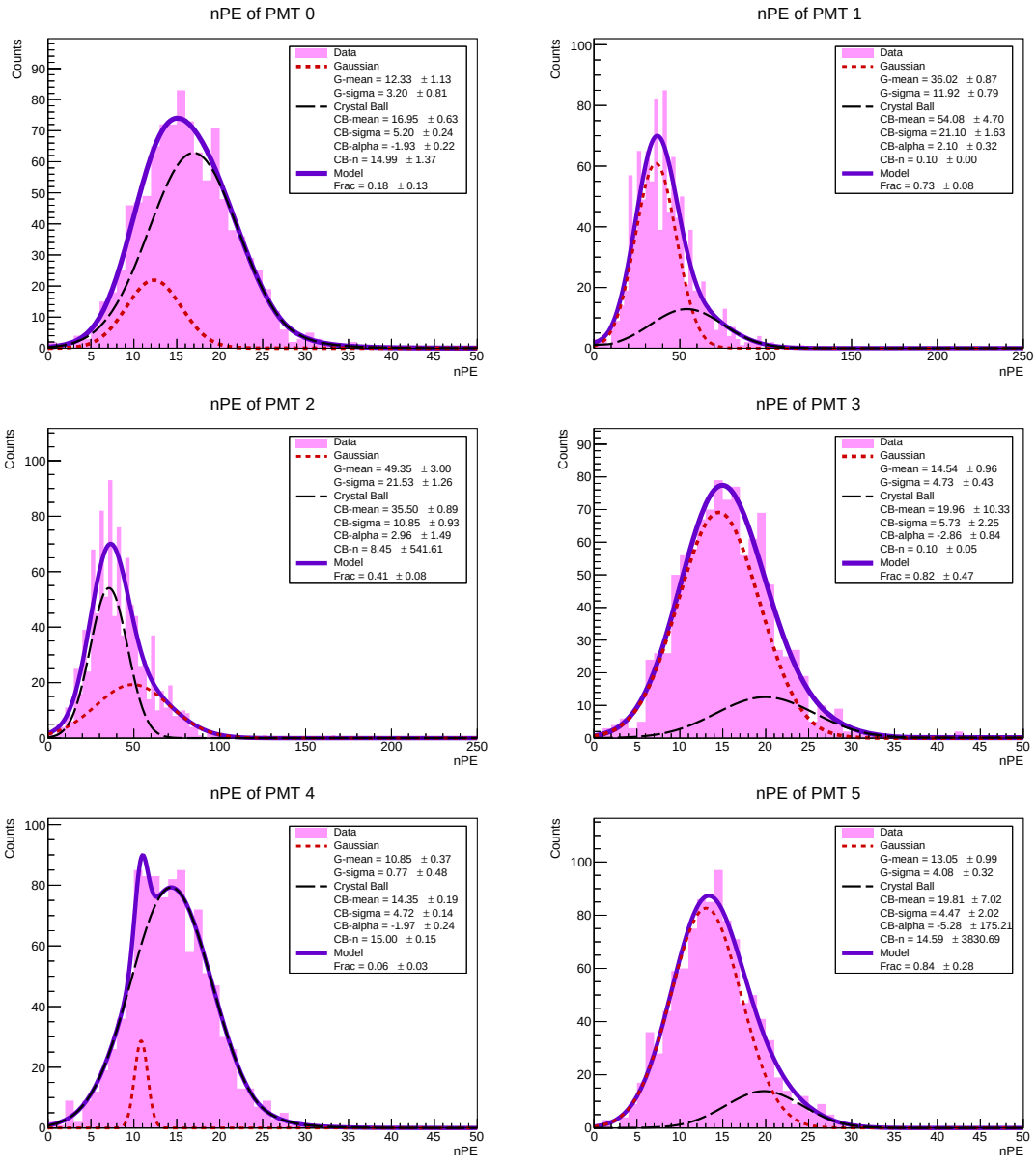

Figure 5.17: Number of photoelectrons recorded by PMTs 0 to 5, for configuration e-_1000_e1GeV_theta60deg_phi180deg_alpha30deg_r180cm_h100cm.root.

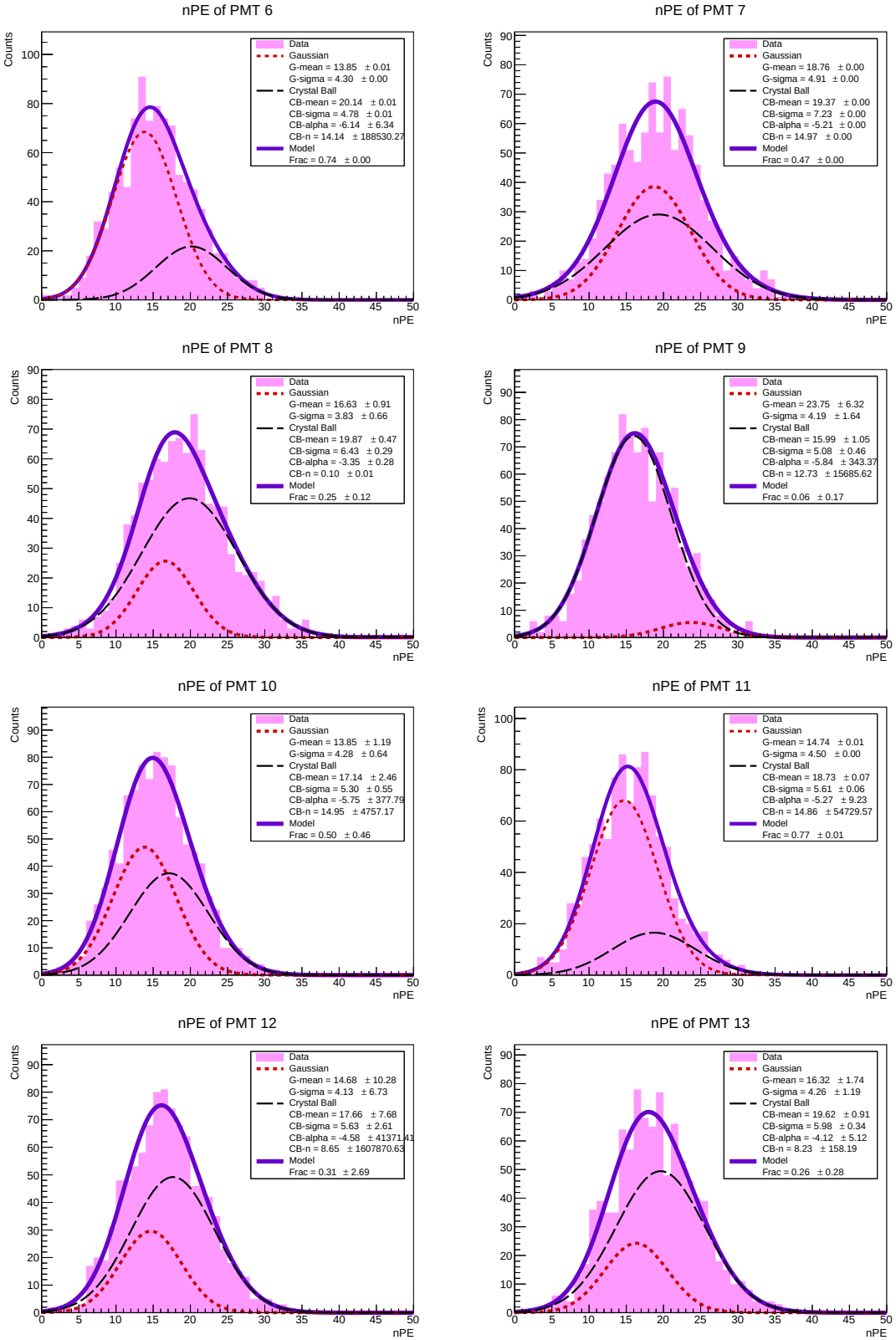

Figure 5.18: Number of photoelectrons recorded by PMTs 6 to 13, for configuration e-_1000_e1GeV_theta60deg_phi180deg_alpha30deg_r180cm_h100cm.root.

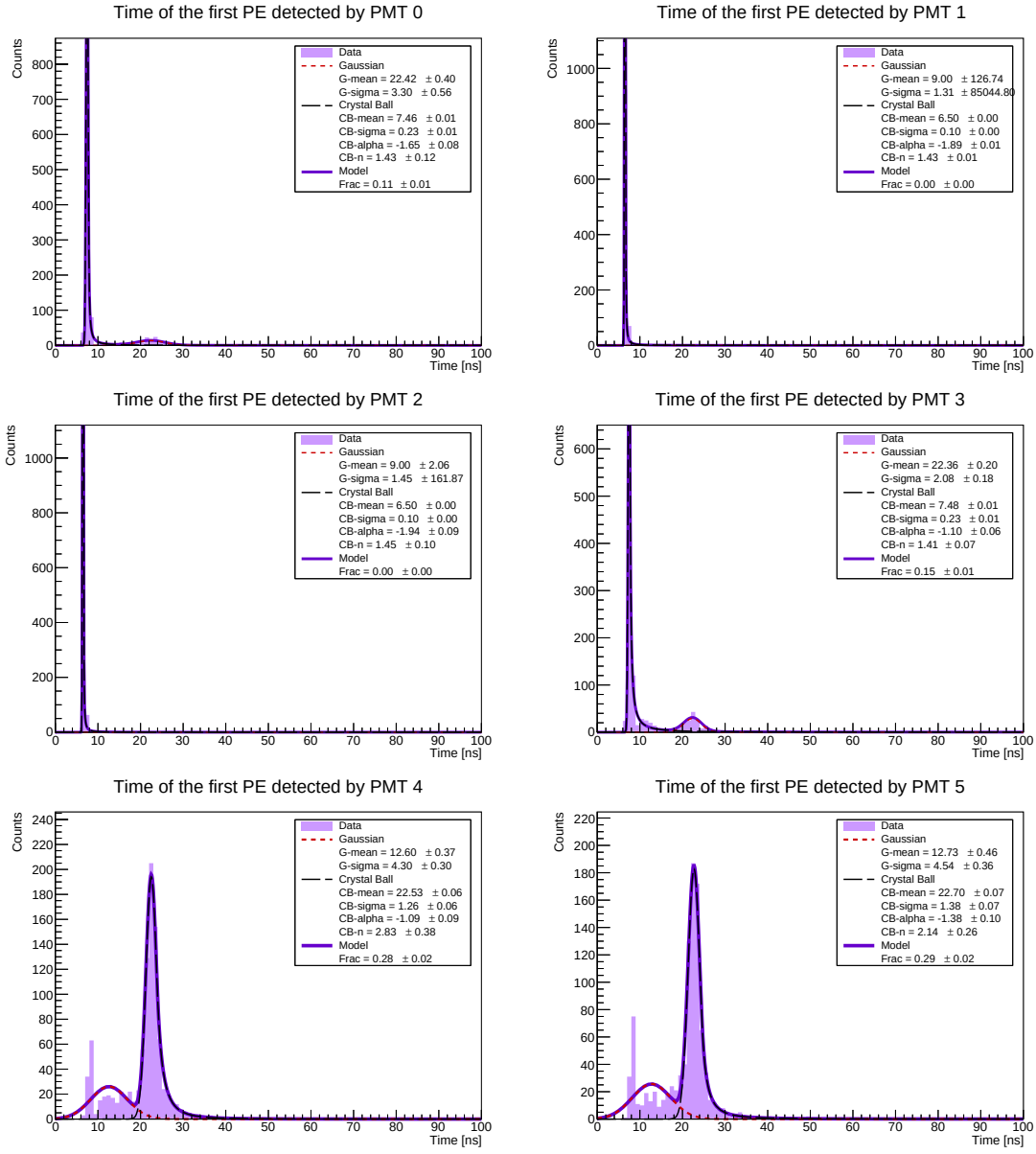

Figure 5.19: First PE arrival time (fTime) at PMTs 0 to 5, for configuration e-_1000_e1GeV_theta60deg_phi180deg_alpha30deg_r180cm_h100cm.root.

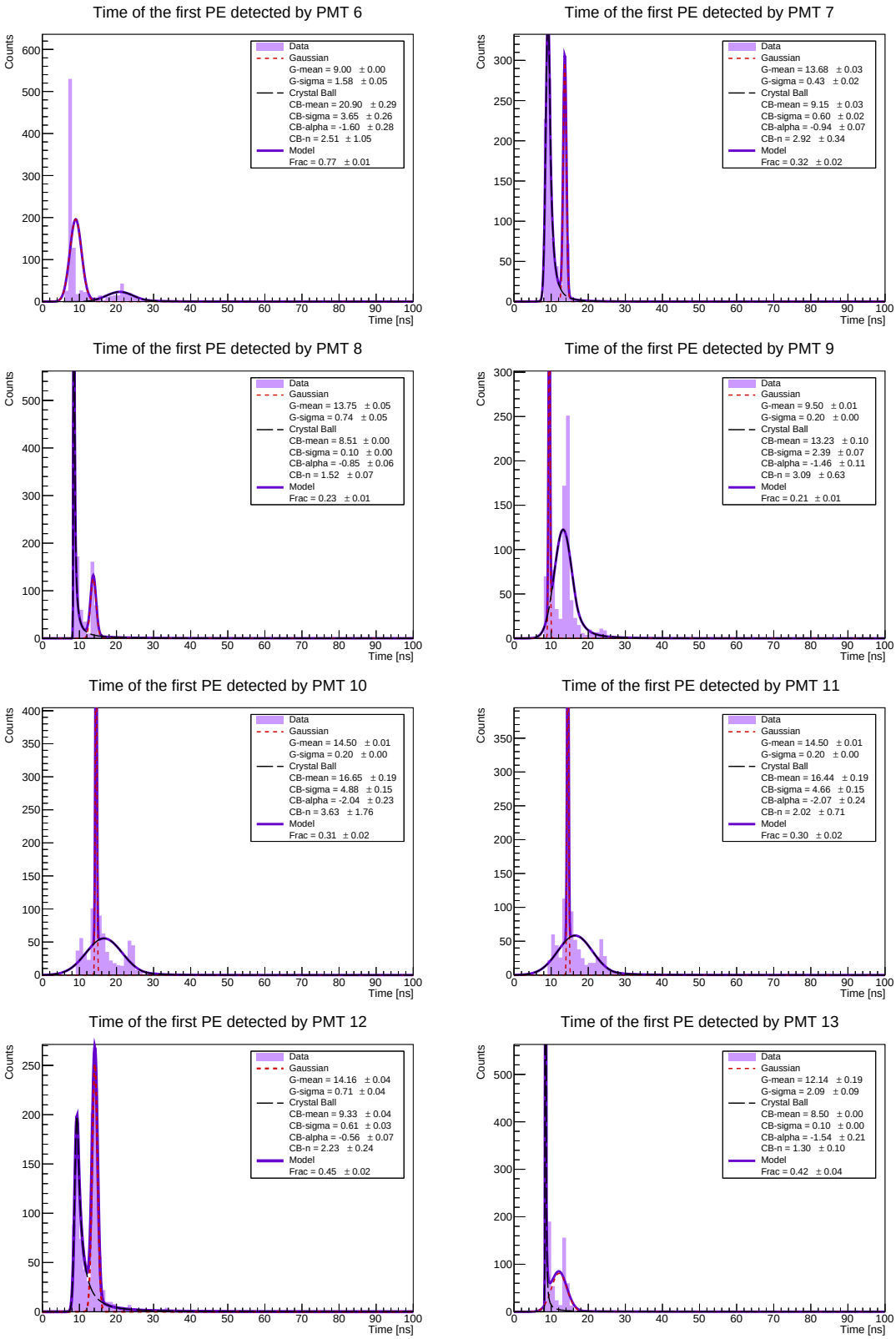

Figure 5.20: First PE arrival time (fTime) at PMTs 6 to 13, for configuration e-_1000_e1GeV_theta60deg_phi180deg_alpha30deg_r180cm_h100cm.root.

e-_1000_e1GeV_theta80deg_phi40deg_alpha30deg_r18cm_h178cm.root

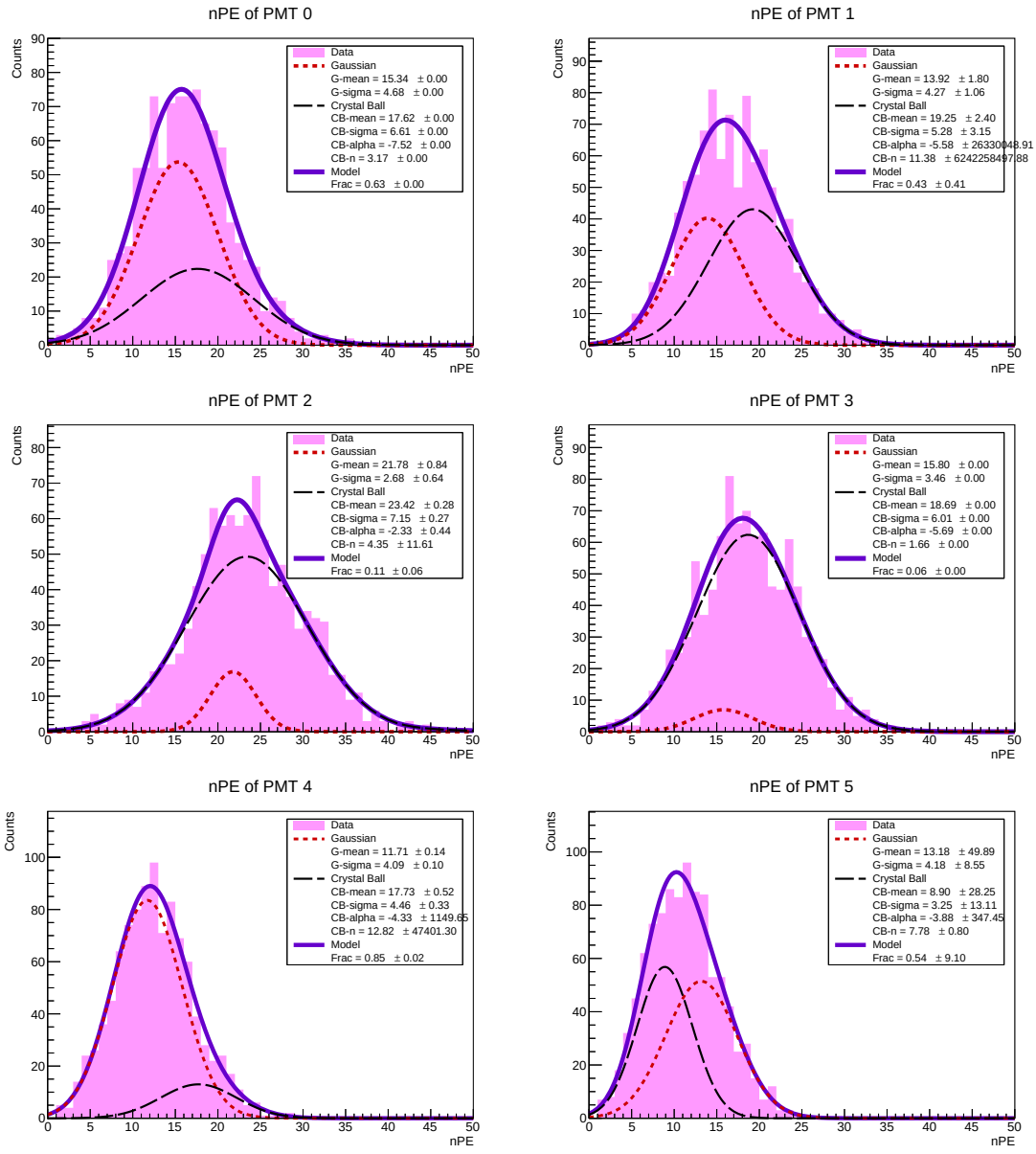

Figure 5.21: Number of photoelectrons recorded by PMTs 0 to 5, for configuration e-_1000_e1GeV_theta80deg_phi40deg_alpha30deg_r18cm_h178cm.root.

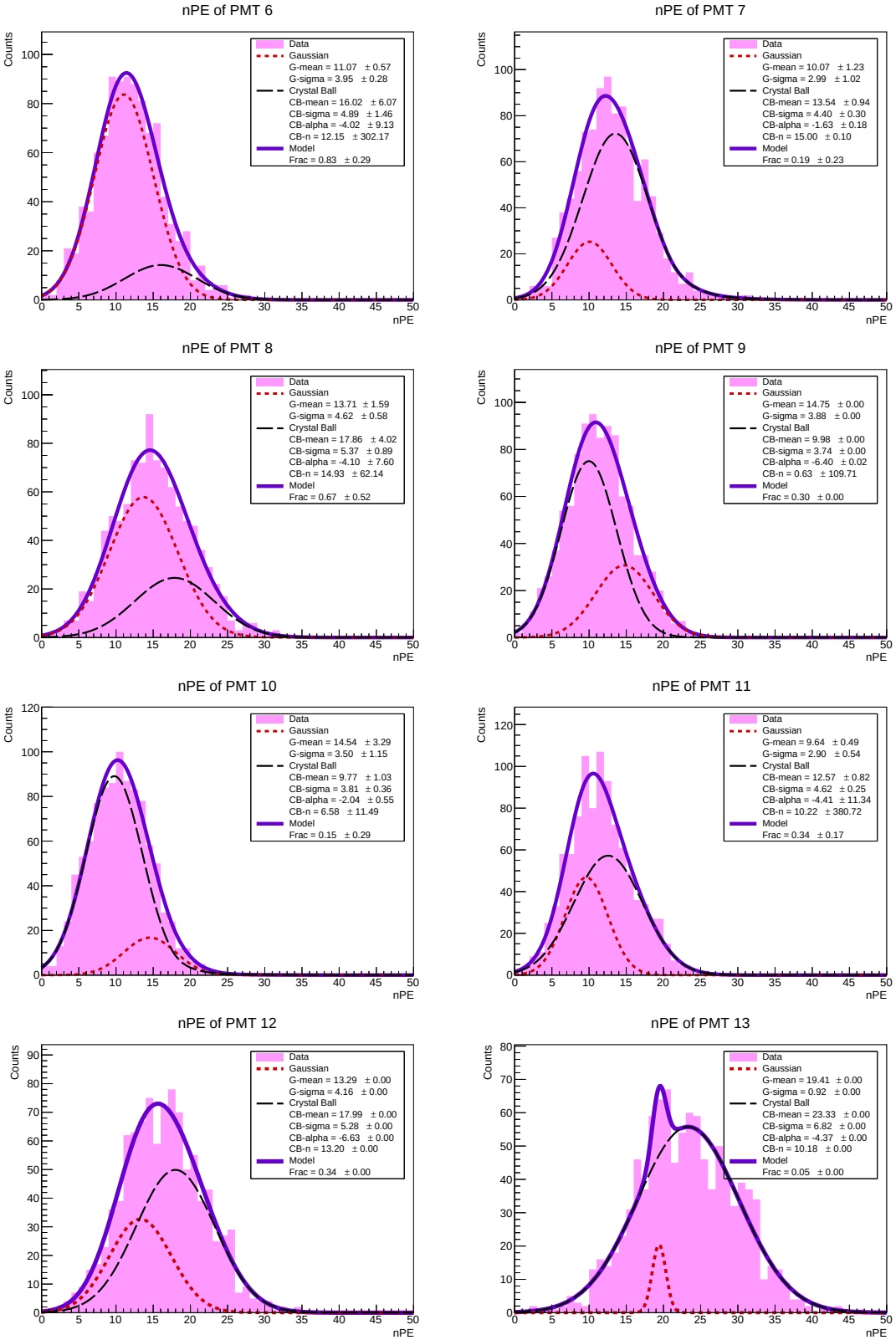

Figure 5.22: Number of photoelectrons recorded by PMTs 6 to 13, for configuration e-_1000_e1GeV_theta80deg_phi40deg_alpha30deg_r18cm_h178cm.root.

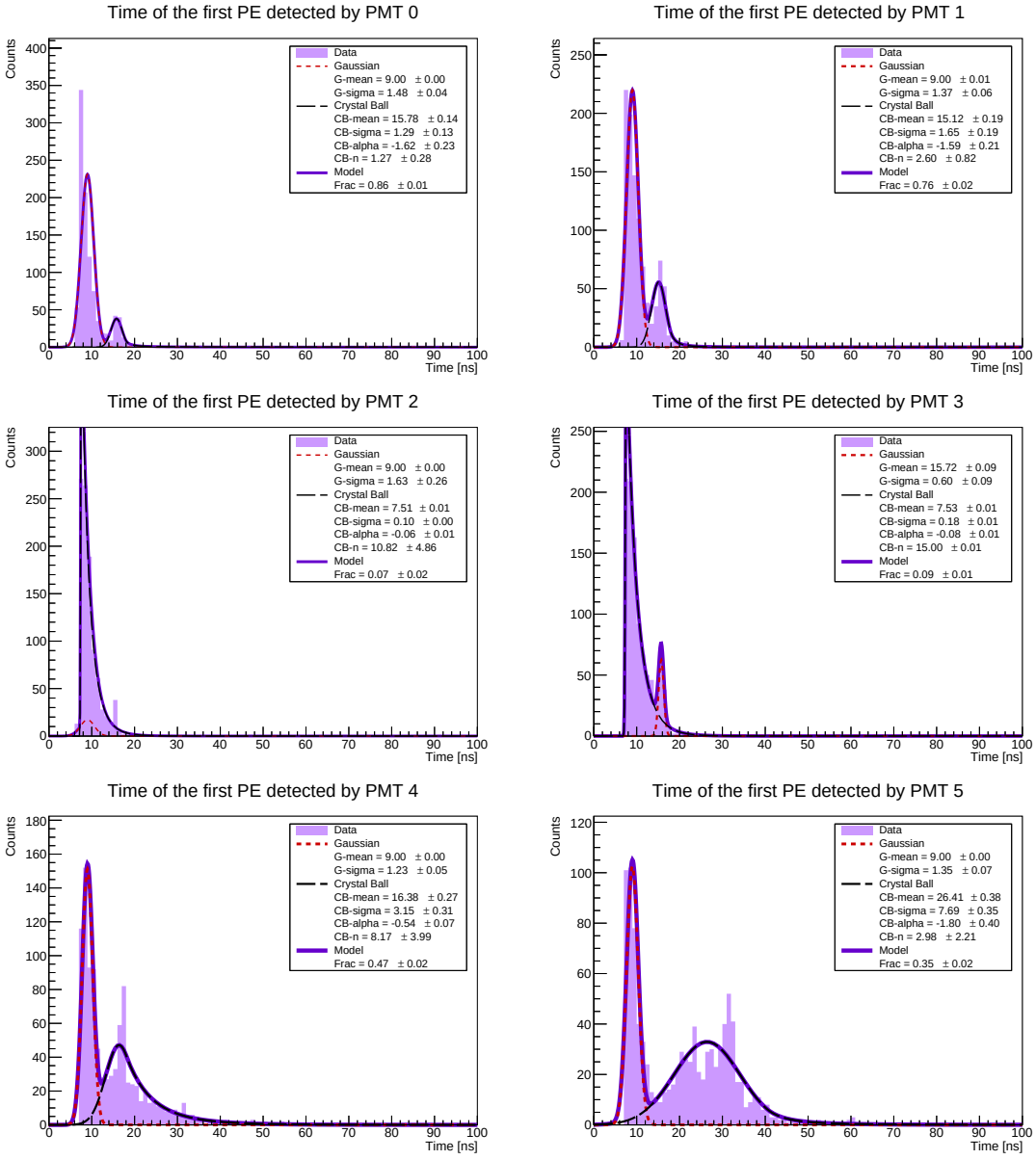

Figure 5.23: First PE arrival time (fTime) at PMTs 0 to 5, for configuration e-_1000_e1GeV_theta80deg_phi40deg_alpha30deg_r18cm_h178cm.root.

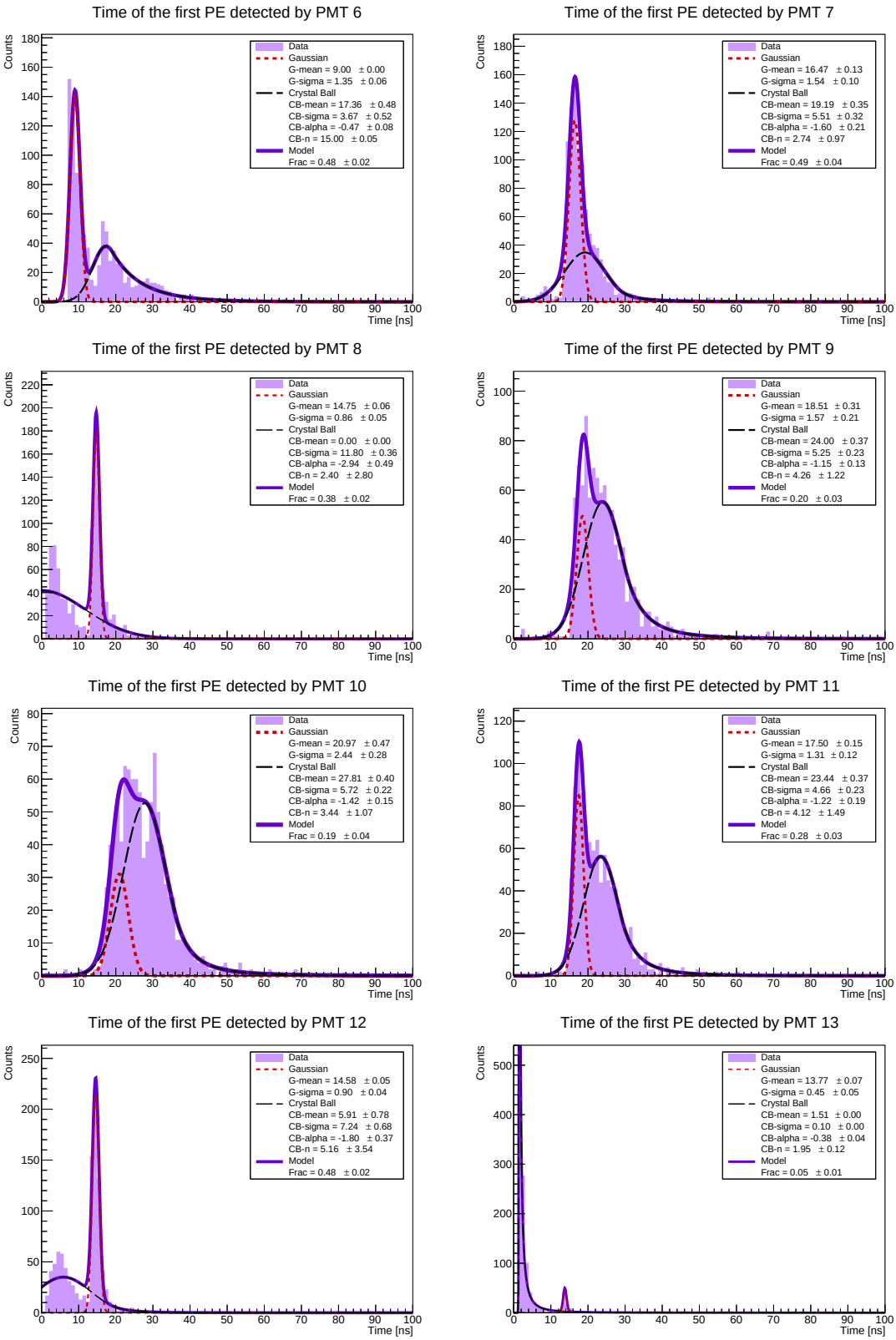

Figure 5.24: First PE arrival time (fTime) at PMTs 6 to 13, for configuration e-_1000_e1GeV_theta80deg_phi40deg_alpha30deg_r18cm_h178cm.root.

e-_1000_e7GeV_theta60deg_phi150deg_alpha30deg_r180cm_h178cm.root

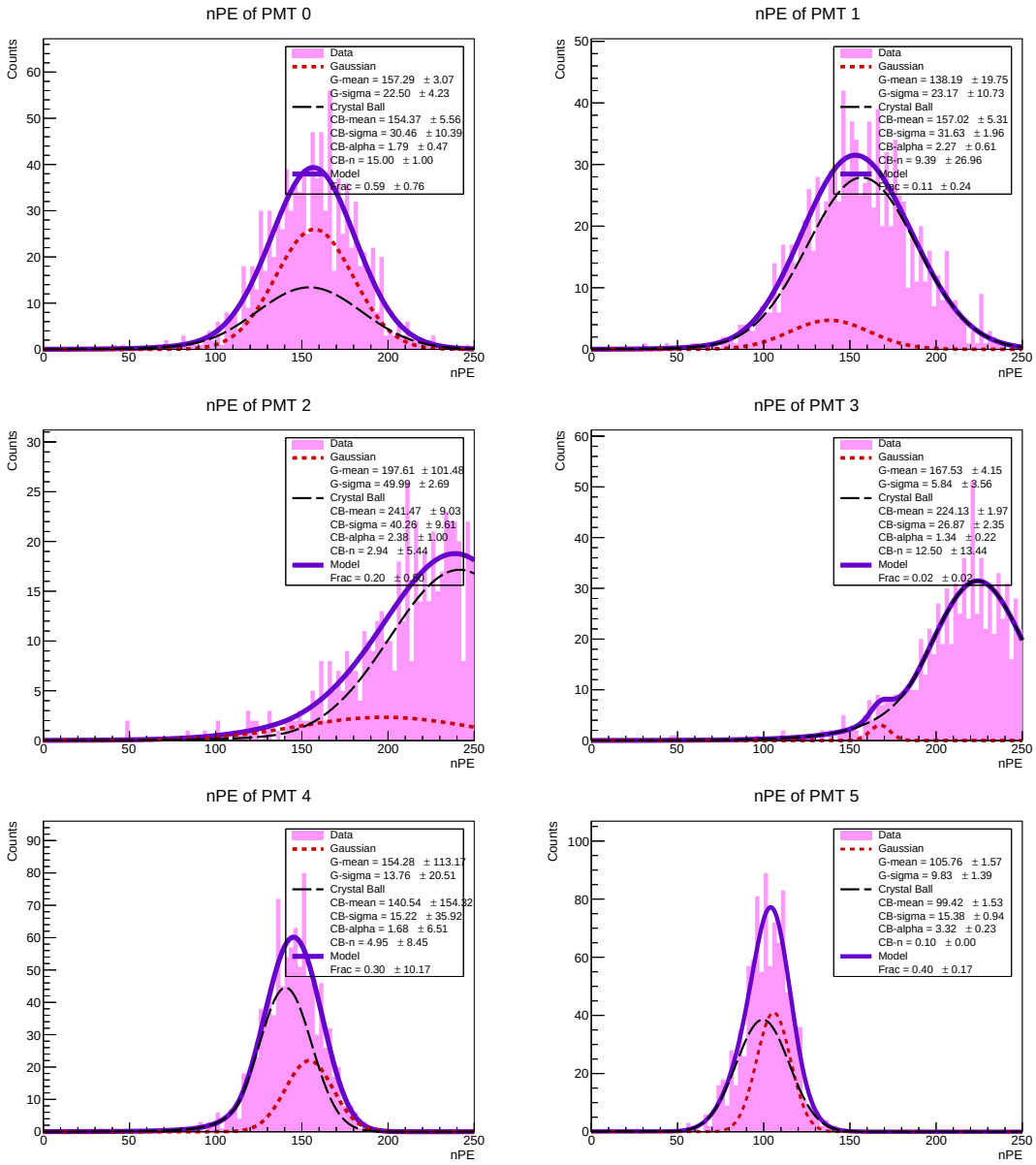

Figure 5.25: Number of photoelectrons recorded by PMTs 0 to 5, for configuration e-_1000_e7GeV_theta60deg_phi150deg_alpha30deg_r180cm_h178cm.root.

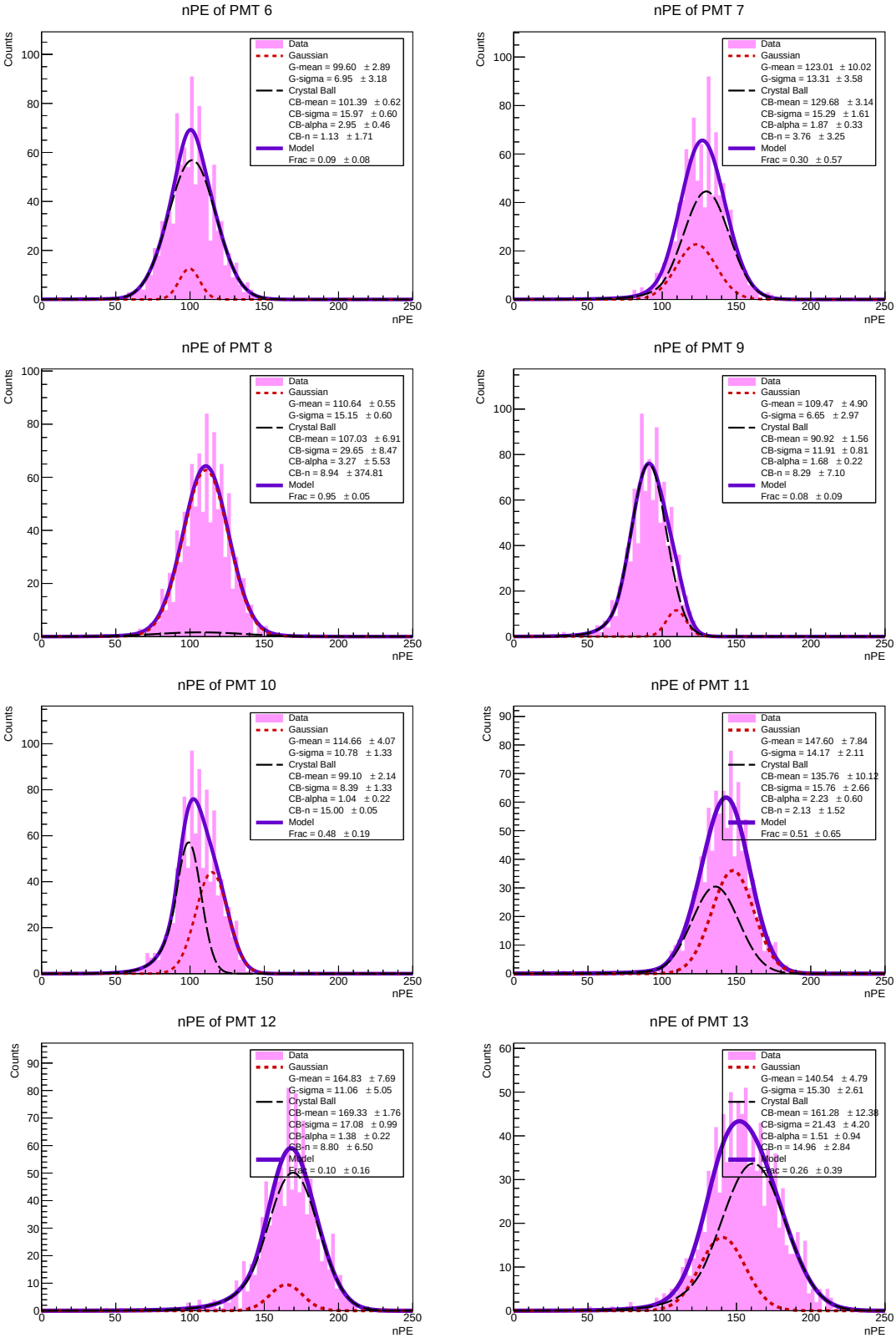

Figure 5.26: Number of photoelectrons recorded by PMTs 6 to 13, for configuration e-_1000_e7GeV_theta60deg_phi150deg_alpha30deg_r180cm_h178cm.root.

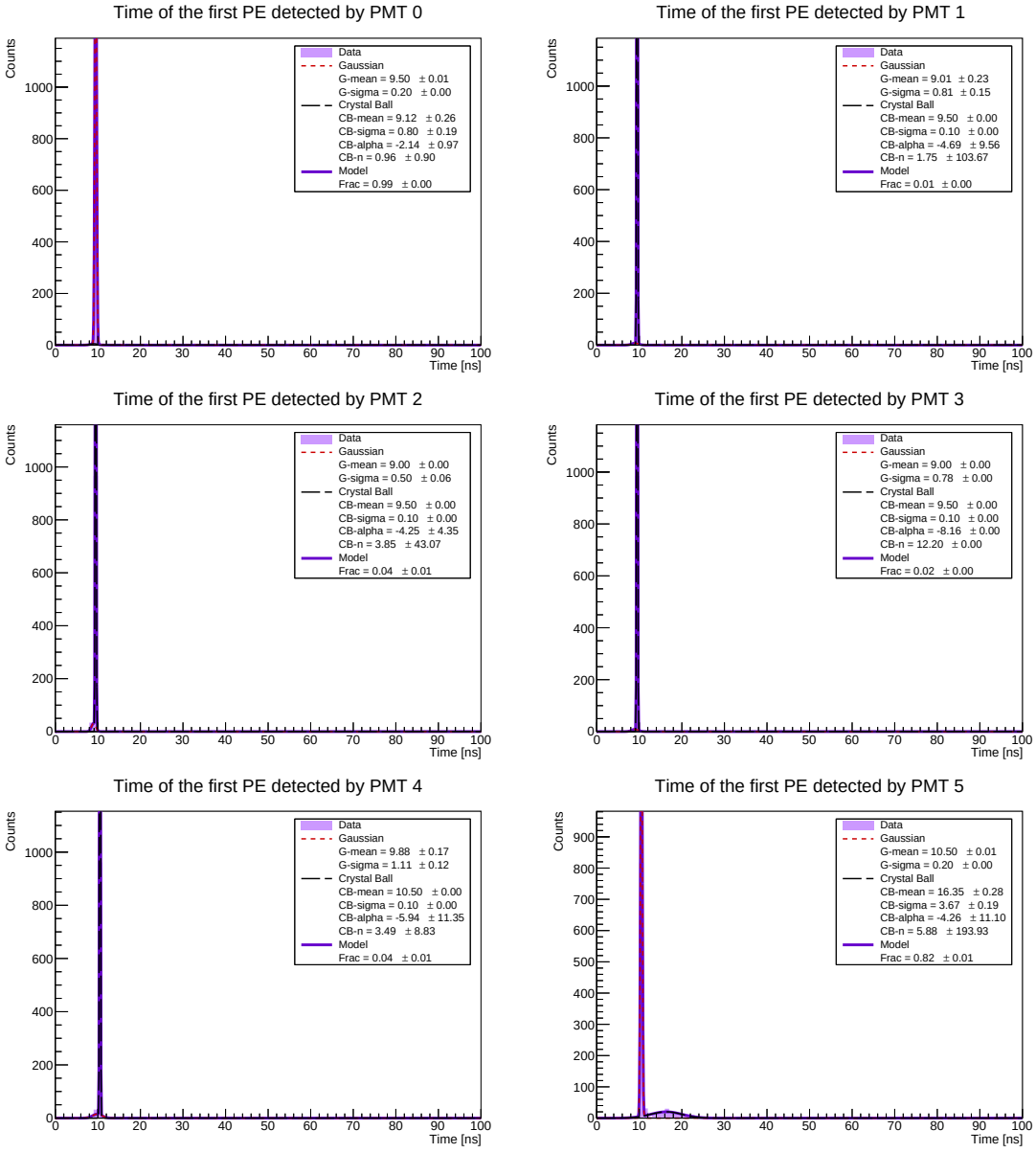

Figure 5.27: First PE arrival time (fTime) at PMTs 0 to 5, for configuration e-_1000_e7GeV_theta60deg_phi150deg_alpha30deg_r180cm_h178cm.root.

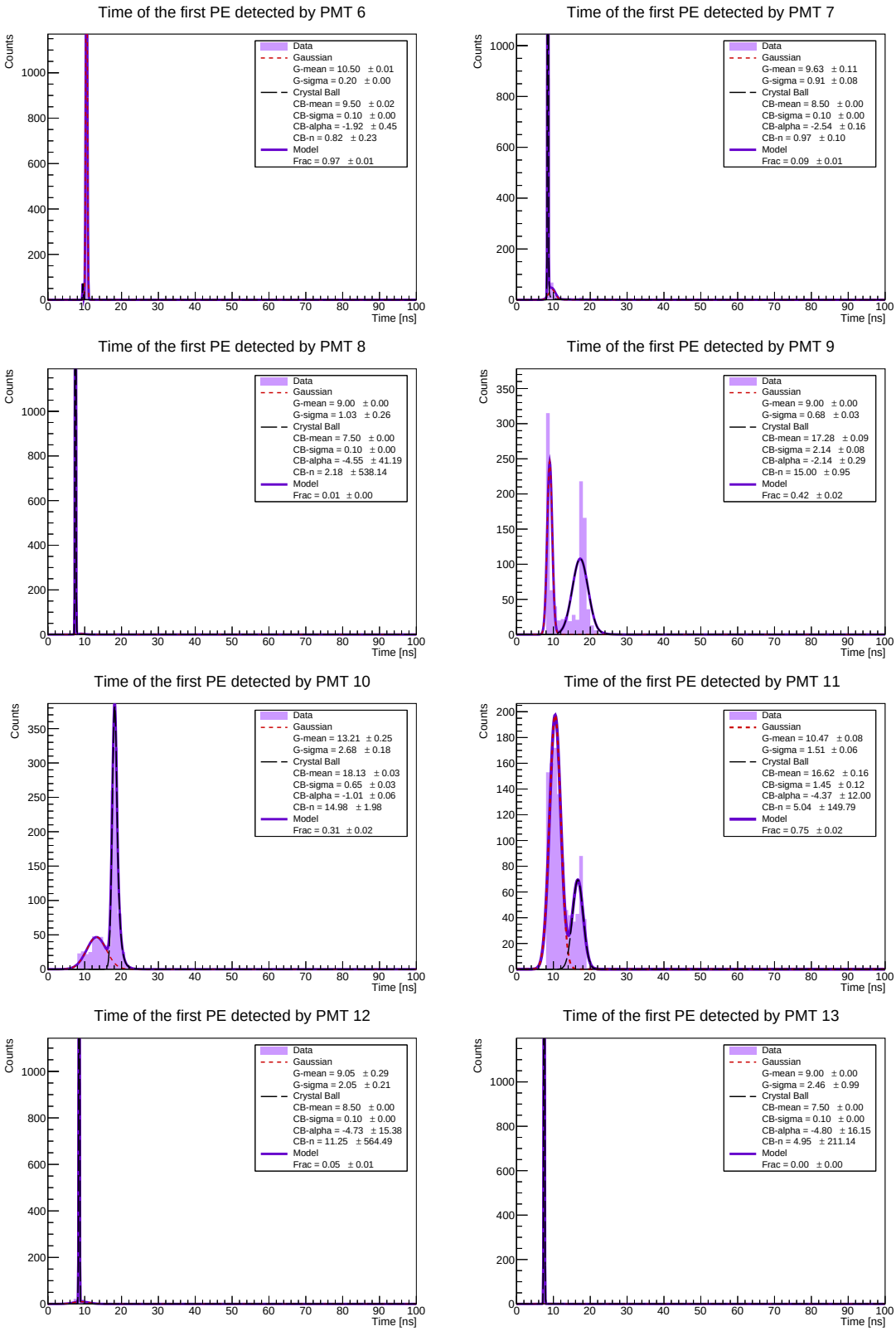

Figure 5.28: First PE arrival time (fTime) at PMTs 6 to 13, for configuration e-_1000_e7GeV_theta60deg_phi150deg_alpha30deg_r180cm_h178cm.root.

e-_1000_e7GeV_theta80deg_phi180deg_alpha30deg_r180cm_h100cm.root

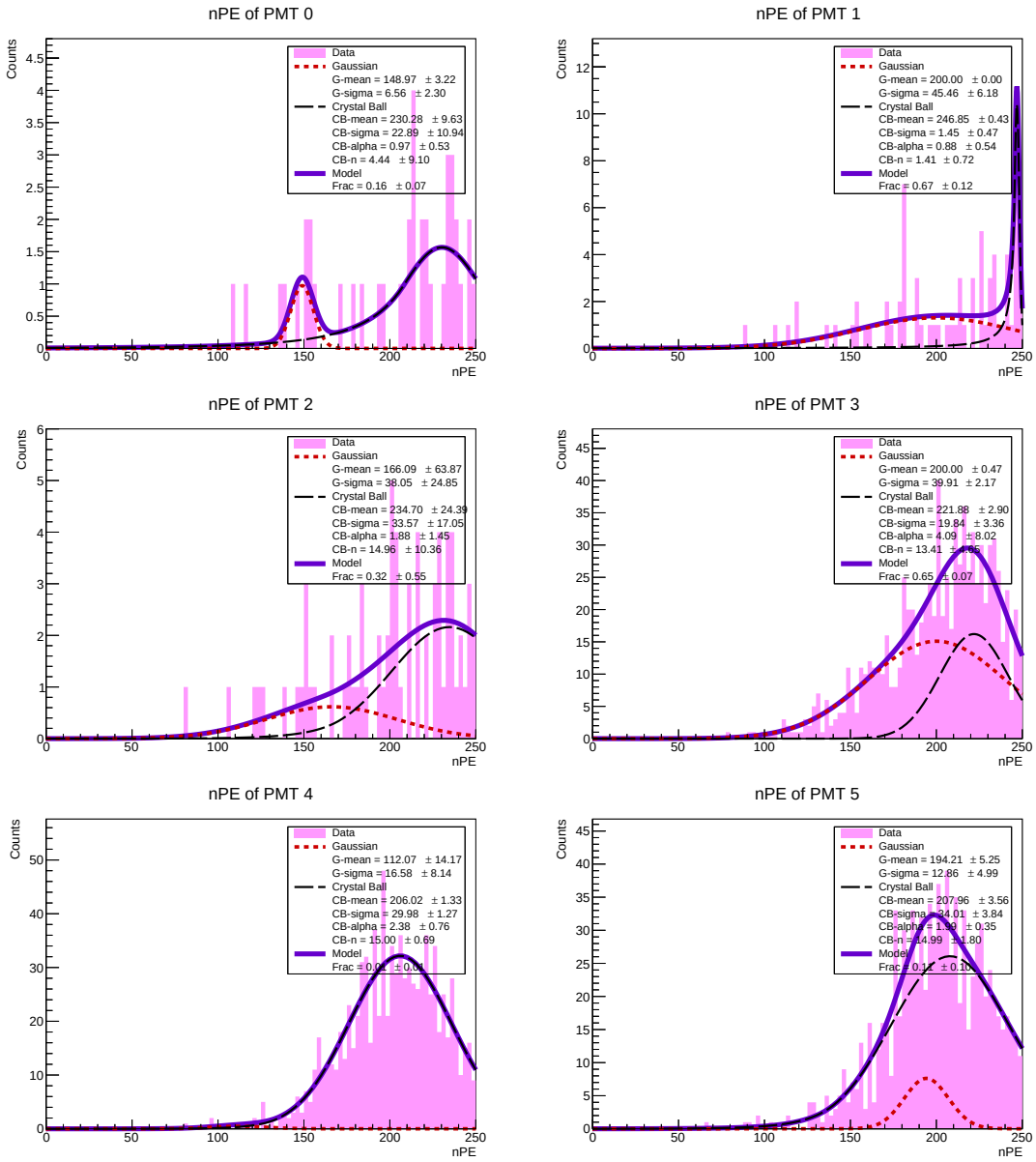

Figure 5.29: Number of photoelectrons recorded by PMTs 0 to 5, for configuration e-_1000_e7GeV_theta80deg_phi180deg_alpha30deg_r180cm_h100cm.root.

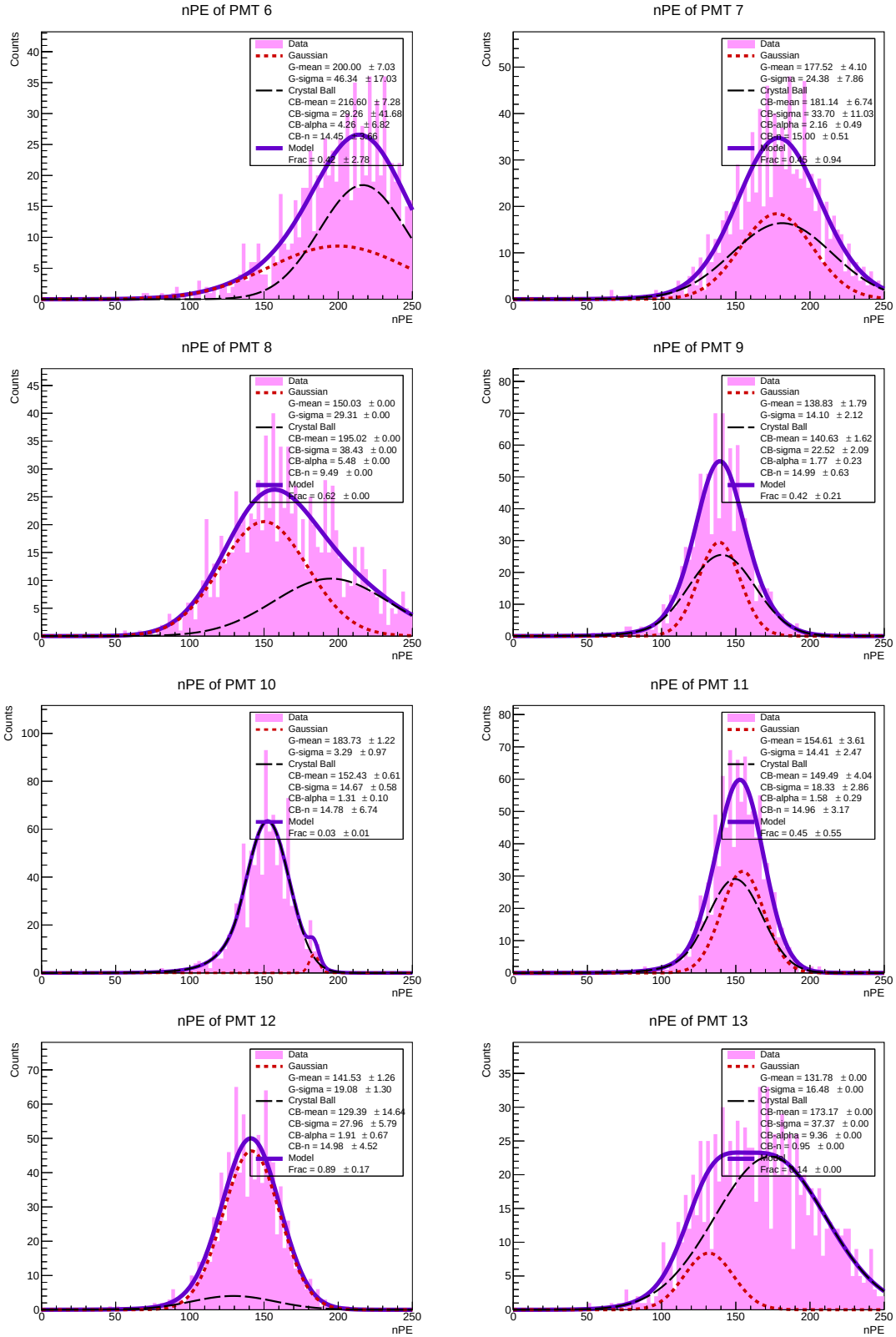

Figure 5.30: Number of photoelectrons recorded by PMTs 6 to 13, for configuration e-_1000_e7GeV_theta80deg_phi180deg_alpha30deg_r180cm_h100cm.root.

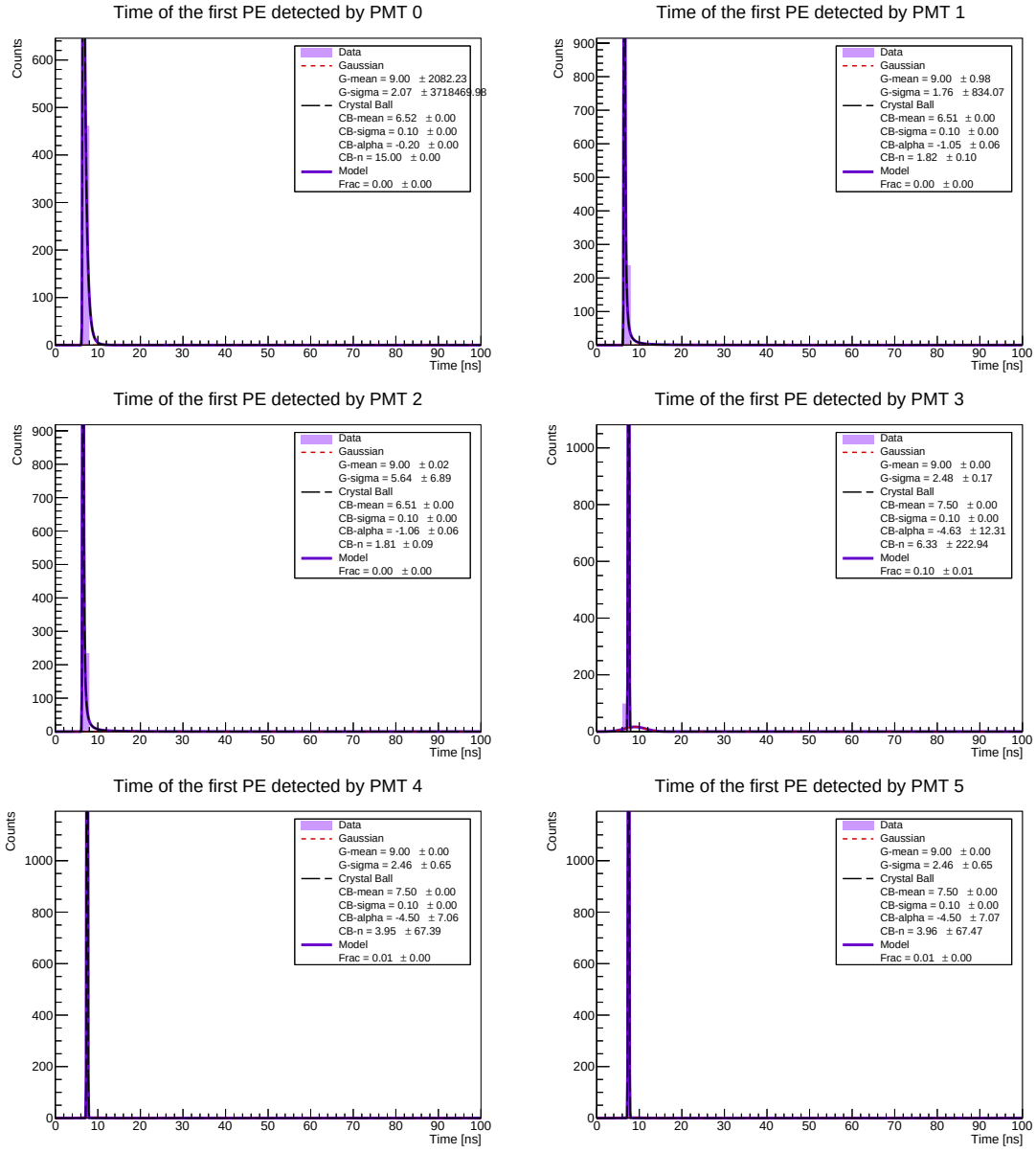

Figure 5.31: First PE arrival time (fTime) at PMTs 0 to 5, for configuration e-_1000_e7GeV_theta80deg_phi180deg_alpha30deg_r180cm_h100cm.root.

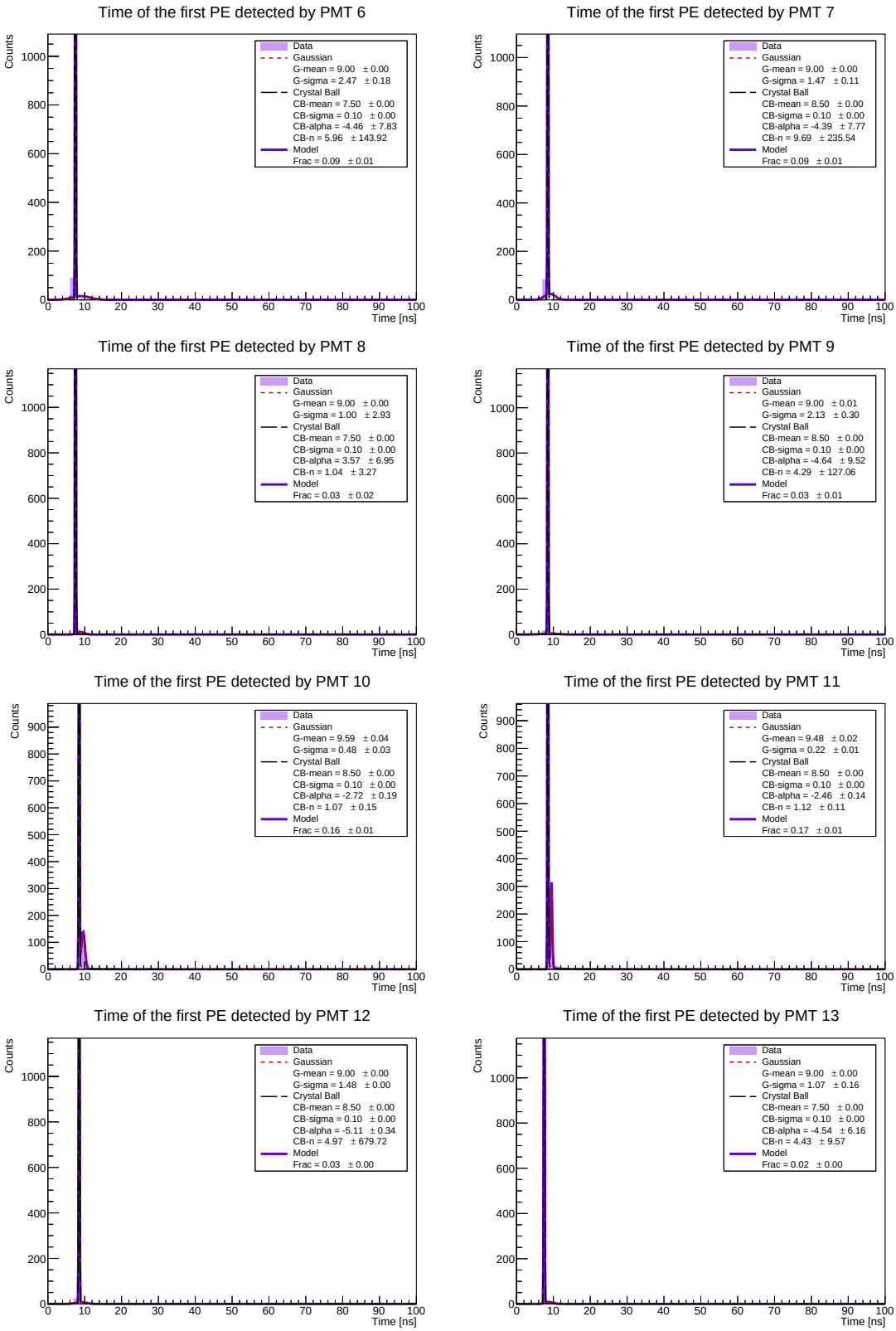

Figure 5.32: First PE arrival time (fTime) at PMTs 6 to 13, for configuration e-_1000_e7GeV_theta80deg_phi180deg_alpha30deg_r180cm_h100cm.root.

gamma_1000_e0.001GeV_theta60deg_phi150deg_alpha30deg_r180cm_h178cm.root

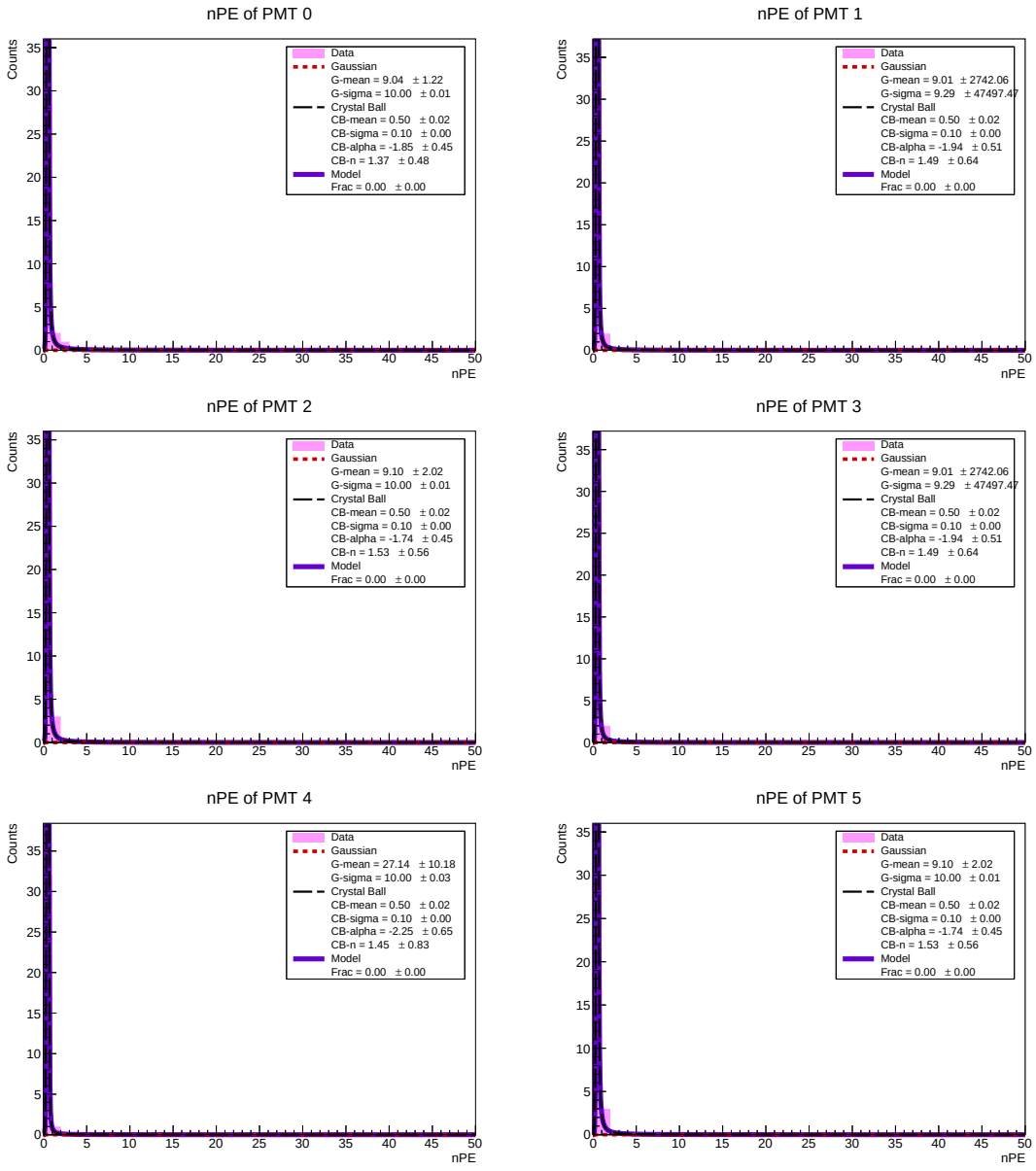

Figure 5.33: Number of photoelectrons recorded by PMTs 0 to 5, for configuration gamma_1000_e0.001GeV_theta60deg_phi150deg_alpha30deg_r180cm_h178cm.root.

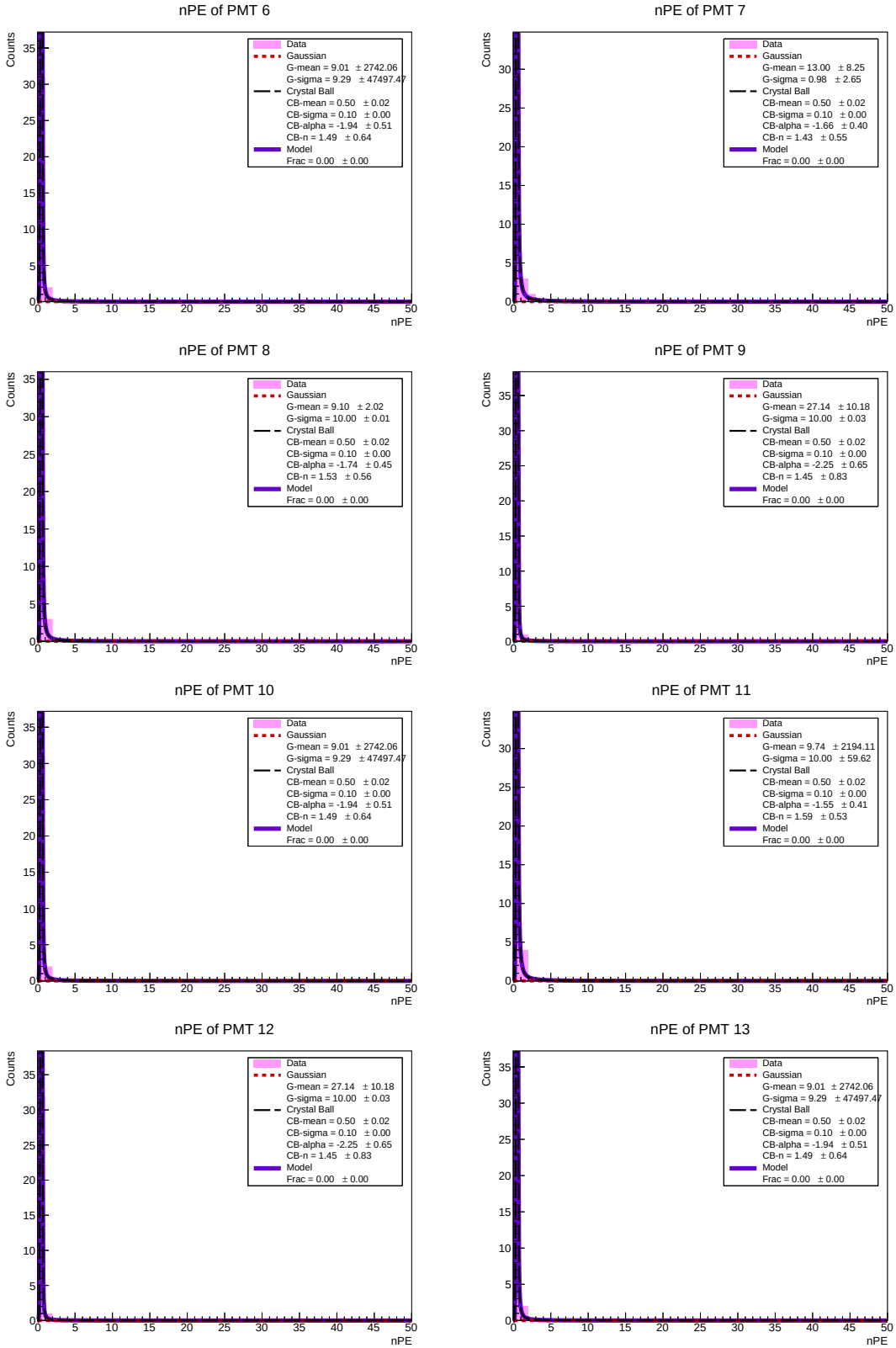

Figure 5.34: Number of photoelectrons recorded by PMTs 6 to 13, for configuration gamma_1000_e0.001GeV_theta60deg_phi150deg_alpha30deg_r180cm_h178cm.root.

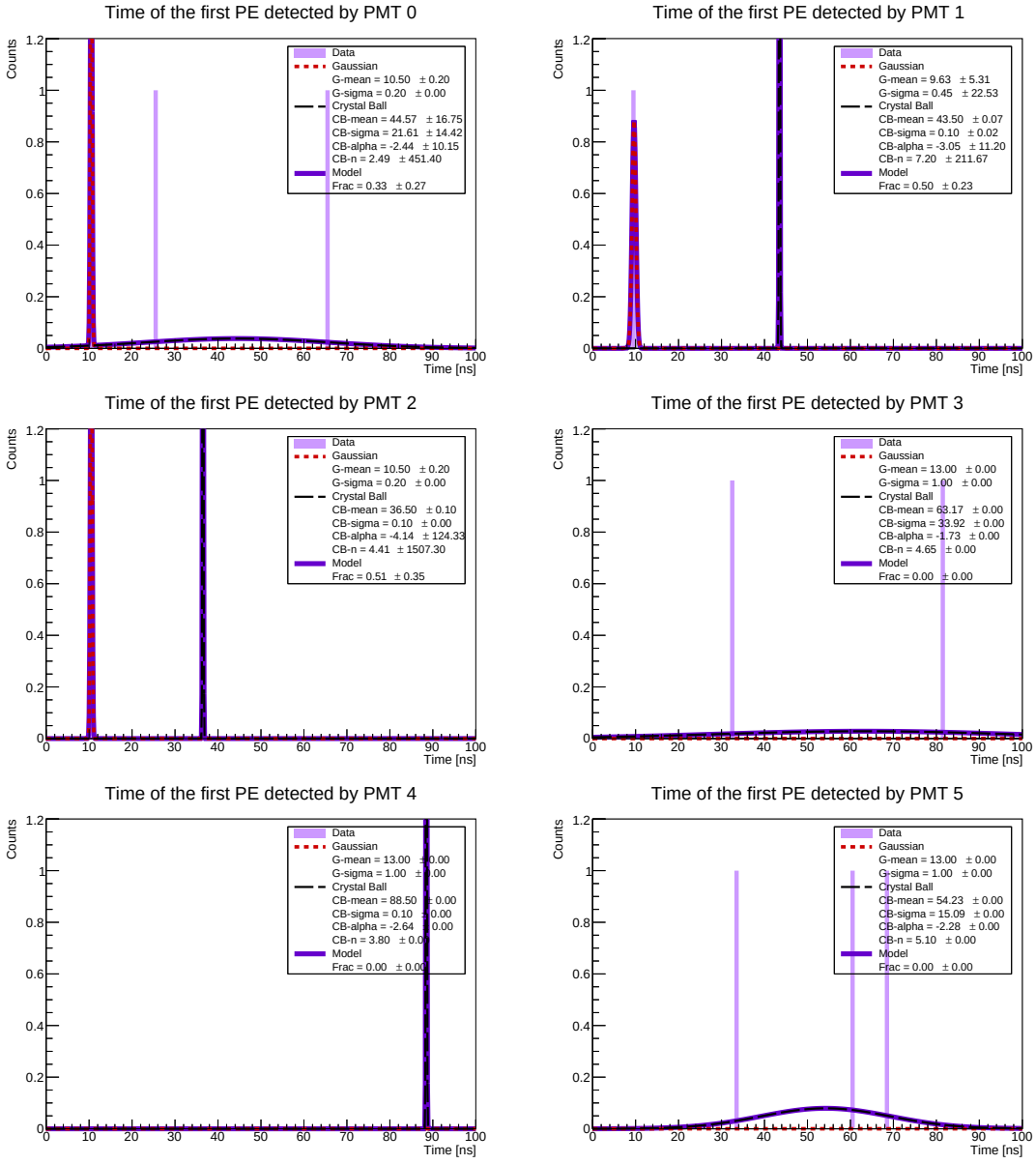

Figure 5.35: First PE arrival time (fTime) at PMTs 0 to 5, for configuration gamma_1000_e0.001GeV_theta60deg_phi150deg_alpha30deg_r180cm_h178cm.root.

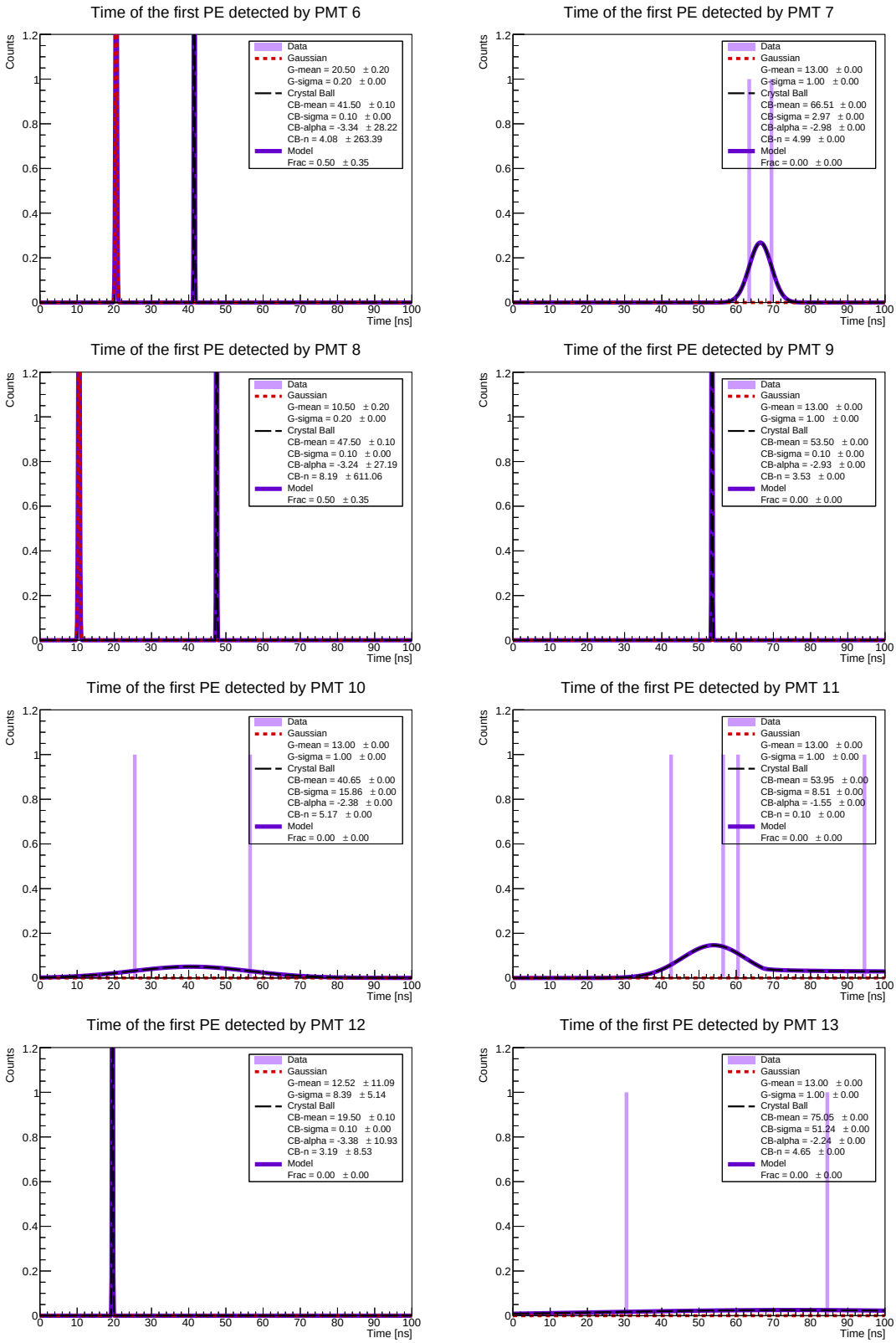

Figure 5.36: First PE arrival time (fTime) at PMTs 6 to 13, for configuration gamma_1000_e0.001GeV_theta60deg_phi150deg_alpha30deg_r180cm_h178cm.root.

gamma_1000_e0.003GeV_theta20deg_phi180deg_alpha30deg_r72cm_h178cm.root

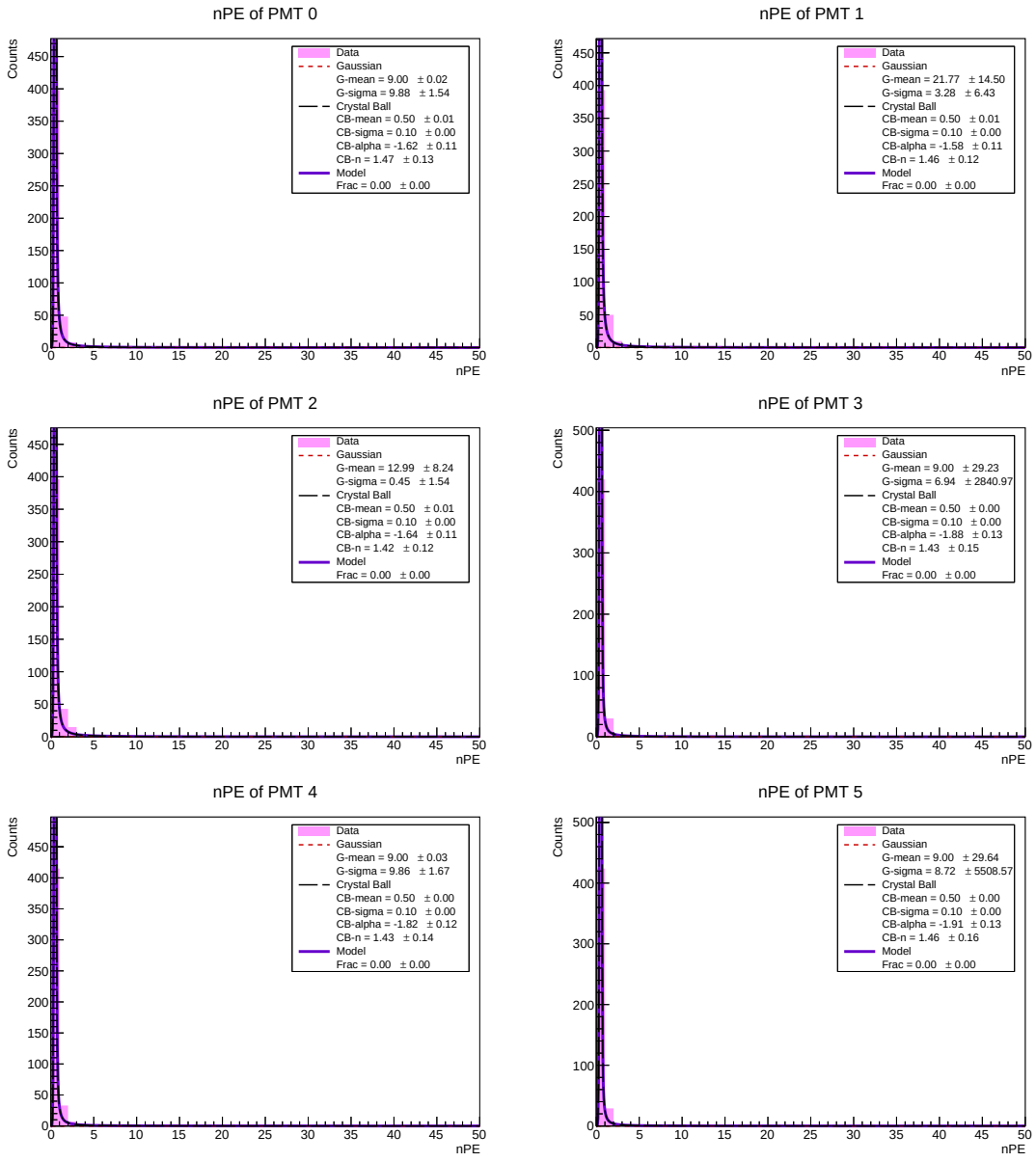

Figure 5.37: Number of photoelectrons recorded by PMTs 0 to 5, for configuration gamma_1000_e0.003GeV_theta20deg_phi180deg_alpha30deg_r72cm_h178cm.root.

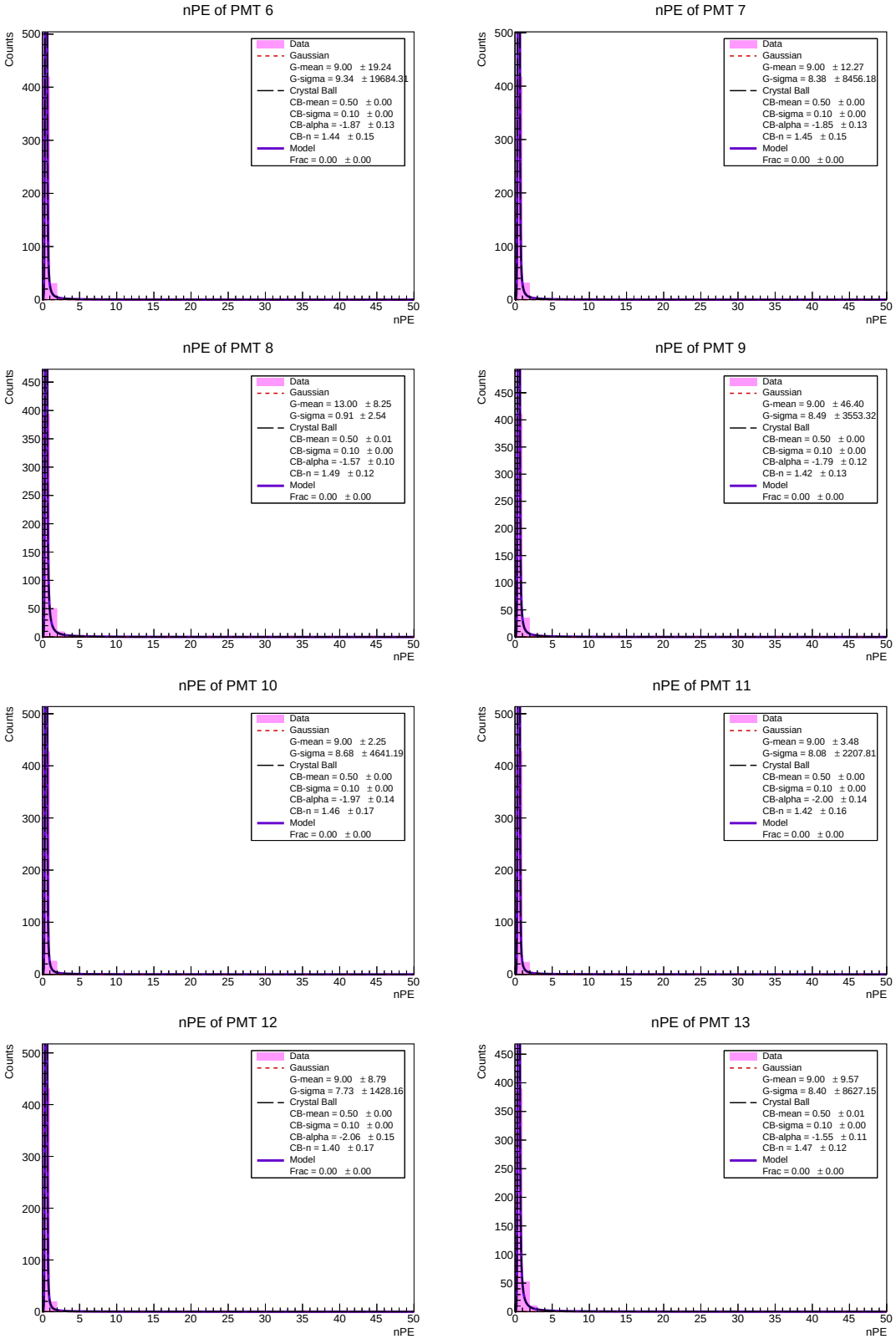

Figure 5.38: Number of photoelectrons recorded by PMTs 6 to 13, for configuration gamma_1000_e0.003GeV_theta20deg_phi180deg_alpha30deg_r72cm_h178cm.root.

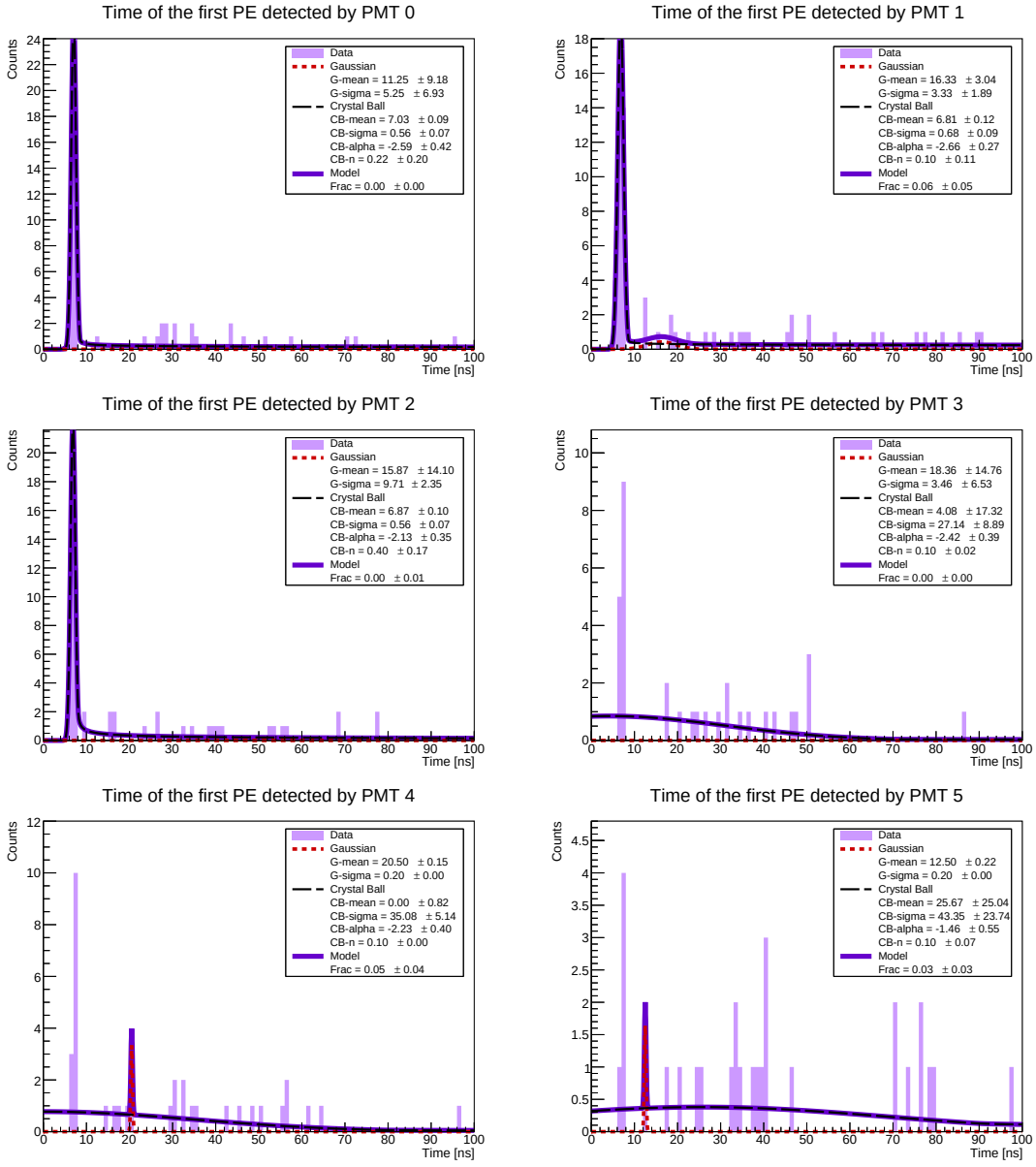

Figure 5.39: First PE arrival time (fTime) at PMTs 0 to 5, for configuration gamma_1000_e0.003GeV_theta20deg_phi180deg_alpha30deg_r72cm_h178cm.root.

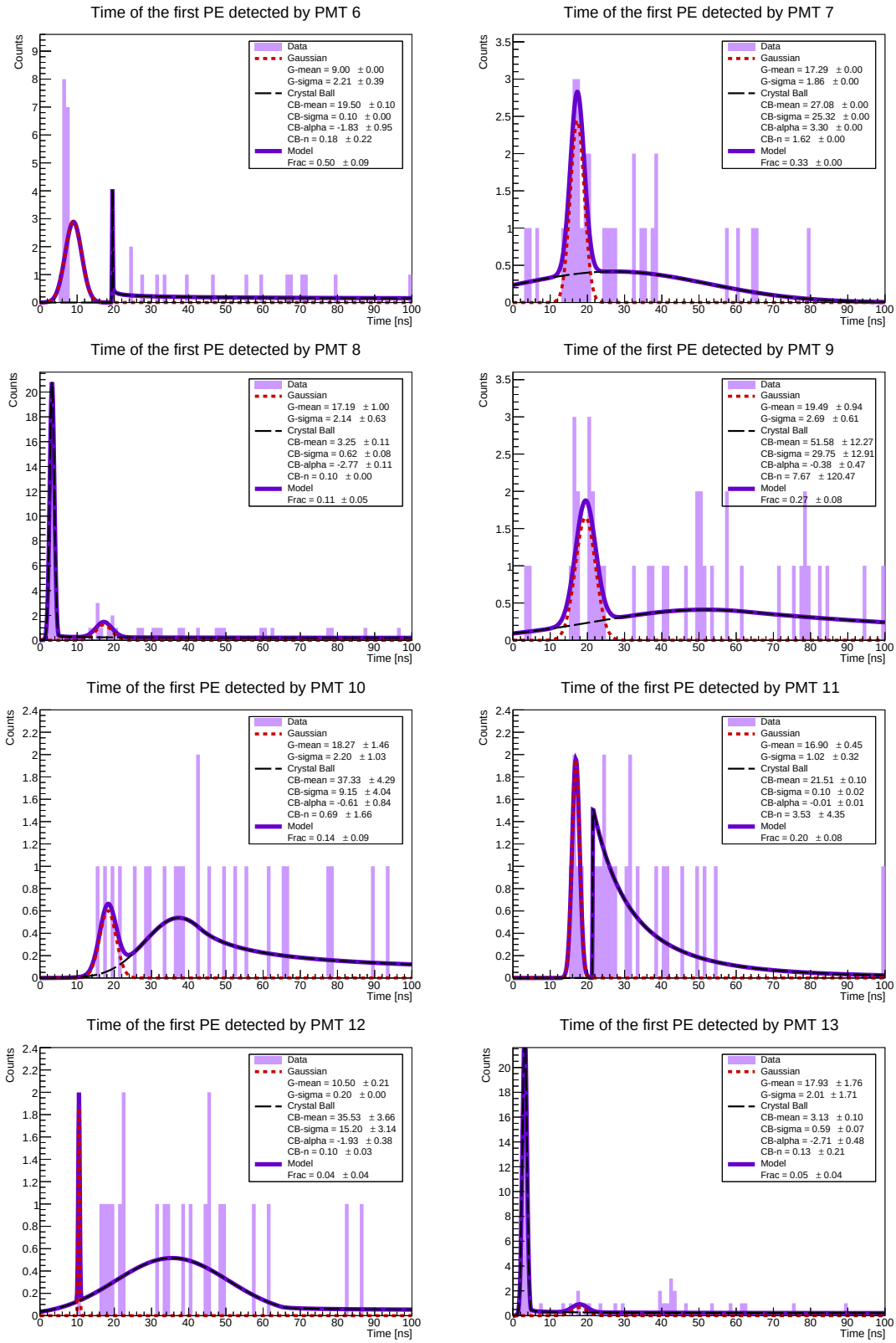

Figure 5.40: First PE arrival time (fTime) at PMTs 6 to 13, for configuration gamma_1000_e0.003GeV_theta20deg_phi180deg_alpha30deg_r72cm_h178cm.root.

gamma_1000_e0.007GeV_theta20deg_phi150deg_alpha30deg_r180cm_h150cm.root

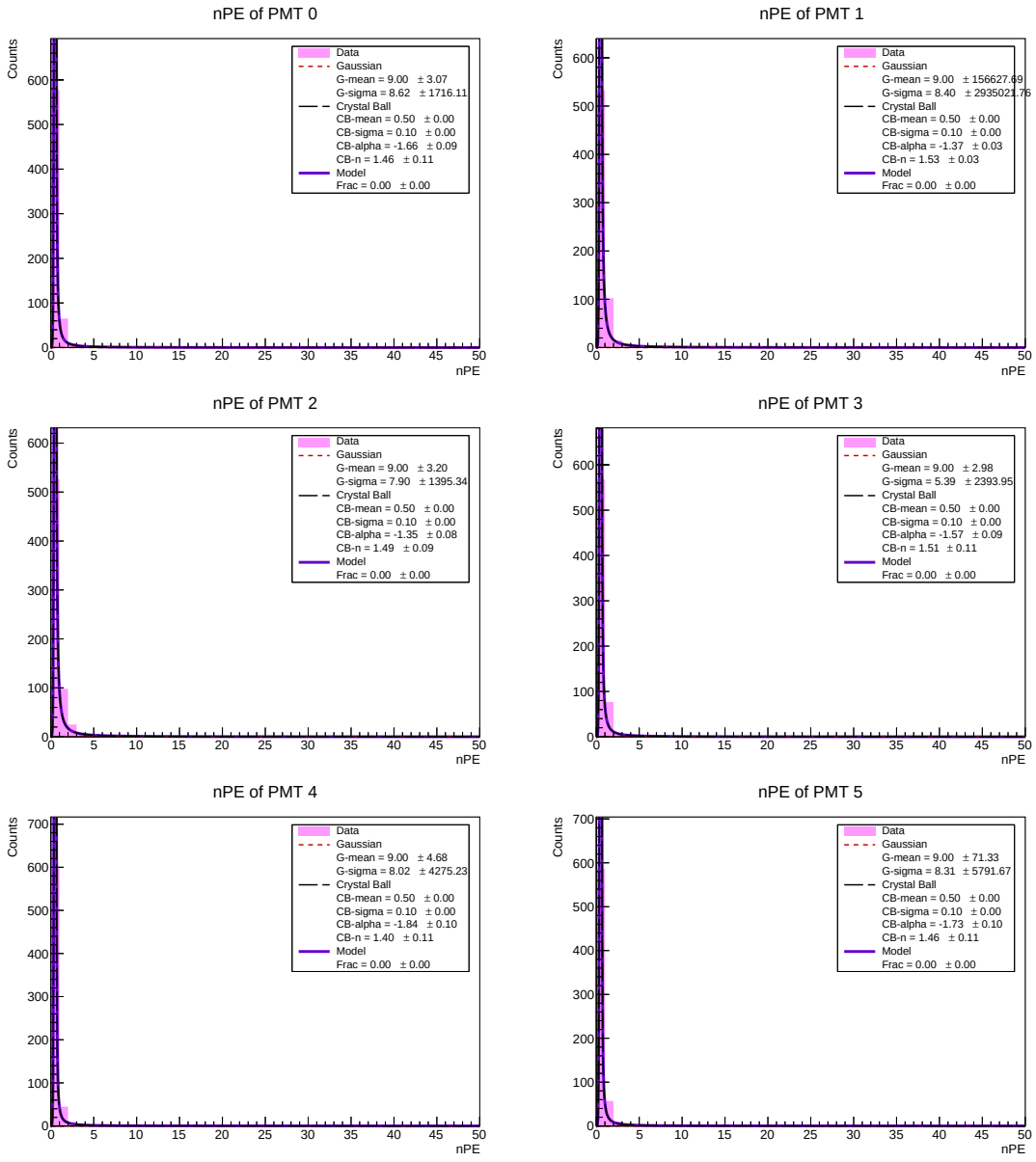

Figure 5.41: Number of photoelectrons recorded by PMTs 0 to 5, for configuration gamma_1000_e0.007GeV_theta20deg_phi150deg_alpha30deg_r180cm_h150cm.root.

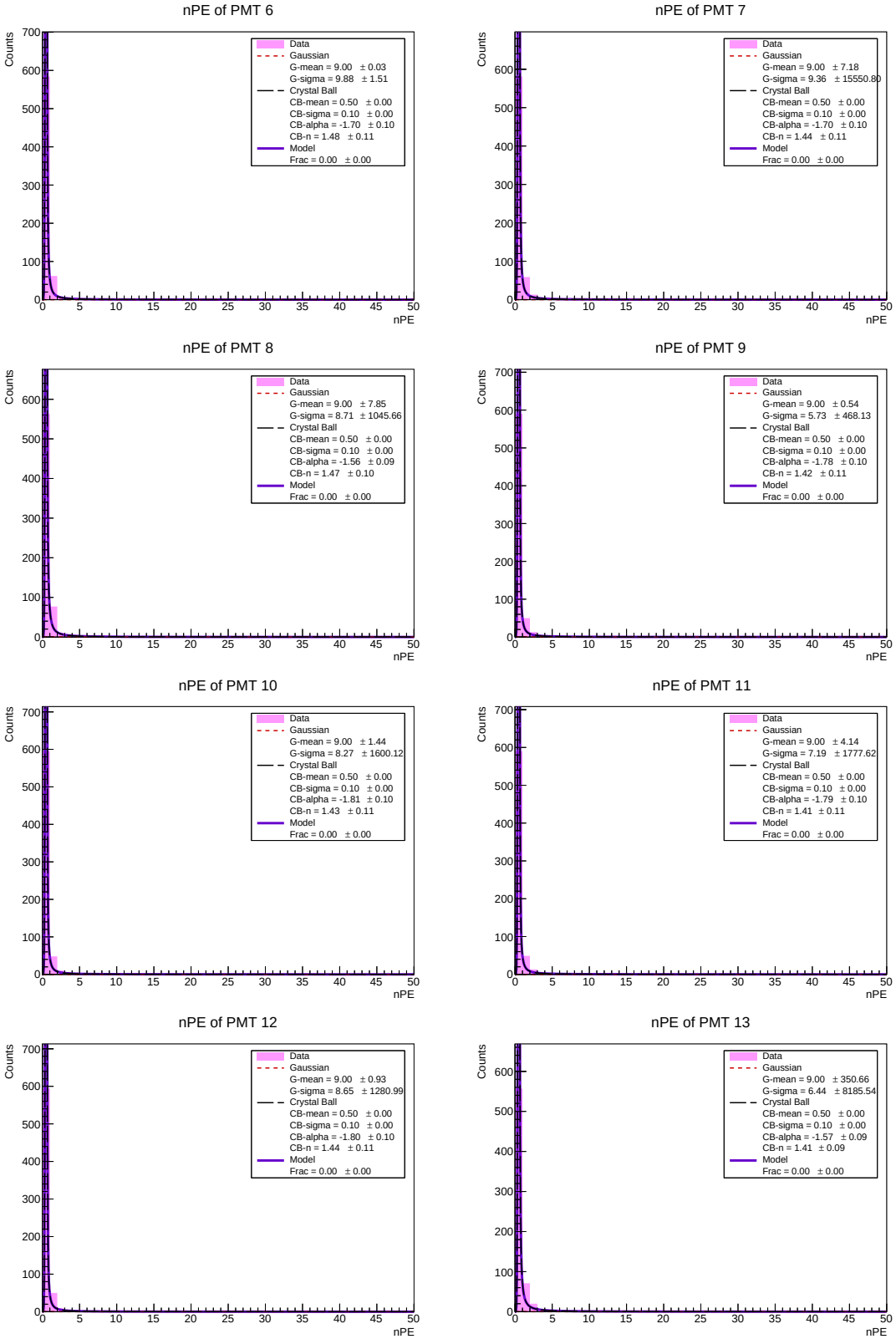

Figure 5.42: Number of photoelectrons recorded by PMTs 6 to 13, for configuration gamma_1000_e0.007GeV_theta20deg_phi150deg_alpha30deg_r180cm_h150cm.root.

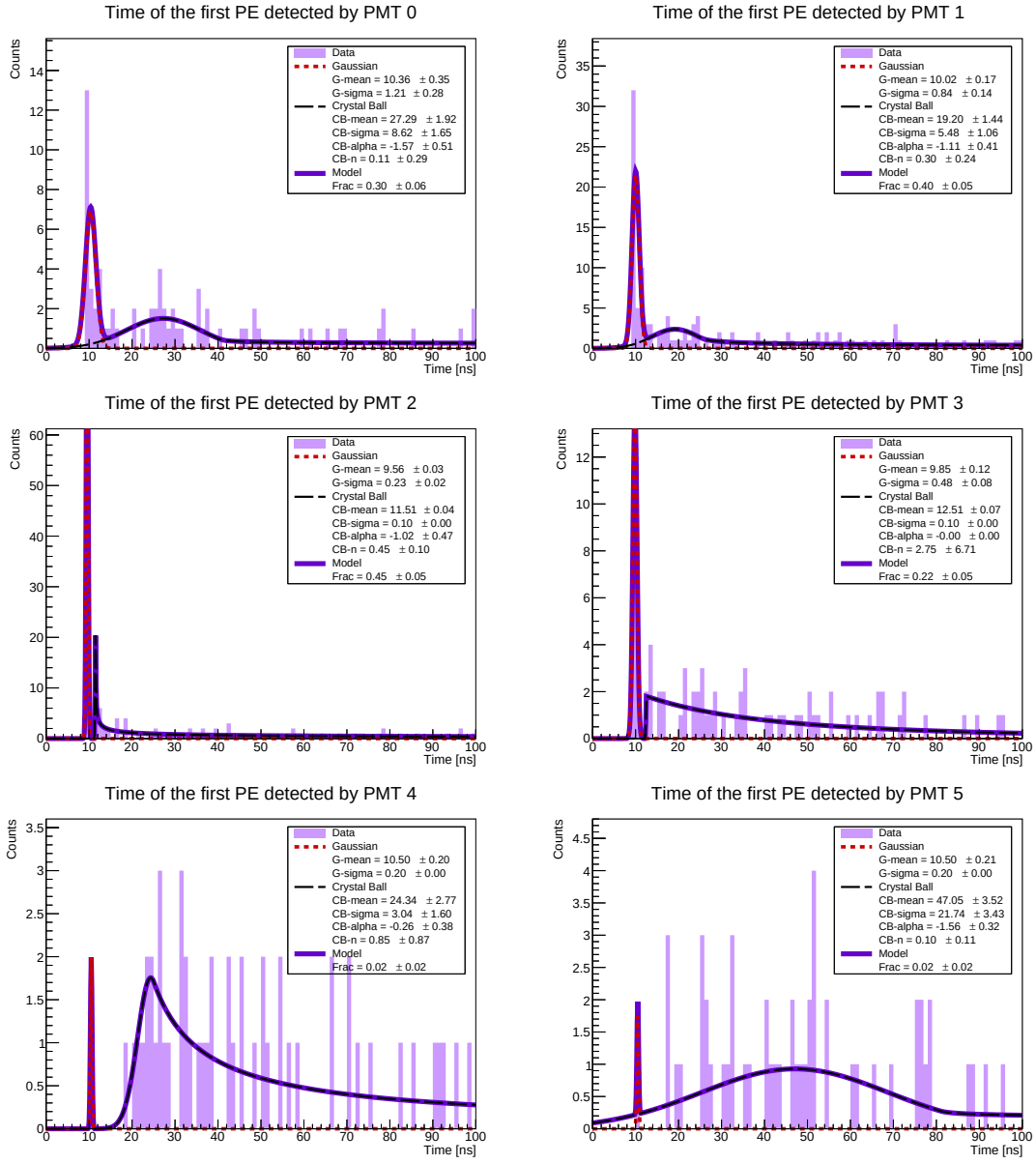

Figure 5.43: First PE arrival time (fTime) at PMTs 0 to 5, for configuration gamma_1000_e0.007GeV_theta20deg_phi150deg_alpha30deg_r180cm_h150cm.root.

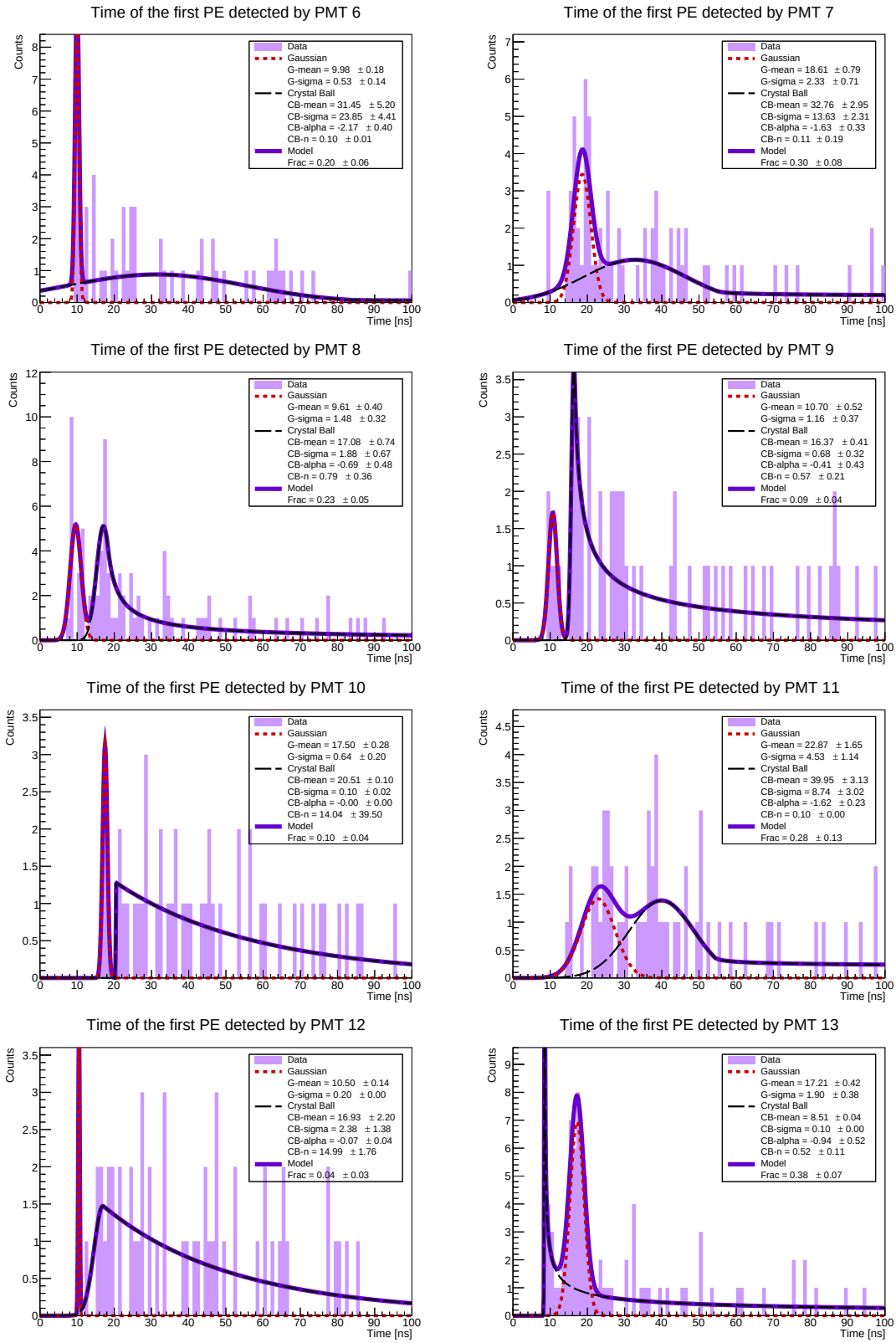

Figure 5.44: First PE arrival time (fTime) at PMTs 6 to 13, for configuration gamma_1000_e0.007GeV_theta20deg_phi150deg_alpha30deg_r180cm_h150cm.root.

gamma_1000_e10GeV_theta60deg_phi40deg_alpha0deg_r126cm_h178cm.root

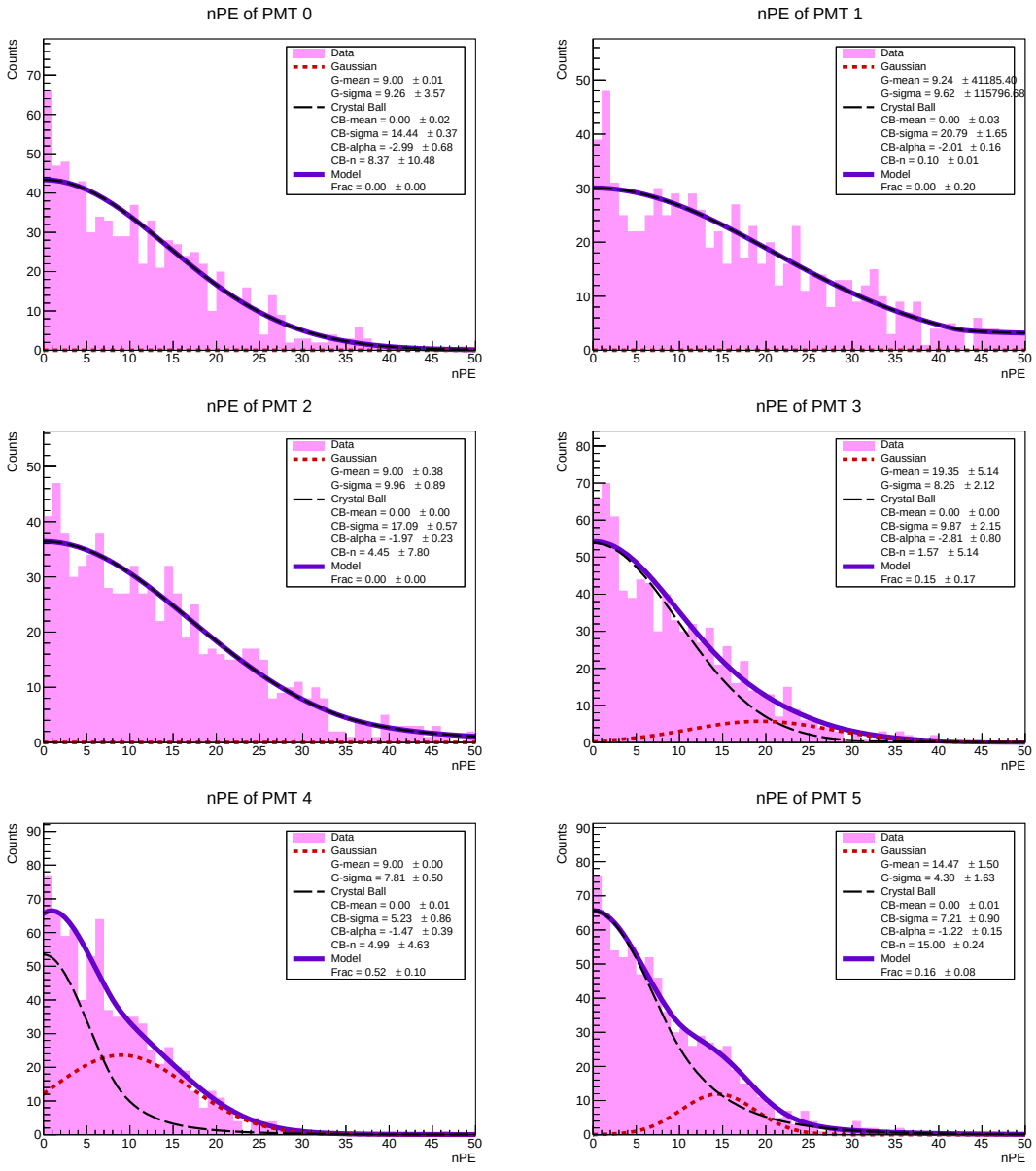

Figure 5.45: Number of photoelectrons recorded by PMTs 0 to 5, for configuration gamma_1000_e10GeV_theta60deg_phi40deg_alpha0deg_r126cm_h178cm.root.

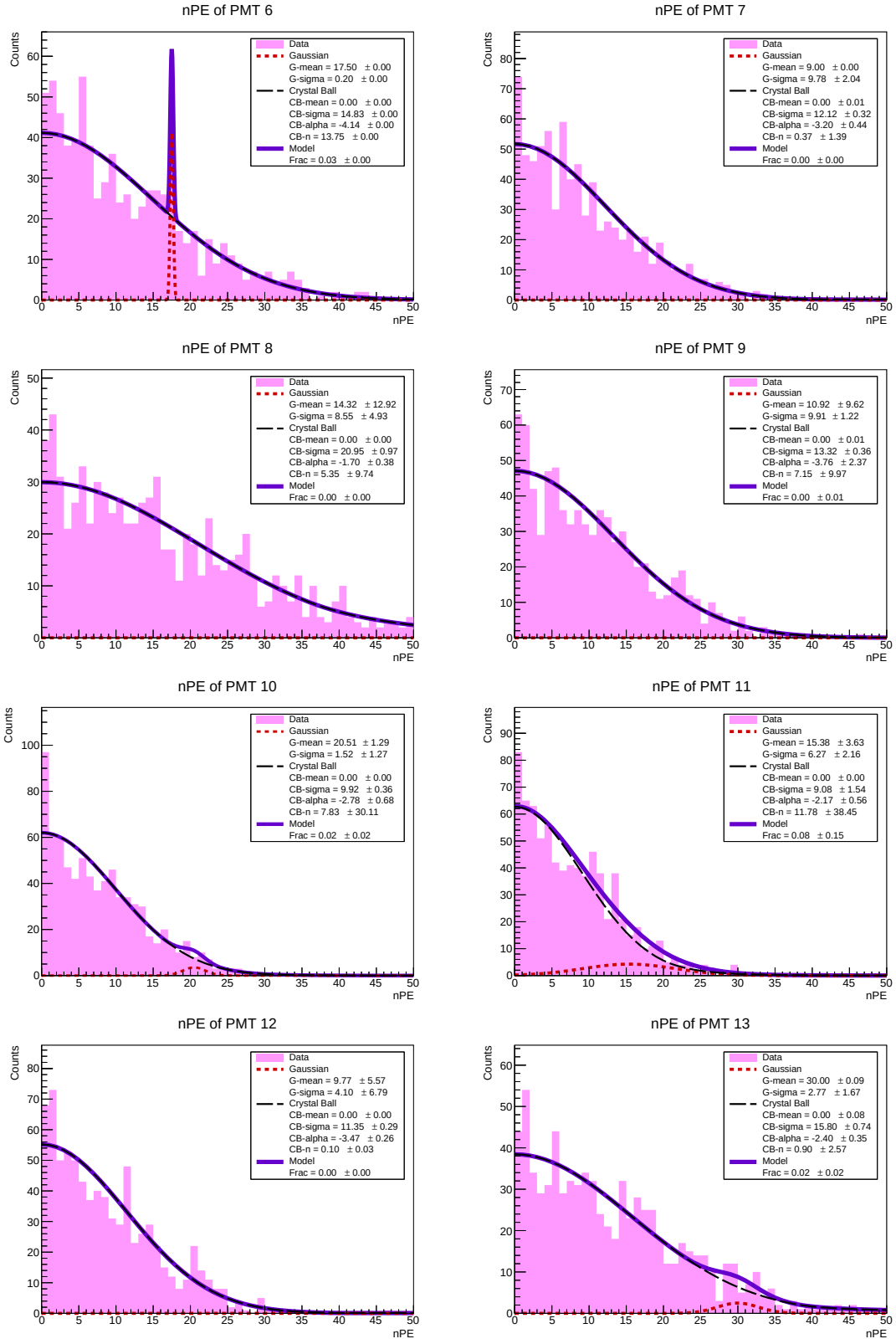

Figure 5.46: Number of photoelectrons recorded by PMTs 6 to 13, for configuration gamma_1000_e10GeV_theta60deg_phi40deg_alpha0deg_r126cm_h178cm.root.

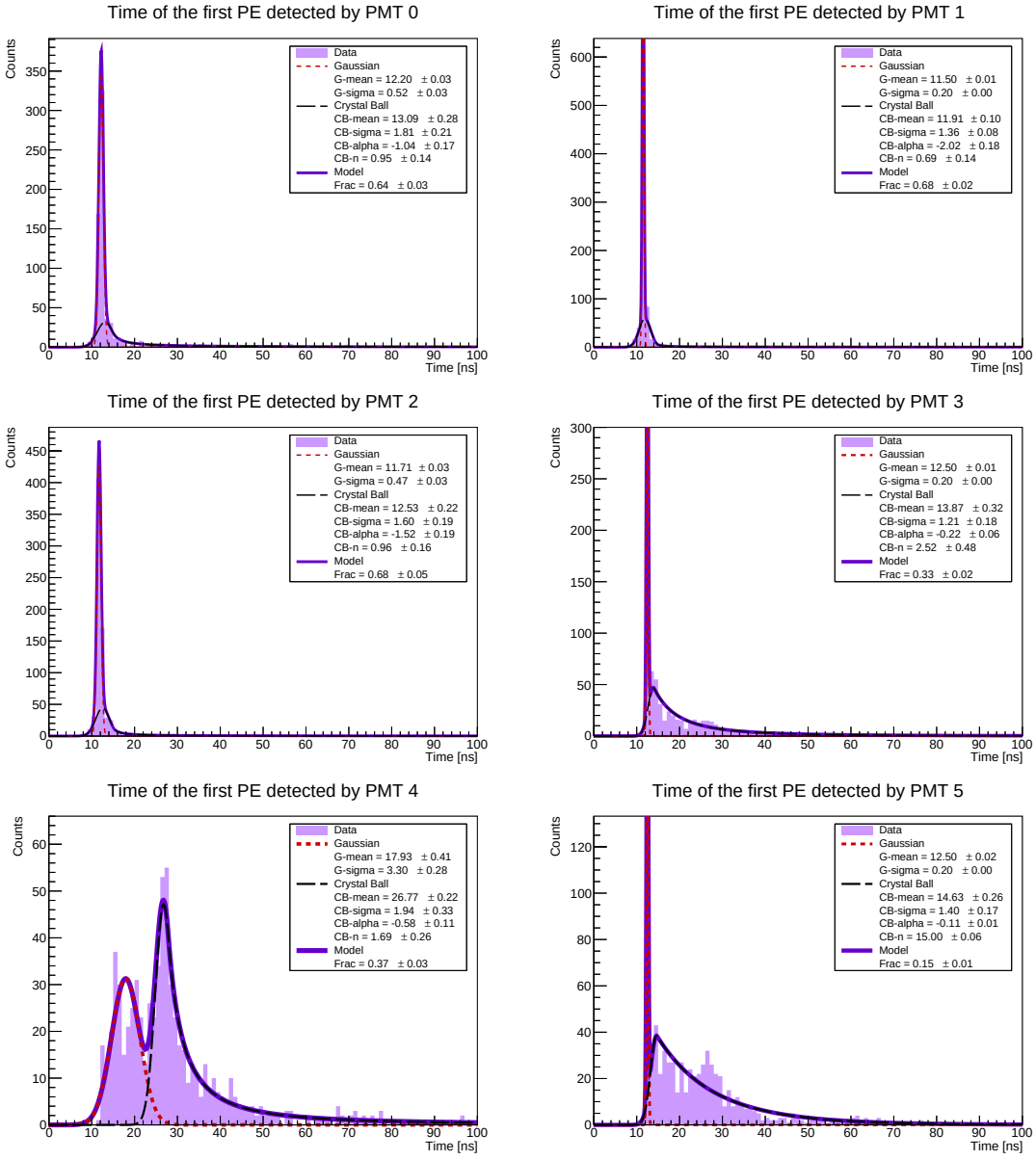

Figure 5.47: First PE arrival time (fTime) at PMTs 0 to 5, for configuration gamma_1000_e10GeV_theta60deg_phi40deg_alpha0deg_r126cm_h178cm.root.

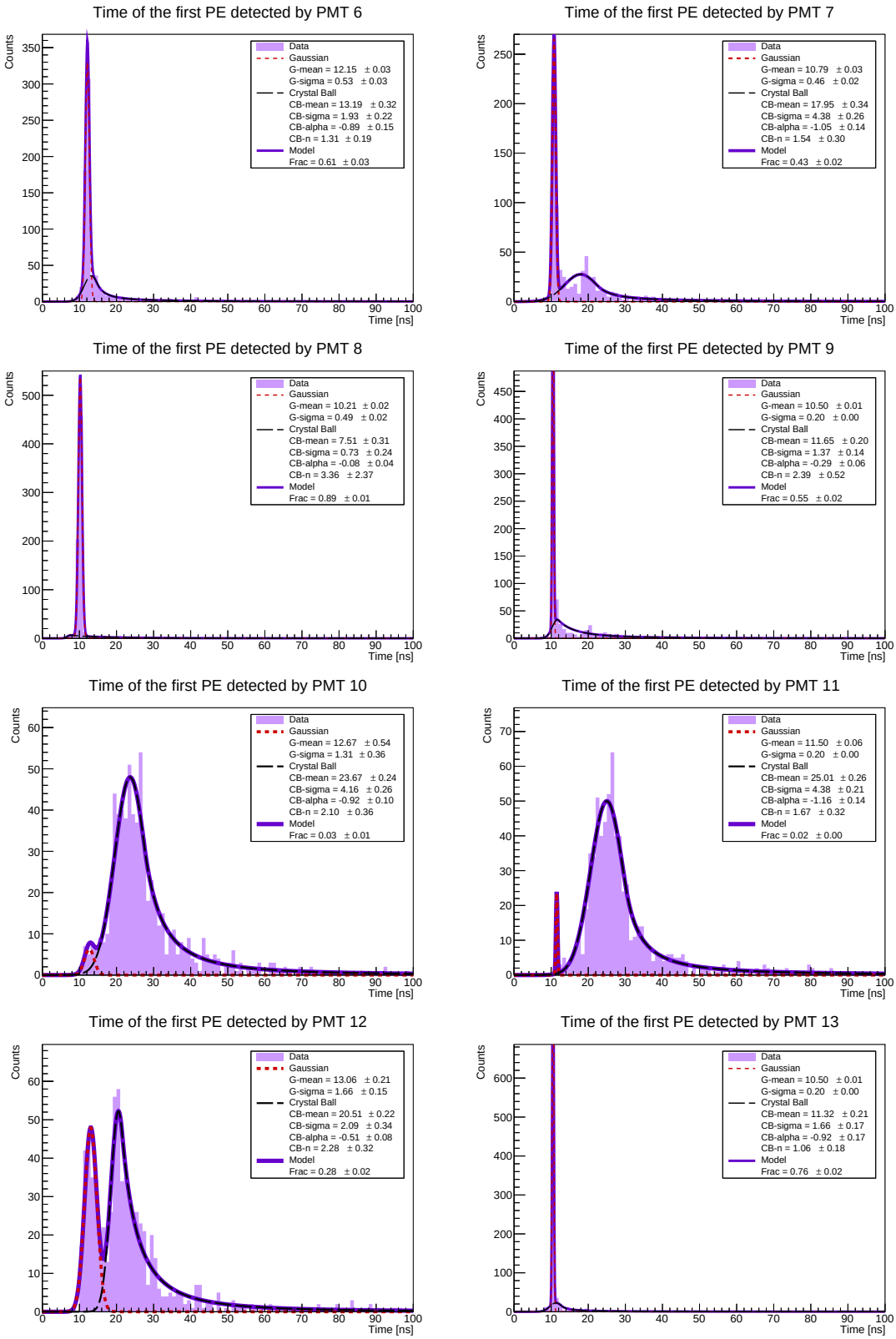

Figure 5.48: First PE arrival time (fTime) at PMTs 6 to 13, for configuration gamma_1000_e10GeV_theta60deg_phi40deg_alpha0deg_r126cm_h178cm.root.

gamma_1000_e10GeV_theta80deg_phi180deg_alpha0deg_r180cm_h50cm.root

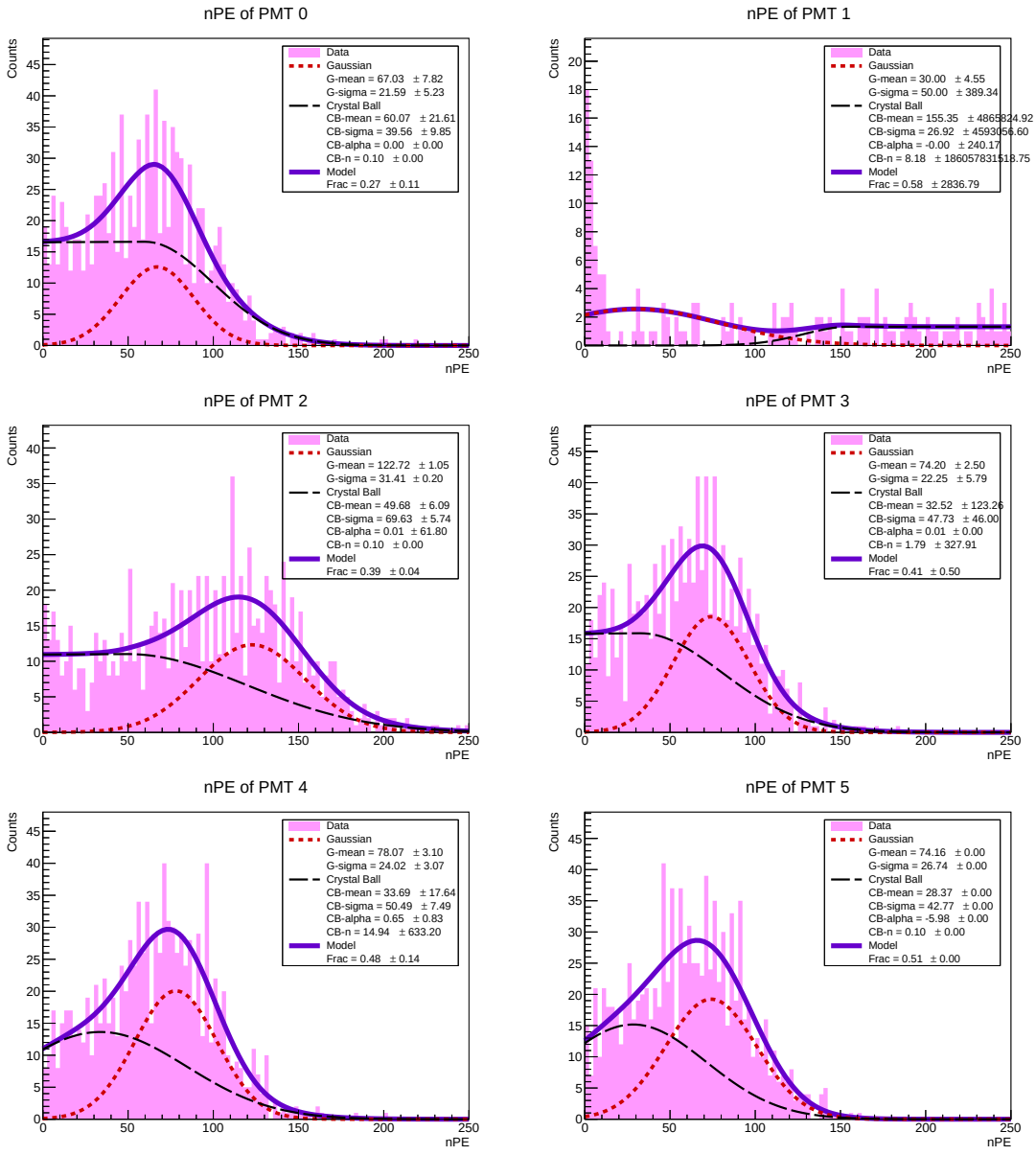

Figure 5.49: Number of photoelectrons recorded by PMTs 0 to 5, for configuration gamma_1000_e10GeV_theta80deg_phi180deg_alpha0deg_r180cm_h50cm.root.

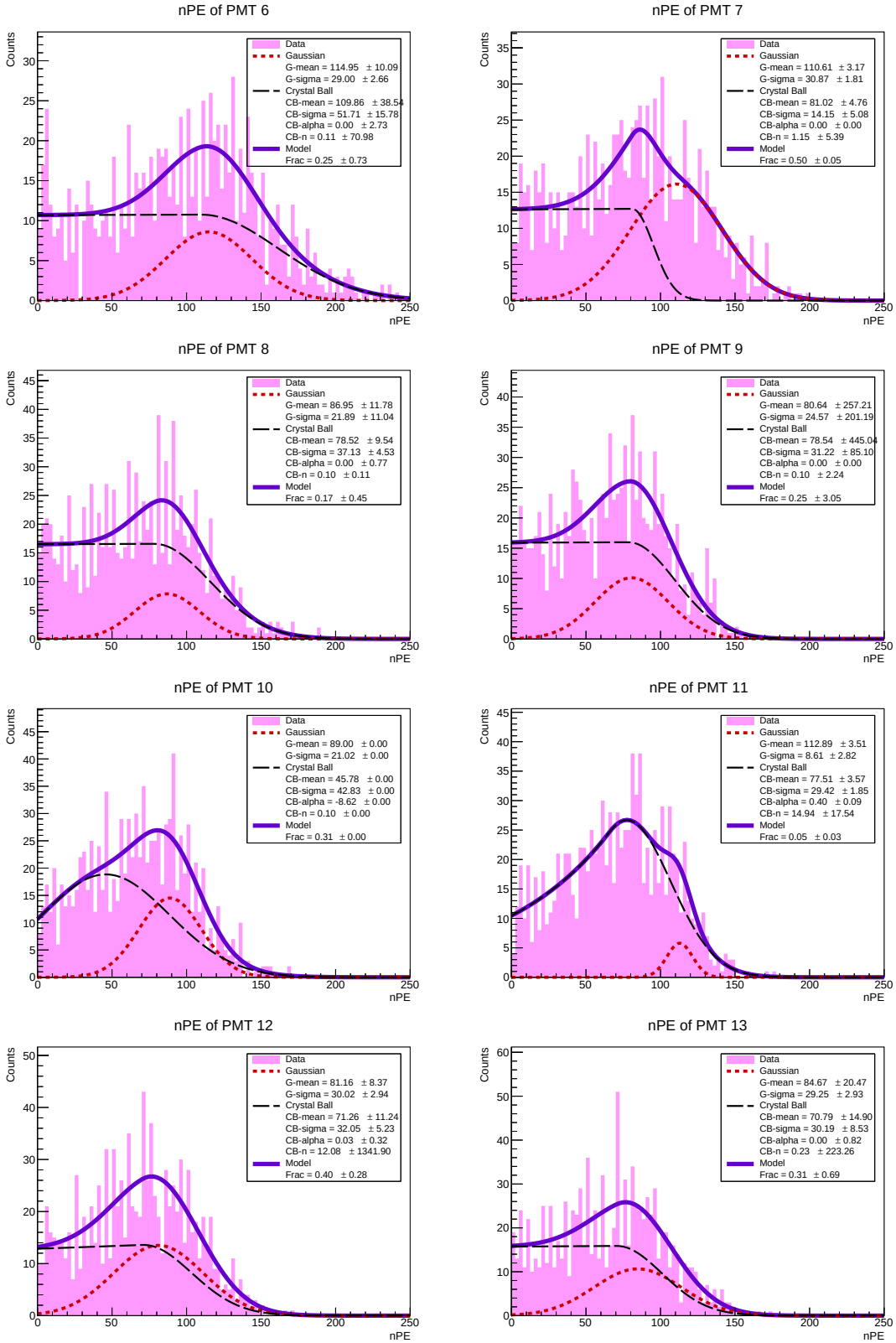

Figure 5.50: Number of photoelectrons recorded by PMTs 6 to 13, for configuration gamma_1000_e10GeV_theta80deg_phi180deg_alpha0deg_r180cm_h50cm.root.

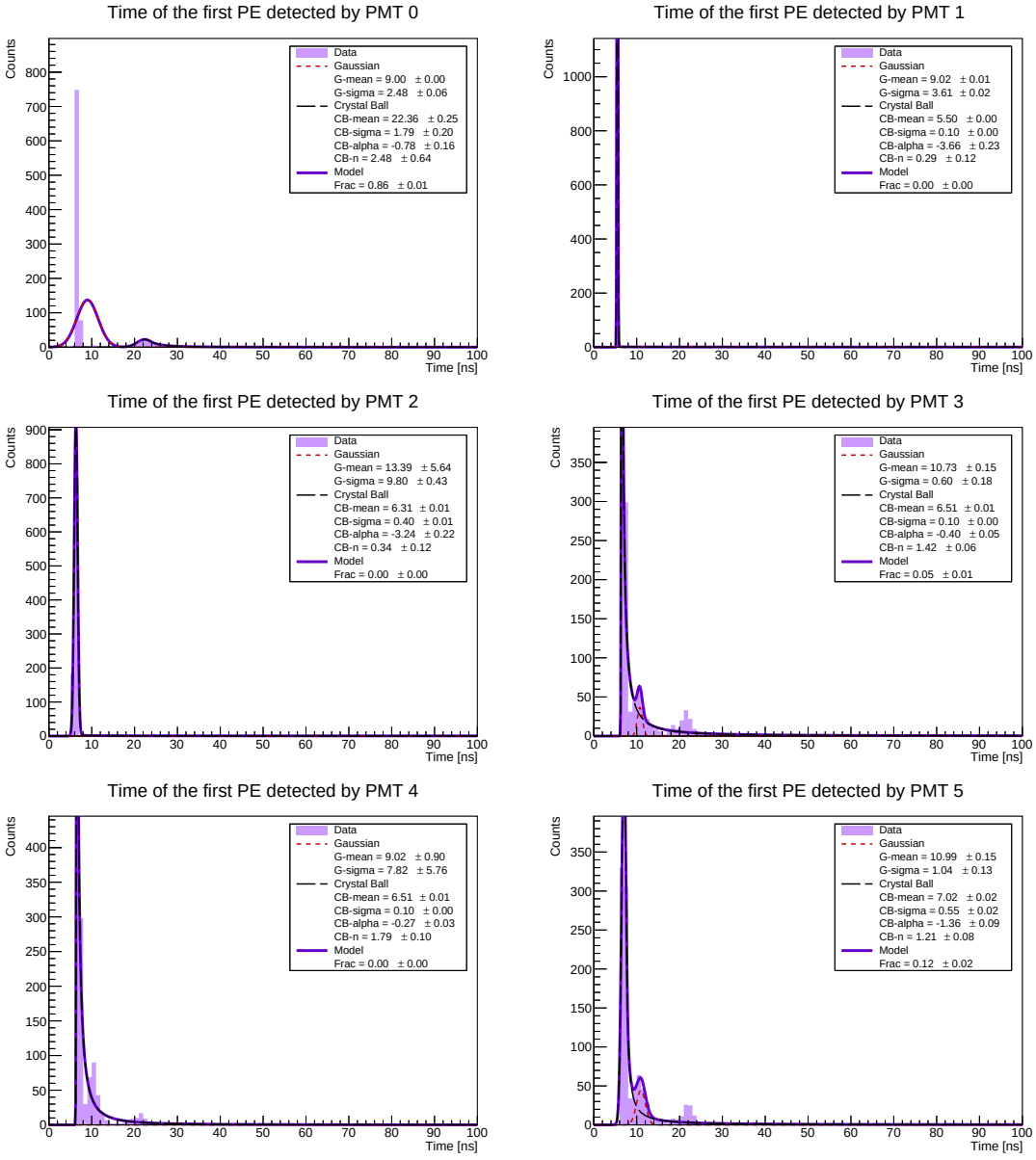

Figure 5.51: First PE arrival time (fTime) at PMTs 0 to 5, for configuration gamma_1000_e10GeV_theta80deg_phi180deg_alpha0deg_r180cm_h50cm.root.

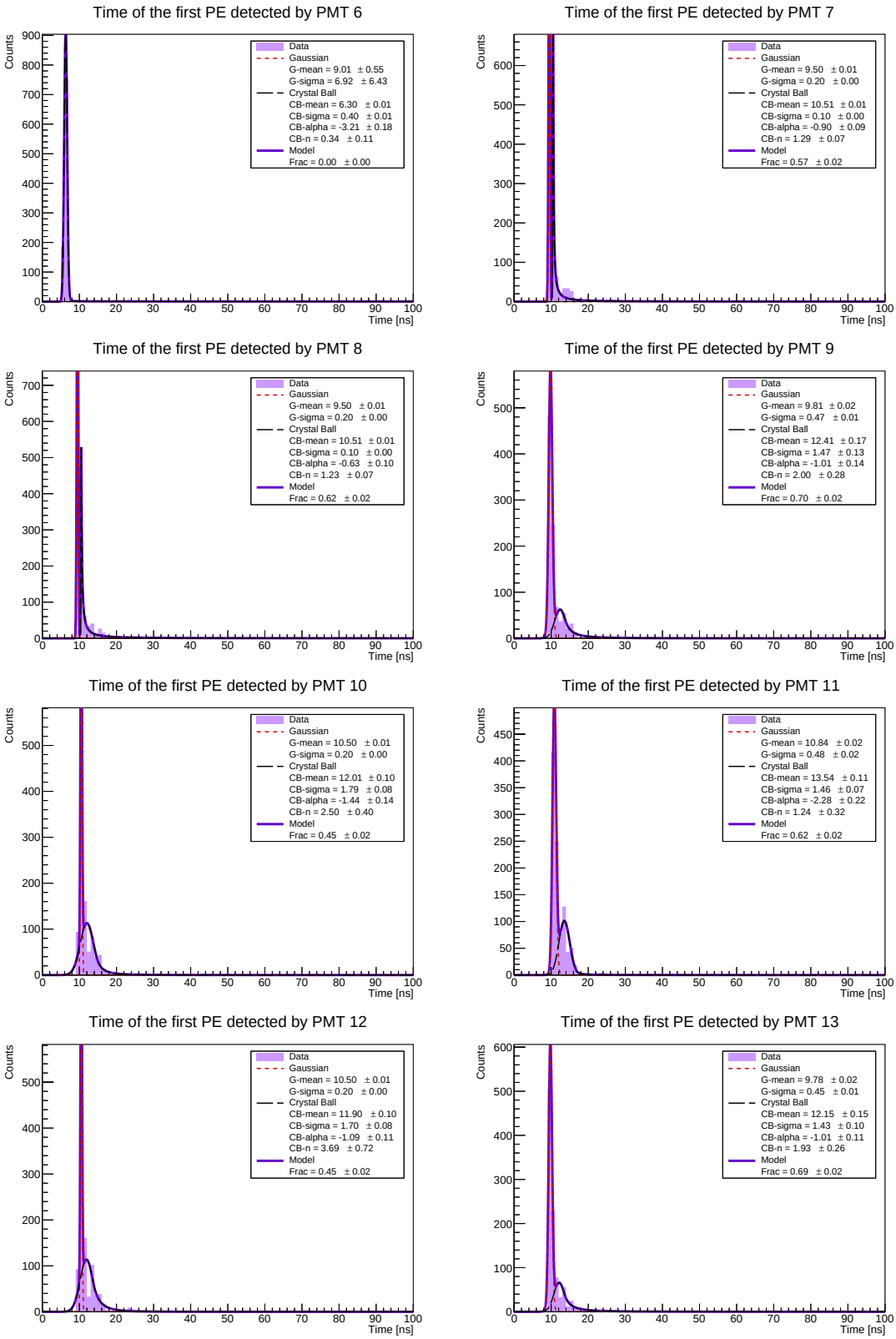

Figure 5.52: First PE arrival time (fTime) at PMTs 6 to 13, for configuration gamma_1000_e10GeV_theta80deg_phi180deg_alpha0deg_r180cm_h50cm.root.

gamma_1000_e3GeV_theta40deg_phi40deg_alpha0deg_r54cm_h178cm.root

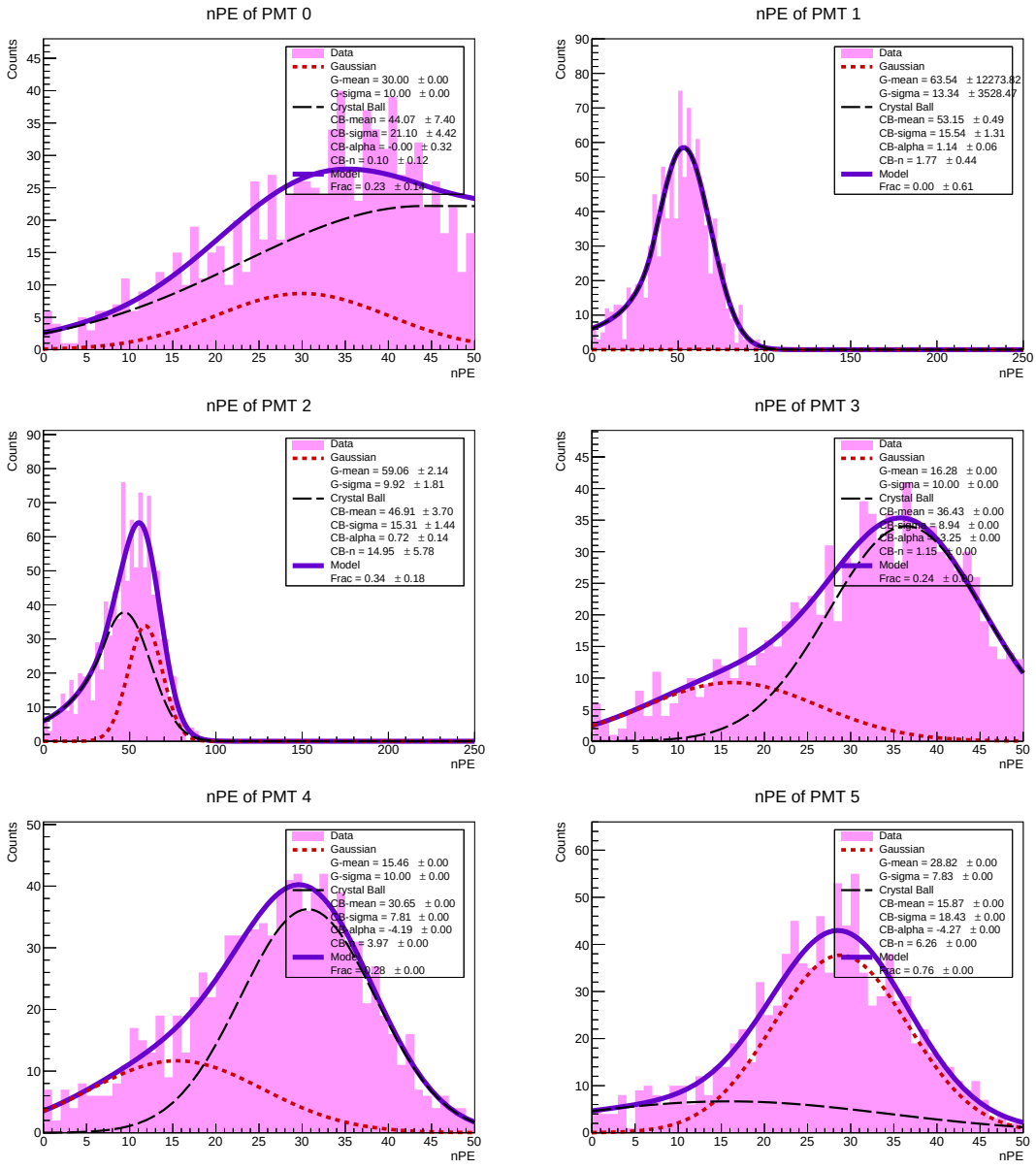

Figure 5.53: Number of photoelectrons recorded by PMTs 0 to 5, for configuration gamma_1000_e3GeV_theta40deg_phi40deg_alpha0deg_r54cm_h178cm.root.

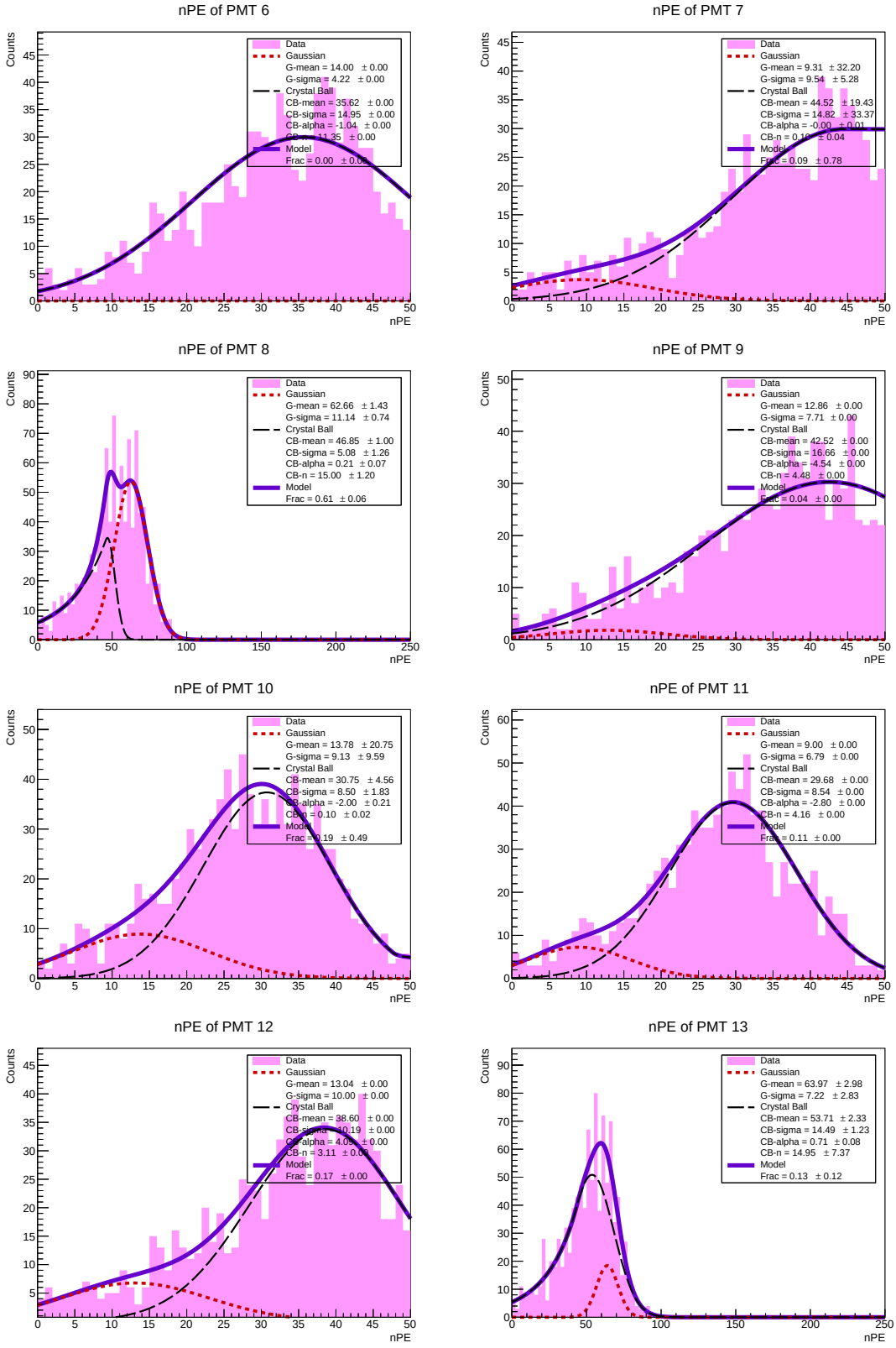

Figure 5.54: Number of photoelectrons recorded by PMTs 6 to 13, for configuration gamma_1000_e3GeV_theta40deg_phi40deg_alpha0deg_r54cm_h178cm.root.

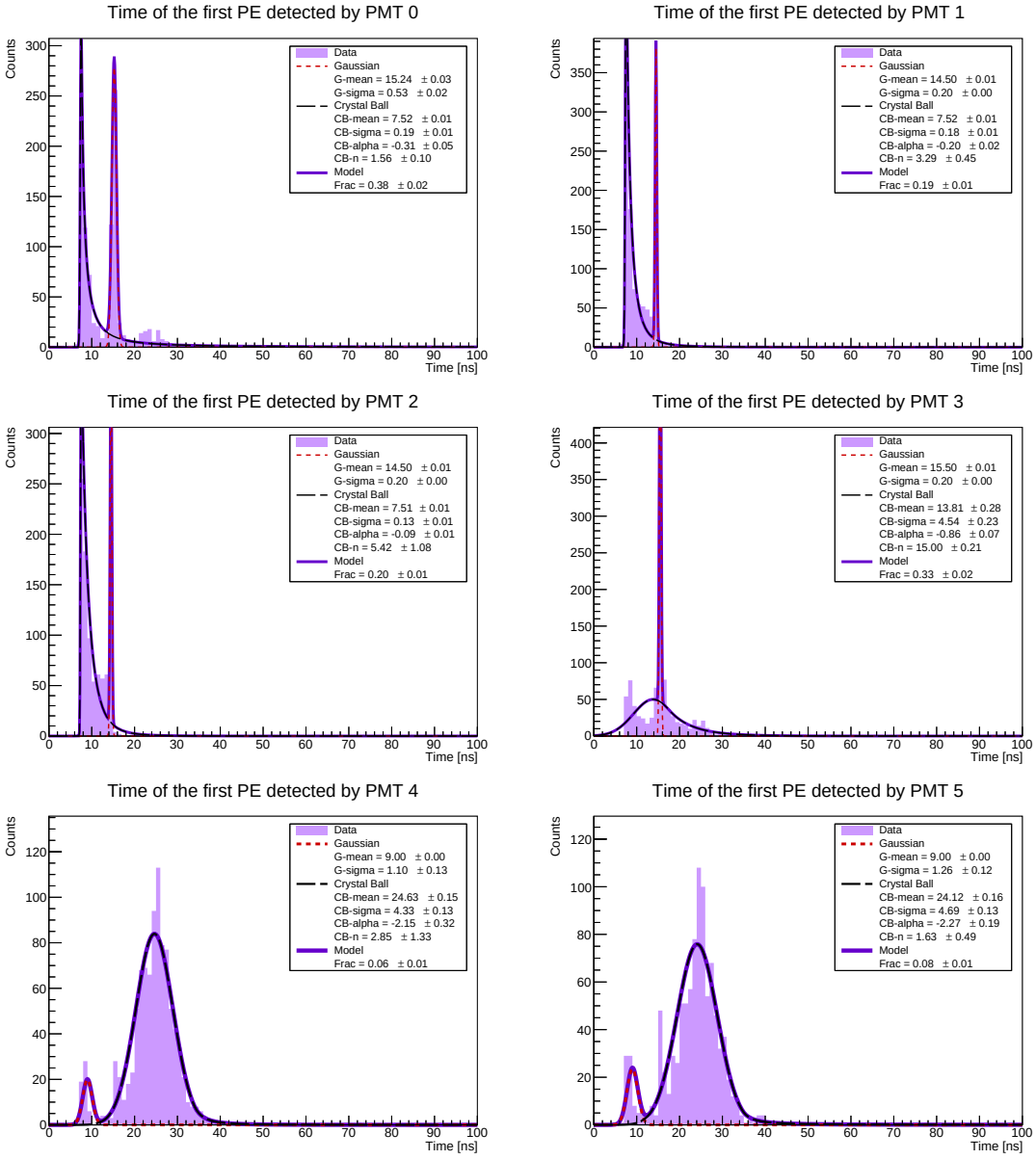

Figure 5.55: First PE arrival time (fTime) at PMTs 0 to 5, for configuration gamma_1000_e3GeV_theta40deg_phi40deg_alpha0deg_r54cm_h178cm.root.

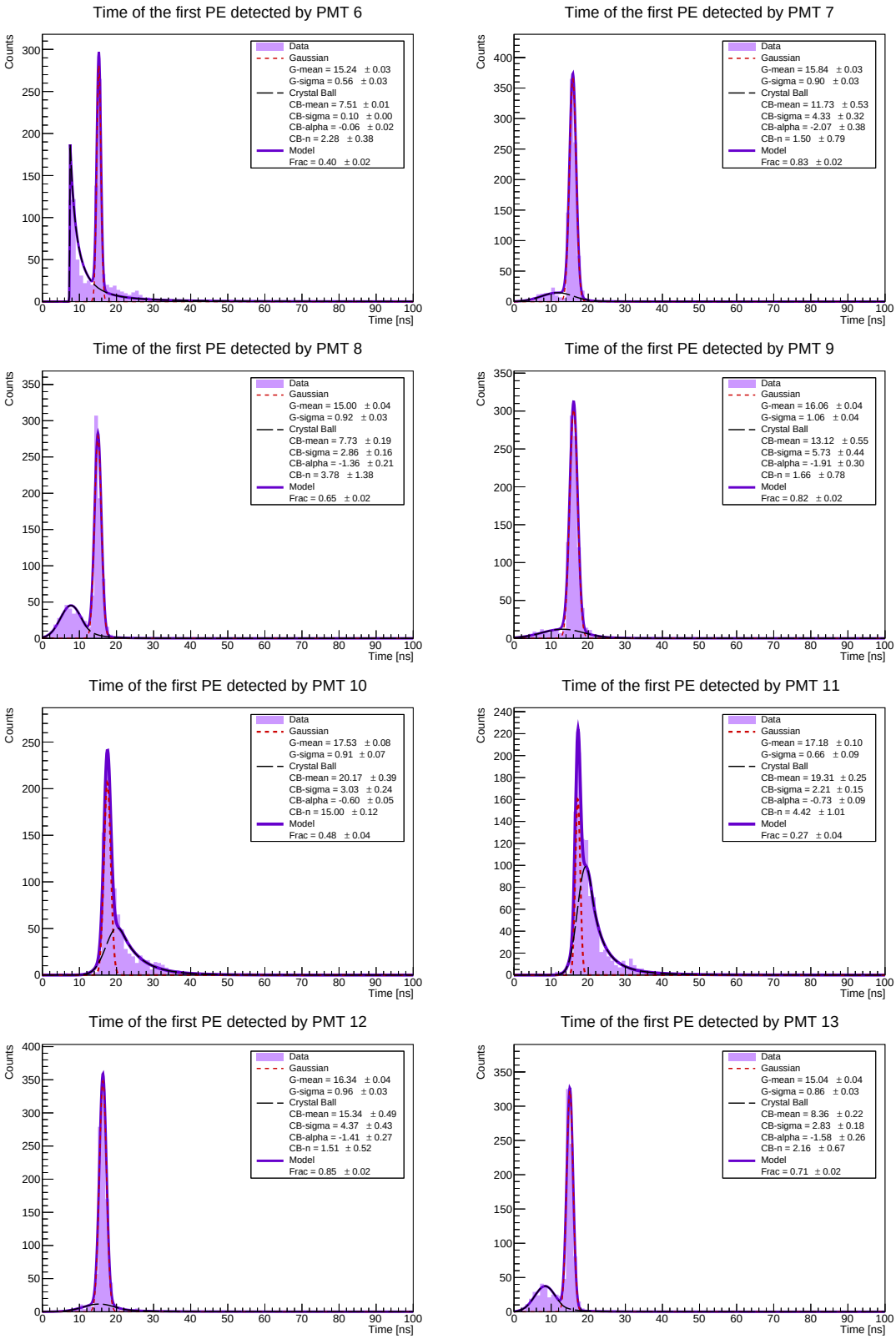

Figure 5.56: First PE arrival time (fTime) at PMTs 6 to 13, for configuration gamma_1000_e3GeV_theta40deg_phi40deg_alpha0deg_r54cm_h178cm.root.

gamma_1000_e7GeV_theta40deg_phi0deg_alpha30deg_r144cm_h178cm.root

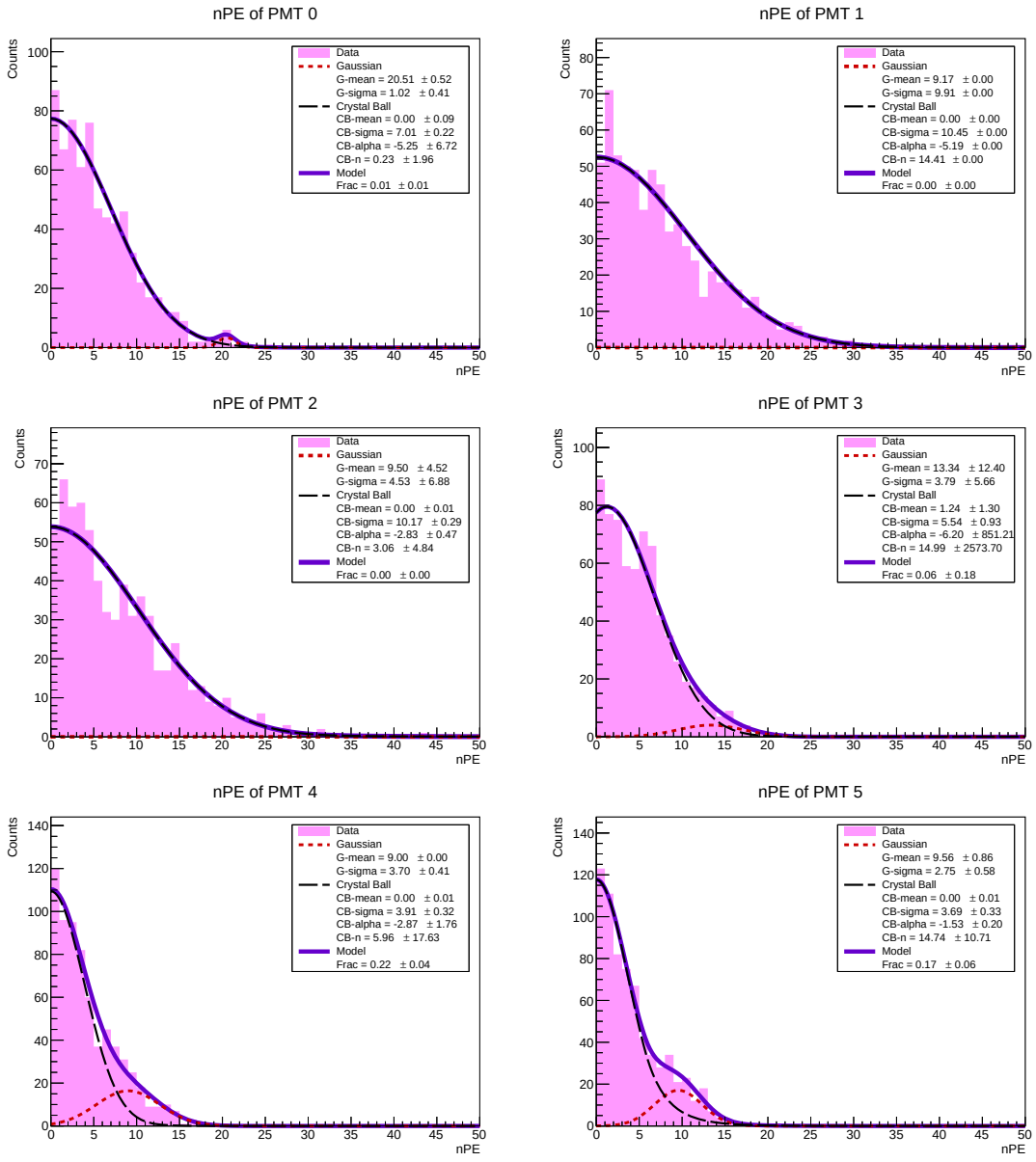

Figure 5.57: Number of photoelectrons recorded by PMTs 0 to 5, for configuration gamma_1000_e7GeV_theta40deg_phi0deg_alpha30deg_r144cm_h178cm.root.

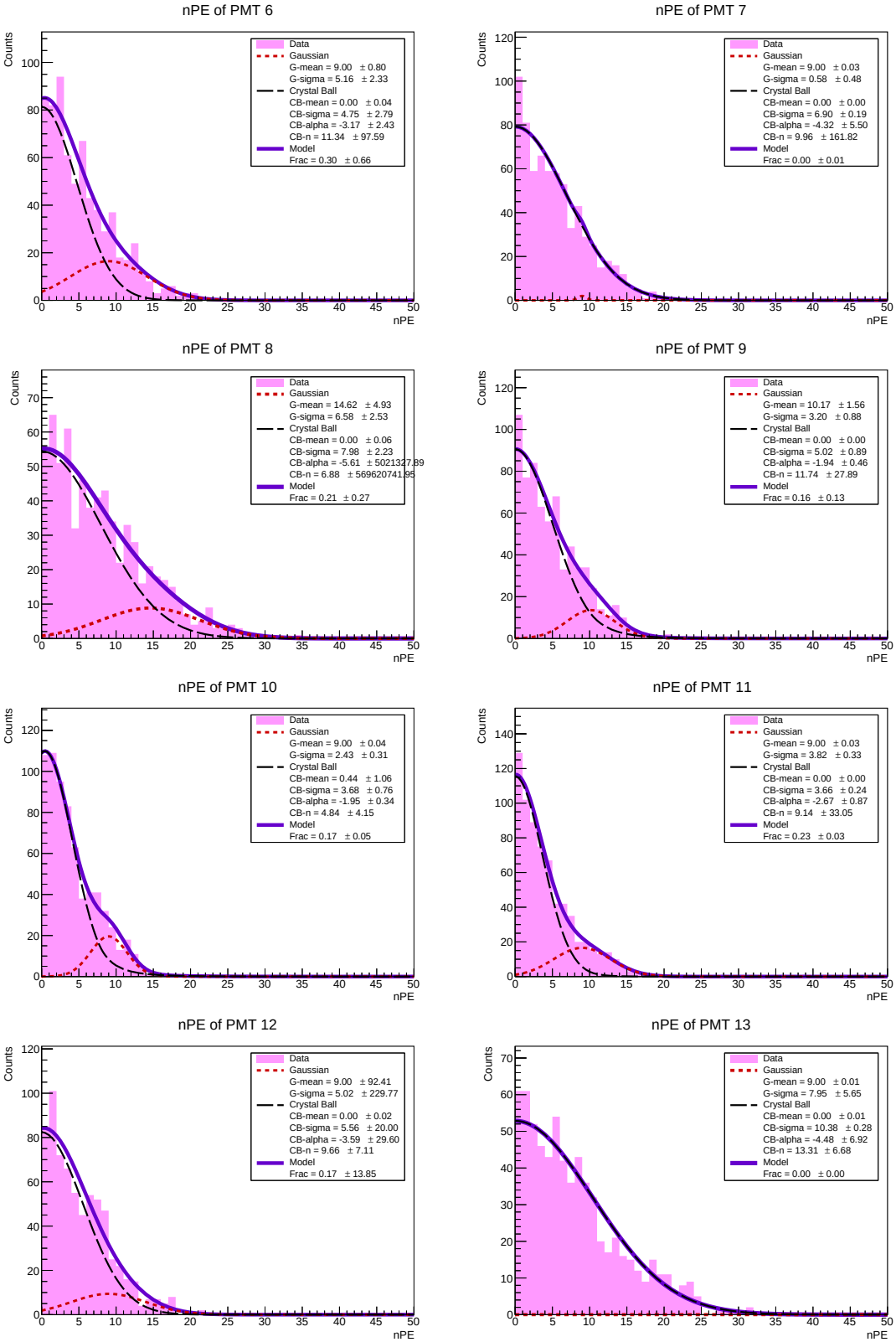

Figure 5.58: Number of photoelectrons recorded by PMTs 6 to 13, for configuration gamma_1000_e7GeV_theta40deg_phi0deg_alpha30deg_r144cm_h178cm.root.

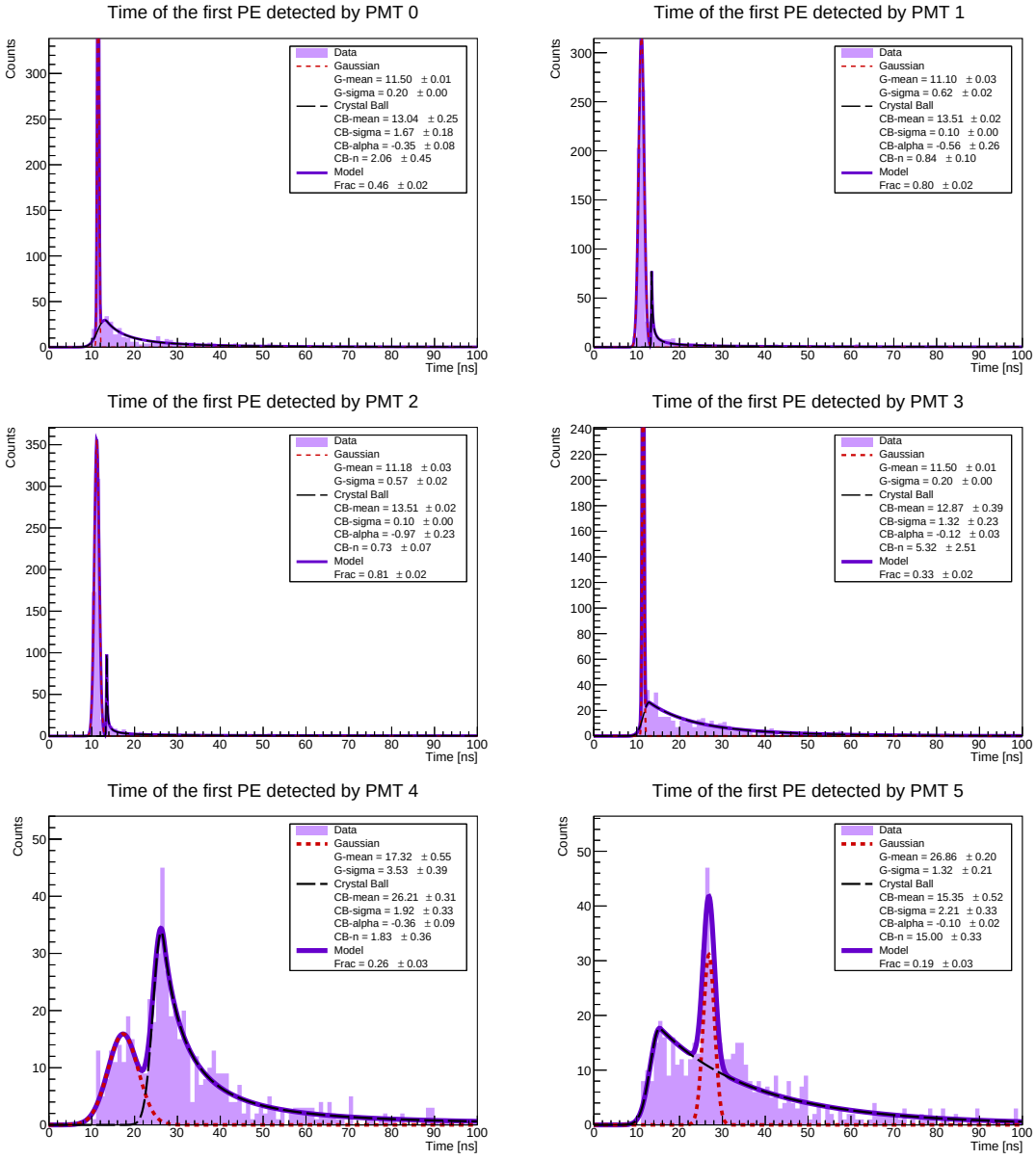

Figure 5.59: First PE arrival time (fTime) at PMTs 0 to 5, for configuration gamma_1000_e7GeV_theta40deg_phi0deg_alpha30deg_r144cm_h178cm.root.

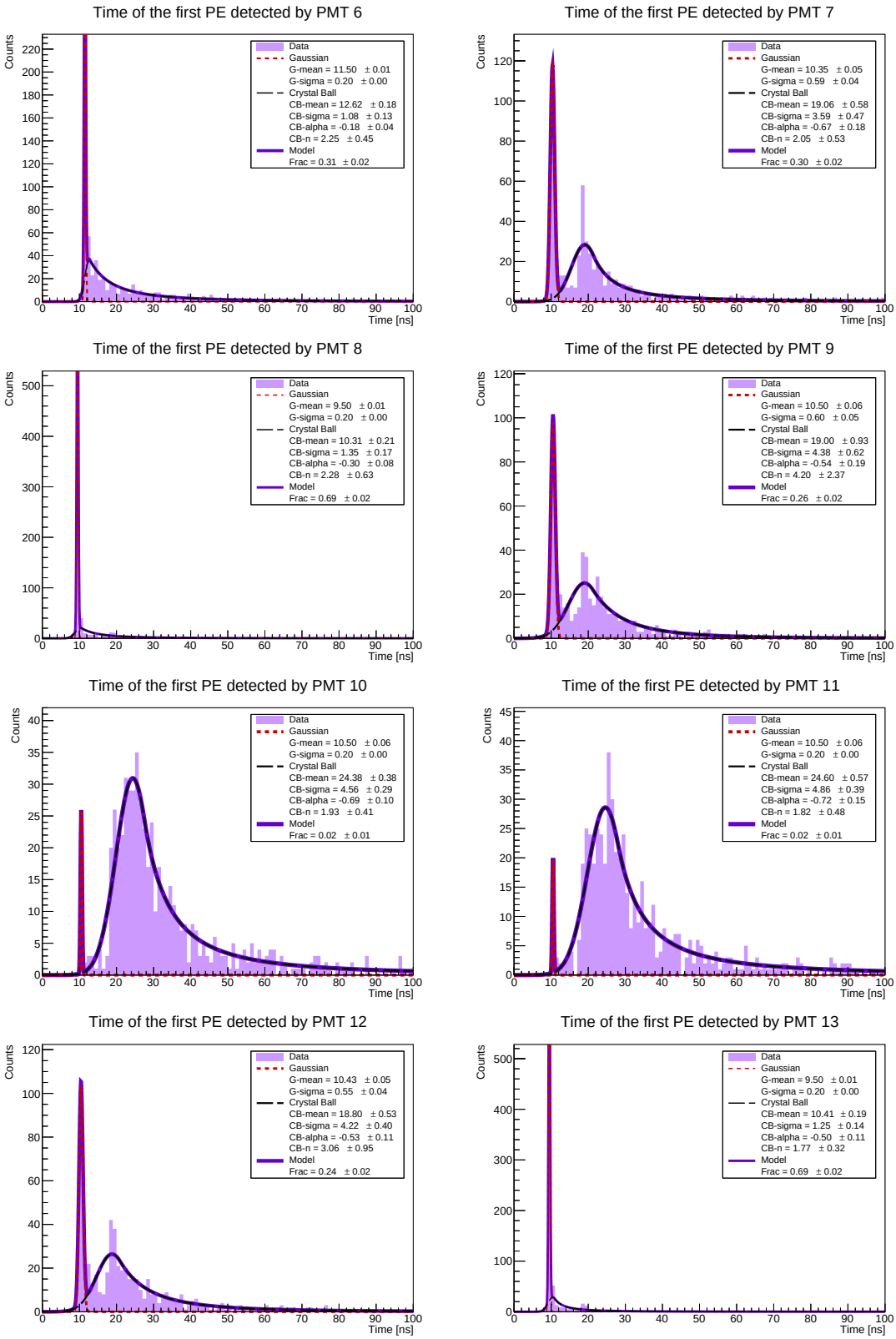

Figure 5.60: First PE arrival time (fTime) at PMTs 6 to 13, for configuration gamma_1000_e7GeV_theta40deg_phi0deg_alpha30deg_r144cm_h178cm.root.

mu-_1000_e0.3GeV_theta60deg_phi150deg_alpha30deg_r180cm_h178cm.root

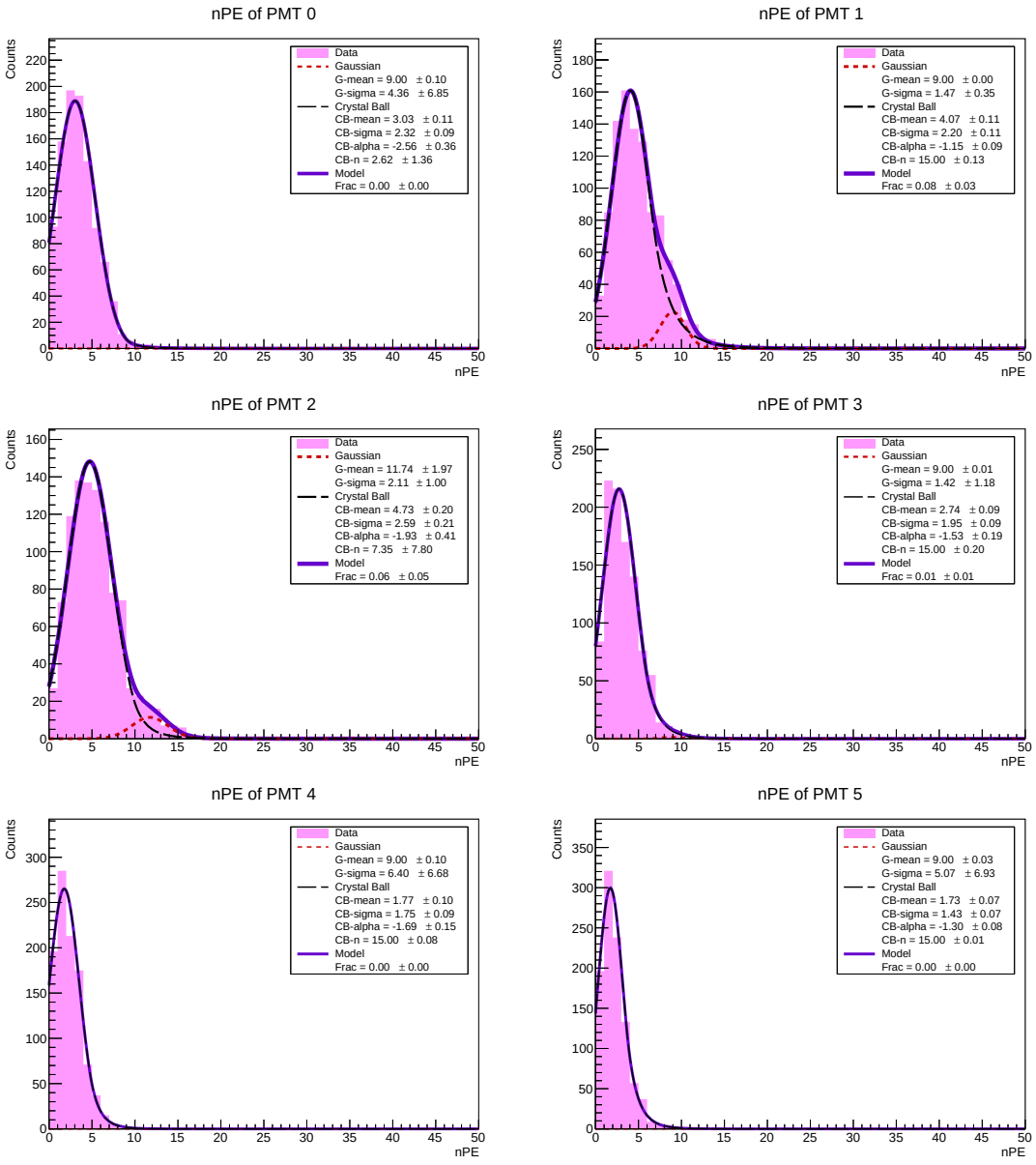

Figure 5.61: Number of photoelectrons recorded by PMTs 0 to 5, for configuration mu-_1000_e0.3GeV_theta60deg_phi150deg_alpha30deg_r180cm_h178cm.root.

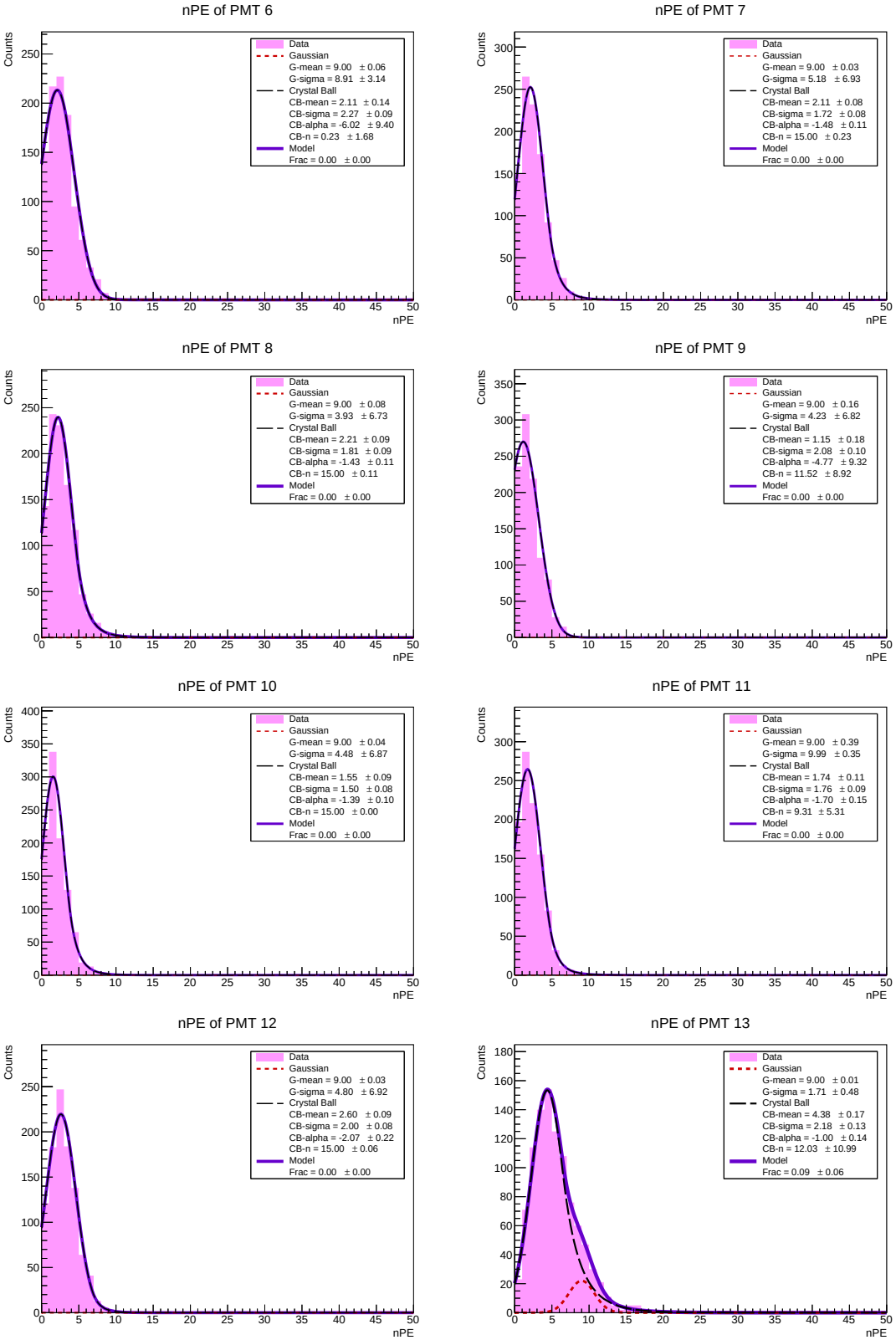

Figure 5.62: Number of photoelectrons recorded by PMTs 6 to 13, for configuration mu-_1000_e0.3GeV_theta60deg_phi150deg_alpha30deg_r180cm_h178cm.root.

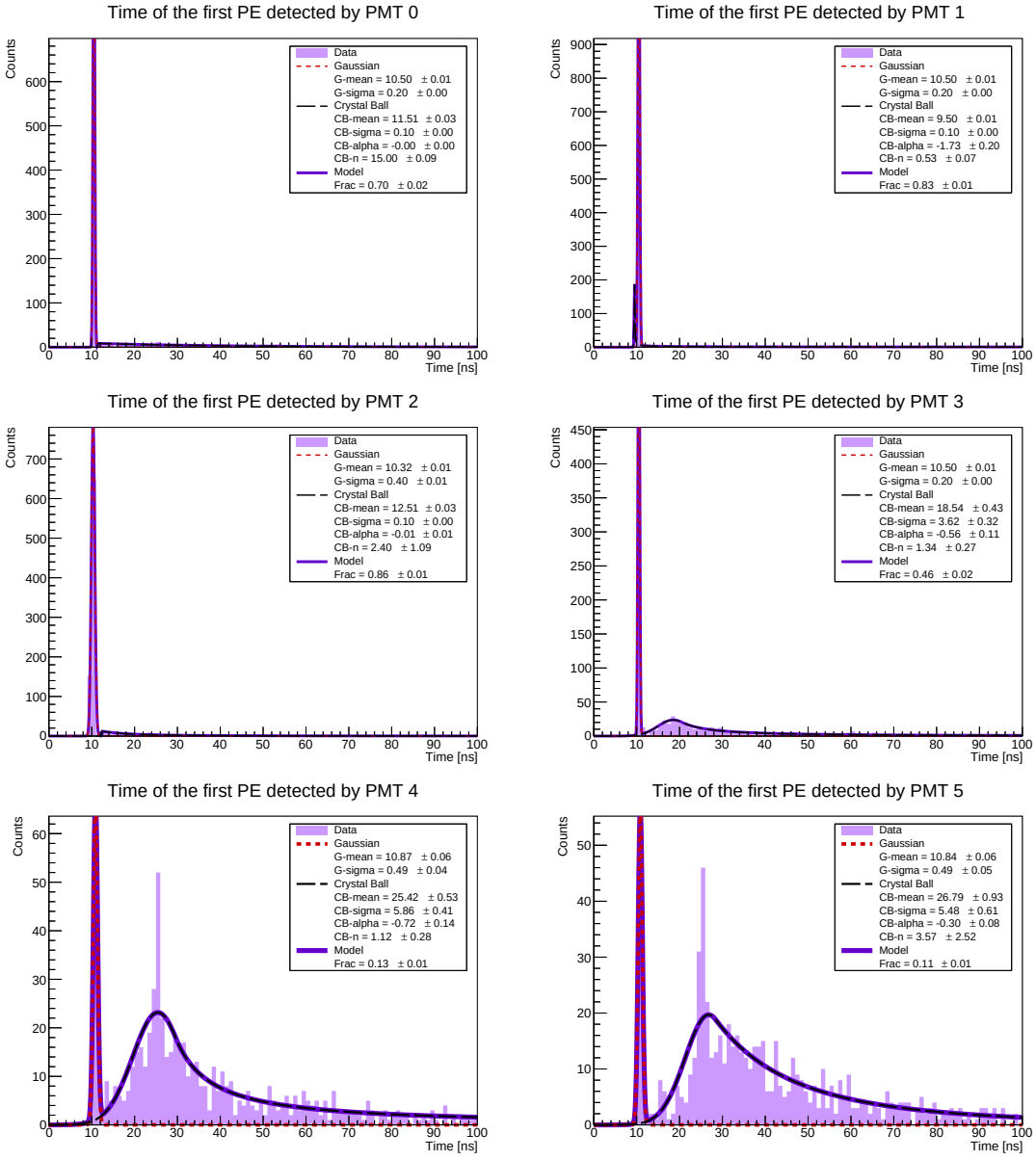

Figure 5.63: First PE arrival time (fTime) at PMTs 0 to 5, for configuration mu-_1000_e0.3GeV_theta60deg_phi150deg_alpha30deg_r180cm_h178cm.root.

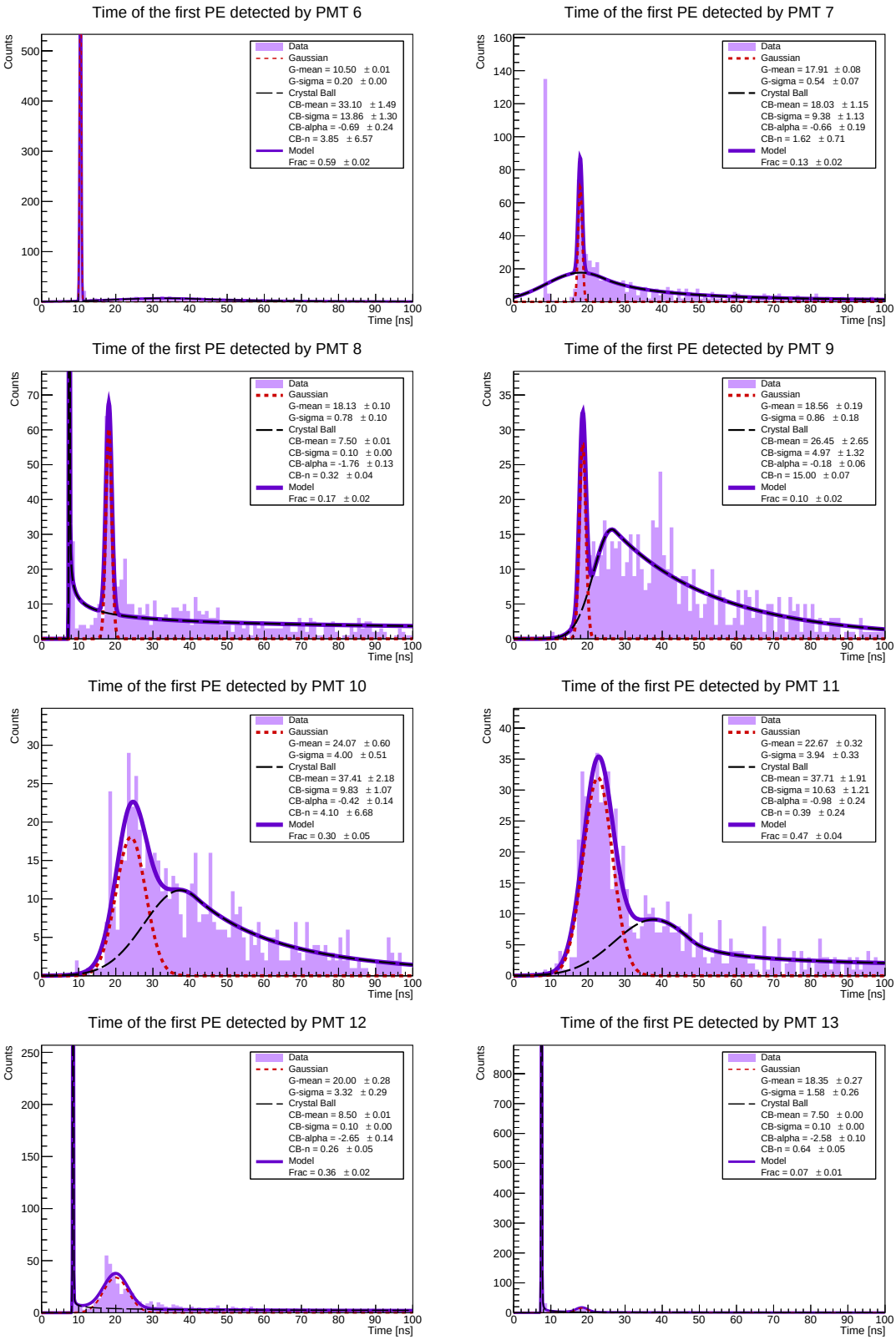

Figure 5.64: First PE arrival time (fTime) at PMTs 6 to 13, for configuration mu-_1000_e0.3GeV_theta60deg_phi150deg_alpha30deg_r180cm_h178cm.root.

mu-_1000_e100GeV_theta0deg_phi0deg_alpha0deg_r72cm_h178cm.root

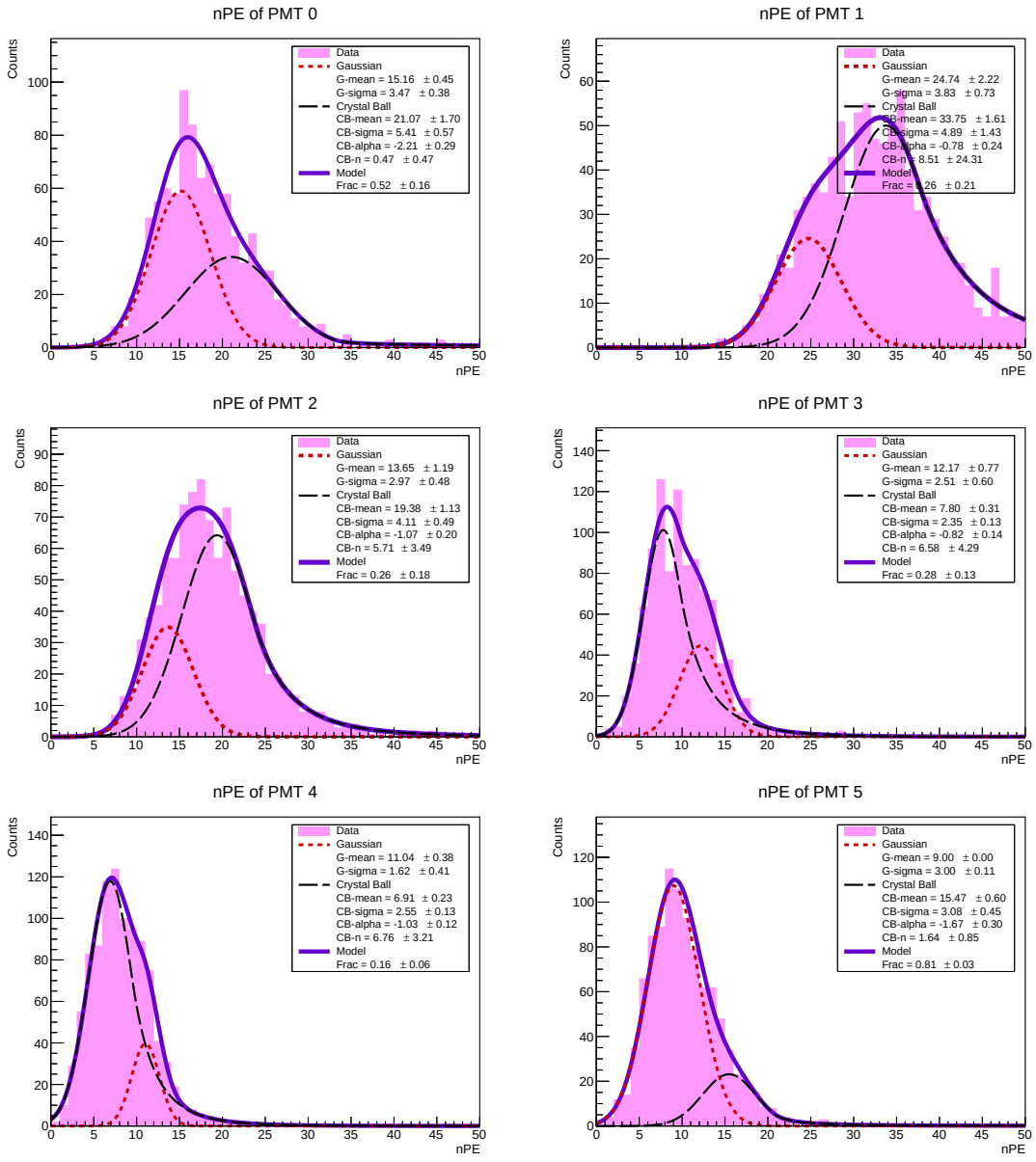

Figure 5.65: Number of photoelectrons recorded by PMTs 0 to 5, for configuration mu-_1000_e100GeV_theta0deg_phi0deg_alpha0deg_r72cm_h178cm.root.

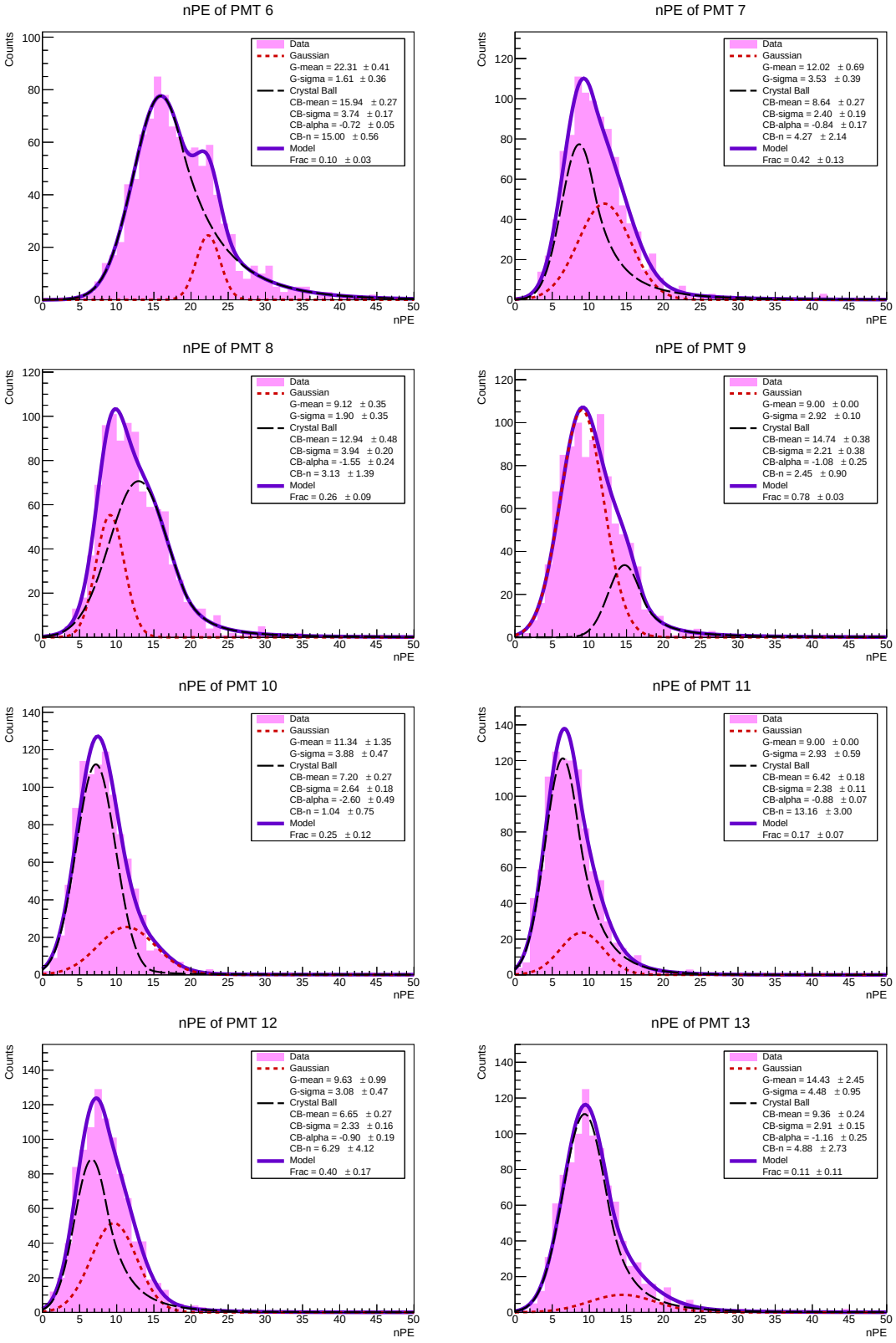

Figure 5.66: Number of photoelectrons recorded by PMTs 6 to 13, for configuration mu-_1000_e100GeV_theta0deg_phi0deg_alpha0deg_r72cm_h178cm.root.

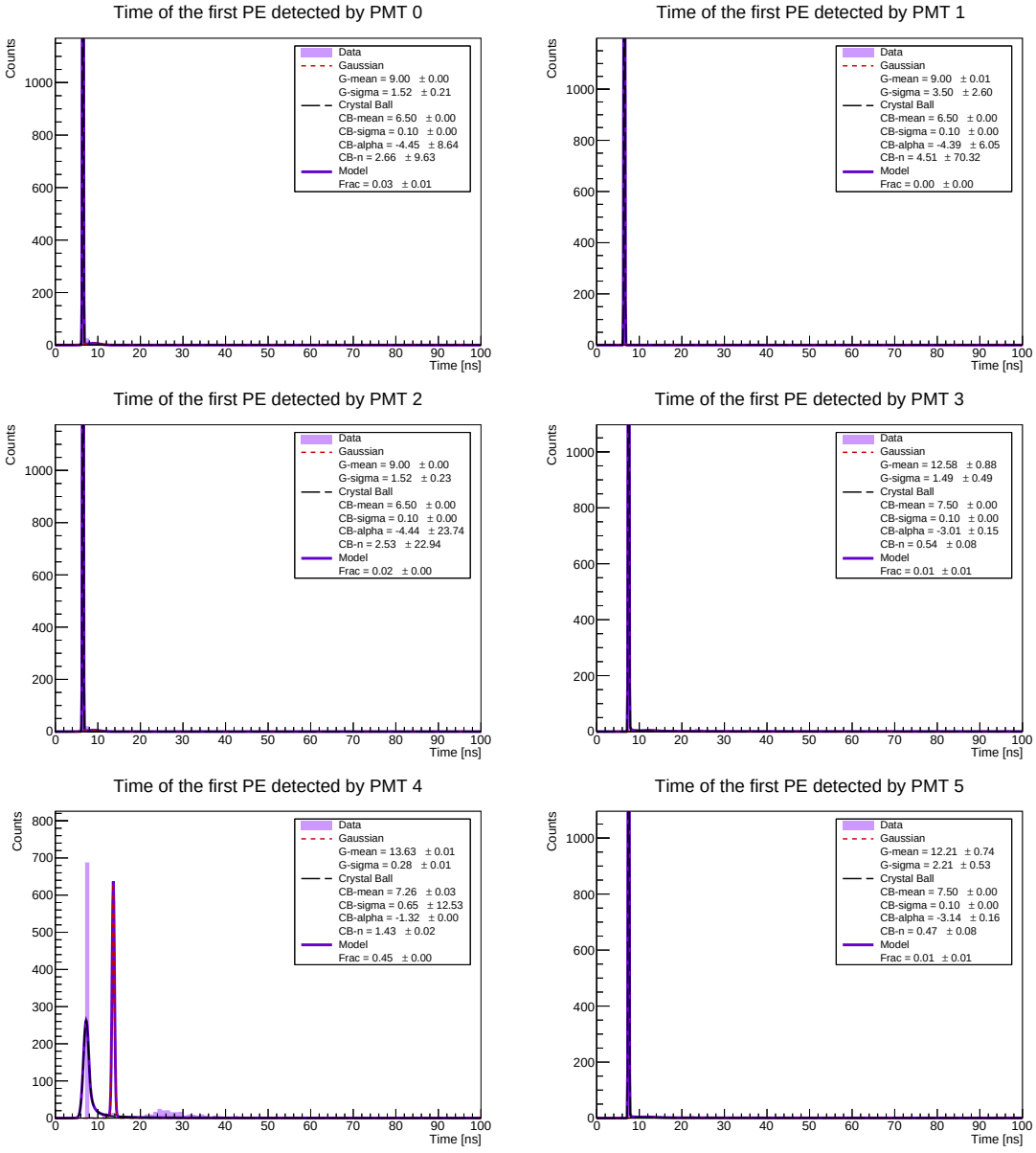

Figure 5.67: First PE arrival time (fTime) at PMTs 0 to 5, for configuration mu-_1000_e100GeV_theta0deg_phi0deg_alpha0deg_r72cm_h178cm.root.

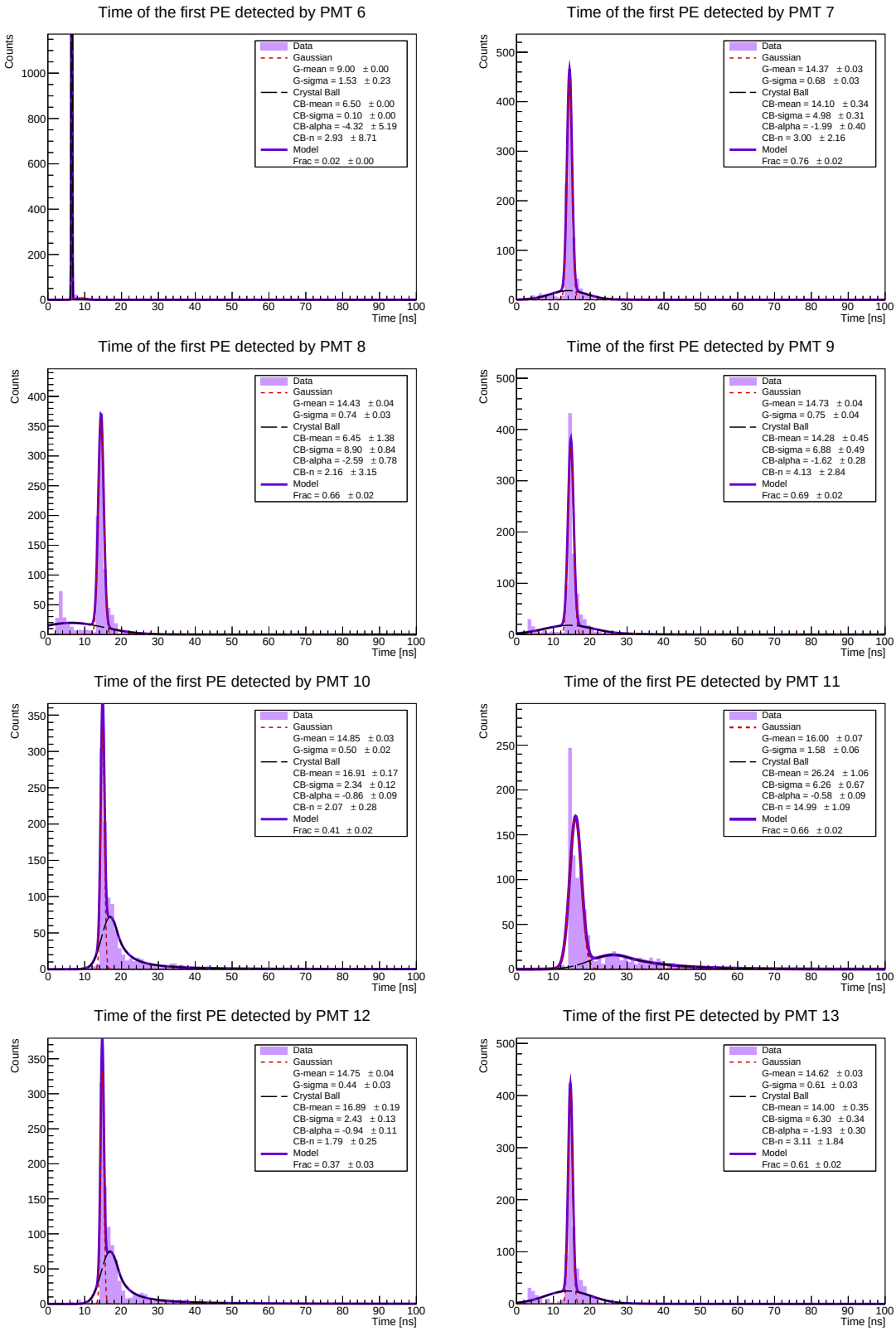

Figure 5.68: First PE arrival time (fTime) at PMTs 6 to 13, for configuration mu-_1000_e100GeV_theta0deg_phi0deg_alpha0deg_r72cm_h178cm.root.

mu-_1000_e10GeV_theta20deg_phi180deg_alpha30deg_r54cm_h178cm.root

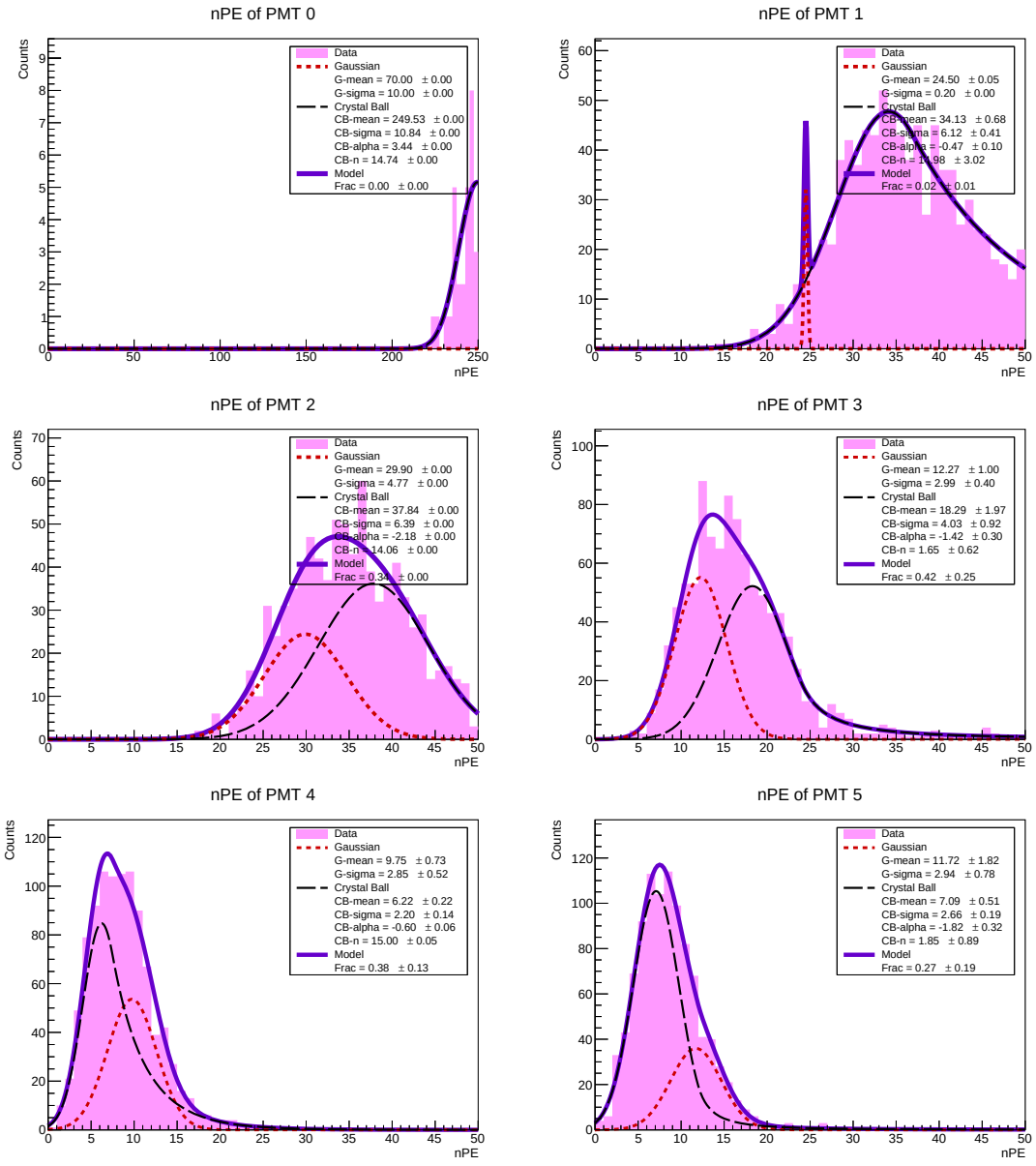

Figure 5.69: Number of photoelectrons recorded by PMTs 0 to 5, for configuration mu-_1000_e10GeV_theta20deg_phi180deg_alpha30deg_r54cm_h178cm.root.

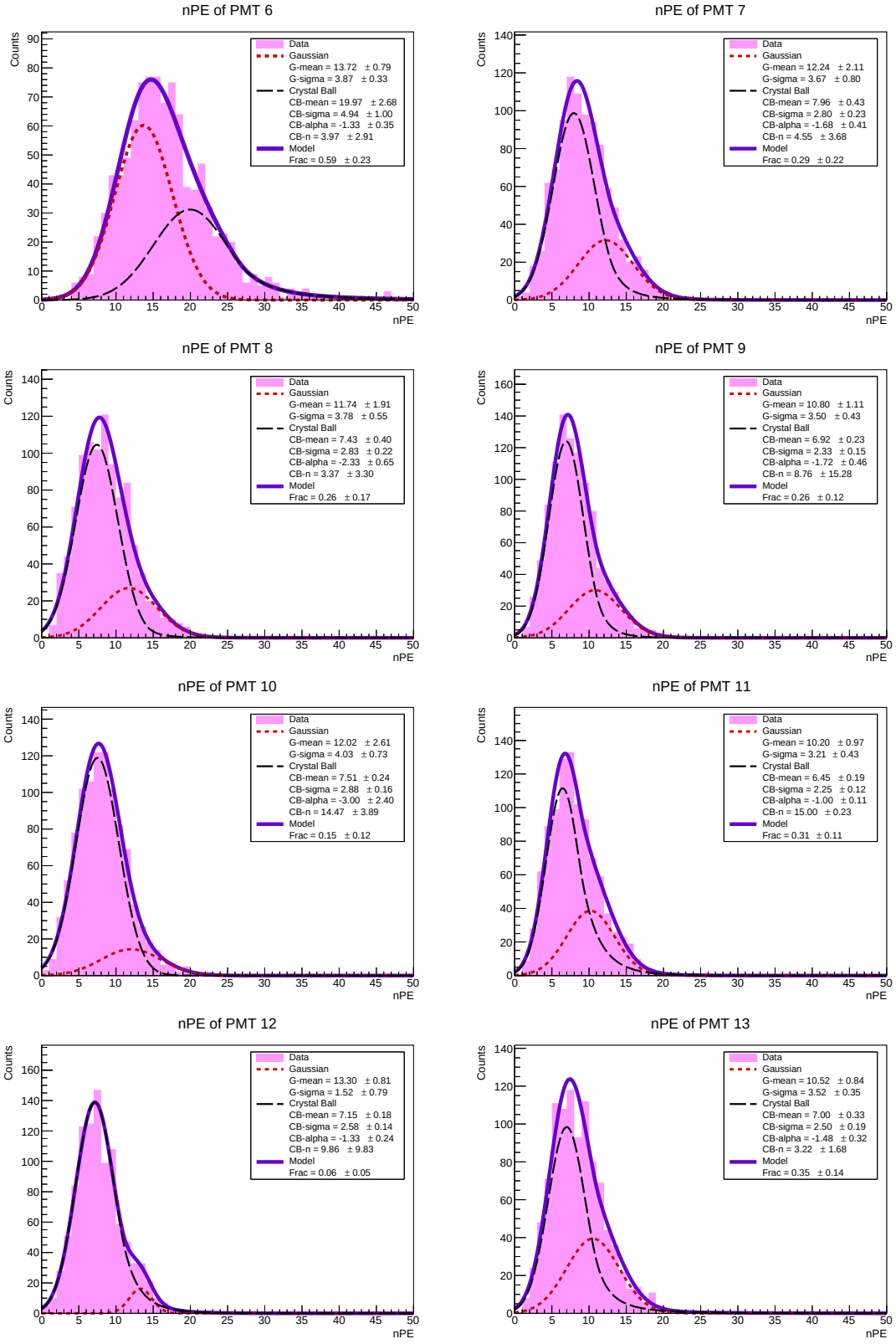

Figure 5.70: Number of photoelectrons recorded by PMTs 6 to 13, for configuration mu-_1000_e10GeV_theta20deg_phi180deg_alpha30deg_r54cm_h178cm.root.

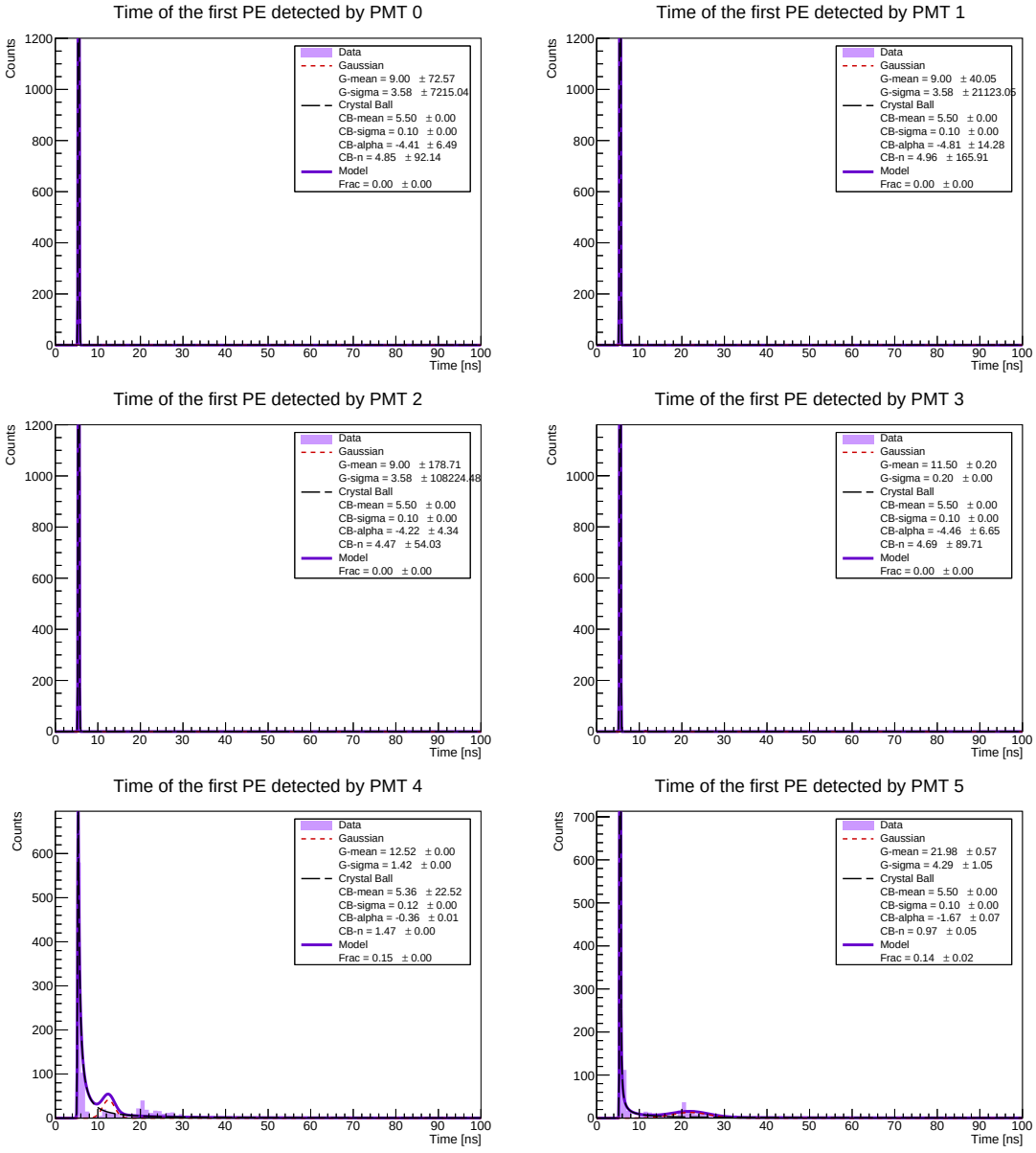

Figure 5.71: First PE arrival time (fTime) at PMTs 0 to 5, for configuration mu-_1000_e10GeV_theta20deg_phi180deg_alpha30deg_r54cm_h178cm.root.

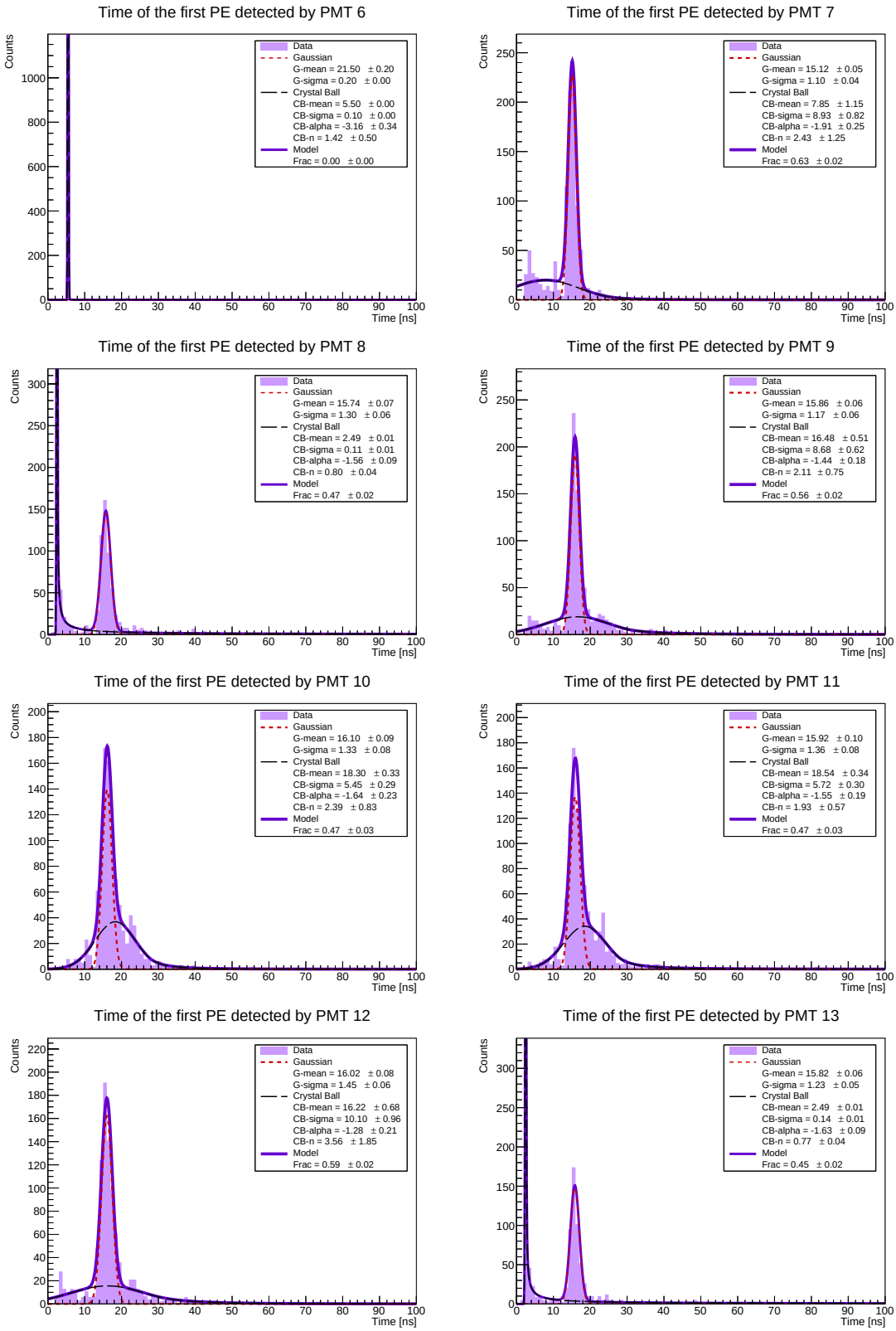

Figure 5.72: First PE arrival time (fTime) at PMTs 6 to 13, for configuration mu-_1000_e10GeV_theta20deg_phi180deg_alpha30deg_r54cm_h178cm.root.

mu-_1000_e1GeV_theta20deg_phi120deg_alpha0deg_r180cm_h178cm.root

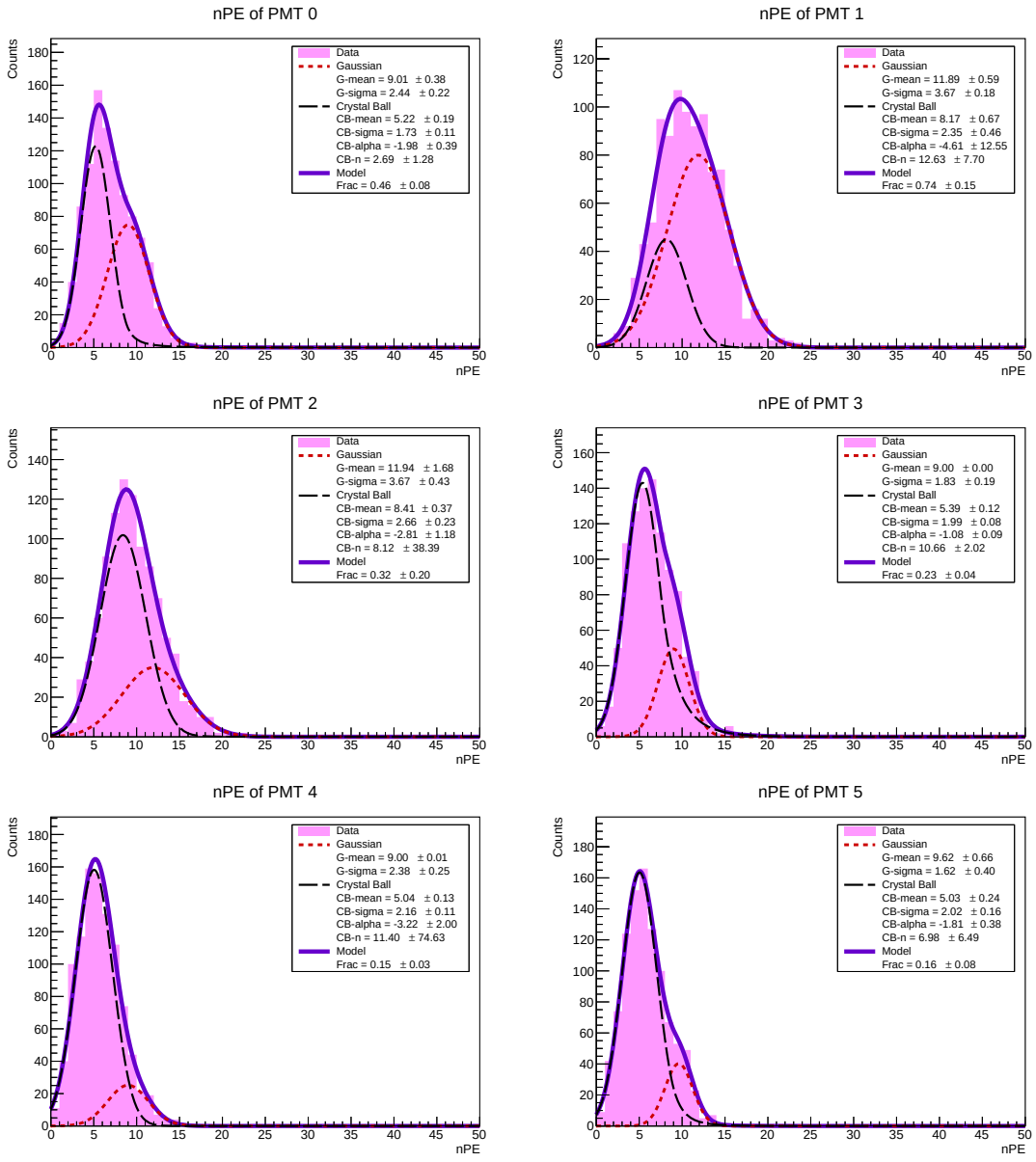

Figure 5.73: Number of photoelectrons recorded by PMTs 0 to 5, for configuration mu-_1000_e1GeV_theta20deg_phi120deg_alpha0deg_r180cm_h178cm.root.

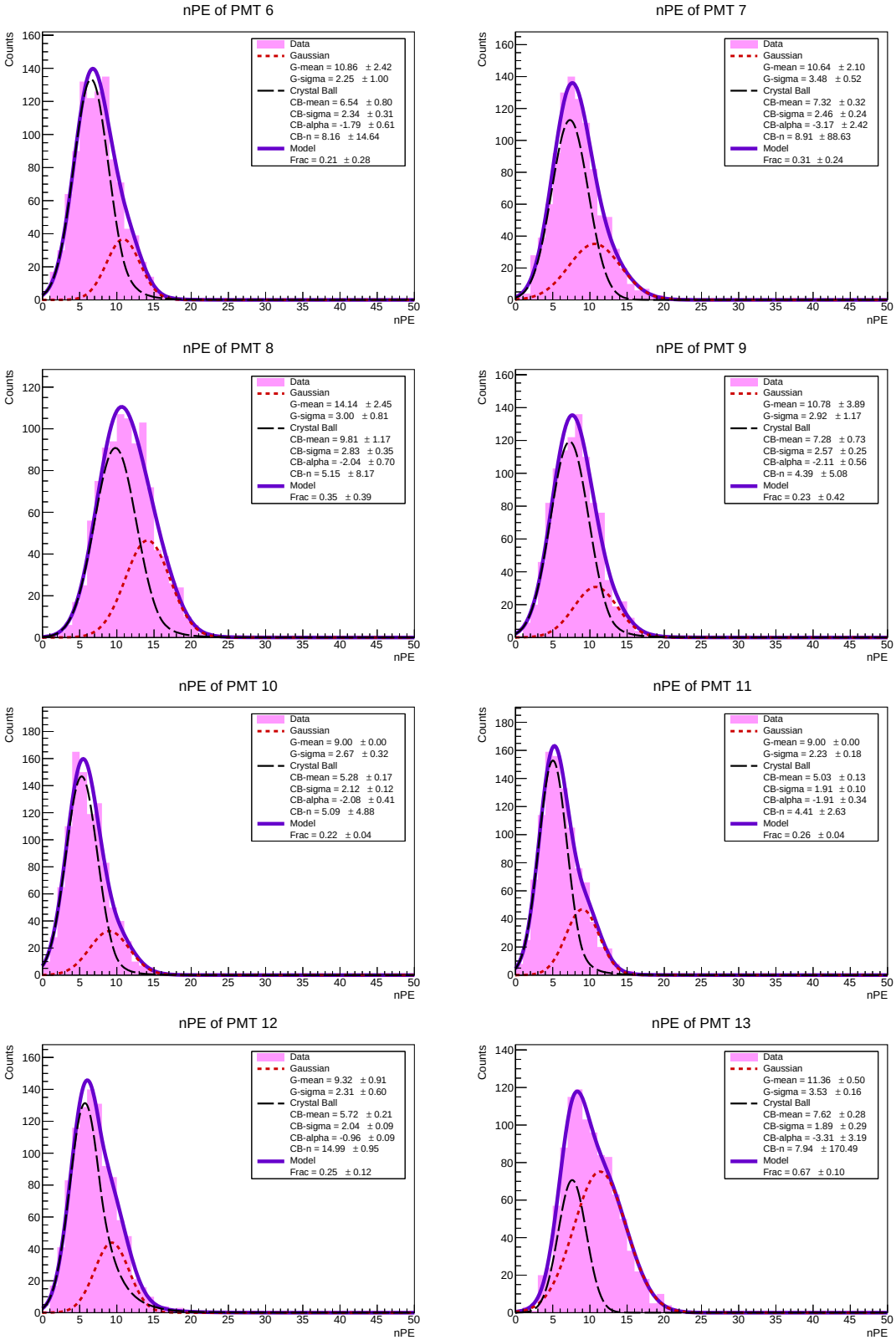

Figure 5.74: Number of photoelectrons recorded by PMTs 6 to 13, for configuration mu-_1000_e1GeV_theta20deg_phi120deg_alpha0deg_r180cm_h178cm.root.

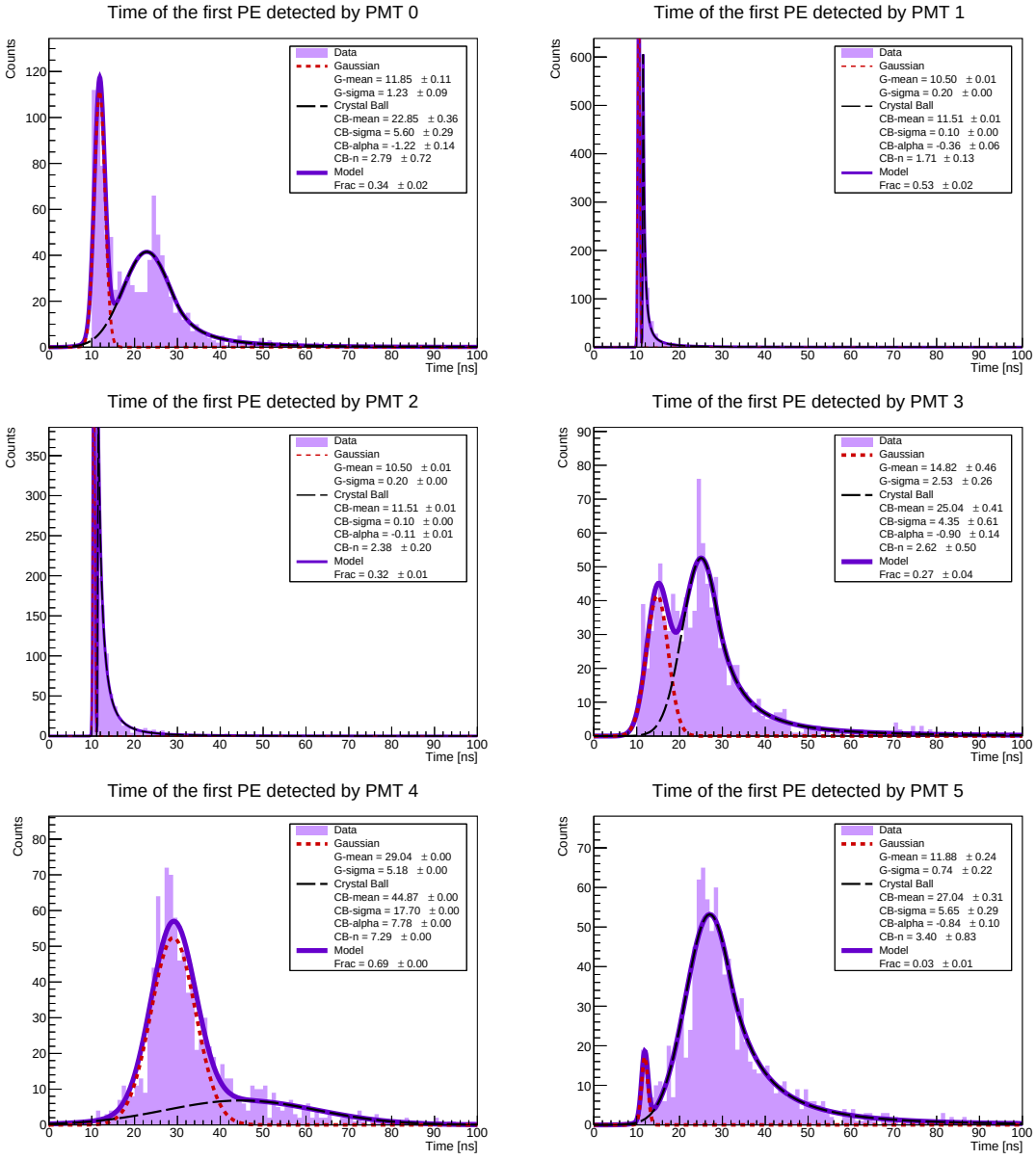

Figure 5.75: First PE arrival time (fTime) at PMTs 0 to 5, for configuration mu-_1000_e1GeV_theta20deg_phi120deg_alpha0deg_r180cm_h178cm.root.

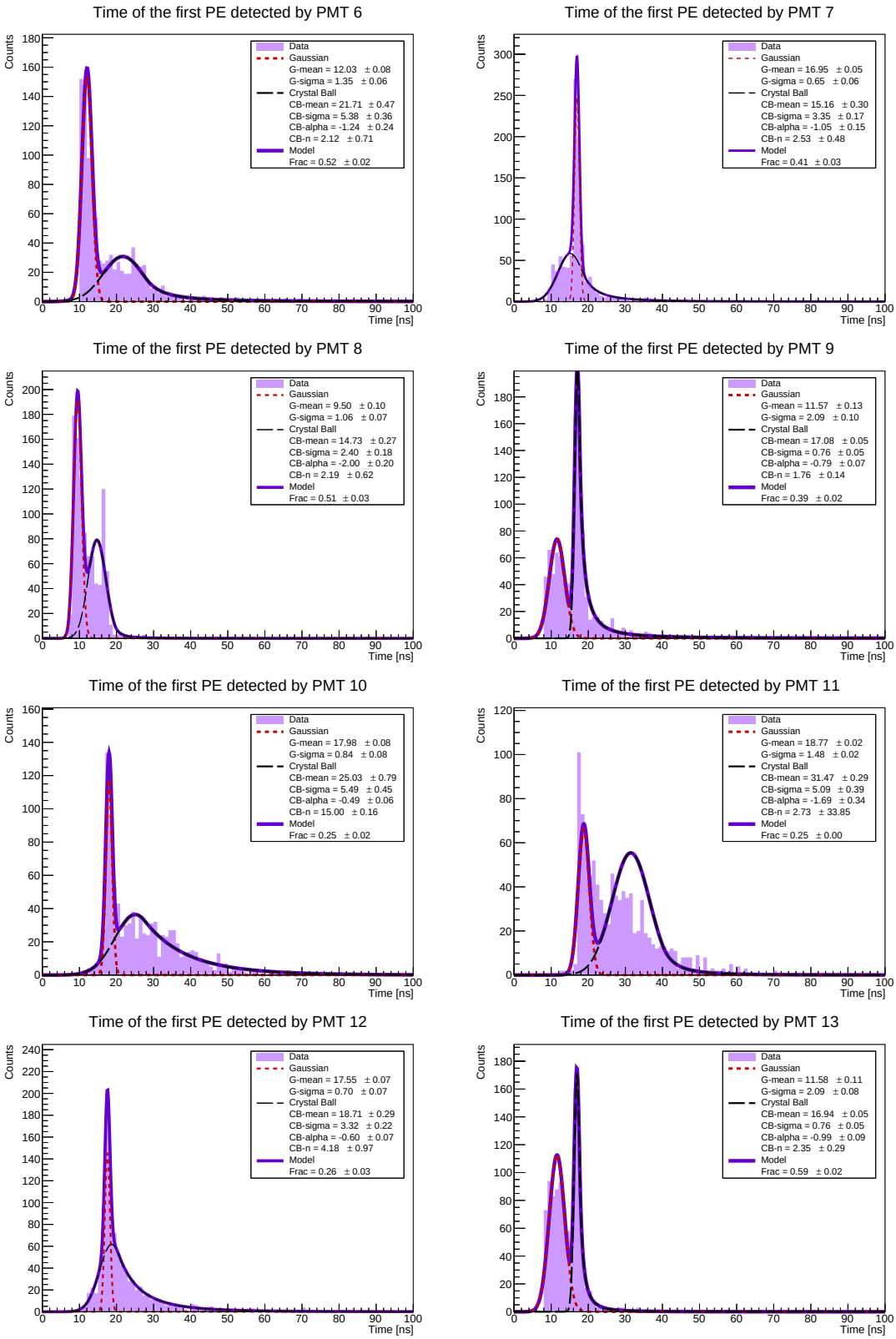

Figure 5.76: First PE arrival time (fTime) at PMTs 6 to 13, for configuration mu-_1000_e1GeV_theta20deg_phi120deg_alpha0deg_r180cm_h178cm.root.

mu-_1000_e1GeV_theta60deg_phi120deg_alpha30deg_r54cm_h178cm.root

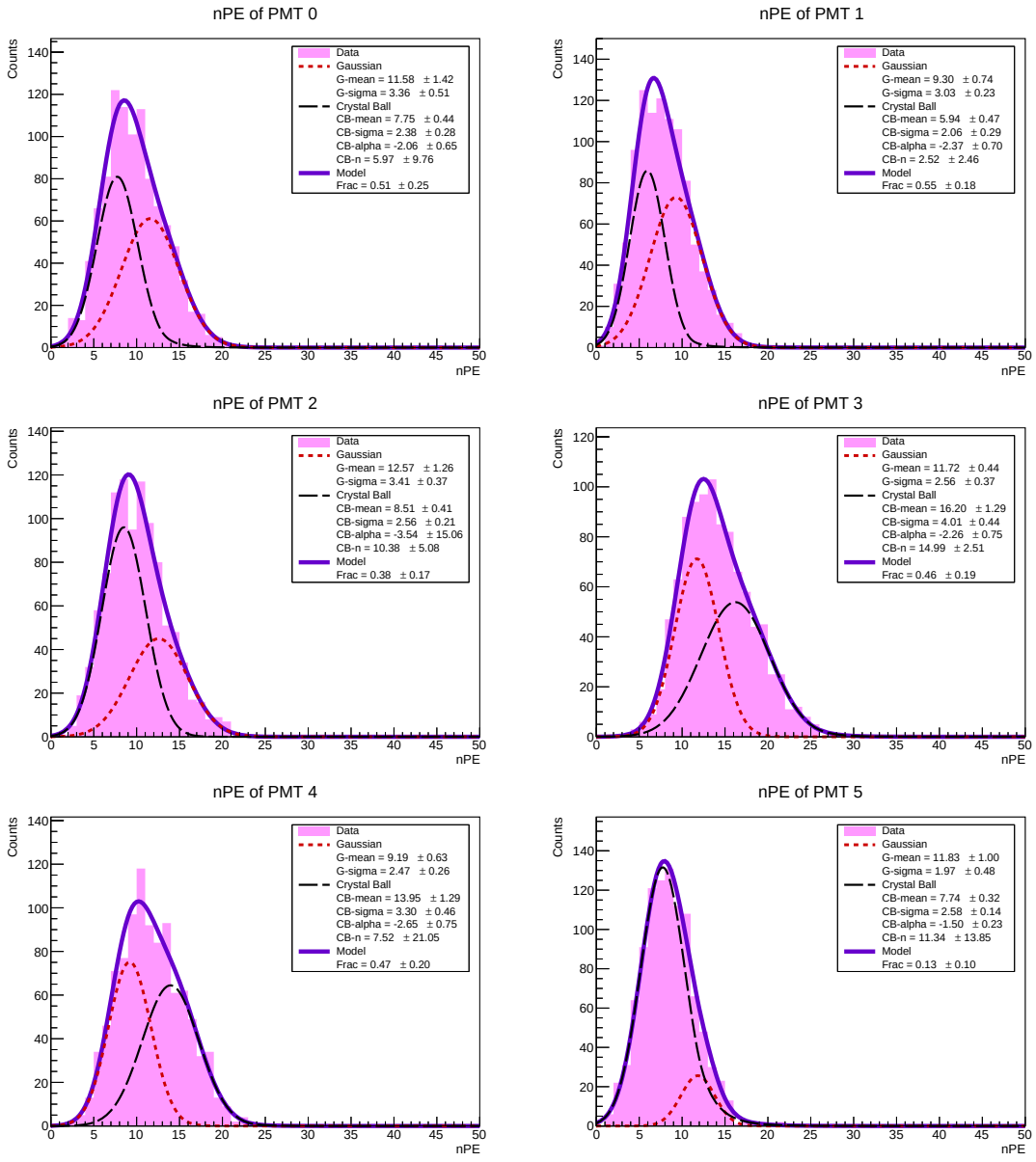

Figure 5.77: Number of photoelectrons recorded by PMTs 0 to 5, for configuration mu-_1000_e1GeV_theta60deg_phi120deg_alpha30deg_r54cm_h178cm.root.

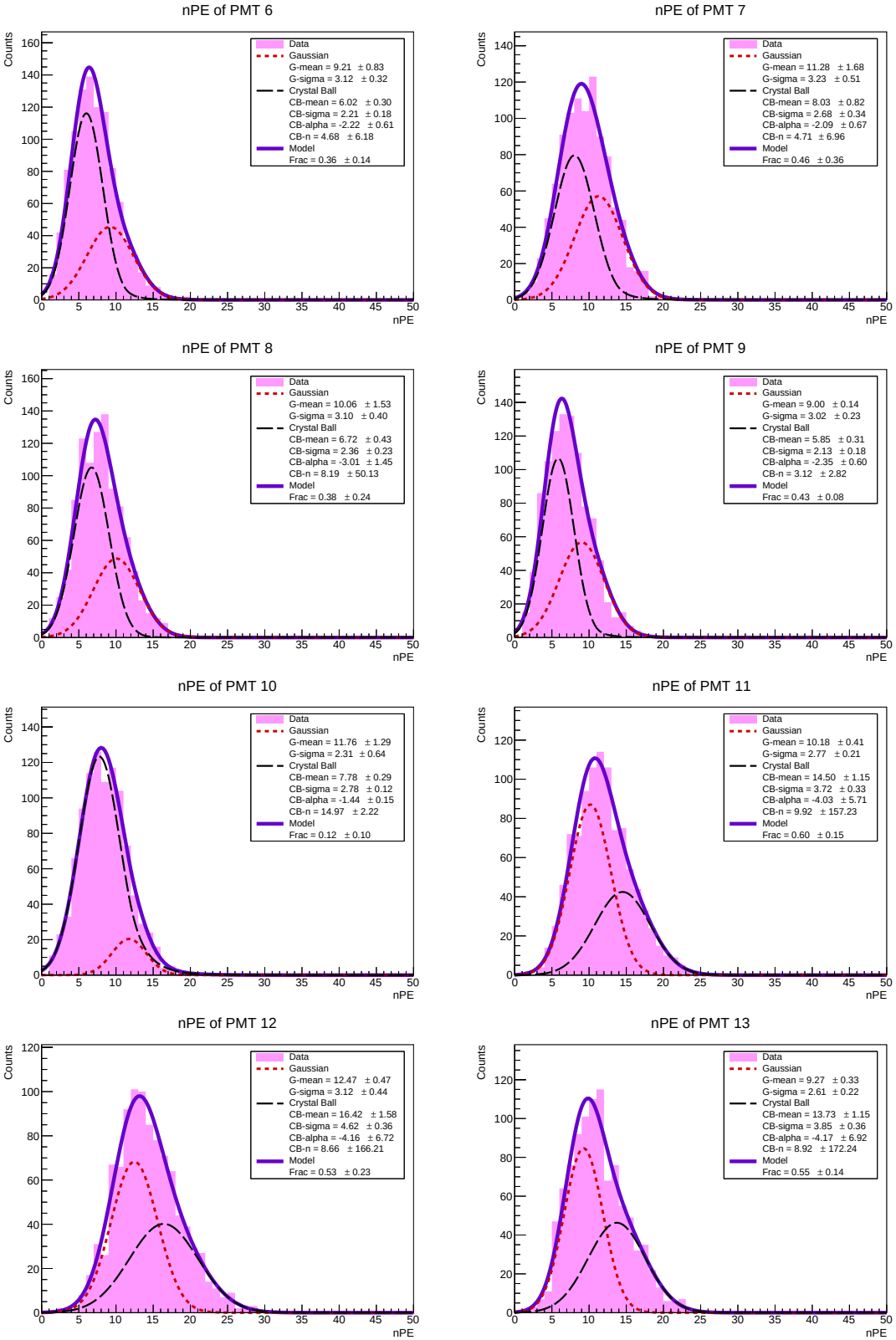

Figure 5.78: Number of photoelectrons recorded by PMTs 6 to 13, for configuration mu-_1000_e1GeV_theta60deg_phi120deg_alpha30deg_r54cm_h178cm.root.

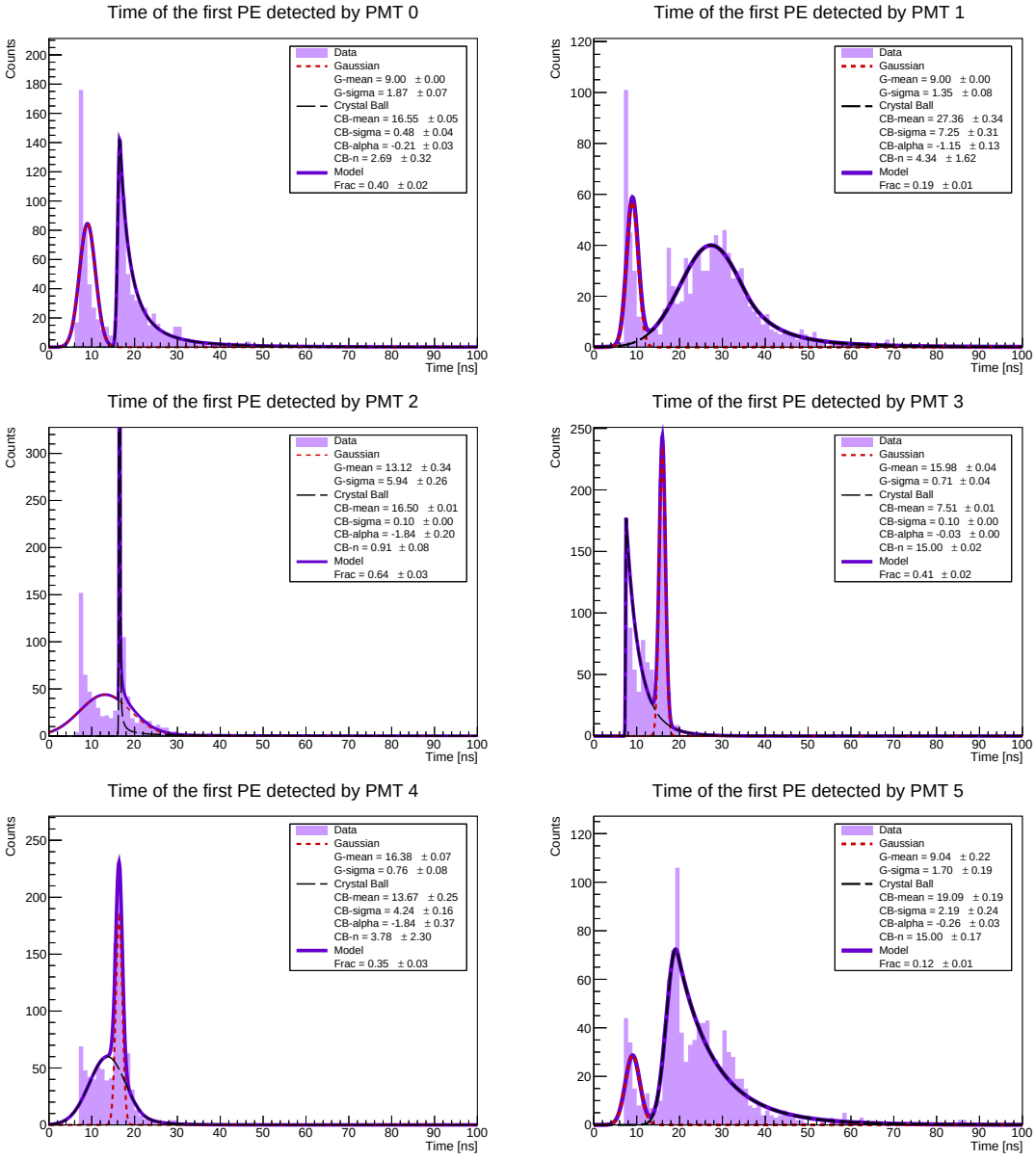

Figure 5.79: First PE arrival time (fTime) at PMTs 0 to 5, for configuration mu-_1000_e1GeV_theta60deg_phi120deg_alpha30deg_r54cm_h178cm.root.

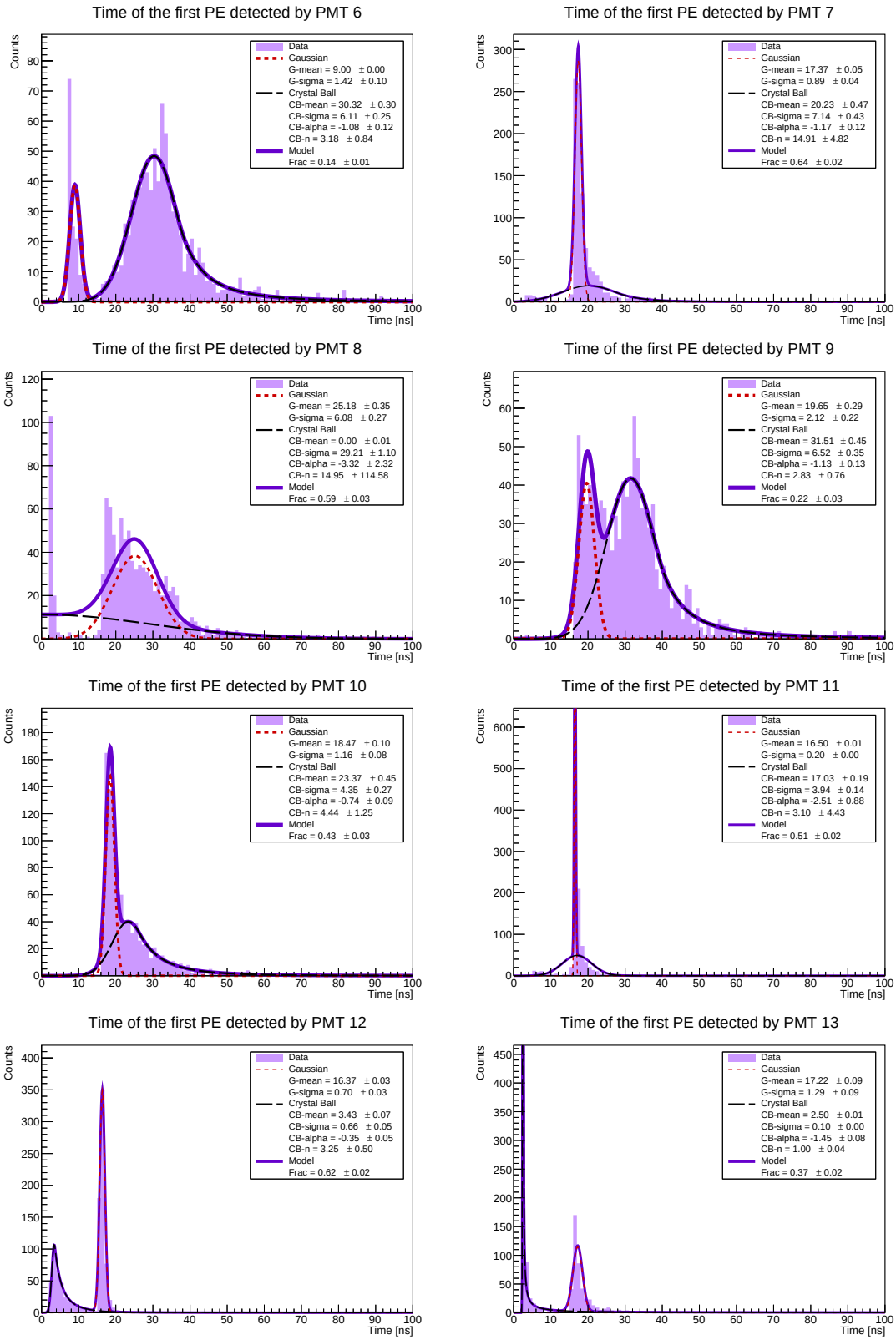

Figure 5.80: First PE arrival time (fTime) at PMTs 6 to 13, for configuration mu-_1000_e1GeV_theta60deg_phi120deg_alpha30deg_r54cm_h178cm.root.

mu-_1000_e30GeV_theta40deg_phi120deg_alpha0deg_r180cm_h50cm.root

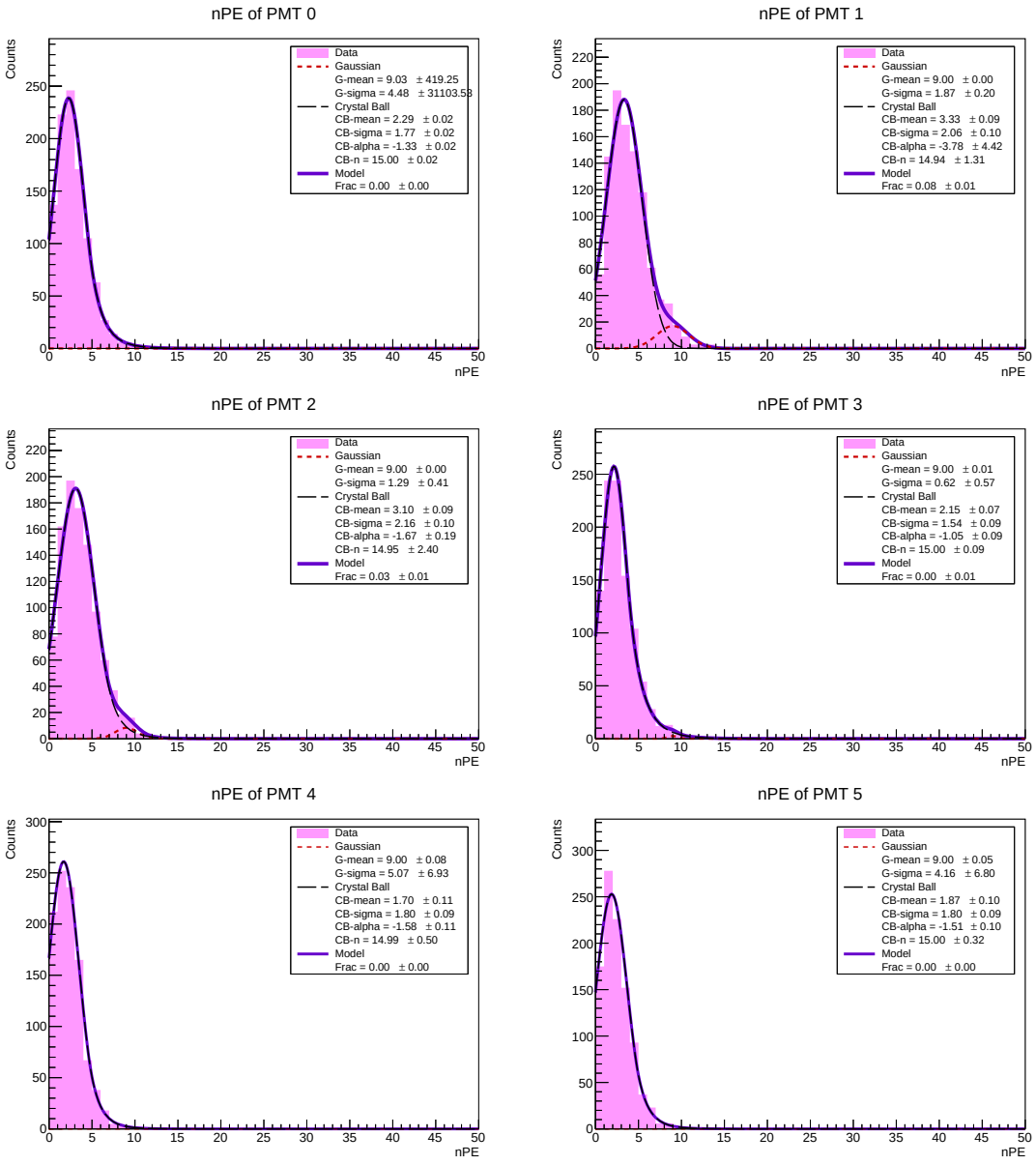

Figure 5.81: Number of photoelectrons recorded by PMTs 0 to 5, for configuration mu-_1000_e30GeV_theta40deg_phi120deg_alpha0deg_r180cm_h50cm.root.

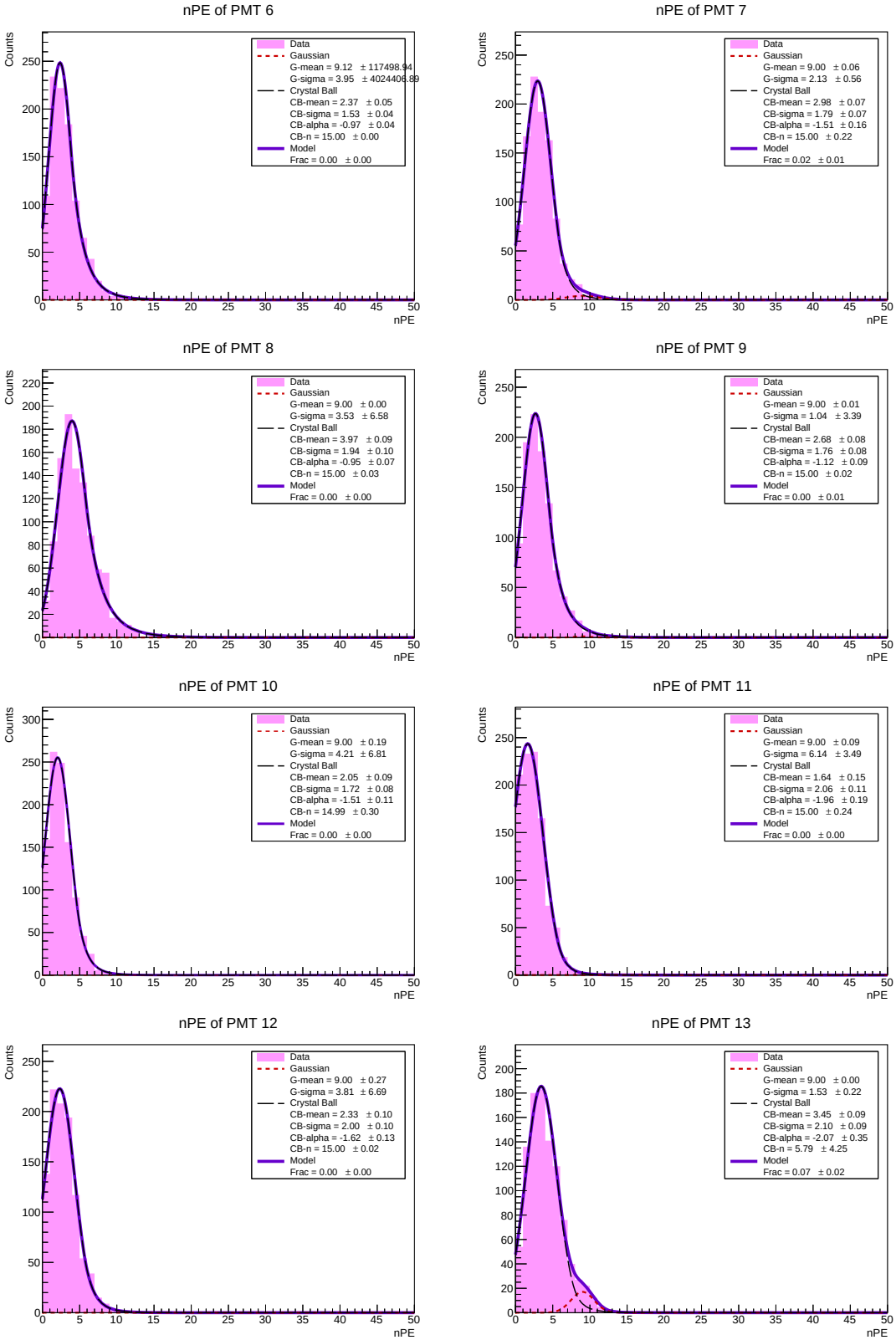

Figure 5.82: Number of photoelectrons recorded by PMTs 6 to 13, for configuration mu-_1000_e30GeV_theta40deg_phi120deg_alpha0deg_r180cm_h50cm.root.

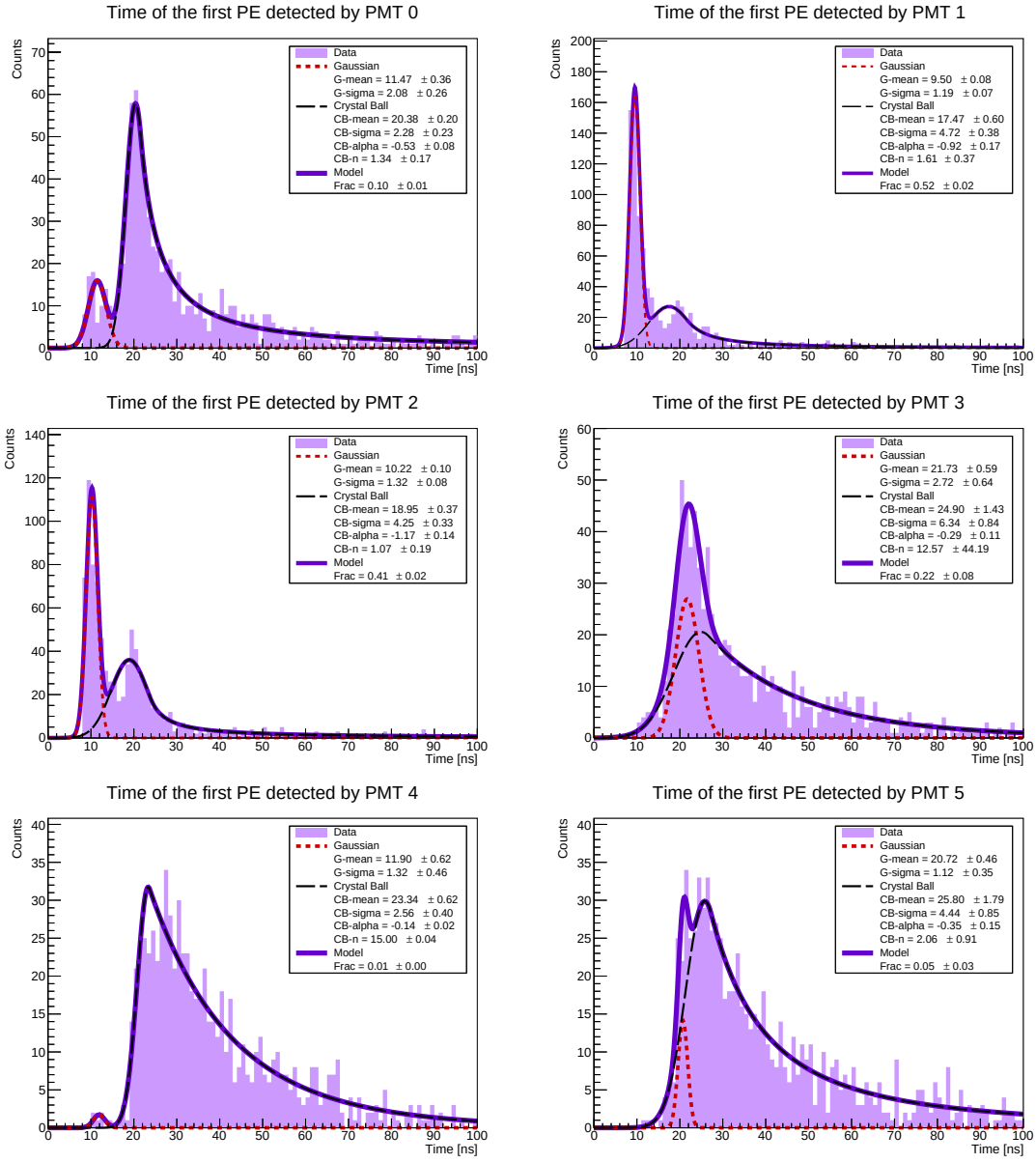

Figure 5.83: First PE arrival time (fTime) at PMTs 0 to 5, for configuration mu-_1000_e30GeV_theta40deg_phi120deg_alpha0deg_r180cm_h50cm.root.

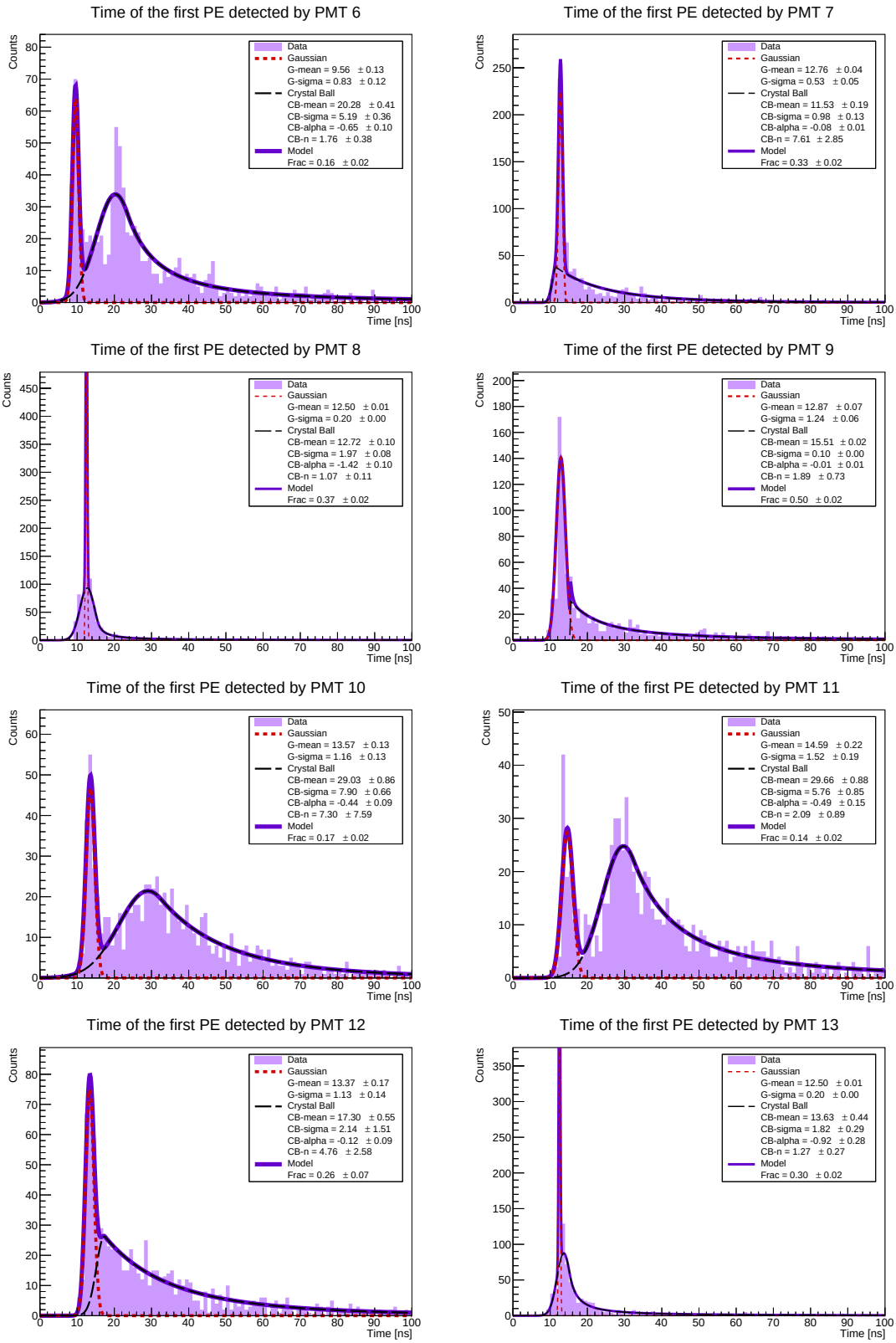

Figure 5.84: First PE arrival time (fTime) at PMTs 6 to 13, for configuration mu-_1000_e30GeV_theta40deg_phi120deg_alpha0deg_r180cm_h50cm.root.

mu-_1000_e3GeV_theta20deg_phi120deg_alpha30deg_r144cm_h178cm.root

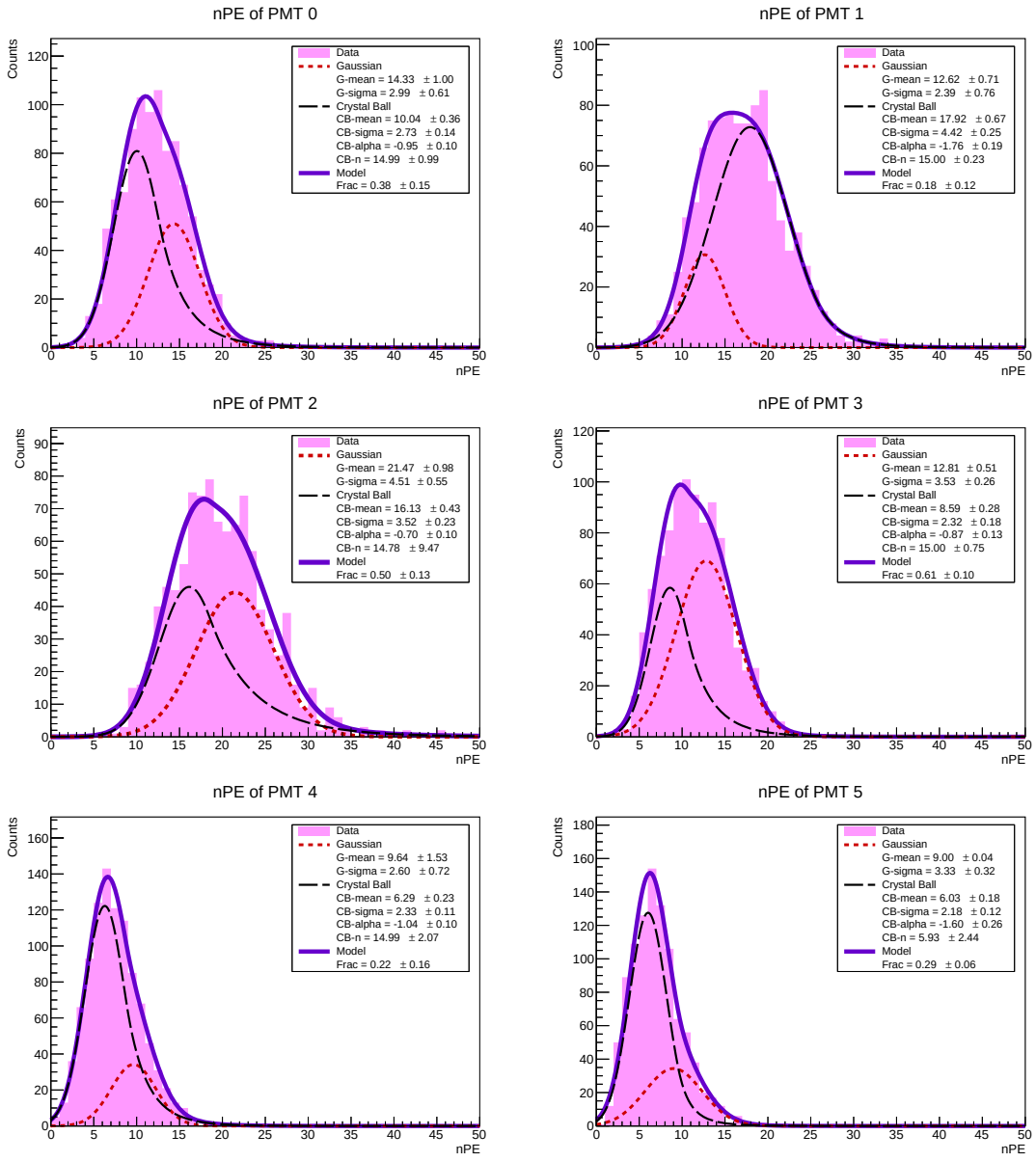

Figure 5.85: Number of photoelectrons recorded by PMTs 0 to 5, for configuration mu-_1000_e3GeV_theta20deg_phi120deg_alpha30deg_r144cm_h178cm.root.

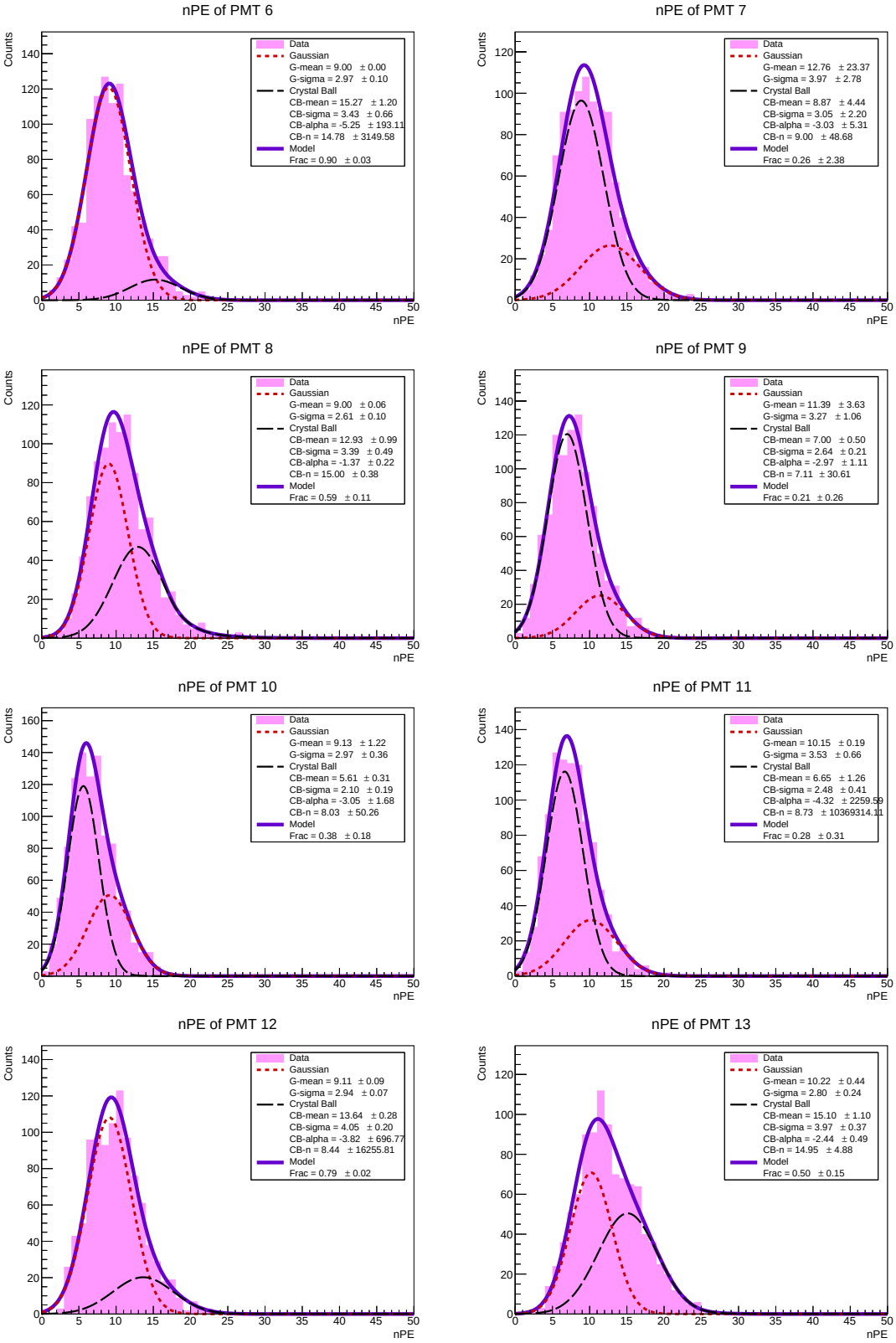

Figure 5.86: Number of photoelectrons recorded by PMTs 6 to 13, for configuration mu-_1000_e3GeV_theta20deg_phi120deg_alpha30deg_r144cm_h178cm.root.

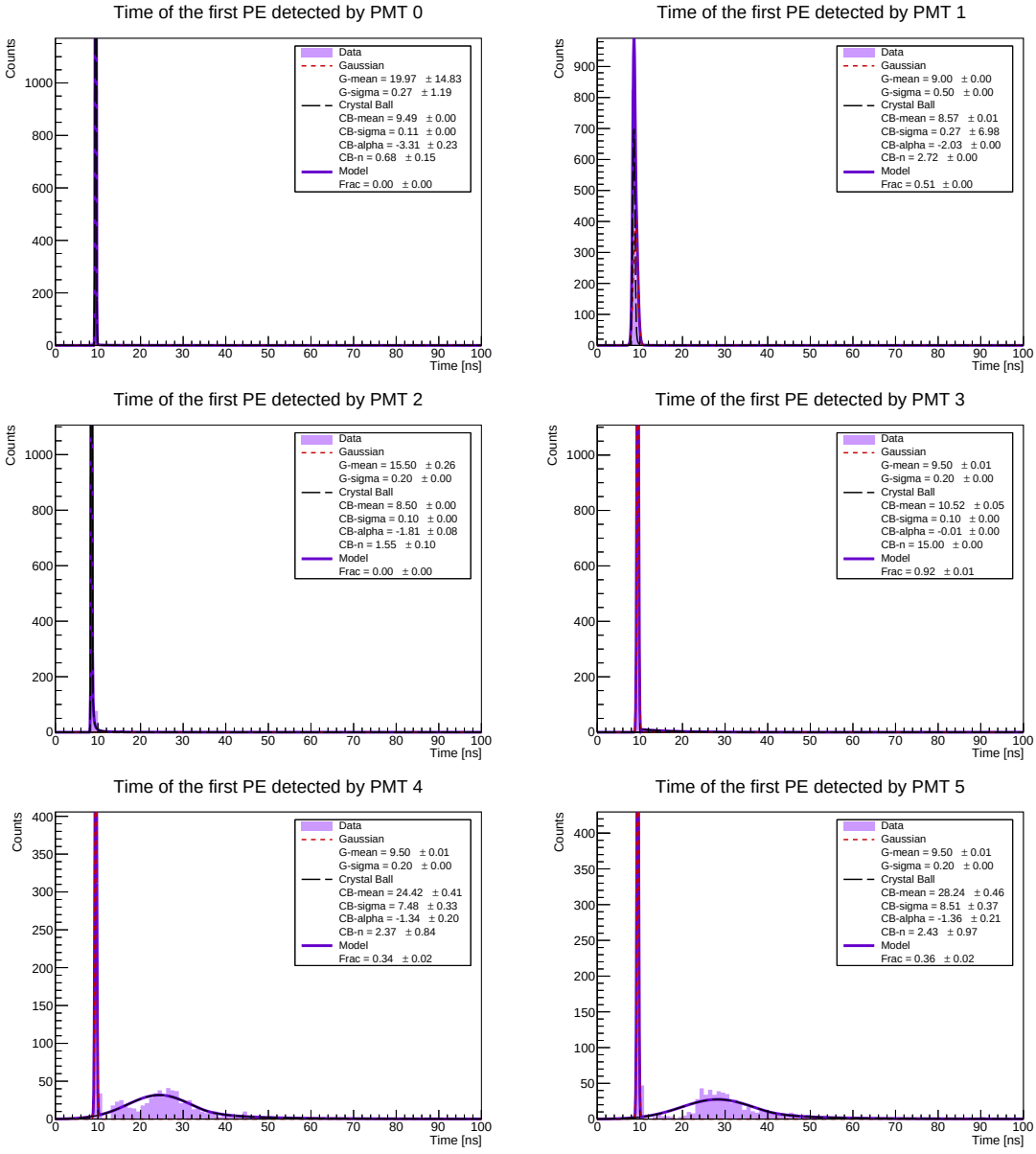

Figure 5.87: First PE arrival time (fTime) at PMTs 0 to 5, for configuration mu-_1000_e3GeV_theta20deg_phi120deg_alpha30deg_r144cm_h178cm.root.

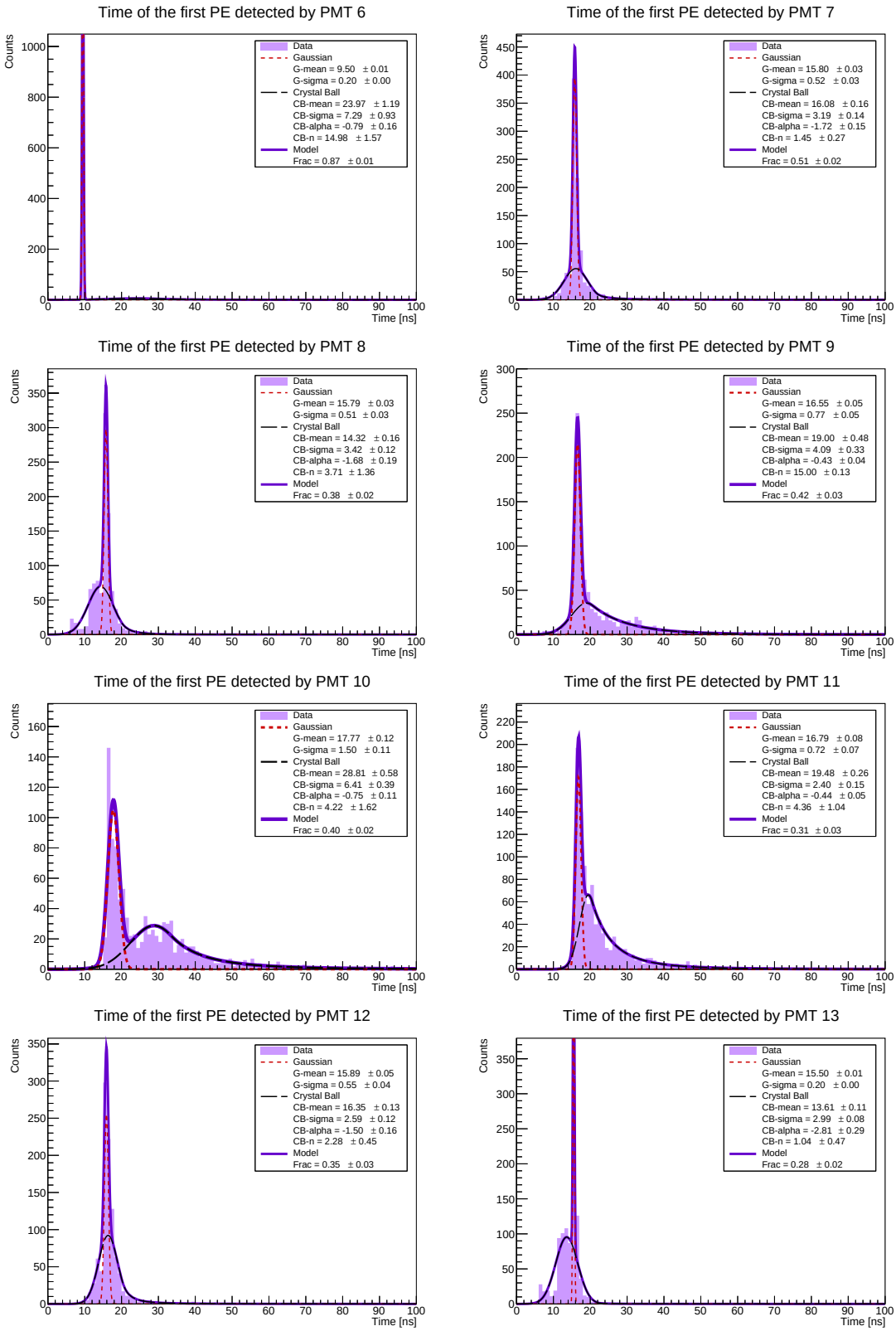

Figure 5.88: First PE arrival time (fTime) at PMTs 6 to 13, for configuration mu-_1000_e3GeV_theta20deg_phi120deg_alpha30deg_r144cm_h178cm.root.

mu-_1000_e3GeV_theta80deg_phi180deg_alpha0deg_r180cm_h75cm.root

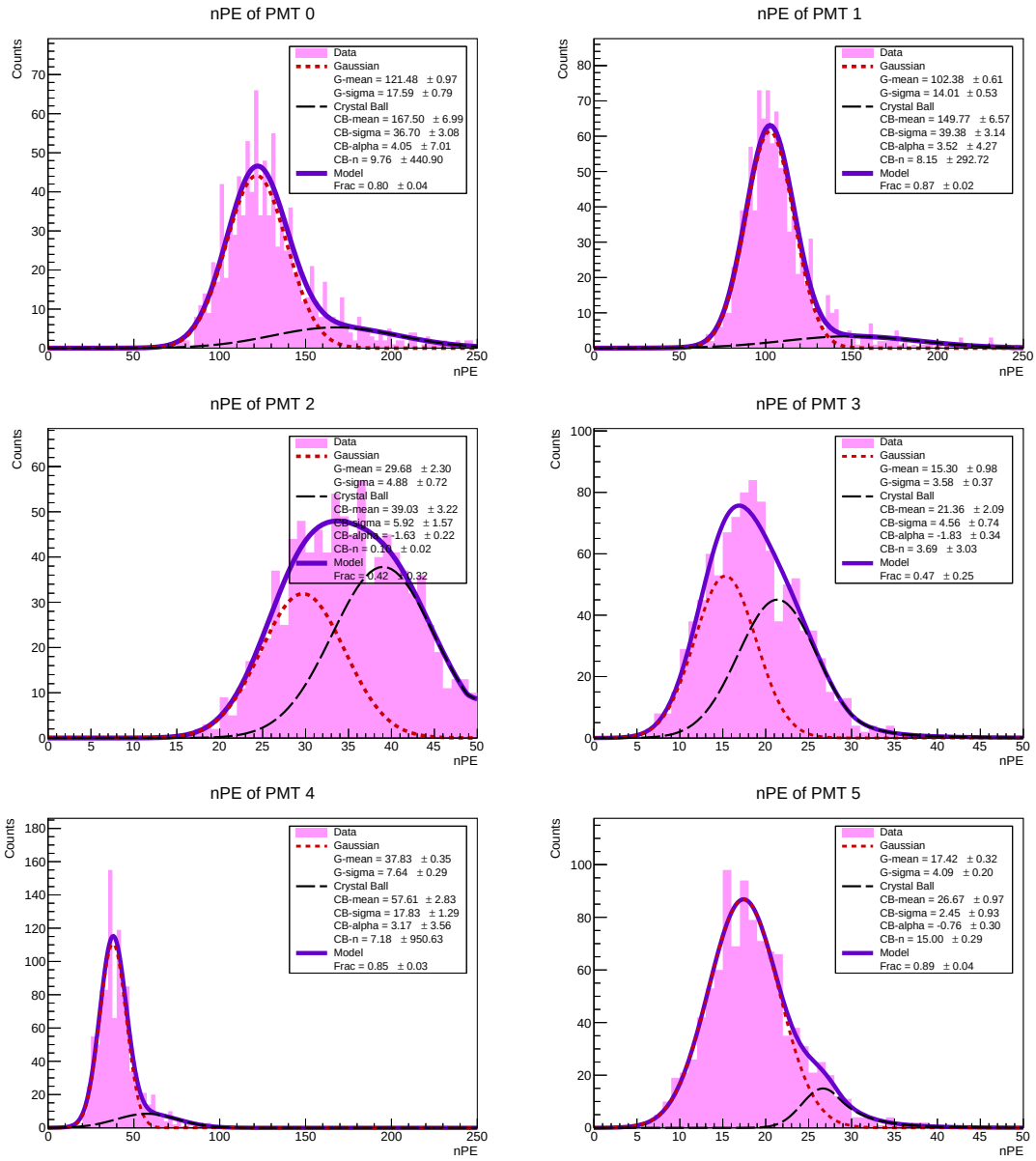

Figure 5.89: Number of photoelectrons recorded by PMTs 0 to 5, for configuration mu-_1000_e3GeV_theta80deg_phi180deg_alpha0deg_r180cm_h75cm.root.

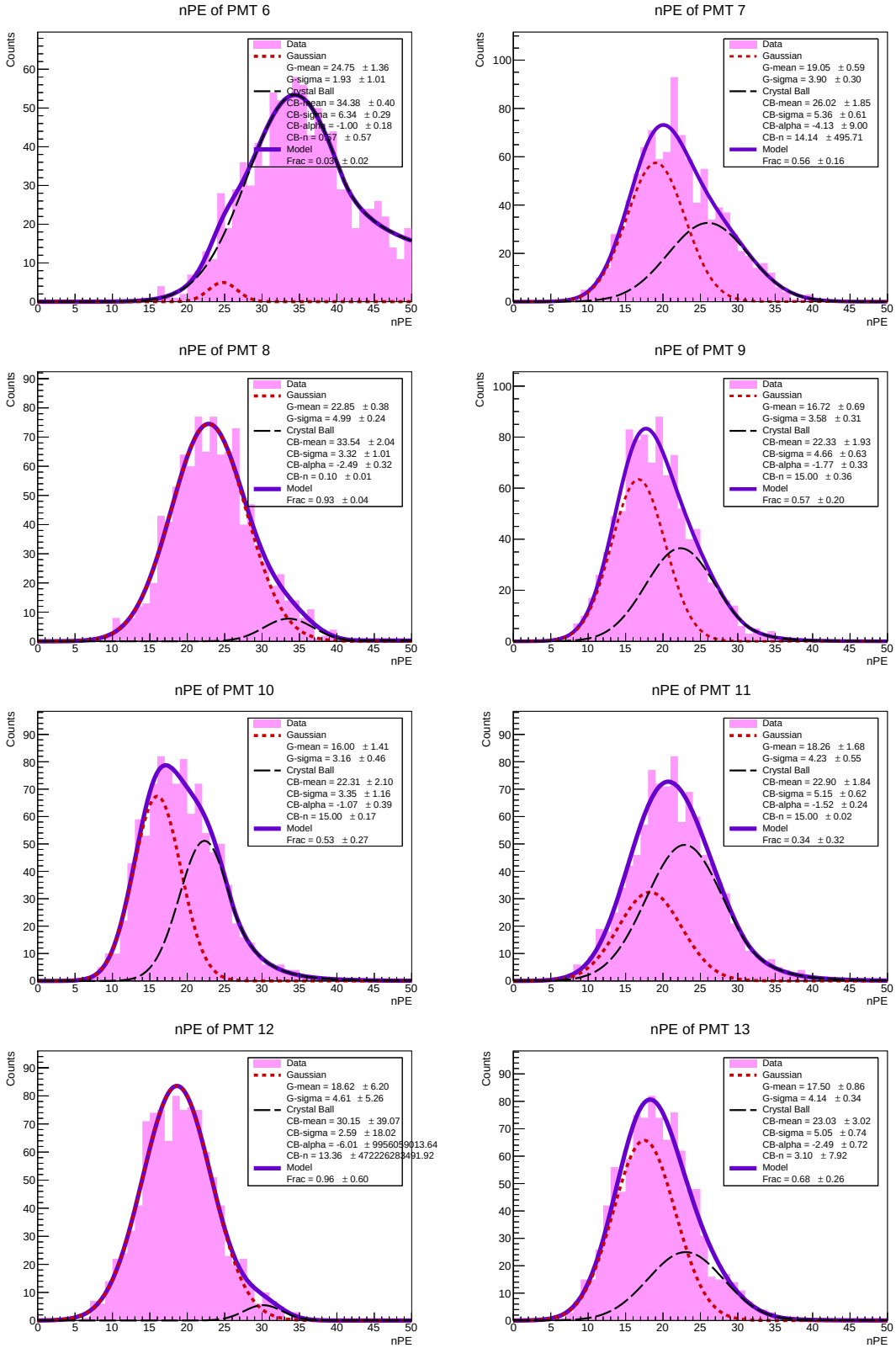

Figure 5.90: Number of photoelectrons recorded by PMTs 6 to 13, for configuration mu-_1000_e3GeV_theta80deg_phi180deg_alpha0deg_r180cm_h75cm.root.

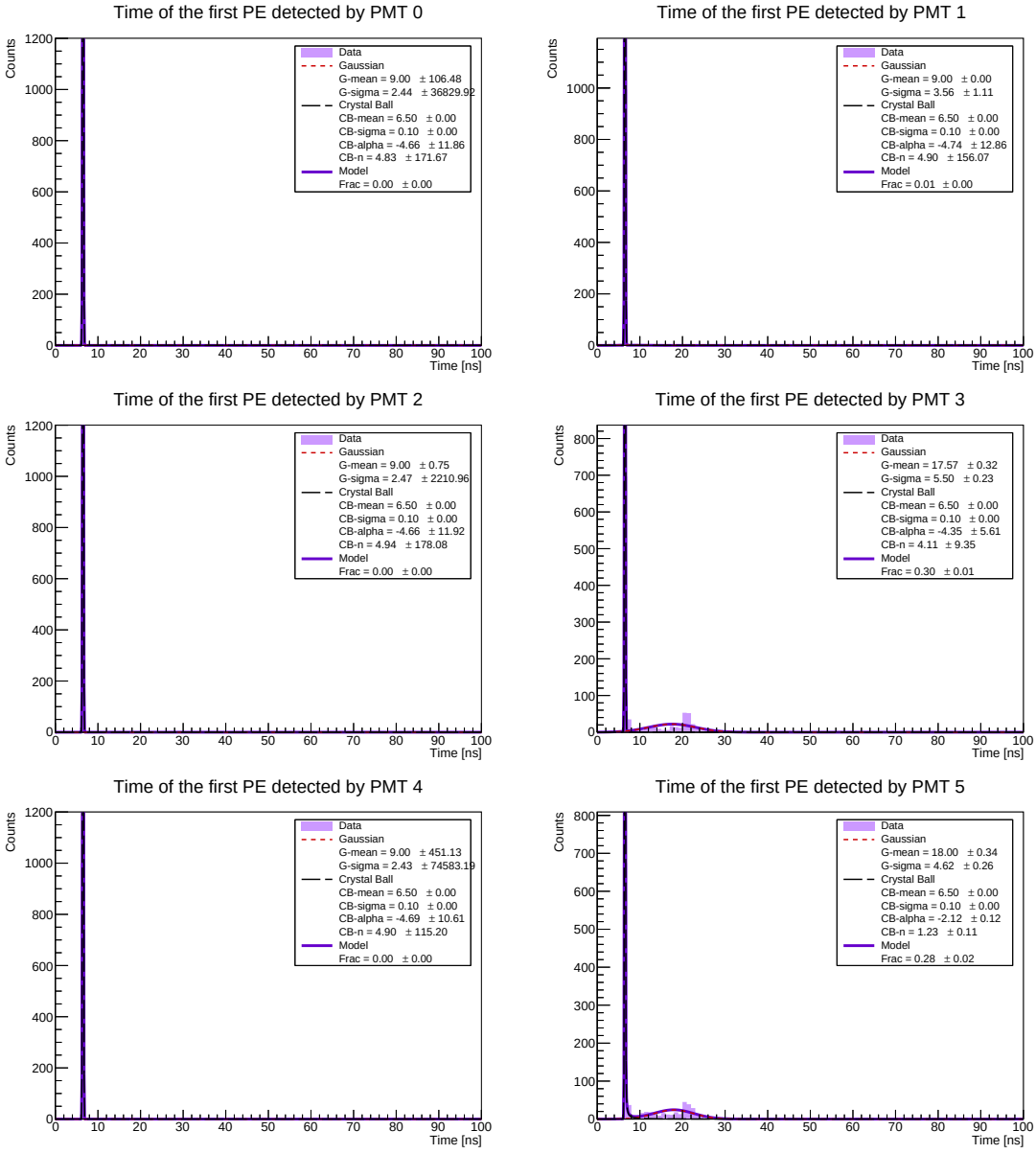

Figure 5.91: First PE arrival time (fTime) at PMTs 0 to 5, for configuration mu-_1000_e3GeV_theta80deg_phi180deg_alpha0deg_r180cm_h75cm.root.

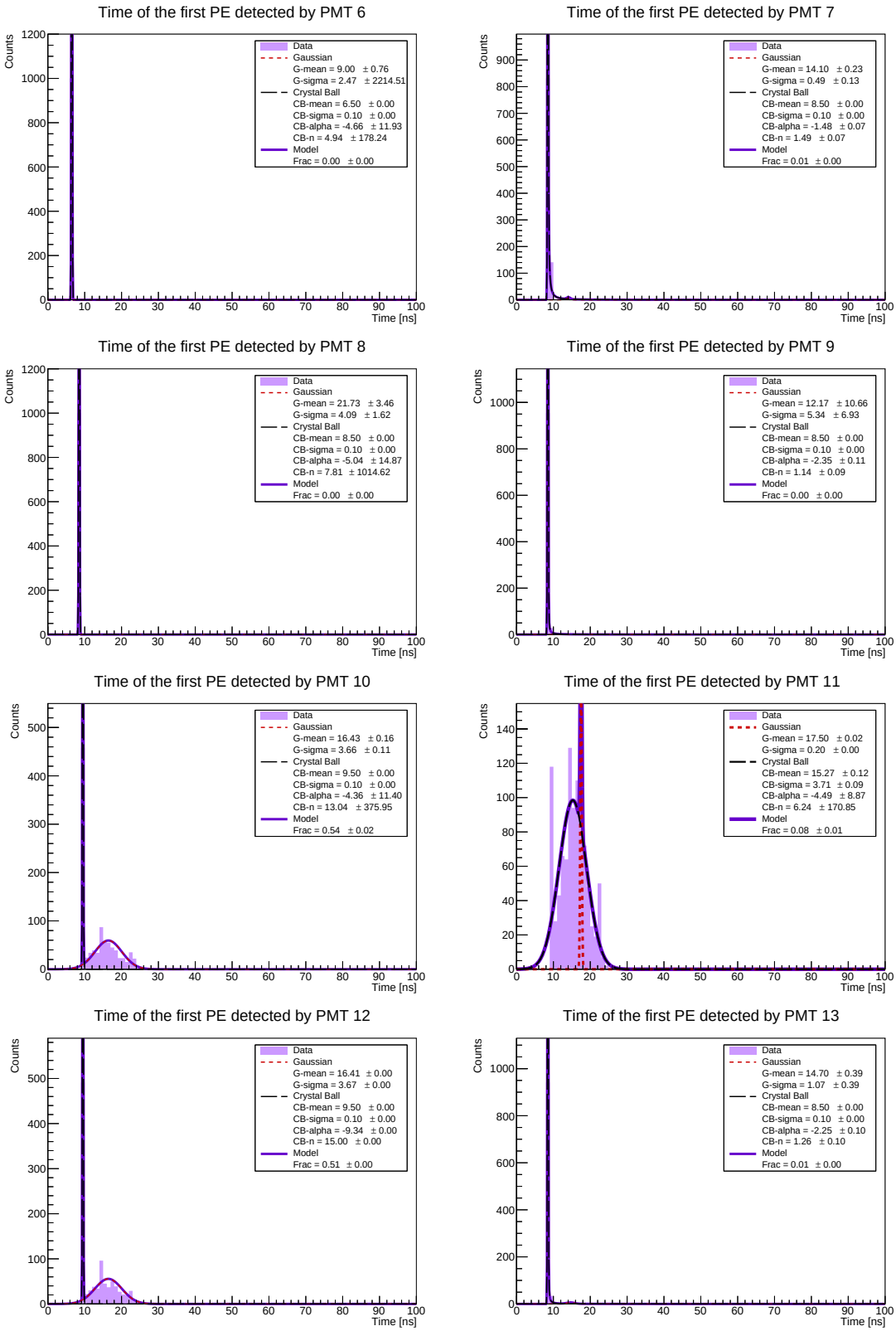

Figure 5.92: First PE arrival time (fTime) at PMTs 6 to 13, for configuration mu-_1000_e3GeV_theta80deg_phi180deg_alpha0deg_r180cm_h75cm.root.

Bibliography

[1] Paul Adrien Maurice Dirac. The quantum theory of the electron. *Proceedings of the Royal Society of London. Series A, Containing Papers of a Mathematical and Physical Character*, 117(778):610–624, 1928.

[2] Carl D Anderson. The positive electron. *Physical Review*, 43(6):491–494, 1933.

[3] Henry N Wagner Jr. A brief history of positron emission tomography (pet). In *Seminars in nuclear medicine*, volume 28, pages 213–220. Elsevier, 1998.

[4] Malcolm S Longair. *High energy astrophysics*. Cambridge university press, 2011.

[5] Paul Villard. Sur les radiations émises par les corps radioactifs. *Comptes Rendus de l'Académie des Sciences*, 130:1014–1017, 1900.

[6] Victor Hess. Über beobachtungen der durchdringenden strahlung bei sieben freiballonfahrten. *Physikalische Zeitschrift*, 13:1084–1091, 1912.

[7] Yataro Sekido and Harry Elliot, editors. *Early History of Cosmic Ray Studies: Personal Reminiscences with Old Photographs*, volume 118 of *Astrophysics and Space Science Library*. D. Reidel Publishing Company, Dordrecht, 1985.

[8] Ray W Klebesadel, Ian B Strong, and Roy A Olson. Observations of gamma-ray bursts of cosmic origin. *Astrophysical Journal, vol. 182, p. L85*, 182:L85, 1973.

[9] Maria D Caballero-Garcia. Astrophysical transients in time domain and multi-messenger astronomy: a review. *arXiv preprint arXiv:2409.15554*, 2024.

[10] P. Mészáros. Gamma-ray bursts. *Reports on Progress in Physics*, 69(8):2259–2322, 2006.

[11] C. A. Meegan, G. J. Fishman, R. B. Wilson, J. M. Horack, M. N. Brock, W. S. Paciesas, G. N. Pendleton, and C. Kouveliotou. Spatial distribution of gamma-ray bursts observed by batse. *Nature*, 355:143–145, 1992.

[12] N. Gehrels, E. Ramirez-Ruiz, and D. B. Fox. Gamma-ray bursts in the swift era. *Annual Review of Astronomy and Astrophysics*, 47:567–617, 2009.

[13] Robert Antonucci. Unified models for active galactic nuclei and quasars. *Annual Review of Astronomy and Astrophysics*, 31:473–521, 1993.

[14] Martin J. Rees. Black hole models for active galactic nuclei. *Annual Review of Astronomy and Astrophysics*, 22:471–506, 1984.

[15] CM Harrison. Impact of supermassive black hole growth on star formation. *Nature Astronomy*, 1(7):0165, 2017.

[16] Grzegorz Madejski and Marek Sikora. Gamma-ray observations of active galactic nuclei. *Annual Review of Astronomy and Astrophysics*, 54:725–760, 2016.

[17] S. R. Kelner, F. A. Aharonian, and V. V. Bugayov. Energy spectra of gamma rays, electrons, and neutrinos produced at proton-proton interactions in the very high energy regime. *Phys. Rev. D*, 74:034018, 2006.

[18] LHAASO Collaboration and Z. et al. Cao. Ultrahigh-energy photons up to 1.4 pev from 12 gamma-ray galactic sources. *Nature*, 594:33–36, 2021.

[19] S. Gabici, F. Aharonian, S. Casanova, and et al. The origin of galactic cosmic rays: Challenges to the standard paradigm. *International Journal of Modern Physics D*, 28(15):1930022, 2019.

[20] Aya Bamba and Brian J Williams. Supernova remnants: Types and evolution. In *Handbook of X-ray and Gamma-ray Astrophysics*, pages 1–12. Springer, 2022.

[21] Gianfranco Bertone, Dan Hooper, and Joseph Silk. Particle dark matter: Evidence, candidates and constraints. *Physics reports*, 405(5-6):279–390, 2005.

[22] Torsten Bringmann and Christoph Weniger. Gamma ray signals from dark matter: Concepts, status and prospects. *Physics of the Dark Universe*, 1(1-2):194–217, 2012.

[23] Andrea Albert, R Alfaro, H Ashkar, C Alvarez, J Álvarez, JC Arteaga-Velázquez, HA Solares, R Arceo, JA Bellido, S BenZvi, et al. Science case for a wide field-of-view very-high-energy gamma-ray observatory in the southern hemisphere. *arXiv preprint arXiv:1902.08429*, 2019.

[24] B.P. Abbott, others (LIGO Scientific Collaboration, and Virgo Collaboration). Multi-messenger observations of a binary neutron star merger. *The Astrophysical Journal Letters*, 848(2):L12, 2017.

[25] Peter KF Grieder. Extensive air showers: high energy phenomena and astrophysical aspects-a tutorial, reference manual and data book. 2010.

[26] R. Engel, D. Heck, and T. Pierog. Extensive air showers and hadronic interactions at high energy. *Annual Review of Nuclear and Particle Science*, 61:467–489, 2011.

[27] Laurits Tani. Monitoring the optical quality of the fact cherenkov telescope, 2020.

[28] Bruno Rossi. *High Energy Particles*. Prentice-Hall, 1952.

[29] L. Cazon, R. Conceição, M. Pimenta, and E. Santos. Extensive air showers and muon production depth. *Astroparticle Physics*, 36:211–223, 2012.

[30] Manlio De Domenico, Mariangela Settimo, Simone Riggi, and Eric Bertin. Reinterpreting the development of extensive air showers initiated by nuclei and photons. *Journal of Cosmology and Astroparticle Physics*, 2013(07):050–050, July 2013.

[31] Jorge Abraham, P Abreu, M Aglietta, C Aguirre, EJ Ahn, D Allard, I Allekotte, J Allen, P Allison, J Alvarez-Muniz, et al. The fluorescence detector of the pierre auger observatory. *Nuclear Instruments and Methods in Physics Research Section A: Accelerators, Spectrometers, Detectors and Associated Equipment*, 620(2-3):227–251, 2010.

[32] David Saltzberg, Peter Gorham, Dieter Walz, Clive Field, Richard Iverson, Allen Odian, George Resch, Paul Schoessow, and Dawn Williams. Observation of the askaryan effect: Coherent microwave cherenkov emission from charge asymmetry in high-energy particle cascades. *Physical Review Letters*, 86(13):2802–2805, March 2001.

[33] Tim Huege. Radio detection of cosmic ray air showers in the digital era. *Physics Reports*, 620:1–52, 2016.

[34] M Nagano and Alan A Watson. Observations and implications of the ultrahigh-energy cosmic rays. *Reviews of Modern Physics*, 72(3):689, 2000.

[35] WB Atwood, Aous A Abdo, Markus Ackermann, W Althouse, B Anderson, M Axelsson, Luca Baldini, J Ballet, DL Band, Guido Barbiellini, et al. The large area telescope on the fermi gamma-ray space telescope mission. *The Astrophysical Journal*, 697(2):1071, 2009.

[36] Adam Bernstein, Mary Bishai, Edward Blucher, David Cline, Milind Diwan, Bonnie Fleming, Maury Goodman, Zbigniew Hladysz, Richard Kadel, Edward Kearns, Joshua Klein, Kenneth Lande, Francesco Lanni, David Lissauer, Sharon Marks, Robert McKeown, William Morse, Regina Rameika, William Roggenthen, and Robert Zwaska. Report on the depth requirements for a massive detector at homestake. 07 2009.

[37] Vikas Joshi. *Reconstruction and analysis of highest energy γ-rays and its application to pulsar wind nebulae*. PhD thesis, 2019.

[38] R. Calderón, H. Asorey, and L.A. Núñez. Geant4 based simulation of the water cherenkov detectors of the lago project. *Nuclear and Particle Physics Proceedings*, 267-269:424–426, 2015. X Latin American Symposium of High Energy Physics.

[39] I. M. Frank and I. E. Tamm. Coherent visible radiation of fast electrons passing through matter. *Comptes Rendus de l'Académie des Sciences de l'URSS*, 14(3):109–114, 1937.

[40] A. De Angelis and M. Mallamaci. Gamma-ray astrophysics. *The European Physical Journal Plus*, 133(8), August 2018.

[41] Kristi Engel, Jordan Goodman, Petra Huentemeyer, Carolyn Kierans, Tiffany R Lewis, Michela Negro, Marcos Santander, David A Williams, Alice Allen, Tsuguo Aramaki, et al. The future of gamma-ray experiments in the mev-eev range. *arXiv preprint arXiv:2203.07360*, 2022.

[42] Felix Aharonian, AG Akhperjanian, AR Bazer-Bachi, M Beilicke, Wystan Benbow, David Berge, K Bernlöhr, C Boisson, Oliver Bolz, V Borrel, et al. Observations of the crab nebula with hess. *Astronomy & Astrophysics*, 457(3):899–915, 2006.

[43] Kevin Meagher. Six years of veritas observations of the crab nebula. *arXiv preprint arXiv:1508.06442*, 2015.

[44] Werner Hofmann and Roberta Zanin. The cherenkov telescope array. In *Handbook of X-ray and Gamma-ray Astrophysics*, pages 2787–2833. Springer, 2024.

[45] AU Abeysekara, A Albert, R Alfaro, C Alvarez, JD Álvarez, R Arceo, JC Arteaga-Velázquez, HA Ayala Solares, AS Barber, B Baughman, et al. The 2hwc hawc observatory gamma-ray catalog. *The Astrophysical Journal*, 843(1):40, 2017.

[46] Cao Zhen, Chen Ming-Jun, Chen Song-Zhan, Hu Hong-Bo, Liu Cheng, Liu Ye, Ma Ling-Ling, Ma Xin-Hua, Sheng Xiang-Dong, Wu Han-Rong, et al. Introduction to large high altitude air shower observatory (lhaaso). *Chinese Astronomy and Astrophysics*, 43(4):457–478, 2019.

[47] SWGO Collaboration. SWGO Wiki. https://www.swgo.org/SWGOWiki/doku.php, 2025. Accessed: April 14, 2025.

[48] Claudia Mignone and Douglas Pierce-Price. The alma observatory: the sky is only one step away. *Science in School*, 15:44–49, 2010.

[49] Pierre Auger Collaboration et al. The pierre auger cosmic ray observatory. *Nuclear Instruments and Methods in Physics Research Section A: Accelerators, Spectrometers, Detectors and Associated Equipment*, 798:172–213, 2015.

[50] Ulisses Barres de Almeida, Pedro Assis, Pedro Brogueira, Ruben Conceição, Luis M Domingues Mendes, Guilherme F Franco, Lucio Gibilisco, Borja S González, Luis F Mendes, Mario Pimenta, et al. The mercedes water-cherenkov detector: a multi-pmt shallow tank design proposal for ground-based gamma-ray observatories. 2023.

[51] Sebastiano Aiello, Arthur Albert, Mohammed Alshamsi, S Alves Garre, Zineb Aly, Antonio Ambrosone, Fabrizio Ameli, Michel Andre, Giorgos Androulakis, Marco Anghinolfi, et al. The km3net multi-pmt optical module. *Journal of Instrumentation*, 17(07):P07038, 2022.

[52] Gianfranca De Rosa, Hyper-Kamiokande Proto-Collaboration, et al. A multi-pmt photodetector system for the hyper-kamiokande experiment. *Nuclear Instruments and Methods in Physics Research Section A: Accelerators, Spectrometers, Detectors and Associated Equipment*, 958:163033, 2020.

[53] Vedant Basu et al. A multi-pmt optical sensor for icecube-gen2. *Journal of Instrumentation*, 16(11):C11009, 2021.

[54] Matsusada Precision Inc. How photomultiplier tubes (pmts) work, 2024. Accessed: 2025-04-15.

[55] Glenn F. Knoll. *Radiation Detection and Measurement*. Wiley, 4th edition, 2010.

[56] Hamamatsu Photonics. Photomultiplier tubes: Basics and applications. Technical report, Hamamatsu Photonics K.K., 2007. Third edition.

[57] Hamamatsu Photonics K.K. Photomultiplier tube r14374, 2024. Accessed: 2025-04-22.

[58] Dieter Heck, Johannes Knapp, JN Capdevielle, G Schatz, T Thouw, et al. Corsika: A monte carlo code to simulate extensive air showers. *Report fzka*, 6019(11), 1998.

[59] S. Agostinelli et al. Geant4—a simulation toolkit. *Nuclear Instruments and Methods in Physics Research Section A: Accelerators, Spectrometers, Detectors and Associated Equipment*, 506(3):250–303, 2003.

[60] John Apostolakis, Dennis H Wright, and Geant4 Collaboration. An overview of the geant4 toolkit. In *AIP Conference Proceedings*, volume 896, pages 1–10. American Institute of Physics, 2007.

[61] Geant4 Collaboration. *Geant4 Physics Reference Manual*. CERN, 2024. http://cern.ch/geant4/UserDocumentation/UsersGuides/PhysicsReferenceManual/html/.

[62] A Chiavassa, C Arcaro, F Bisconti, F De Nardi, M Doro, T Dorigo, T Guercio, R Lui, A Negro, M Peresano, et al. Simulation of pev atmospheric showers for swgo. In *Proceedings of 38th International Cosmic Ray Conference (ICRC2023)*, 2023.

[63] Wouter Verkerke and David Kirkby. The roofit toolkit for data modeling. In *Statistical Problems in Particle Physics, Astrophysics and Cosmology*, pages 186–189. World Scientific, 2006.

[64] M. Oreglia. A Study of the Reactions $\psi' \to \gamma\gamma\psi$. Ph.D. Thesis SLAC-R-236, Stanford University, 1980. Appendix D contains the definition of the Crystal Ball function.